SOFT X-RAY MICROIMAGING OF WHOLE WET CELLS

Dissertation By

John Richard Gilbert

In Partial Fulfillment of the Requirements
for the Degree of
Doctor of Philosophy

California Institute of Technology
Pasadena, California
1992
(submitted January 6, 1992)

At last, the chance to write the acknowledgements! Without these people I would not be here today.

First, there is my advisor Jerry Pine. Jerry first took me into his lab in the early eighties, and then again three years ago for this project. We've banged heads often, especially in the controlled chaos of running at BNL, but he's supported me beyond rational expectations.

I had a splendid time at the X1 beamline, mostly because I found a splendid group of physicists there to collaborate with and play with. They are especially Janos Kirz, who runs his group as he runs the beamline (better than anyone I know!), Chris Buckley, the best man to share a night shift with, Chris Jacobsen, who likes to calculate more than I do, Kaarin Goncz, the other Bio/Physics/Microscopist in the country (who will be writing one of these soon), and Ian McNulty, another guy who likes to brainstorm late at night. Thank you all. In no small measure these physicists gave science back to me.

The 80's were not my favorite decade. I would not have come through them at all well without a small group of faithful family, friends and colleagues. They all mean more to me than I'll ever be able to say. My parents and sister, who have, as we say, been there from the beginning. My friends, who have been ready with a lunch or a phone call or an ear through all the darkest and lightest days, Bob and Rachel Grossman, Kate and Larry Brostoff, Iris Ratowsky, Moira Feary, Roni Birkner, Sandy Heft and Elizabeth Williams. My fellow grad students in Jerry's lab, who followed me into it, and led the way out, Chi-Bin Chien and Tina Garyantes. The world glows brighter because every one of these people are in it with me.

Abstract

We have produced images of whole wet tissue culture cells with the Stony Brook/BNL scanning transmission x-ray microscope (STXM). For fixed cells we have taken images at theoretical resolutions of ~50-75nm, and in practice have measured FWHM of features down to near 100nm, without any exotic processing. For un-fixed (i.e., initially live) cells we have imaged with 100nm pixels and measured features down to 250nm.

We have developed, tested and used a wet cell for maintaining fixed or live cells on the STXM stage during imaging. Our design of the wet cell and the culture substrates that go with it make the STXM compatible with almost all standard systems for surface adherent tissue culture.

We have made measurements of radiation damage to STXM images due to the process of imaging. The damage we see in the STXM is mass loss from the sample. Our measurements give two principal results. One, the damage caused by absorption of radiation in fixed cells is a linear loss of x-ray absorbing mass with cumulative energy absorbed. Two, the measured value for the slope of that linear relationship is found to be $\alpha=-0.78\pm0.35$ in units of [C atom equivalent absorption] per [eV absorbed]. These observations allow us to model several different aspects of the imaging of fixed tissue.

We have also produced a pair of carbon and oxygen mass distribution maps of a fixed chick fibroblast that shows some differences in composition among sub-micron features. This pair of maps is the result of taking x-ray transmission images at two different wavelengths, and decomposing that data into carbon and oxygen mass maps.

Our results on radiation damage suggest that the STXM may not be able to do much better than 50nm resolution on unprotected tissue culture cells. Both the ability of the STXM to measure the radiation hardness α and its ability to produce elemental decompositions suggest that the best feature of the STXM may be its ability to provide novel types of quantitative analysis of whole wet samples at high resolution.

I Table of Contents

II List of Figures and Tables

1 Introduction

The work that this dissertation is founded on was directed towards developing tools (hardware, software and procedures) to permit the use of a Scanning Transmission X-ray Microscope (STXM hereafter) for imaging whole wet tissue culture cells. My adviser and I used the BNL/Stony Brook STXM at the National Synchrotron Light Source at Brookhaven Laboratory. We worked in collaboration with Janos Kirz's group at SUNY Stony Brook, and Chris Buckley of Kings College, London. While there are three fuctioning STXM's in the world at the moment, the one at the NSLS is certainly the most productive, in large part because it has the best light source, by using it we have produced the highest resolution and quality x-ray images of whole wet tissue culture cells. Those images form much of the content of this dissertation. The bulk of this work was done between January 1989 and late 1991. I had two considerations in mind when writing this dissertation. First, the dissertation must be a description of the the microscope, its design, its use, the images we've taken with it, as well as the benefits and limitations of using the STXM. Second, I wanted to write the dissertation mostly so that it is illuminating to biologists who are potential users of the STXM, that is biologists who at least want to get their feet wet with the details of the microscope and the physical nature of the images. This has perhaps given the dissertation a certain neither fish nor fowl flavor, falling as it does between physics and biology. I am, of course solely responsible for the compromises in each chapter, over what to include and what to leave out, and readers will have to judge for themselves the quality of those choices.

We did not design or build the microscope itself. We have been perhaps some of its most demanding users over the last few years, and have contributed to its development in that manner. What we have done is to develop an environmental chamber (the "wet cell") and tissue culture substrates (the "culture chips") that will allow essentially any conventional primary surface adherent tissue culture system to be used in the microscope. This compatibility with conventional tissue culture methods was a major design goal, since it will enable the widest possible set of biologists to make use of the microscope.

We have also developed a Macintosh software package, ObjectImage,[1] that helps to analyze and present the images produced by the BNL STXM. It has been particularly oriented towards the analysis done in chapter 5 (radiation damage) and chapter 7 (elemental analysis). The program, while functional, is not yet bulletproof enough for wide distribution (it will available as an alpha version, including source code).

For the most part we have used the microscope, to demonstrate what can be done with it now, and suggest what can be done in the future. This has involved producing some of the first data on radiation effects on images, as well as a first attempt on elemental analysis of the bulk components of tissue culture cells.

Various tools have been used in writing this dissertation, and producing the images and models that make up its parts. The dissertation was written on a Macintosh computer using Microsoft Word v4.0. Equations were set using MathType v2.0. Excel v3.0 was used for most of the graphs in the dissertation. Images were produced and analyzed in our ObjectImage software and exported in PICT format to a slide/print maker. Underlying all modelling was the images themselves and the set of soft x-ray absorption data that is available through the software package SF from Lawrence Berkeley Laboratory.[2] Actual numerical modelling and most underlying calculations were done with MathCAD v2.06. The ObjectImage software was written in Think C v4.0, a Macintosh version of C++.

What follows in this introduction is a brief perspective discussion of scanning transmission x-ray microscopy, then an outline of the dissertation itself.

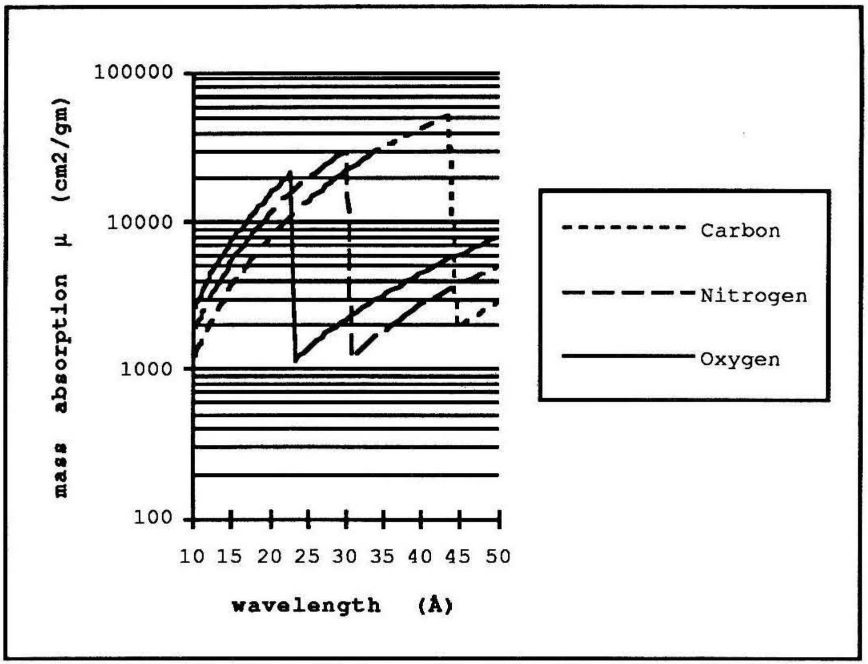

Figure 1.1 The Water Window The Mass Absorption Coefficients vs Wavelength in Å. The "water window" lies between the oxygen K edge at 23Å and the Carbon K edge at 44Å. In the window carbon gives high contrast, and water does not block much light.

1.1. A Short Perspective on X-Ray Microscopy

In order to place this work in context we'll discuss three questions: Why X-Rays? Why Scanning Transmission? How do STXM's relate to Visible Light Microscopy and Electron Microscopy?

Why x-rays? We expect visible light microscopes (without using extensive image processing) to have limiting resolution at about $s=\lambda/(2NA)$, where NA is the numerical aperture of the image forming lens (at best about 1.6) and λ is the wavelength of the illuminating light.[3] For visible light of λ=500nm s, the spatial resolution, is about 150nm. So to get better spatial resolution decreasing the wavelength makes sense. When the desired targets are biological samples, and wet ones at that, we need to have carbon give decent contrast, and water not block too much light. This suggests using soft x-rays in the "water window" from λ=23Å to λ=44Å. A look at the graphs of mass absorption coefficients of carbon and oxygen in figure 1.1 shows the nature of the water window. It is the region between the absorption edges of oxygen and carbon.

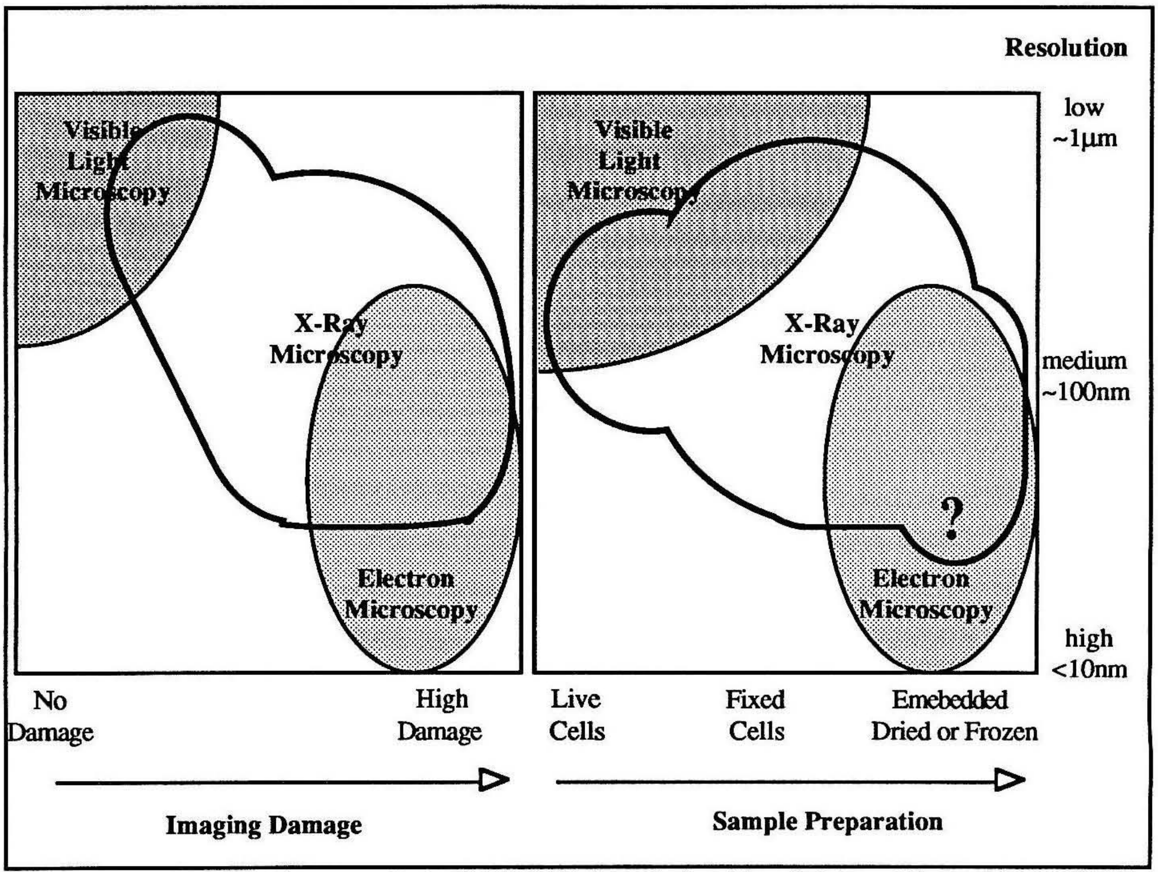

Figure 1.2 Microscopies Two sketches of the relationship of X-Ray Microscopy to Visible Light Microscopy and Electron Microscopy. Imaging Damage vs. Resolution and Sample Preparation vs. Resolution.

Why scanning transmission microscopy? The basic notion behind the STXM is that one set of optics focusses the x-rays to a narrow probe, and the sample is scanned in 2 dimensions through that probe. At each position of the sample the transmitted photons are counted, giving the raw value of the image at that pixel. While there are several working and/or proposed types of x-ray microscope,[4] this one has two advantages. One, there is only one set of optics, which operate before the sample. Two, essentially every photon that is incident on the sample is either absorbed or transmitted straight through (few are scattered) and therefore for every photon that is absorbed (and thus could damage the sample) we get a signal of 1 less photon in our detector. The first is important because the state of the art for soft x-ray focussing gives us optics that is rarely better than 10% efficient, and if that efficiency were placed after the sample, as it is in an imaging microscope with a condenser and an objective, we would get an immediate factor of 10 increase in dose applied to the sample per photon of signal in the detector. The second is important because we waste as little information as possible.

How does x-ray microscopy (XM) relate to visible light microscopy (VLM) and electron microscopy (EM)? There are three main axes on which to compare the microscopies in general. One is resolution, in which we can say that VLM < XM < EM, just due to the simple relation between wavelength and resolution we discussed above. A second axis of comparison is in damage to sample in imaging. If we use dose absorbed as an index to damage, some work has been done on modelling the relation between XM and EM,[5] and it is found that XM should inflict less dose than EM when extracting comparable information. It is generally found that VLM inflicts a negligible dose on biological specimens. A third axis of comparison is the severity of sample preparation. Just considering the simplest variations, VLM usually works with live cells (i.e., the natural state). The STXM allows imaging of whole, wet unfixed cells (initially live though they receive a lethal dose) and is also useful (and reaches higher resolutions) on whole wet fixed cells. EM usually requires at a minimum operation in a vacuum so samples must be dried or frozen, and for TEM it is usually necessary to embed and cut thin sections of tissue.

On the most simplified level it is instructive to illustrate these axes as in figure 1.2. There we see roughly the target niche of x-ray microscopy, between VLM and EM in several ways. There are complications that are left out of this simple analysis. On the one hand dose and damage are not truely the same, and specimen preparation may well harden the specimen against damage from a given dose of radiation, so such preparation may be advantageous even for XM. On the other hand aside from limits on imaging due to radiation damage, the current x-ray microscopes are limited by the state of the art in x-ray optics.[6] While the x-ray optical elements of the type we use are expected to improve, they are not expected to improve to the level of the best EM resolution (~1-2nm.) Therefore much of the virtue of XM over EM will continue to lie in causing less sample damage and requiring less extreme sample preparation.

X-ray microscopy also offers the ability to do elemental mapping of biological samples. In a transmission microscope the signal is dominated by the atomic absorptions of the elements in the sample. By taking images at different wavelengths, the relative abundances of the elements in the sample can be deduced. This has been done for calcium in samples exhibiting biomineralization,[7] and can in principle be extended to other elements. A further discussion of elemental analysis is presented in chapter 7.

1.2. Outline of the Dissertation

Beyond this introduction the dissertation has 7 chapters and 4 appendices. What follows is a brief outline for the reader. Chapters 2 and 3 present background on the STXM in general. Chapter 4 covers the Sample handling devices we have designed and built at Caltech. Chapters 5, 6 and 7 cover our results from using the STXM. And Chapter 8 is a brief conclusion to sum up this work.

1.2.1. Chapter 2 The STXM I

Chapter 2 will describe the physical parts of the STXM, what role each part plays in the microscope, and how the user aligns them and finds focus on a sample. A discussion also begins here about the parameters that describe the microscope. However, it must be remembered that the STXM is a developing microscope and has been worked with over several years. Many of its calibrations are not done automatically or frequently, though this situation is improving. The measurements and stated parameters discussed in this dissertation were correct (within stated errors) at the time each were measured. They may never have all been correct at one instant.

1.2.2. Chapter 3 The STXM II

Chapter 3 will discuss what a STXM image is, give an overview of the procedures for imaging with the STXM, and try to pin down some ways of looking at image quality. It will commence with a brief description of the computer hardware and software that controls the STXM, and acquires its images.

1.2.3. Chapter 4 The Wet Cell

Chapter 4 will start by describing the Caltech Wet Cell, both its design and operation. It will also discuss the relative merits of the Caltech wet cell design vs the LBL wet cell design, for particular imaging applications, and for effects on the STXM images taken with them. The chapter also contains a brief sketch of the two primary culture systems that have been used in the work with the STXM. Some tests will be summarized which establish that exposure in the wet cell, without x-ray irradiation, causes no significant damage to live neurons or fibroblasts. The section dealing with testing live cells in the wet cell has appeared elsewhere.[8] Finally we describe the process for fabrication of our culture chips.

1.2.4. Chapter 5 Radiation Damage

Chapter 5 will present a discussion of radiation damage in STXM imaging and the limits it imposes on resolution. It will discuss the observation of such damage on fixed cells, and the modeling of resolution of simple biological specimens. A presentation of the real data that has been acquired, along with its shortcomings, will follow. Finally the results of the measured damage are used to generate some limits on what can be done with fixed tissue, and to suggest an optimum wavelength region in which to operate the STXM.

1.2.5. Chapter 6 Cell Images

Chapter 6 will present the best images of whole wet cells that have been taken with the STXM. A few of these images have appeared elsewhere.[9] Images are included that were taken with the microscope having underlying resolution of better than 75nm on fixed cells, and 100-200nm on unfixed cells. This approaches the current diffraction limited resolution of the STXM, which at latest report[10] (this is a moving target) is about 43nm for Rayleigh resolution, reaching 36nm if the image is oversampled and deconvolution techniques are applied. Selected images of fixed chick fibroblasts and fixed rat hippocampal neurons are shown. As well as the best set of initially live fibroblast images that have been recorded. These series of images will also illustrate the flexibility of the microscope, with regard to magnification (i.e., pixel size), which lets the user zero in on regions of interest. Some quantitative feature profiles will be shown, as a demonstration of what can be resolved in the microscope.

1.2.6. Chapter 7 Elemental Analysis

Chapter 7 will present a discussion of elemental analysis in the STXM. This has been done in the past for calcium deposits in biological samples.[11] This chapter focusses on the extension of elemental analysis to bulk carbon and oxygen (or protein and water) distributions.

1.2.7. Chapter 8 Conclusion

The purpose of chapter 8 is to tie the dissertation back together. A brief discussion of what improvements can be envisioned is included, along with an attempt to sort out what are the fundamental and instrumental limits on STXM imaging.

1.2.8. Appendices

Appendix A outlines the fabrication procedure for making STXM compatible culture substrates. Appendix B is a set of mechanical drawings for the Caltech wet cell.

1.3. Chapter 1 References

---

1 J. Gilbert, ObjectImage v1.0 Manual, in preparation (1992).

2 B.L. Henke, P.Lee, T.J. Tanaka, R.L. Shimabukuro, and B.K. Fujikawa, "Low Energy X-ray Interactions: Photoionization, Scattering, Specular and Bragg Reflection," in Atomic Data and Nuclear Data Tables **27**, 1 (1982) and the SF software as described in: M.M. Thomas, J.C. Davis, C.J. Jacobsen, and R.C.C. Perera, "A Program for Calculating and Plotting Soft X-ray Optical Interaction Coefficients for Molecules," (Lawrence Berkeley Laboratory, Berkeley, 1989) document LBL-27668

3 F.A. Jenkins and H.E. White, Fundamentals of Optics, 4th ed. (McGraw Hill, 1981), p.332.

4 M.R. Howells,J. Kirz, and W. Sayre, "X-ray Microscopes," Scientific American **264**, February, pp.88-94. (1991)

5 D. Sayre, J. Kirz, R. Feder, D.M. Kim, and E. Spiller, "Transmission Microscopy of Unmodified Biological Materials: Comparative Radiation Dosages with Electrons and Ultrasoft X-ray Photons," Ultramicroscopy **2**, pp.337-341 (1977).

6 C. Jacobsen, S. Williams, E. Anderson, M.T. Browne, C.J. Buckley,D. Kern, J. Kirz, M. Rivers, and X. Zhang "Diffraction-Limited Imaging in a Scanning Transmission X-ray Microscope," submitted to Optics Communications (1991).

7 J.M. Kenney, Ph.D. thesis, State University of New York at Stony Brook, 1985.

8 J. Pine and J.R. Gilbert "Live Cell Specimens for X-ray Microscopy," in X-ray Microscopy III, edited by A.G. Michette, G.R. Morrison, and C.J. Buckley, (Springer, Berlin, to be published 1991)

More References:

9 J.R. Gilbert, J.Pine, J. Kirz, C. Jacobsen, S. Williams, C.J. Buckley, and H. Rarback, "Soft X-ray Absorption Imaging of Whole Wet Tissue Culture Cells," in X-ray Microscopy III, edited by A.G. Michette, G.R. Morrison, and C.J. Buckley, (Springer, Berlin, to be published 1991)

10 see reference 5.

11 see reference 6.

2. The STXM I (The Microscope)

2.1. Introduction to this Microscope

This chapter will describe the physical parts of the Scanning Transmission X-ray Microscope (called STXM or "stiksum"), the role each part plays in the microscope, how the user aligns them and finds focus on a sample. We'll also start the discussion of the parameters that describe the performance of the microscope. There is a very important caveat that must go before any discussion of the microscope. The STXM is a developing instrument which we have worked with over several years. Features and devices are added and modified on a monthly basis. Many of its calibrations are not done automatically or frequently (though this situation is improving over time). The measurements and parameters that we will quote were correct (within stated errors) at the time each were measured. They may never have all been correct at one instant. This is especially true since the stage was replaced in August of 1990. Also in the November 1990 run, when most of the radiation damage measurements (chapter 5) were taken, the stability of the flux/current ratio was noticeably worse than in the previous runs.

2.2. Microscope Overview

The basic concept of the STXM is as follows. Electrons in the storage ring are transversely accelerated by the X1 undulator to make x-rays. The x-rays reflect off the grating monochromator, and a slit (the exit slit) selects a narrow wavelength band that is directed onto the zone plate. The zone plate focuses the near monochromatic x-rays into a spot of about 50nm full width at half max (FWHM), at a focal length of about 1mm. The specimen is held in the focal plane of the zone plate, and its position scanned in the plane (x-y) perpendicular to the x-ray beam axis (z.) At each specimen position in the x-y plane, we dwell for a time τ while counting the x-rays which are transmitted through the specimen. In a "raw" pixel image the value at each pixel is the count of transmitted photons at the corresponding x-y position of the specimen.

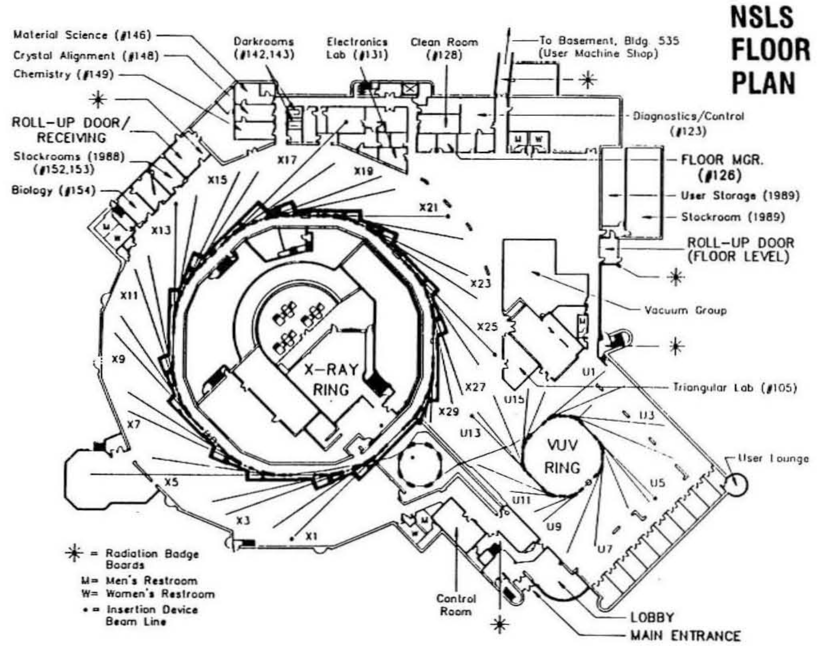

Figure 2.1 The Synchrotron The floor plan of the National Synchrotron Light Source (NSLS) X-ray ring. The microscope is located on the X1 beamline. The ring is 50ft in diameter.

For this discussion we'll divide the STXM into two parts, which we will call "source" and "instrument". The storage ring, a plan of which is in figure 2.1, and most of the beamline, sketched in figure 2.2, are the "source." while the "instrument" lies at the downstream end of the beamline, separated from the source by the vacuum exit window as in figure 2.2. The instrument itself, consisting of focussing element, sample mount, scanning stage, and detector, is illustrated in figure 2.4. The storage ring and the beam line components that we are calling the source must all be maintained and operated in ultra high vacuum (UHV), varying from 10^{-7}T at the exit window to 10^{-10}-10^{-11}T in the ring itself.

The instrument, however, is in the open atmosphere, or at times, in an helium enriched environment. The two parts of the STXM are separated by the vacuum exit window, a 1200Å silicon nitride membrane.

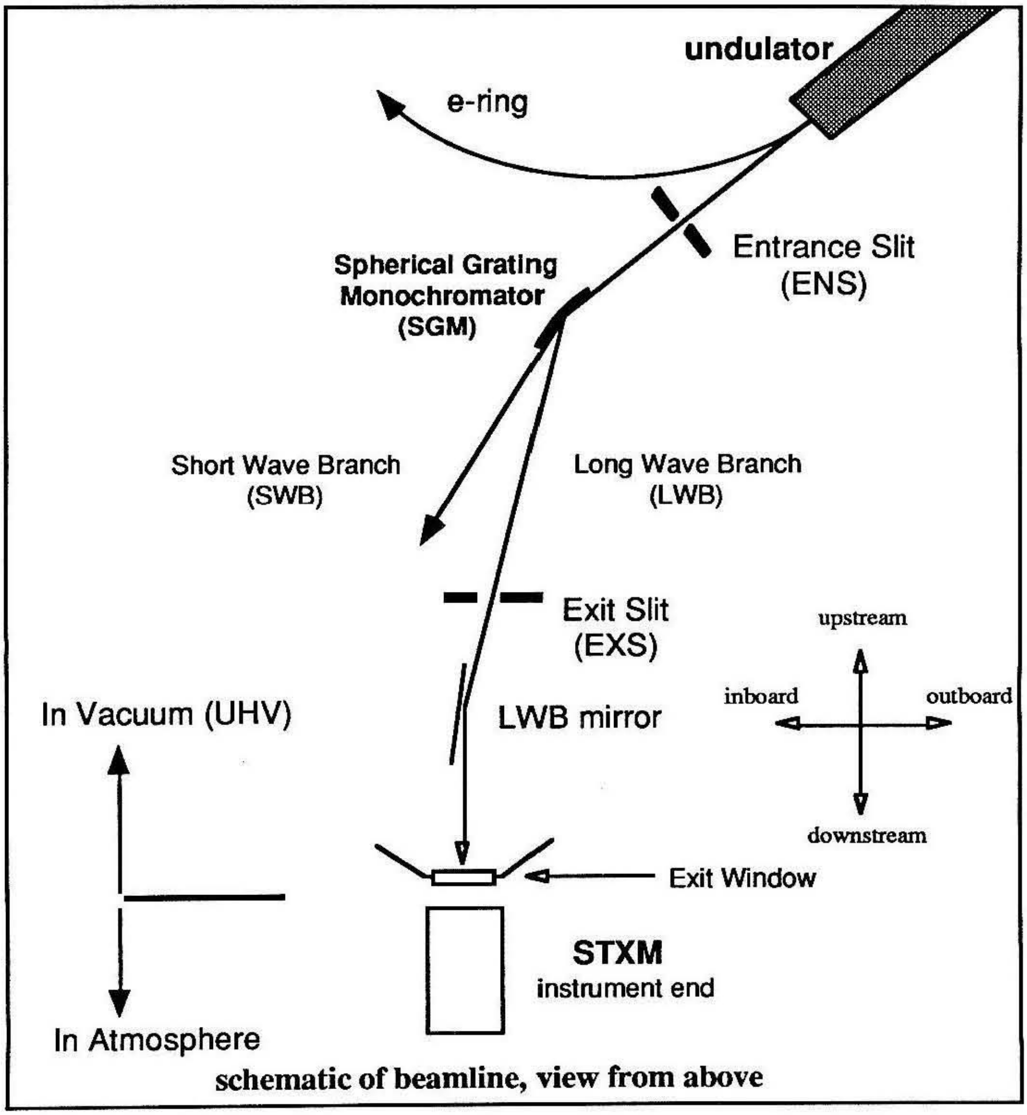

Figure 2.2 The Beamline A limited schematic of the beamline, showing only some critical elements, and the orientation system used at the synchrotron.

The rest of this chapter contains an outline of the parts of the "source" and the "instrument", then a description of the operation of the STXM which attempts to put its parts in the context of its operation. We will not try for a full discussion of each component of the STXM, though we will reference such discussions, but rather we'll try to describe them as they affect the operation of the STXM, and the user of the STXM.

In descriptions of the STXM a coordinate system is used that is conventional at the x-ray synchrotron. Upstream is towards the source of x-rays, along a beamline. Downstream is away from that source of x-rays. Inboard is to the left of each beamline when facing upstream, and outboard is to the right. As in figure 2.1 all beamlines are at start a tangent to the ring, and they extend in the clockwise direction, looking at the ring from above. This coordinate system is drawn in figure 2.2 and 2.3.

2.3. The X-Ray "Source"

2.3.1. The X-Ray Synchrotron

The NSLS x-ray synchrotron, a floor plan of which is shown in figure 2.1, provides a reliable flux of electrons circulating at 2.5GeV. It has about 30 operating beamlines at the moment. A beamline is typically arrayed along a tangent to the ring running out clockwise (when viewed from above) from the ring. The beamlines are drawn in figure 2.1, though only some are labeled. The STXM is located at the X1 beamline (just below the x-ray ring in figure 2.1.) The synchrotron ring typically is filled to a current of 190-250mA which decays exponentially to 90-100mA at which point a new fill is injected. A fill usually lasts more than 10 hours. When we have stable beamline optics, and stable electron orbits, the x-ray flux at the instrument end is directly proportional to the current in the ring. To achieve good stability of x-ray flux there is a feedback on the electron orbits through the undulator. The position of the x-ray beam is detected at the front end of the beamline and stabilized by orbit trim magnets before and after the undulator.[1,2]

2.3.2. The X1 Undulator

The undulator,[3] installed in the X1 straight section in the summer of 1988, provides a bright soft x-ray source to experiments at X1 at the NSLS. The undulator is the first element in the beamline, as shown in figure 2.2. An undulator[4] is a periodic array of magnets that, when in place in a straight section of the electron ring, wiggles the electron beam transverse to its unmodified path. If the maximum deflection angle of the beam is less than the angular aperture of the cone of synchrotron radiation ($\sim\gamma^{1}$) then the array is considered an undulator. For sufficiently strong transverse fields and large N the flux in the forward direction will be especially concentrated at wavelengths that are near λ_1 as given in equation 2.1 and its odd harmonics. λ_0 is the period of the undulator and θ is the angle of observation (usually near 0.) K is a factor dependent on the magnetic field intensity B_0. The fundamental at λ_1 can be moved by changing K. In the X1 undulator this is done by varying the vertical gap size, between poles of the transverse magnets, and so changing B_0. This can vary the peak of the flux from 17Å to 70Å. Such changes in the gap change the x-ray spectrum at all elements of the beamline. From the point of view of a user of the microscope a gap change is simple, but takes 5 - 10 minutes at least, more if the user is required to give advance warning of the change to the synchrotron control room.

$$\lambda_1 = \left(\frac{\lambda_0}{2\gamma^2}\right)\left(1 + \frac{K^2}{2} + \gamma^2\theta^2\right) \qquad K \propto B_0\lambda_0 \qquad [2.1]$$

Further discussion and observations of the flux provided by the undulator at various gaps are given in the next chapter, when we discuss estimating the incident flux in section 3.4.

2.3.3. The SGM -- a grating monochromator

The spherical grating monochromator,[5] (the SGM), is sketched in figure 2.3, along with its entrance slit and exit slits. The entrance slit, upstream of the SGM, collimates the x-ray beam from the undulator. The two exit slits, at fixed angles ϕ_S and ϕ_L collect first inside order reflected flux from the grating. The slit at ϕ_S provides a narrow band of wavelengths to the short wave branch (or SWB) while the one at ϕ_L provides a narrow band to the long wave branch (or LWB.) Selection of the center wavelength of the band that goes through the exit slit is done by adjusting the angles θ_1 and θ_2 by tilting the SGM relative to the beam. $\theta_1+\theta_2= \pi - \phi_L$ remains fixed, and the relation between the wavelength at the center of the LWB exit slit and θ_1 and θ_2 is given by the grating equation,[6] which is equation 2.2, where d is the spacing on the grating.

$$\sin\theta_1 - \sin\theta_2 = \frac{\lambda}{d} \qquad \theta_1, \theta_2 > 0 \qquad [2.2]$$

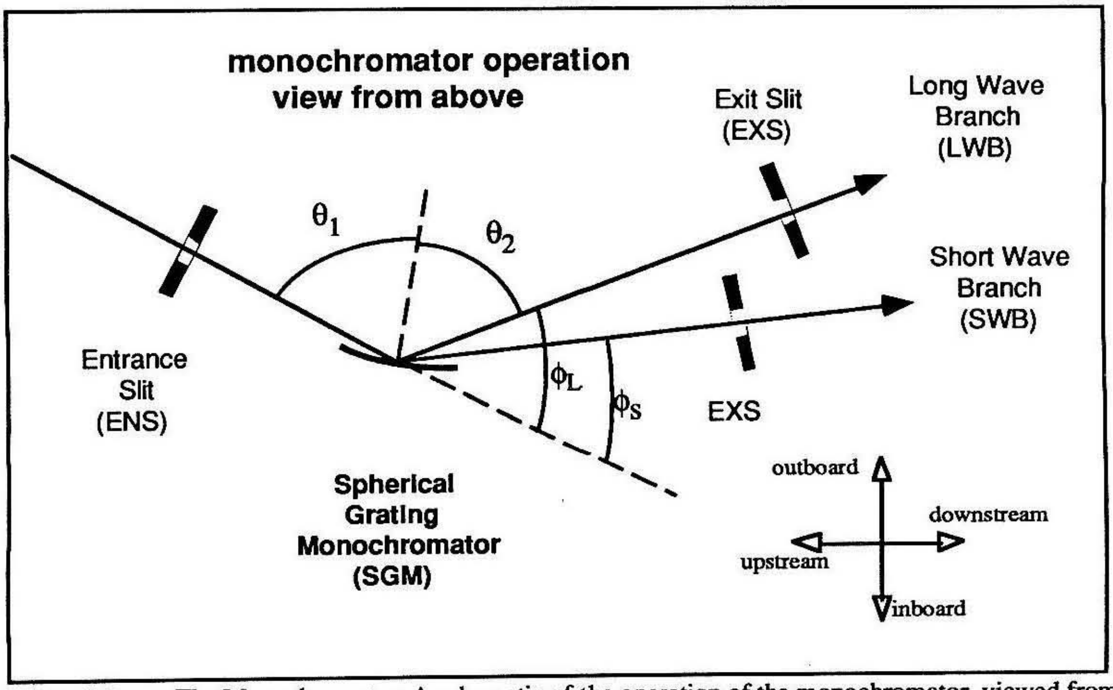

Figure 2.3 The Monochromator A schematic of the operation of the monochromator, viewed from above. Showing monochromator entrance slit, ENS, exit slits, EXS for the 2 downstream branches, the Long Wave Branch (LWB) and the Short Wave Branch (SWB).

The result of this design is that both branches of the beamline may operate at the same time, though their operating wavelengths are not independent, that is they change together as the SGM is tilted. The bandwidth ($\Delta\lambda/\lambda$) or resolving power ($\lambda/\Delta\lambda$) is controlled by opening and closing the exit slits. A resolving power of up to 1800 can be achieved on the long wave branch.[7]

Usually the long wave branch will be receiving photons of the fundamental peak of the undulator, while the short wave branch will at the same time be operating on or near the second harmonic of the undulator. The LWB operates over $20Å<\lambda<70Å$, while the SWB operates over $16Å<\lambda<25Å$. The STXM is mounted on the long wave branch, and we will not discuss the SWB any further. The SGM has a radius of curvature of 40m, and it also serves to concentrate the flux incident on the zone plate along the horizontal axis.

2.3.4. The Long Wave Branch

Downstream from the monochromator we have the long wave branch (LWB) exit slit, followed by the LWB mirror. Several different mirrors can be mounted in this position, for different effects. This mirror adds to the separation between the branches, which is convenient for purely mechanical reasons (more space is available to work in between the branches). It is also possible to use a curved mirror here to concentrate the x-ray flux along the vertical axis. Such refocussing can in principal add up to a factor of 10 to the flux incident on the zone plate. When we tried this during our runs, it led to a separation of the focal planes in x and y, causing some degradation in resolution. We found that the increased flux was not worth operating at lower resolution, therefore we did not do much imaging with vertical refocussing.

Downstream of the LWB mirror we have the vacuum exit window, a 1200Å silicon nitride window, about 250μm square. This is strong enough to hold 1atm without breaking (though it does flex), and is similar in material to the windows of the Caltech wet cell described in chapter 4.

2.4. The "Instrument"

After the exit window, the rest of the microscope is in the open atmosphere. In the most common usage this part of the microscope is considered the STXM. Figure 2.4 summarizes its parts. The five basic components are: the exit window on the snout of the beamline, the zone plate, the order sorting aperture (OSA), the wet cell (or sample mount), and the proportional counter (PC). Each of these is separately mounted mechanically, with independent x, y, and z micrometers, or in the case of the specimen mount, stepper and piezoelectric (pzt) drivers. Their relative positions must be adjusted to align and focus the microscope. This alignment, of the parts with each other,and to the x-ray beam provided by the upstream parts of the beamline will be discussed later.

Since the instrument is at atmospheric pressure and only imperfectly enclosed, and air is capable of considerable absorption of soft x-rays we continuously flow helium into the spaces upstream aand downstream of the wet cell. The helium inlets are illustrated in figure 2.4 and are located below the zone plate and the proportional counter.

Each of the 5 principal parts labeled in figure 2.4 has a plane where its action takes place. The plane of the exit window itself, the zone plate membrane, the plane of the aperture of the OSA, the specimen plane of the wet cell, and the front window of the PC. All these are perpendicular to the plane of the drawing in figure 2.4. When correctly aligned all these planes should be parallel to each other and perpendicular to the x-ray beam axis(though the parallelness of the exit window and the PC is not at all critical. Parameters that are important for the modelling of the microscope, and estimating its flux losses are labeled at the top of figure 2.4. They are Z_{ex}, the distance from exit window to sample; f, the focal length; Z_{wcell}, the air gap in the wet cell, and Z_{pc}, the distance from exit window of the wet cell to the proportional counter window.

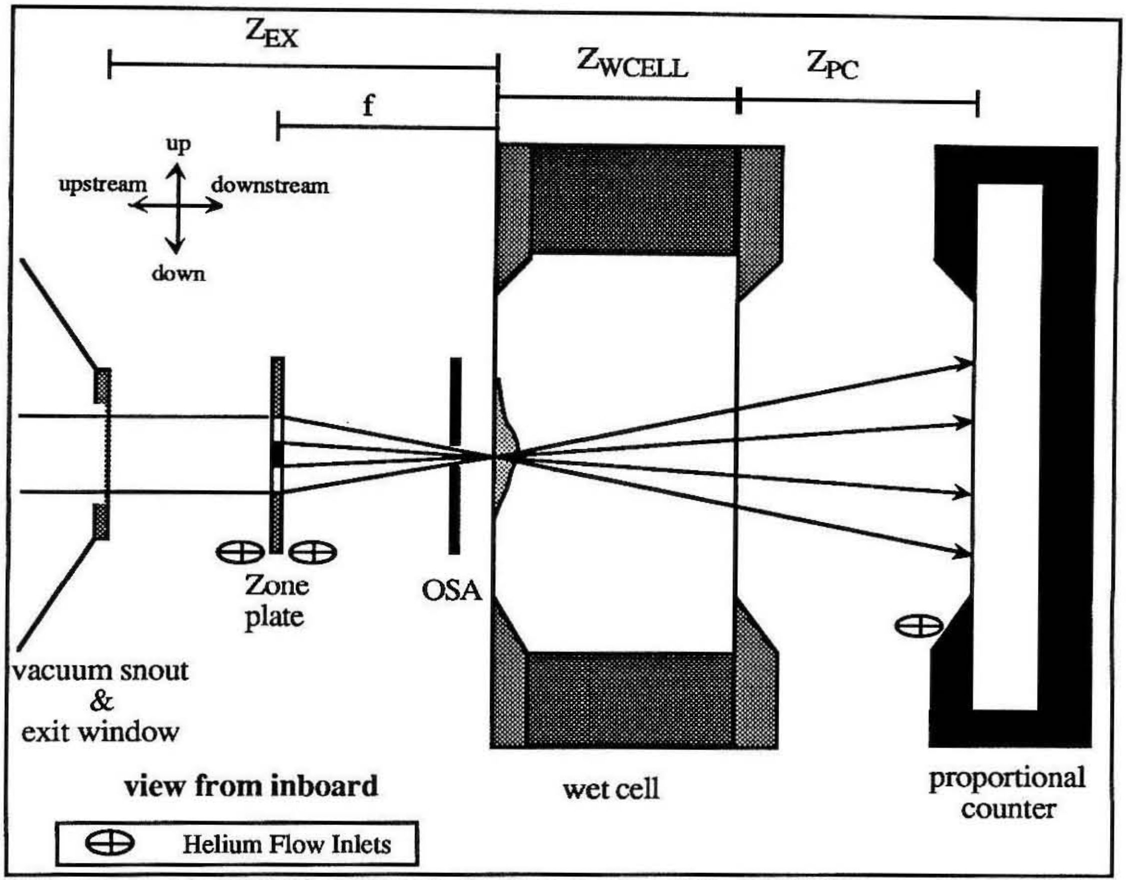

Figure 2.4 The STXM from Inboard A schematic view of the STXM from vacuum exit window to the proportional counter. The view is from inboard. The functional parts are; the exit window on the vacuum snout, zone plate, order sorting aperture (OSA), caltech wet cell, and the proportional counter (PC). Helium flow inlets are illustrated below the zone plate and PC.

2.4.1. The Zone Plate and OSA

The STXM uses a fresnel zone plate to form a focussed beam of x-rays. A good basic description of zone plates, from which this discussion is derived, is found in reference 6 chapter 8. The simplest type of zone plate is formed by alternating opaque and transmissive annular zones in a disk. A zone plate focuses light of wavelength λ at a distance f from its center by constructive interference. Figure 2.5 provides a sketch of the dimensions. We illuminate the zone plate from the left by a plane wave. We let r_0 be the radius of the start of the first zone (an open one) and r_n be the radius of the end of the n^{th} zone. If we let the path length difference be $s_n - s_0 = n\lambda/2$ then since every other zone is open, all the open zones constructively interfere. Substituting for s_n and s_0 we get equation 2.3. Solving for r_n gives equation 2.4, which reduces to equation 2.5 in the regime $r_0 << f$ and $n\lambda << f$. These are very good approximations for the current generation of x-ray zone plates.

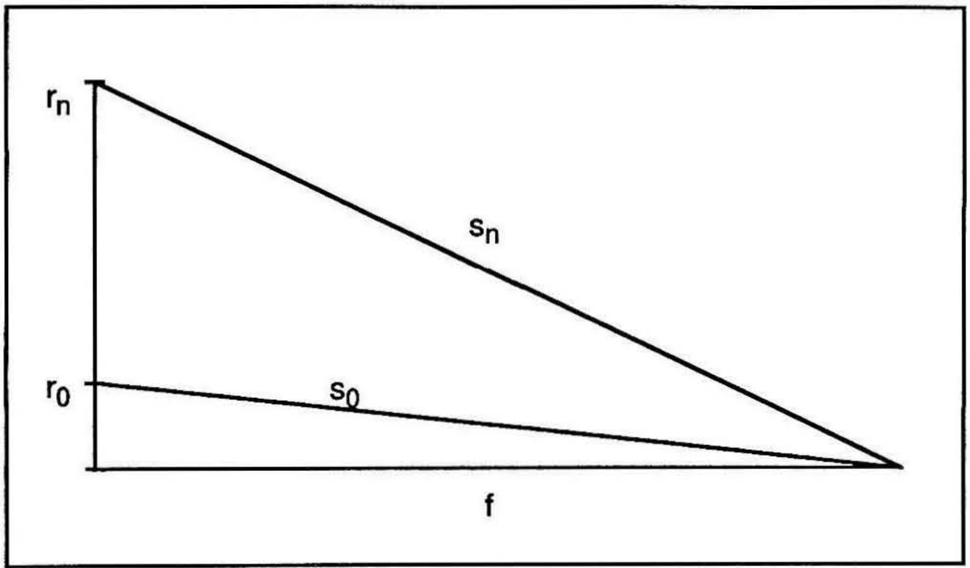

Figure 2.5 Radii of Zones A simple drawing to show zones starting at r_0 and r_n, and their corresponding path lengths s_0 and s_n to the focus a distance f from the zone plate. This drawing corresponds to a derivation in which a plane wave is incident on the zone plate from the left.

$$\sqrt{\left(r_n^2 + f^2\right)} - \sqrt{\left(r_0^2 + f^2\right)} = n\frac{\lambda}{2} \qquad [2.3]$$

$$r_n^2 = \left(n\frac{\lambda}{2}\right)^2 + r_0^2 + n\lambda f\sqrt{\left(1 + \left(\frac{r_0}{f}\right)^2\right)} \qquad [2.4]$$

$$r_n^2 = r_0^2 + n\lambda f \quad \text{using} \quad r_0 << f, \qquad n\lambda << f \qquad [2.5]$$

Since a zone plate focusses by diffraction, it is expected to have higher order foci. Using the same approximations as above, if we let the path length difference be s_n-s_0=n(mλ/2) (for odd m) then the same zone r_n's give a focal length f/m. So a zone plate with first order focus at f will have higher order foci at f/3, f/5,...f/m, for all odd m (as long as nmλ<<f is still good.) In a similar manner there must be negative orders at f/(-m), for odd m. There is also undiffracted radiation (called 0th order.)

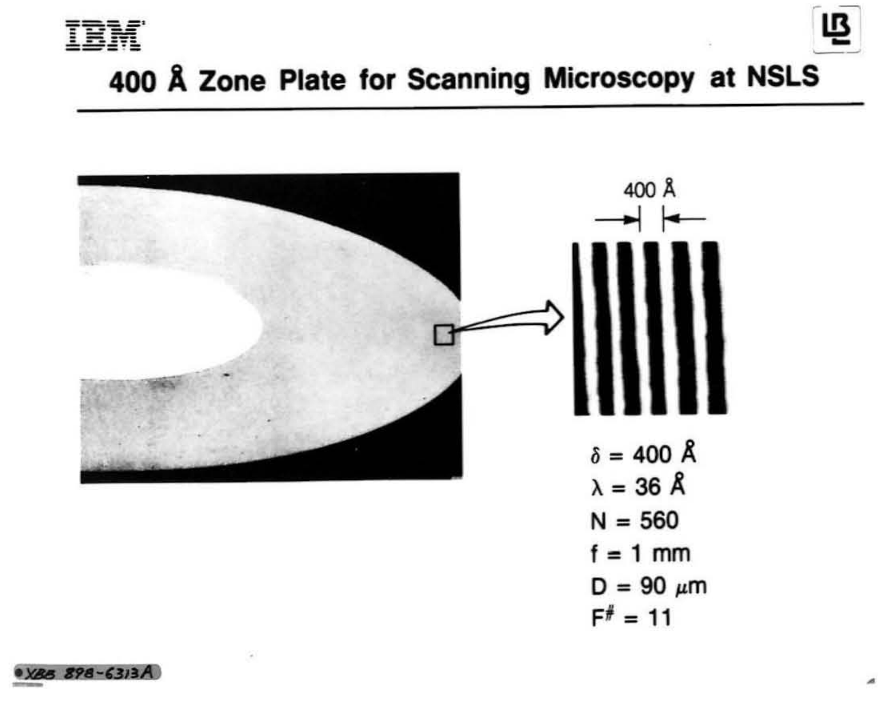
IBM

400 Å Zone Plate for Scanning Microscopy at NSLS

δ = 400 Å
λ = 36 Å
N = 560
f = 1 mm
D = 90 μm
F# = 11

XBB 898-6313A

Figure 2.6 A Zone Plate An SEM photograph of a 400Å zone plate. This zone plate was built at IBM using e-beam lithography, in a collaboration between IBM and the CFXO.

The zone plates in use during our runs were fabricated by e-beam lithography by a collaboration between the Center For X-ray Optics (the CFXO is at LBL) and IBM.[8,9] Figure 2.6 is an SEM image of a zone plate from that collaboration, though not the zone plate we have used. The standard ones are made to have opaque gold zones on a near transparent SiN membrane. In the sense that a lens takes near parallel light and delivers some fraction of it to a point one focal length away, with little light anywhere else in the focal plane, the analogous part of the STXM is the combination of the zone plate and Order sorting aperture (OSA) which is designed to block all but first order light. Figure 2.7 illustrates the zone plate - OSA combination, its correct alignment, and gives the labels for its dimensions.

Important points to remember about zone plates are listed in table 2.1. The zone plate we've been working with has diameter d_{Zp}=90μm, and at λ=36.4Å we observe f=1285μm, giving d_r=52nm in reasonable agreement with its design 50nm finest zone width. The rayleigh resolution of our zone plate is ~57nm (we have a 33% stop.) The expressions for resolution are discussed at greater length when we discuss measuring the resolution in an image in the next chapter. More detailed discussions of zone plates and their efficiencies can be found elsewhere.[10]

We want to use only the first order focus as our x-ray probe. To do that without undue background requires blocking both the 0th order unscattered light as well as the light from all higher order foci. This is done by blocking all unwanted orders with the combination of a central stop fabricated on the zone plate (diameter d_{stop}), and an aperture (the OSA, aperture diameter d_{OSA}) with $d_{stop}>d_{OSA}$. The zone plate and OSA must be aligned as in figure 2.5, with the OSA as close as possible to the zone plate without clipping the 1st order focus cone. As labeled in figure 2.7, the working distance of the microscope (maximum distance from the sample to the closest part of the microscope) is $d_{work} = (f - Z_{OSA})$.

$r_n^2 = nf\lambda + r_0^2$	a zone plate has zones at r_n .
$\pm f, \pm 3f, \pm 5f$	the foci of a zone plate, for orders $m=\pm 1, \pm 3, \ldots$
$f = \frac{d_{Zp} d_r}{\lambda}$	f can be described in terms of λ, d_{Zp} and d_r .
$\delta r = \frac{1.22\lambda f}{d_{Zp}} = 1.22 d_r$	gives the rayleigh resolution at the 1st order focus, for a zone plate with no stop.
$\delta r = \frac{1.1\lambda f}{d_{Zp}} = 1.1 d_r$	gives the rayleigh resolution at the 1st order focus for a zone plate with a 33% stop.
Efficiencies:	For ideal plates with purely opaque zones.
50%	blocked by opaque zones
25%	0th order
$1/\pi^2$	1st order
$1/(m\pi)^2$	mth order (for odd m)

Table 2.1 Facts About Zone Plates A table of basic facts about zone plates. f is the focal length. d_{Zp} is the diameter of zone plate. λ is the wavelength. δr is the size of x-ray beam in plane of focus (Rayleigh definition). d_r is the finest zone width in the zone plate (i.e., outer zone width).

$$Z_{OSA} = f - d_{WORK} = f\left(1 - \frac{d_{OSA}}{d_{Zp}}\right) \qquad [2.6]$$

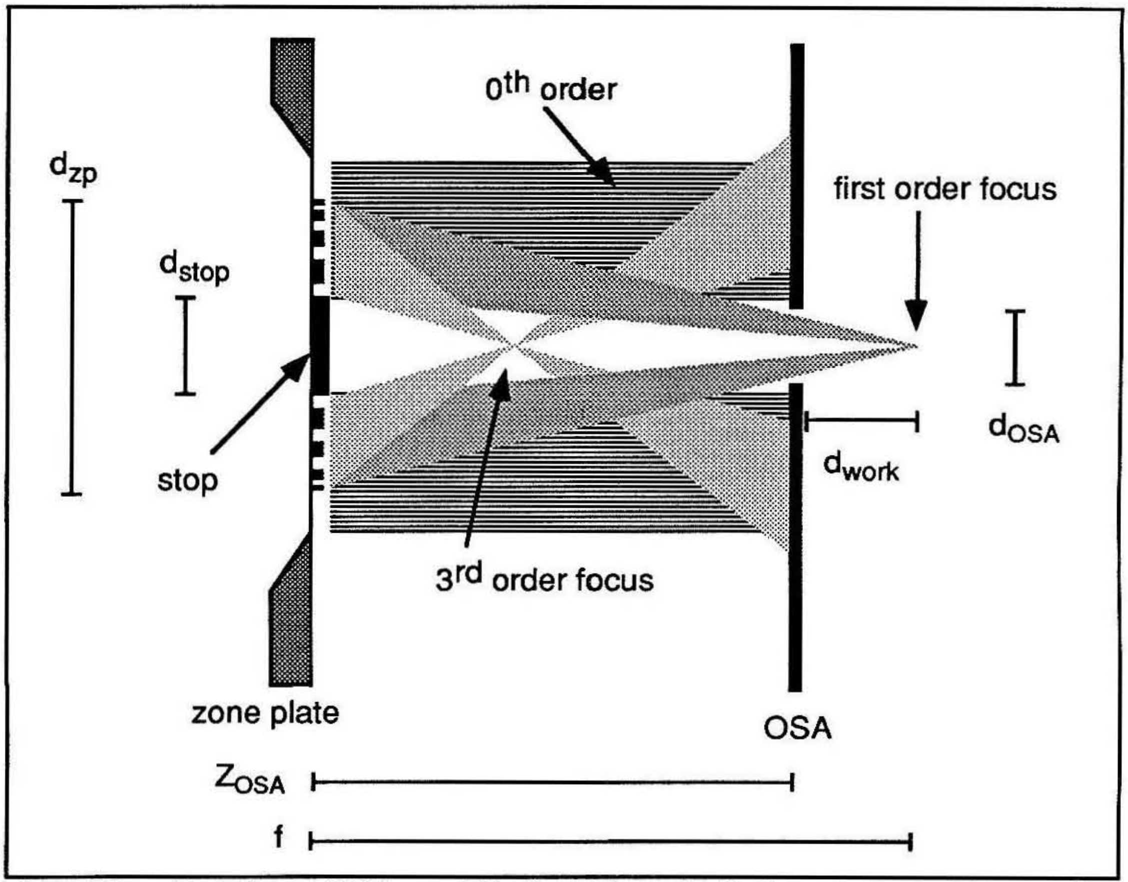

Figure 2.7 Zone Plate and OSA This figure shows the ideal arrangement of the zone plate and the order sorting aperture (OSA). The OSA is meant to block all light except the first order. The hole in the OSA must be aligned to be in the shadow cast by the central stop in the zone plate. The correct positioning distance Z_{OSA} can be calculated using equation 2.5.

We need as much working distance as we can get, most of the time. We can calculate where to put the OSA, for any given stop size and aperture size by using eq. 2.6, which results from requiring the OSA to precisely touch the edge of the 1st order cone. Usually, to allow for misalignment, and the imperfections of the fabrication of OSAs we subtract about 4μm from the actual size of the OSA, in order to calculate Z_{OSA} with equation 2.6.

We then have d_{Zp} = 90μm, d_{OSA} = 28μm, and d_{stop}=30μm so at λ=36.4Å and f=1285μm we get (subtracting 4μm from d_{OSA}) Z_{OSA}=942μm and a corresponding working distance of 343μm, between the OSA and the sample. As f changes with λ, the optimum Z_{OSA} changes, as does the working distance.

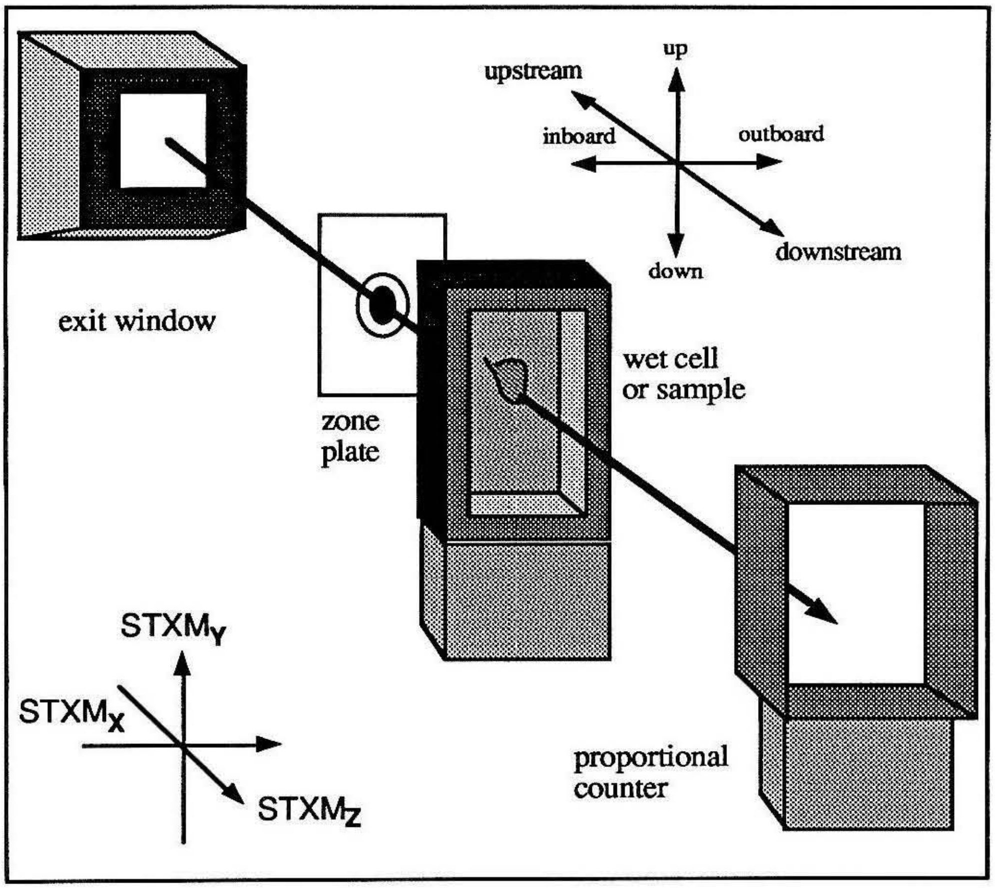

Figure 2.8 Various Coordinate Systems By convention inboard is to the left when facing the beam, and outboard is to the right. The x-ray beam comes from upstream and goes downstream. Up and down, complete the set of orientations around the beam axis. When scanning the x-axis is the inboard-outboard axis, y is the vertical (up-down) axis, and the z-axis is the ideal axis along the beam.

2.4.2. The Sample Mount (scanning and positioning)

The sample, in our case the Caltech wet cell, slips on to a magnetic pad that is mounted on x-y piezoelectric drivers (the pzts), which are in turn mounted on x-y stepper motors (the steppers). The steppers give a coarse motion to set image centers and take orientation scans. The pzts give a fine motion for taking high quality images. While we have been running at the microscope there has always been a z driver, usually on the zone plate - OSA pair, but sometimes on the sample mount. We'll really only discuss the case where the z motion moves the zone plate and OSA. In any case the sample mount is meant to hold the sample plane parallel to the zone plate, and the axes of the sample motion (x and y) are set up in that plane.

The coordinate system used in the images: x, y and z (also known as $STXM_X$,, $STXM_Y$ and $STXM_Z$) is illustrated in figure 2.8. These coordinates are related to the physical coordinates as shown in the figure. Inboard-Outboard is the x axis, up-down is the y axis, and upstream-downstream is the z axis. All images are made by taking successive x scans at different y positions (for regular images) or different z positions (for focus scans--which are discussed later in this chapter).

x and y pzt finest step (dx and dy)	5nm
x and y stepper finest step (dx and dy)	.1µm
z stepper finest step (dz)	.1µm
image to image registration (after excursions)	>1µm

Table 2.2 Stage Parameters The smallest step sizes available from the STXM ample stage drivers. For the STXM after August 1990. The image to image registration parameter means that the same pixel in successive images, cannot be counted on to be closer than 1µm.

The parameters of the scanning and positioning system are given in table 2.2. These have been a moving target, especially during our runs in 1989-1991, as the stage drivers have been constantly overhauled. The finest step sizes are now (since Aug '90) considerably finer than the resolution of the zone plate. The image to image registration of the stepper+pzt system is not better than 1µm, even for successive images. To overlay images they must be shifted in software. We have also observed variations in dx and dy, the image pixel sizes, at the 1% level and some rotations in x and y when comparing successive images.

2.4.3. The Detector --- single photon counting of soft x-rays

The x-ray detector is an argon gas proportional counter (the PC). It is mounted on its own micrometer positioners and is simply aligned to the zone plate, to catch all transmitted x-rays. It is a single wire counter, with a .5mm window. The window is a 1000Å SiN membrane, with estimated flux absorption of 27% at λ=36Å. Not including the losses in the window we expect a >95% quantum efficiency in counting single photons for rates less than 1MHz.[11] The PC saturates between 2 and 3MHz and is beginning to lose quantum efficiency, and thus miss photons, at 1MHz.

2.5. Aligning the STXM

Figure 2.4 showed the five in air components of the STXM. These must all be aligned together in order to produce x-ray images. The x-ray beam must be centered on the exit window. The proportional counter should have its window centered around the projection of the exit window. The zone plate must be centered in the exit window (the exit window is 250µm square, the zone plate is 90µm in diameter). The OSA must be positioned at the correct distance Z_{OSA} (using eq. 2.5) downstream from the zone plate and must be aligned in x and y to be inside the projection of the stop while not clipping the 1st order cone. The STXM must be aligned after changing the zone plate, and sometimes after shifting the undulator gap. In order to do this we start at the upstream end and work downstream, using the following four tools/methods.

2.5.1. Methods of Alignment

On the back (vacuum side) of the snout that holds the exit window there is a coating of x-ray phosphor. Where the x-ray beam hits the phosphor we get visible fluorescence. The beam at that point has a rectangular cross-section about 3mm high and .5mm wide.

The shaft that the exit window is mounted over provides a gap in the phosphor, and thus a circular hole in the fluorescent rectangle. The first alignment of the microscope is to adjust the LWB mirror to center the fluorescent rectangle around that circular hole. We observe the phosphor with a mirror mounted upstream of the exit window, as shown in figure 2.9.

For crude positioning we use the visible light microscope (VLM), which is mounted at the furthest downstream end of the microscope as in figure 2.9. The VLM is a long working distance (18mm) objective on a CCD video camera. The VLM is mounted on three axis micrometers, which give us the coordinates VLM$_X$, VLM$_Y$, and VLM$_Z$, for the point in focus at the center of the VLM image.

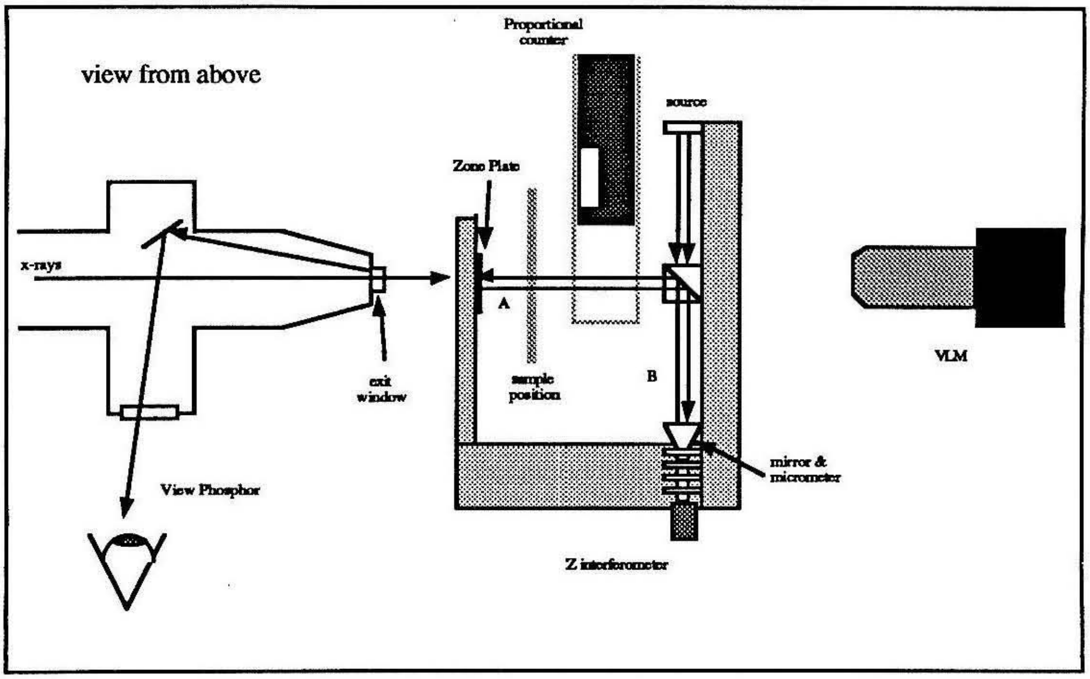

Figure 2.9 Tools For Alignment Three tools for aligning the microscope are: The phosphor viewing window and mirror. The Visible Light Microscope (VLM) and the Z interferometer (Z$_{int}$). The phosphor view is used to center the x-ray beam on the exit window. The VLM is used to crudely align the centers of the exit window, zone plate, OSA, and the sample or pinhole. The Z$_{int}$ is used for precise setting of the z position of the OSA relative to the zone plate. It is also useful to measure the distance from the exit window to the zone plate, and the focal length of the zone plate. The dotted line shows the operating position of the PC, it must be out to use Z$_{int}$ or the VLM.

For finer positioning along the z-axis we use the Z interferometer (Z_{int}). This is a 2 arm white light interferometer, which uses the the z-axis between any of our in-line objects (exit window, zone plate, OSA, or sample) and a prism as one arm. The 2nd axis of the interferometer runs along the microscope x-axis and has a mirror mounted on the Z_{int} micrometer. This interferometer is sketched out in figure 2.9. When the two arms are equal in length we observe fringes in the VLM on the in-line object. Z_{int} provides relative z coordinates of the target object to better than 5 microns. The Z_{int} is physically mounted on the holder of the zone plate.

The finest alignments are done with the STXM itself. By placing a 6μm pinhole in the sample mount, and scanning it in x and y, we can take images of the x-ray distribution in the plane of the pinhole due to whatever is upstream of that plane.

It is worth noting that to use the VLM or Z_{int} we must move the PC up and out of the way, so x-ray images may not be taken at the same time as VLM observations.

2.5.2. Alignment Procedure (seven steps to harmony)

This section details the procedure for fully aligning the instrumnet end of the microscope, as is appropriate after the zone plate has been changed (or bumped). It is included principally for those who might become users of the microscope, but also to give the correct impression to the reader, that the established procedures and tools for aligning and operating the microscope are every bit as important to its usability as are its principal components.

First, we remove everything between the exit window and the VLM. The zone plate is removed from its mount (a magnetic pad). The OSA is cranked up and out of the beam path with its y-micrometer. The sample is removed from the sample mount (also on a magnetic pad.) The PC is raised out of the way using its micrometer drivers.

Second, we observe the phosphor and steer the beam to surround the exit window. The beam is steered for this purpose with the LWB mirror. This is a gross centering (by eye at this point). We can also adjust the position of the snout and exit window, using the snout's micrometer positioners. The snout is attached to the beam line with a bellows -- it will move a few cm in x, y or z without breaking vacuum.

Third, we focus the VLM on the exit window and center it. This should be done with the VLM micrometers or the snout micrometers, depending on which we think is better in line. We record the VLM coordinates of the center of the exit window. We also at this point find the Z_{int} coordinates of the exit window by putting the fringes on it. The interferometer has a limited range so putting fringes on the exit window may require moving the exit window forward towards the plane of the zone plate.

Fourth, put a 6µm pinhole in the sample mount, and using the x-y steppers, move it to the center of the VLM image, where it should be roughly in line with the exit window. Bring down the PC and do a large scan with the pinhole to get an image of the exit window. The exit window will usually not be perfectly centered, though it should be close. Move the center of the pinhole to the center of the exit window by using the steppers and record its STXM coordinates,. Then remove the pinhole and raise the PC.

Fifth, mount the zone plate on its magnetic pad, it will rest against stops to roughly position it in the center of the x-y plane. Move the zone plate back to ~2mm from the exit window with the $STXM_Z$ stepper. Move the zone plate to the center of the VLM image (remember this is still centered on the exit window), it is best to do this by dragging the zone plate with forceps, since long motions with the zone plate micrometers will disrupt the view of the fringes on the exit window. Now put the pinhole back in, and move it back to its position centered on the exit window. Bring down the PC, and take a large scan, to find the image of the zone plate overlapping the exit window. This is an image mostly of 0^{th}

order light, possibly with some 1st order light near the center of the zone plate. It should resemble figure 2.10. We then use the x-y micrometers on the zone plate mount to center the zone plate in the exit window. Figure 2.10 is an illustration of the overlay of the zone plate on the exit window as we see it in a pinhole scan. In the figure the exit window is a transparent square window (in white) framed by opaque silicon (in grey). The zone plate is a circular object centered in a similar window. The zone plate is mounted in front of the exit window and must be lined up with it. In the figure this is shown in the lower tow images. The trick is to center the zone plate disk in the opening of the exit window. After centering the zone plate record the STXM_X and STXM_Y coordinates of the pinhole at the center of the zone plate, and remove the pinhole and PC. Then put fringes on the zone plate and record its Z_{int} coordinates.

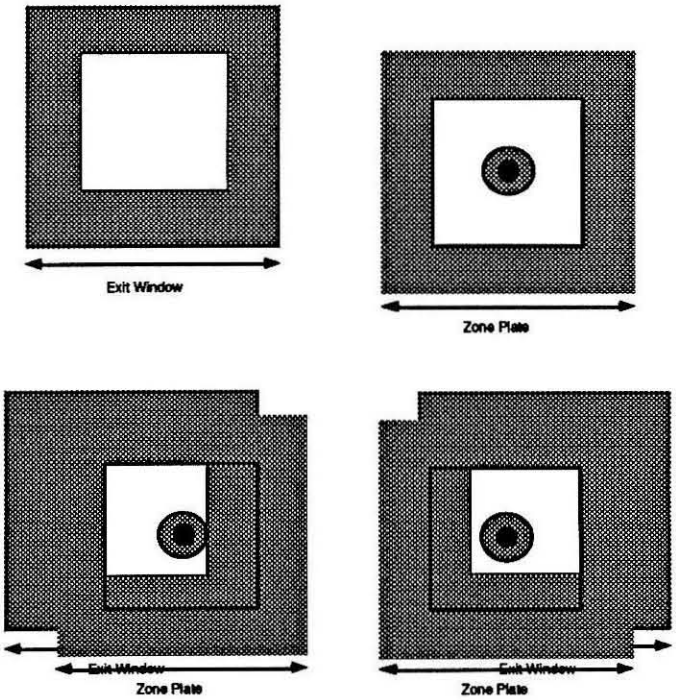

Figure 2.10 Exit Window and Zone Plate Illustrating first pinhole scans for aligning zone plate with exit window. Taking repeated scans of this sort we center the zone plate in the exit window.

Sixth, now we bring down the OSA, observing in the VLM, and adjust its x - y position with the OSA micrometers until it is centered in the VLM image -which aligns it with the zone plate center. Using the eq. 2.5 we calculate the desired distance Z_{OSA}, and set the Z_{int} micrometer to that. Now using the OSA z micrometer, move the OSA until the interferometer fringes appear on the VLM image of the OSA. At this point we are close to correct OSA to zone plate alignment, what is left is fine tuning that with the x-ray images.

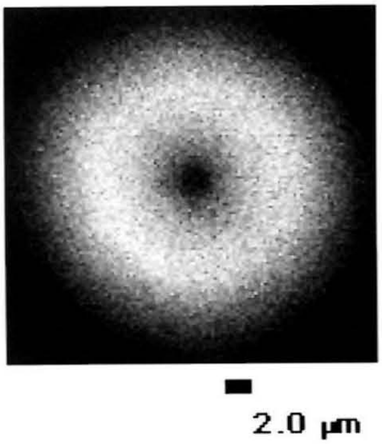

Figure 2.11 The Donut A good donut, which demonstrates correct alignment of the OSA with the zone plate.

Seventh, put back in the pinhole, at the same location that it last had in step five, and bring down the PC. Now take an image. Assuming things are reasonably well aligned, we get the "donut".

The donut is a minor eccentricity that all STXM users get to spend some time with. A good donut is shown in figure 2.11. Its genesis is sketched in figure 2.12. If the pinhole lies in a plane upstream or downstream of the focal plane, then an image taken by scanning that pinhole cuts the 1st order cone as in figure 2.12A. If the OSA is mis-aligned, for example is to low, then we have the situation in figure 2.12B. Here the cone is clipped, and this shows up in two different ways in the pinhole scan.

If the pinhole is upstream of the focal plane, then the 1st order donut is clipped on top. If the pinhole is downstream of the focal plane, then the 1st order donut is clipped on the bottom. In both cases, if the OSA is down far enough, it will not be completely within the shadow of the stop, and some 0th order light will get through. 0th order light leakage will be on the same side for upstream or downstream planes. The observed pinhole images for the case in figure 2.12B, are illustrated in figure 2.12C. Using this understanding of the pinhole scans, we adjust the OSA position with its x and y micrometers to get a perfect donut, and no 0th order leakage. An example of a pinhole scan donut is shown in figure 2.11. At this point the basic alignment is done, and we have only to check the focal length, and find the $\mathrm{STXM_Z}$ position for the wet cell (or any sample holder) to be in focus. The procedures we have outlined above can take anywhere from a couple of hours to 20 minutes to go through. They are only difficult if the elements of the microscope are seriously out of line (as after a major mechanical change).

From the procedures above one can see that if the VLM has its z axis aligned along the x-ray axis, and parallel to the $\mathrm{STXM_Z}$ stepper motion then all VLM alignments should be very close to the true alignment. However, the x-ray beam and the $\mathrm{STXM_Z}$ stepper motion are often misaligned by 10-30 milliradians (1-3%), and likewise the VLM z axis. A 1-3% misalignment is 10-30 μm in 1mm, not fatal , but the OSA is that far from the zone plate, and thus is usually 10-30μm (1/2 the OSA diameter) off position when we start step 7. One can see that more error might put the OSA off the zones in the zone plate entirely, and sometimes that happens -- causing some delay in alignment.

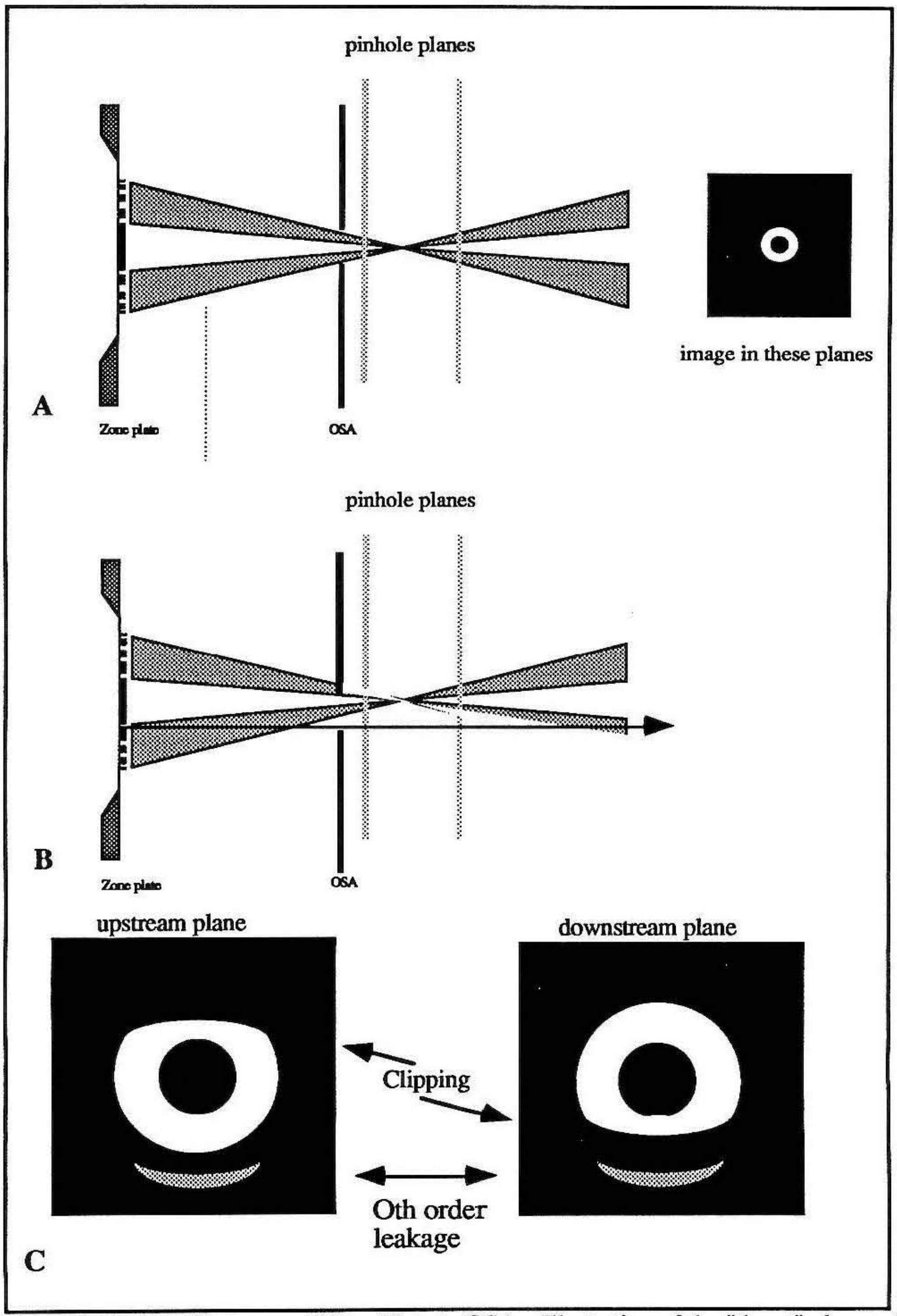

Figure 2.12 Alignment of Zone Plate to OSA Illustration of the "donut" observed when aligning the OSA to the zone plate. **A** is correct alignment. **B** is OSA to low. **C** is pinhole images for the case in **B**.

2.6. Finding the Focus Plane

The last step in alignment of the microscope is to find the $STXM_Z$ coordinate that puts the sample in focus, and to check the focal length f. The procedure is to put in a dummy sample (usually an empty wet cell, with just a clean front window and exit window) about .5mm downstream of the estimated focal plane. Then we take focus scans, and step towards the true focus. The test sample has gold focus marks (150Å thick) on a thin SiN membrane (1000Å), and they provide near knife edges of about 50% absorption to focus on. We can also remove the PC, and look through the back of the wet cell, to focus the VLM on the front window's gold marks. This allows us to see the interferometer fringes, and thus find a Z_{int} coordinate for the sample membrane when it is in focus, and thus measure the focal length f which is the difference between the Z_{int} coordinates of the zone plate itself and the sample when it is in focus. The $STXM_Z$ coordinate that we find for one sample, will not be precisely right for any other sample chips, if only because the thickness of the silicon frames is controlled to no better than 25µm (see chapter 4.)

2.6.1. Focus Scans

A extremely useful feature of the STXM and its controlling software is the ability to take focus scans, a kind of image that graphically shows how good, and where the focus is. A focus scan is a scan in x and z, as opposed to the normal image in x and y. In both cases the horizontal axis is the x axis, and between each x scan we step in y (for normal images) or z (for focus scans). Figure 2.13 illustrates this for the image of a focus mark in the plane of focus. In figure 2.13A we have an drawing of an image of a focus mark, in focus. Its edges are sharp. We are at $STXM_{X,Y,Z}$ for the center of the image. Figure 2.13A is an x-y scan at $z=STXM_Z=f$, the horizontal dotted line is the $y=STXM_Y$ scan line. In figure 2.13B we illustrate a focus scan taken centered at the same $STXM_{X,Y,Z}$. The STXM driver software lets us set the dz, for each scan line, just as we set dx and dy for a normal image. The center scan line is the same y=$\mathrm{STXM_Y}$, z=f=$\mathrm{STXM_Z}$ scan as in figure 2.13A. So for an NxN pixel image the focus scan looks at z positions from z=$\mathrm{STXM_Z}$ - (N/2)dz to $\mathrm{STXM_Z}$ + (N/2)dz, and a typical choice for dz is 1µm. If we want to observe the edge near the limit of resolution we might set dx=0.05µm. With those choices a 1% misalignment in the stepper Z and the x-ray beam becomes a noticeable 20%=1%dz/dx slope in the pixel image. Figure 2.13C illustrates how such a misalignment will show up in a focus scan. This is in fact how focus scans always appear, as the STXM is currently aligned to about 1% in stepper Z vs. the x-ray beam.

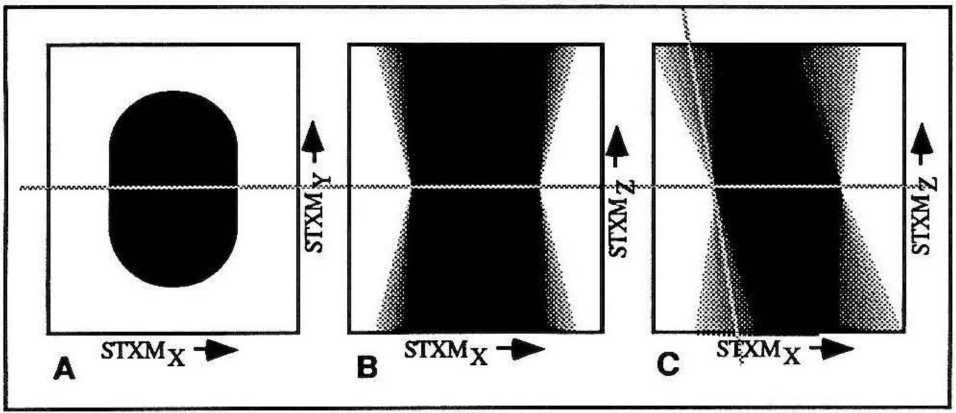

Figure 2.13 Focus Scans An illustration of the nature of focus scans. A is an image of a focus mark in the plane of focus. The horizontal dotted line is $\mathrm{STXM_Y}$=image center. **B** illustrates a focus scan taken at the same place. Now the dotted line is $\mathrm{STXM_Z}$=f, scans lines N above the center are offset from the current $\mathrm{STXM_Z}$ by +Ndz, scan lines n below the center are offset by -Ndz. **C** illustrates a more realistic focus scan, where the tilt (along the dotted line) reflects the misalignment of the z stepper from the x-ray beam.

When we take a focus scan, we can use the on-line software to click the mouse on a pixel of sharpest focus. The software then gives us the $\mathrm{STXM_Z}$ coordinate of that pixel, and by moving there, the sample is moved to the focus plane.

2.6.2. Depth of Focus

We can look at the probe formed by the zone plate and OSA as having a FWHM of δr, or a rayleigh radius of δr as in Table 2.1. This is a measure of the width of the waist of the first order cone of x-rays produced by the zone plate. The waist, or narrowest region, of the probe is illustrated in figure 2.14C. The angle spanned by the zone plate is θ, and $\theta = d_{Zp}/f = \lambda/d_r \sim .072$ radians, at λ=36Å. The concentration of the x-ray beam is maximal in the plane of focus and naturally gets worse as the sample moves out of that plane.

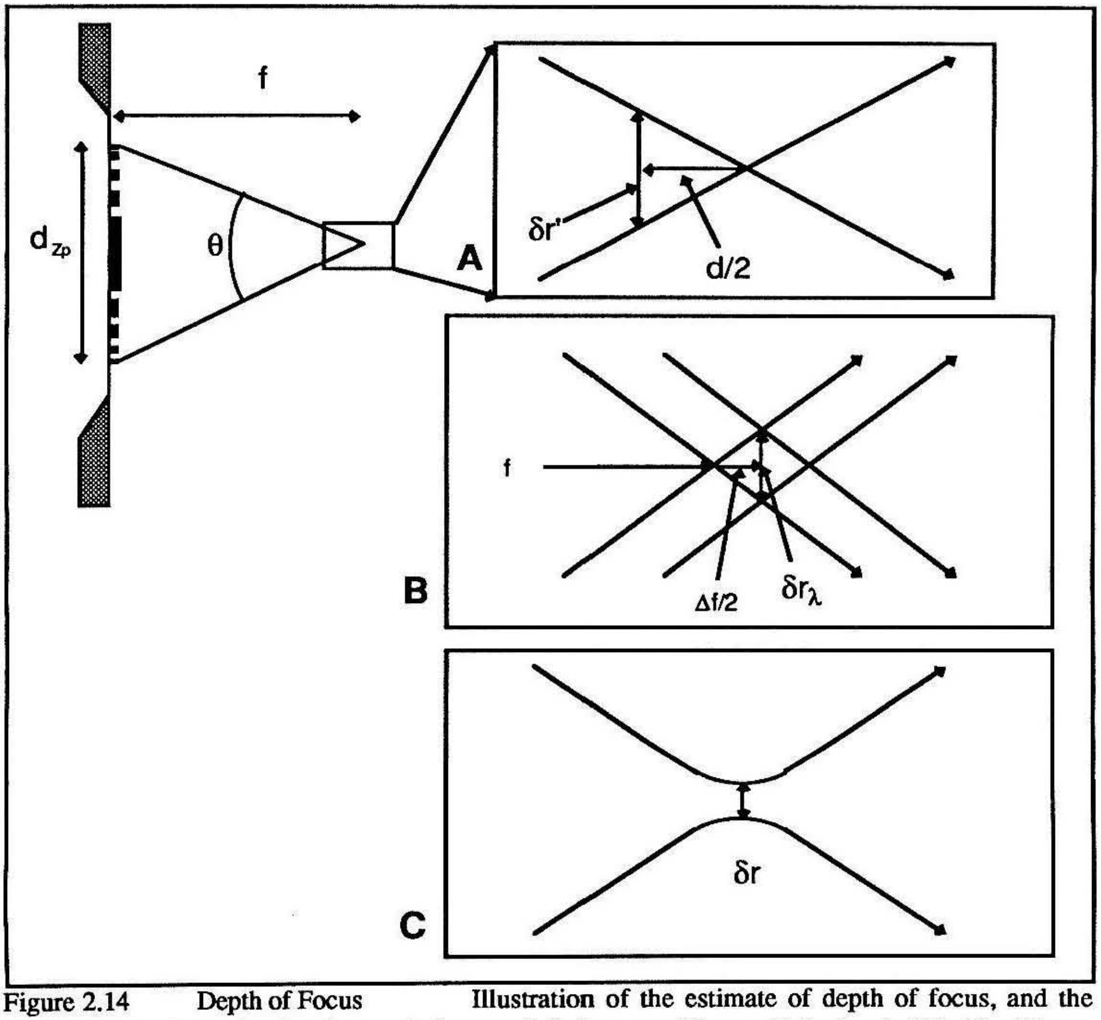

Figure 2.14 Depth of Focus Illustration of the estimate of depth of focus, and the broadening of the probe size due to: **A** the sample being out of focus. **B** the bandwidth $\Delta\lambda$ of the x-ray beam. **C** the theoretical width of the focus of a monochromatically illuminated zone plate.

The depth of focus d is a number meant to measure how far a thin sample can be out of the plane of focus without affecting the image too much. Or how thick a layer of the sample can be and still give adequately sharp features in an image. These definitions of the depth of focus purposely leave in the notions of "too much" and "adequately", which need to be further refined in light of the nature of the sample or the desired x-y resolution (or pixel size).

A commonly used definition of d/2 is the distance at which the geometric broadening of the cone of light is equal to the natural probe width δr. The geometric broadening of the probe is illustrated in figure 2.14A, and it is assuming the cone focusses to a point. Then the broadening due to moving d/2 out of focus is given by dr' in equation 2.7, and the d required to make $\delta r'=\delta r$ is given in equation 2.8, using $\theta = \lambda/d_r$. With $\delta r=0.057\mu m$, $d_r=0.052\mu m$ and $\lambda=36Å$, we find $d=1.6\mu m$. When a thin sample is placed at such a distance d/2 from focus the size of the probe δr_1 that intersects it is given roughly by equation 2.9 (considering the total broadening a convolution of independent distributions).

$$\delta r' = d\frac{\theta}{2} \qquad for \qquad \theta << 1 \qquad [2.7]$$

So that

$$d = \frac{2\delta r d_r}{\lambda} \qquad for \qquad \delta r' = \delta r, \qquad \theta << 1 \qquad [2.8]$$

$$\delta r_1 = \sqrt{\left((\delta r')^2 + (\delta r)^2\right)} \qquad = \sqrt{2}\delta r \qquad for \qquad \delta r' = \delta r \qquad [2.9]$$

A further cause of broadening of the probe size is the imperfect bandwidth of the microscope. X-rays of different wavelength are focussed to different planes. A basic estimate of the effect of bandwidth $\Delta\lambda$ (due to exit slits) is given following the illustration in figure 2.14B. Using the expression for focal length in table 2.1, and expanding to first order in $\Delta\lambda/\lambda$ we find equation 2.10. A wavelength spectra $\Delta\lambda$ wide leads to a focal length broadening Δf and a probe width δr_λ given in equation 2.11. With $d_{Zp} = 90\mu m$ to get $\delta r_\lambda=0.057\mu m$ we need $\Delta\lambda/\lambda < 1.26\times10^{-3}$, or a resolving power of ~800. That will give no more broadening from bandwidth than from the monochromatic probe size δr. If this condition is met, δr_1 in equation 2.12 is derived by the same approximation as in equation 2.9.

$$\frac{\Delta f}{f} = \frac{\Delta\lambda}{\lambda} \qquad [2.10]$$

$$\delta r_\lambda = \frac{\Delta f}{2}\theta = \frac{\Delta f}{2}\frac{d_{Zp}}{f} = \frac{d_{Zp}}{2}\frac{\Delta\lambda}{\lambda} \qquad [2.11]$$

$$\delta r_1 = \sqrt{\left((\delta r')^2 + (\delta r)^2 + (\delta r_\lambda)^2\right)} \qquad = \sqrt{3}\delta r \qquad for \qquad \delta r' = \delta r = \delta r_\lambda \qquad [2.12]$$

The expression of δr_1 in equation 2.11 gives two qualitative features of interest to potential users of the microscope. If the user wishes to take images at worse resolution δr_1 than $1.7\delta r$ then the user can relax either the requirement on $\Delta\lambda/\lambda$ (gaining more flux) or the depth of focus $d=1.6\mu m$ (allowing dr_1 imaging of thicker samples). If the user wants to look at samples that are thicker than $1.6\mu m$ then restrictions on $\Delta\lambda/\lambda$ can be relaxed or the pixel size should be increased or both, since the minimal $1.7\delta r$ could no longer be reached anyway.

While this discussion is admittedly crude, its main purpose has been to first give some notion of depth of focus, and second to show something of the relation of depth of focus to achievable resolution, and x-ray bandwidth. The microscope is in these features broadly similiar to visible light microscopes, except that the depth of focus d is much greater than the corresponding limits to x-y resolution δr_1. That difference is essentially due to the fact that the zone plate optics give $\theta<<1$ unlike the best visible light microscopes.

2.7. Conclusion

In this chapter we have tried to summarize the parts of the microscope, and to describe how the user aligns them. We've also started a discussion of the nature of the probe formed by the zone plate that is used to make an image. The intention here was to give a view of the STXM as an apparatus, the next chapter will discuss the STXM from the point of view of its images, and go further into the explanation of the parameters of table 2.1, for our images.

2.8. Chapter 2 References

---

1 P. Mortazavi, M. Woodle, H. Rarback, and D. Shu, "High Flux Photon Beam Monitor," Nucl. Instrum. Methods A **246**, p.389 (1986).

2 R.J. Nawrocky, J.W. Bittner, Li Ma, H. Rarback, D.P. Siddons, and L.H. Yu, "Automatic Beam Steering in the NSLS Storage Rings Using Closed Orbit Feedback," Nucl. Instrum. Methods A **266**, p.164 (1988).

3 C.J. Buckley, H. Rarback, R. Alforque, D.Shu, H. Ade, S. Hellman, N. Iskander, J. Kirz, S. Lindaas, I. McNulty, M. Oversluizen, E. Tang, D. Attwood, R. DiGennaro, M. Howells, C. Jacobsen, Y. Vladimirsky, S. Rothhman, D. Kern, and D. Sayre, "Soft X-ray Imaging with the 35 Period Undulator at the NSLS," Rev. Sci. Instrum. **7**, p.2444 (1989).

4 G. Margaritondo, Introduction to Synchrotron Radiation, (Oxford University, Oxford, 1988) pp.42-48.

5 see reference 3.

6 A.G. Michette, Optical Systems for Soft X Rays, (Plenum Press, New York, 1986) p.128.

7 see reference 3.

8 Vladimirsky Y., et al., "Zone Plate Lenses for X-ray Microscopy," Nucl. Instrum. Methods A **266**, pp.324-328 (1988).

9 E.H. Anderson and D. Kern, "Nanofabrication of Zone Plate Lenses for High Resolution X-ray Microscopy," in X-Ray Microscopy III, edited by A.G. Michette, G.R. Morrison, and C.J. Buckley, (Springer, Berlin, to be published in 1991.)

10 A.G. Michette, Optical Systems for Soft X Rays (Plenum Press, London, 1986) chapter 8.

More References:

11 C. Jacobsen, S. Williams, E. Anderson, M.T. Browne, C.J. Buckley,D. Kern, J. Kirz, M. Rivers, and X. Zhang "Diffraction-Limited Imaging in a Scanning Transmission X-ray Microscope," submitted to Optics Communications (1991).

3. The STXM II (Its Images)

In this chapter we will discuss what a STXM image is, give an overview of the procedures for imaging with the STXM, and try to pin down some ways of looking at image quality. We will first have a brief description of the computer hardware and software that controls the STXM, and acquires its images.

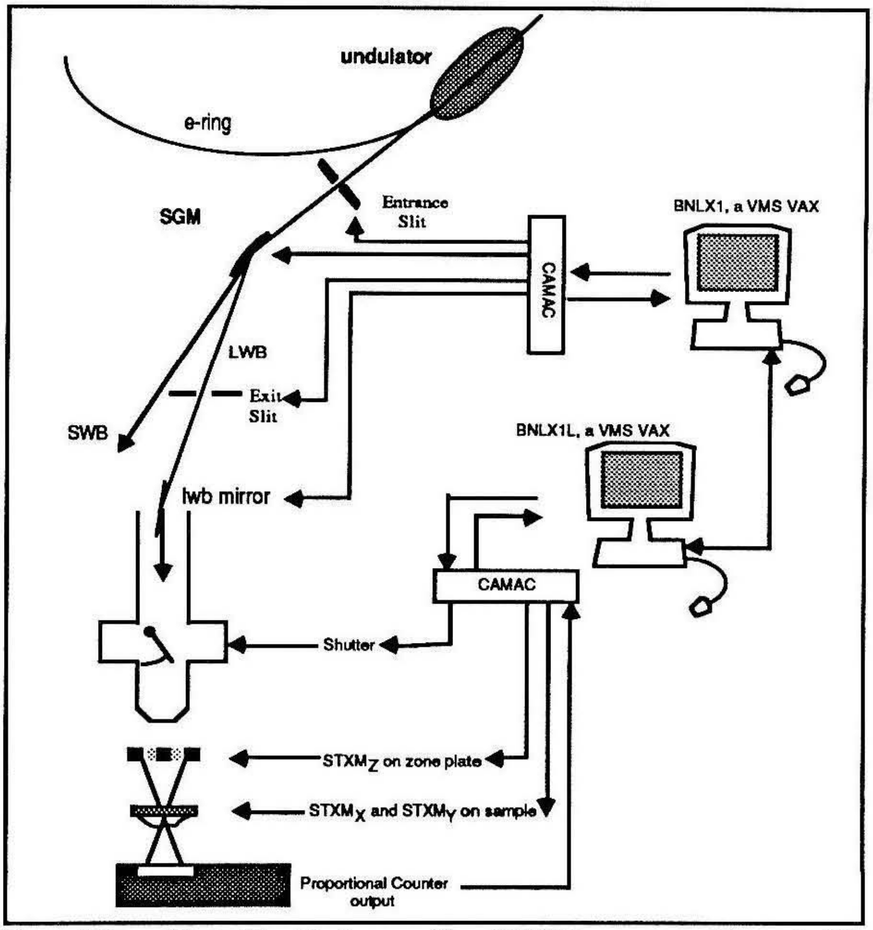

Figure 3.1 Controlling Hardware Two VMS Vaxes are used to control the beam line and the STXM. BNLX1 is the controller for the LWB mirror and everything upstream of that point. BNLX1L is the principal STXM controller and the STXM on-line software resides there. The drivers controlled by BNLX1L are the stepper on the STXM_Z axis, which moves the zone plate. The steppers and pzts on the STXM_X and STXM_Y axes, which move the sample. And the shutter which unblocks the beam during an image.

In the discussion of what an image is we'll briefly outline the image file format that the STXM uses, BSIF, (which is more completely described in Appendix D) then we'll explain the methods of normalizing images. In the discussion of the quality of our images we'll go over the notions of noise and resolution and contrast. We'll also discuss some simple models of cells as imaging targets. We will finish up with a first look at the relation between achievable Signal:Noise, incident flux per pixel, and pixel size.

3.1 On-Line Image Hardware and Software

The beamline and microscope are controlled by 2 VMS Vaxes. The controllers are shown in figure 3.1. All aquisition of images is controlled by the STXM[1] program, running from the VAX BNLX1L. The operator's main screen is on BNLX1L, though there are subsidiary screens for controlling the upstream parts of the microscope (as described last chapter: ENS, SGM and EXS) through BNLX1. The Vaxes control the various components of the beamline and microscope through two CAMAC contollers, as illustrated in figure 3.1.

3.2 Recording an image

The elements of the recording of an image are presented in figure 3.2. The zone plate (and OSA etc.) makes a narrow x-ray probe that is fixed during an image. The sample is scanned in x and y (i.e., $STXM_X$ and $STXM_Y$) in front of the x-ray probe. The STXM is designed to acquire three data values at each pixel. At each x and y position of the sample we count the transmitted x-rays in the proportional counter (PC). That count constitutes the "transmitted intensity" datum of the pixel having coordinates x and y . Simultaneously (i.e., pixel by pixel) we can record the other pixel data, "incident intensity" and "clock pulses". Though it is not now in use, when an incident intensity monitor is installed, "incident intensity" data will be a signal that is proportional to the flux of x-ray photons incident on the sample during the aquisition of transmitted photons at that pixel. The "clock pulses" data is a value proportional to the actual aquisition time at each pixel.

In a scan, the x and y motion, and the timing of data aquisition from the PC are all calculated to give the desired image settings τ, N,M,dx,and dy. τ is the dwell time per pixel. The image has N rows and M columns. The pixel step sizes are dx and dy.

STXM image files are stored using the Brookhaven Standard Image Format[2] (BSIF). A STXM image has a header, containing data about the nature if the image and sample and three data "frames", or parallel subimages. The first is the "transmitted intensity" frame, that contains the count of transmitted photons captured at each pixel. The second is an "incident intensity" frame that is currently not used, and the third is the "clock pulses" frame, which records the dwell time in each pixel. As we shall discuss below, the timing information was necessary before August 1990, though it is not currently in use. Though the raw frames often look adequate, images are generally normalized, both to improve their quality and to allow their quantitative interpretation.

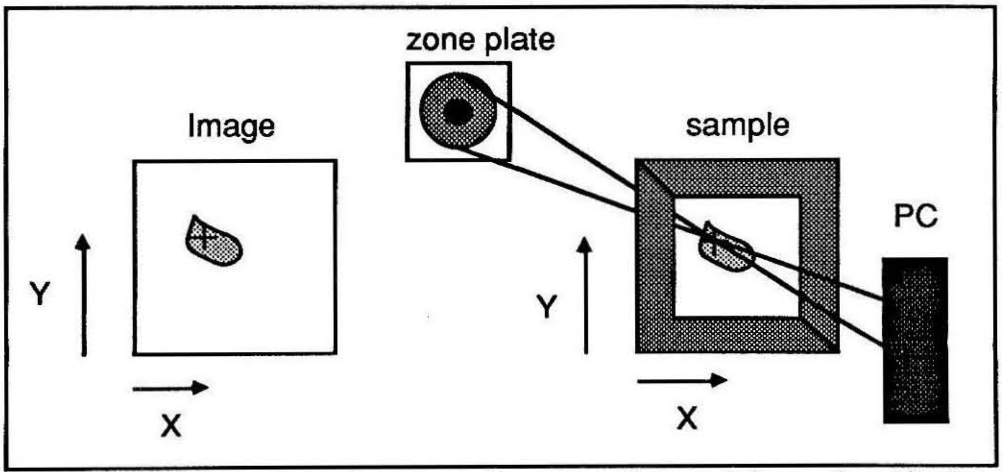

Figure 3.2 Constructing an Image As we scan the sample in x and y while the x-ray probe and detector are fixed, the count of transmitted photons at each location constitutes the "transmitted intensity" frame of the STXM image.

3.2.1 1st Normalization: Photons per Pixel

The ObjectImage off-line software produces a normalized image frame. At each pixel this frame has the value of normalized photons detected. It generates this by multiplying each "transmitted intensity" pixel by β=(average dwell time)/(pixel dwell time). Where the average dwell time is the average over the clock pulses frame of the image. This normalization provides a normalized absolute transmission count in photons per pixel. It is essentially calculating what the photon count would have been in each pixel if all the pixels had exactly equal dwell times. This value is very convenient to work with for estimating shot noise in the image, as well as absorbed energy in the sample. This value is also convenient to handle as an integer, which ObjectImage usually prefers for the sake of speed.

In the first half of our work at the microscope, before August 1990, its scans were driven by interferometer measurements[3] of the x and y STXM coordinates. In a scan, the x and y stepper or pzt was put into motion at a velocity V_x and V_y estimated (by a pre-scan) to give the desired image settings τ, N,M,dx,and dy. Interferometer measurements of the x position of the stage would signal when a pixel ends and a new one begins. This is considered a "position based" scan, as opposed to a "timing based" or "free running" scan where we tell the end of a pixel by the end of a fixed dwell time. The position based method has the advantage that the spatial grid is independently set by (in principal) independent measurements of position. All errors in the estimation or generation of the stage velocity turn into irregularities in dwell time.

When we used position based scanning the clock pulses frame could be quite significant, as shown in figure 3.3. Figure 3.3A shows the "transmitted intensity" frame of an image (a chick DRG fibroblast) while 3.3B shows the corresponding "clock pulses" frame, and 3.3C the resulting normalized image.

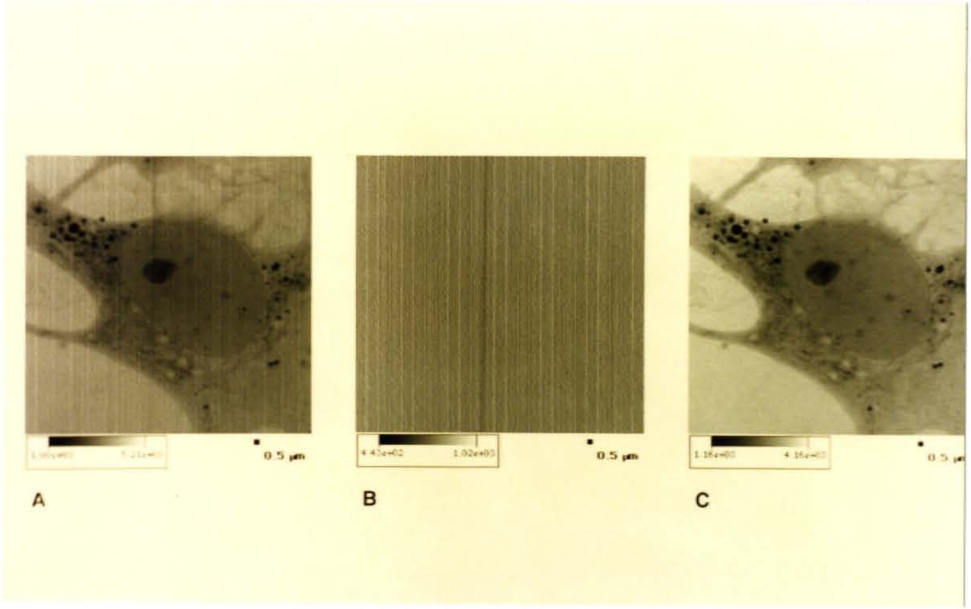

Figure 3.3 First Normalization Illustrating first normalization of STXM images before August 1990. A is the "transmitted intensity" frame. B is the "clock pulses" frame. C is the normalized image, made with the ObjectImage software.

After August 1990 the microscope dispensed with the interferometers, and switched to "free running" formation of images. The "clock pulses" frame became constant since the dwell time counter was starting and stopping the pixels. It cannot really be said that one method of scanning is in principle better than another. If the interferometers were better in reliability or accuracy than the stage drivers, then a position based image could be better, otherwise in both cases, all images will reflect the same imperfections in the drivers. The interferometers were somewhat unreliable, and had a limitation on finest pixel size of 32nm, which is why they were replaced along with the x-y drivers then in use at that time.

The new drivers are used with timing based scans, and have performed quite well in that mode. They give the STXM a finest step size of 5nm, and show no particular errors in high resolution imaging. However low resolution imaging, using the steppers alone, is noticeablely worse than before. In high resolution imaging, using the new pzts, the clock pulses frame now contains no information, since by nature the desired dwell time sets the pixel. Therefore the first normalization is no longer necessary, and the transmitted intensity frame may be used unprocessed for further analysis.

3.2.2 2nd Normalization: percentage Transmission

The physical process that underlies the contrast in a STXM image is transmission of x-rays through the sample. We can write the observed count of photons in the PC as equation 3.1. I_{PC} is number of photons counted in the PC in one pixel, i.e., the quantity we get after the first normalization, as discussed above. I_0 is the number of photons incident on one pixel of the sample. T_{loss} and T_{sample} are fractional transmissions. T_{loss} is the transmission through all the material after the sample and before the PC. T_{sample} is the transmission through the sample itself.

$$I_{PC} = T_{loss} T_{sample} I_0 \qquad [3.1]$$

Now T_{loss} and I_0 are usually nearly constant, or slowly varying, over an image, so it makes sense to divide I_{PC} by an estimate for $T_{loss}I_0$, to get T_{sample}. If an image has a region that we can tell has $T_{sample}=1$ (i.e., there is no sample there) then we can find $T_{loss}I_0$ from I_{PC} in that region. This process, extended across the entire image, we call background normalization. We choose 3 regions which appear to have no sample cells or debris, and construct a plane from the I_{PC} values in those regions. Then that constructed plane gives us an estimate of $T_{loss}I_0$, over the entire image. Dividing through the normalized image by this $T_{loss}I_0$ plane we get a T_{sample} image. Our ObjectImage software scales the 3 background regions to 10000 (=100% transmission.) This procedure removes much of any slow variation in I_0 or T_{loss}. All this is illustrated in figure 3.4. Figure 3.4A shows a cell after first normalization. The three green squares are the background regions that we selected with the ObjectImage software (point and click!) Figure 3.4B is the same cell after background normalization, i.e., it is now a transmission image. Full scale on the image is from 34% to 112%. We get values greater than 100% for two reasons. First because we remove a plane, while the true variation of I_0 and T_{loss}, across the image, is not linear. Second, because we normalize 100% to a mean, and we therefore expect shot noise to carry actual background pixel values to several standard deviations away from that mean in a large image.

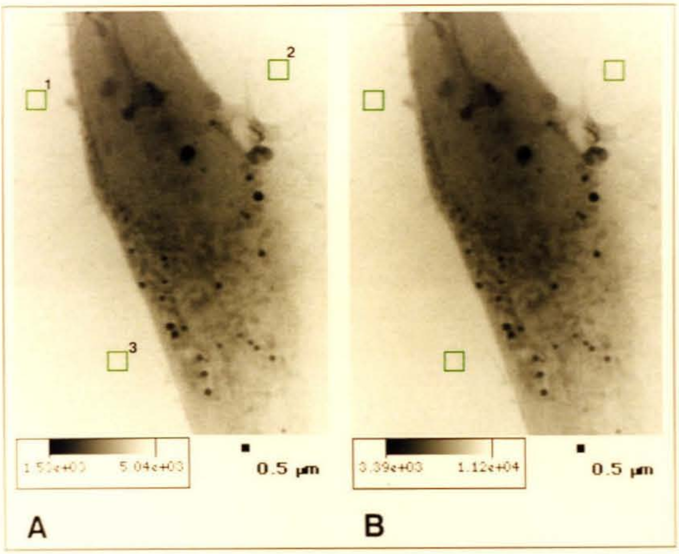

Figure 3.4 Background Normalization An illustration of background normalization. A is an image of a chick fibroblast, after the first normalization. The pixel values in A are the normalized number of photons observed in the PC, which vary from 1500 to 5000. B is the image after background normalization. We have used the 3 background regions (green boxes) to normalize the image to 100% transmission = 10000 in the background regions. The image now falls between 34% transmission in the darkest areas, and 112% in some of the corners

3.3 Noise

	Mean I_{PC}	sd (%)
1	4.4e3	1.73%
2	4.6e3	1.83%
3	4.5e3	1.54%

Table 3.1 Shot Noise Mean (in photons per pixel) and sd (in %) for the background regions of figure 3.4A

The dominant noise in most images is shot noise, occuring because we generally have few photons counted per pixel. We construct a measure of the statistical noise in an image by calculating the standard deviation (sd) in one of the background boxes that we select for second normalization. In figure 3.4A, each background box is 12x12 pixels and the ObjectImage software calculates the values shown in Table 3.1. This observed background noise is very near the 1.5% expected from shot noise when the mean count per pixel is 4.5×10^3 photons.

There are 3 known sources of error that will increase the statistical noise as observed in background regions. If $T_{loss}I_0$ is changing slowly over the background region, (in a manner that is not completely removed by the 2nd normalization) then that will broaden or smear the histogram of photon counts, causing the observed noise to excede expected shot noise. Examples of this are in the effect of a rather steeply changing water layer over the sample (downstream and so contributing to T_{loss}) or (in long images) the effect of the slow exponential decay in I_0. A second contribution to excess observed noise is due to "beam oscillations". These are ripples in I_0 due to variations in the electron orbits in the synchrotron. The observed oscillation is usually at low frequencies ~10-60Hz. As far as "beam oscillations" go, figure 3.4 is a quiet image (near statistical noise.) Figure 3.5 shows an example of beam oscillations. The oscillations can be seen as ripples across the image at about 30 degrees from the vertical. Beam oscillations can vary from negligible to intolerable, depending on the quality of the fill and what other experiments are disrupting the ring. Usually beam oscillations are not intense and we do not find this a significant barrier to microscopy with the STXM. This kind of distortion can also be removed with software and when the microscope gets an incident intensity monitor these oscillations will be automatically removed.

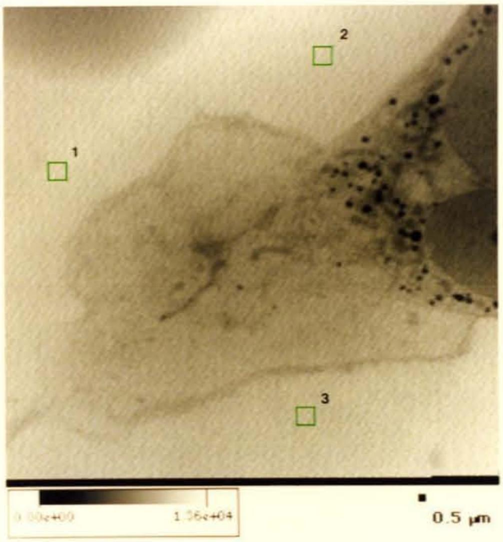

Figure 3.5 Image With Beam Oscillations Shows a thin veil of a chick fibroblast. Beam oscillations are visible as intensity lines at about 30 degrees from the vertical.

The third source of excess statistical noise is due to change in T_{loss} from fluctuations in helium flow during an image. When we flow helium into the open air parts of the STXM, to cut down T_{loss} and increase I_0 we can get variations in the percentage of helium in the x-ray path. If these variations are faster than the imaging time then they appear as streaks on the image. Figure 3.6 illustrates this, it is a long extended filopodium of a fibroblast, and shows some of the characteristic horizontal streaking of helium associated fluctuations.

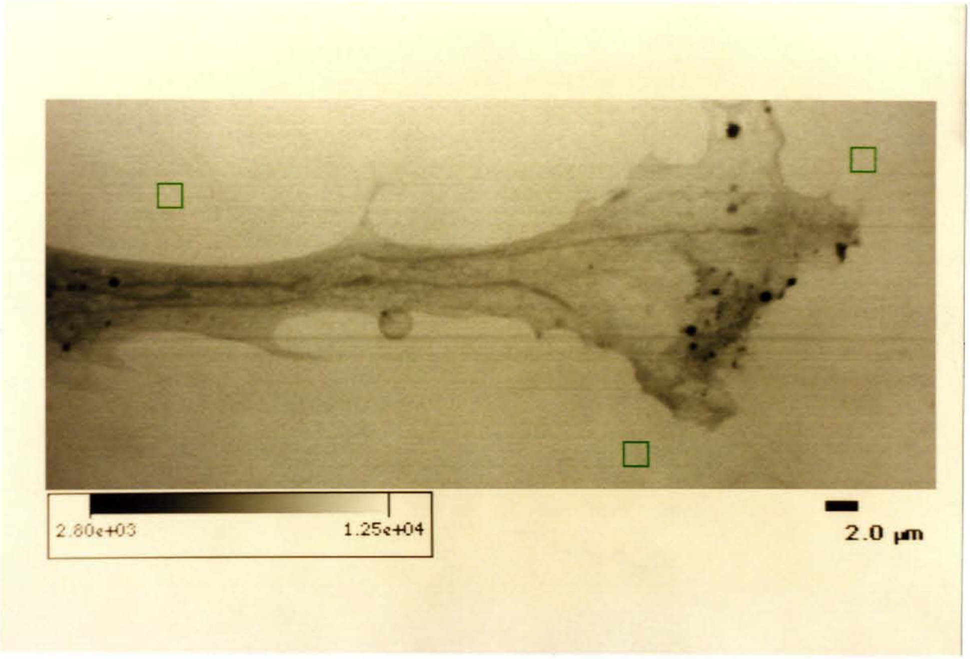

Figure 3.6 Image With Helium Fluctuations A chick fibroblast image that exhibits the horizontal streaking characteristic of helium flow fluctuations.

The dominant noise in STXM images is due to shot noise from counting photons with the PC, and our images get close to this level. Other fluctuations in the source (I_0) or in the x-ray path T_{loss}, may contribute to our observation of statistical noise in images, but they are not usually limiting (or even significant). The expected noise in an image is given by N_{net} in equation 3.2, with background noise as N_{back} in eq 3.4. We can also look at these noises as fractional noise over signal, as in eqs. 3.3 and 3.5. Where signal is the photon count in the pixel. We learn from equation 3.3 that if T_{sample} decreases (sample absorbs more) then the fractional noise in that region increases. This means that if we look for small features on top of large features they will be harder to see, than if they were over an empty background. In this sense the measure of noise we get from looking at background boxes is somewhat better than we expect to be able to do in interesting regions of a sample. We'll discuss this sort of analysis more later.

$$N_{net} = \sqrt{T_{loss} T_{sample} I_0} \qquad [3.2]$$

$$\left(\frac{N}{S}\right)_{net} = \frac{1}{\sqrt{T_{loss} T_{sample} I_0}} \qquad [3.3]$$

$$N_{back} = \sqrt{T_{loss} I_0} \qquad [3.4]$$

$$\left(\frac{N}{S}\right)_{back} = \frac{1}{\sqrt{T_{loss} I_0}} \qquad [3.5]$$

I_0 is the number of photons incident on the sample in the observed pixel. I_0 therefore increases arbitrarily as we increase the dwell time, and so the fractional noise can be reduced arbitrarily at the cost of longer imaging time. There is a limit to this process imposed by radiation damage to the sample, but we will discuss that limit in chapter 5 which discusses radiation damage.

For a given I_0 the wavelength dependence of the background noise is due to T_{loss}. Between the sample and the PC there is the gap in the wet cell (1.25mm of air,) the exit window of the wet cell (1000Å SiN), the air gap from the wet cell to the PC window (about 2mm) into which we flow Helium with fraction f_{He}, and last the PC window (another 1000Å SiN). T_{loss} breaks down into T_{SiN}, T_{PC}, and T_{wcell} as in equation 3.6. Each of those transmissions is given in equations 3.7, 3.8, and 3.9 respectively. Critical parameters are Z_{PC} and Z_{wcell} from figure 2.3 as well as f_{He} ,the fraction of helium in the air gap to the PC, and Z_{water}, the thickness of any water layers in the drained wet cell.

$$T_{loss} = \left(T_{SiN}\right)^2 T_{PC} T_{wcell} \qquad [3.6]$$

$$T_{SiN} = e^{\left(-2\mu_{SiN} Z_{SiN} \rho_{SiN}\right)} \qquad [3.7]$$

$$T_{PC} = e^{\left(-(1-f_{He})\mu_{air} Z_{PC} \rho_{air} - (f_{He})\mu_{He} Z_{PC} \rho_{He}\right)} \qquad [3.8]$$

$$T_{wcell} = e^{\left(-\mu_{air} Z_{wcell} \rho_{air}\right)} e^{\left(-\mu_{water} Z_{water} \rho_{water}\right)} \qquad [3.9]$$

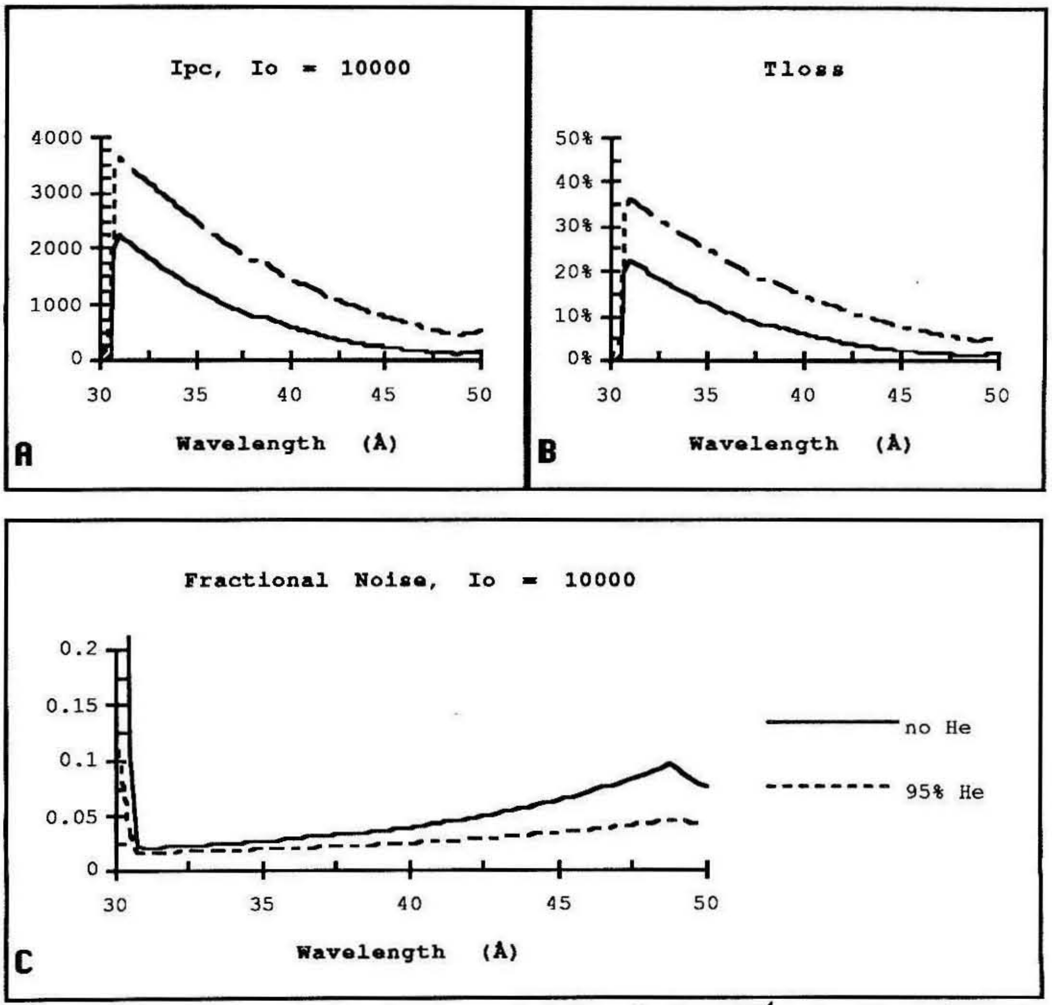

Figure 3.7 I_{PC} and Noise Fraction **A** is I_{PC} for $I_0 = 10^4$ using T_{loss} from the model of eqs 3.6-3.9, using 2mm 95%He in air or 0% He in air + 1.25mm air +2 SiN 1000Å windows and no water layer. **B** is T_{loss} as in **A**. **C** is the matching background fractional noise as in eq. 3.5. **C** contains the legend for all three graphs.

Figure 3.7A shows the wavelength dependence of I_{PC} for f_{He} = 95% or 0%. Figure 3.7B shows the corresponding T_{loss}. Figure 3.7C shows the consequent wavelength dependence of the fractional background noise (as in eq. 3.5), for the same models as 3.7A. All of these figures suggest some superiority for imaging just above the N edge near λ=31Å. We'll have more on that subject at the end of this chapter and in the chapter on radiation damage (chapter 5). The appropriate generalization here is that minimizing T_{loss} will reduce the fractional noise in images, and we can expect mechanical design, quality of helium flow and imaging wavelength all to influence noise through T_{loss}.

3.4 Incident Flux

We have chosen to use the quantity I_0, the count of incident photons on the sample in the pixel, as our measure of incident flux. The reason we chose this particular form is because it is most closely related to absorbed radiation dose, as we will discuss later. However, I_0 is not directly measurable by any of our instrumentation at the STXM, indeed the STXM is particularly weak in the area of incident intensity monitoring. The best we can do is to insert a dry wet cell in the STXM, positioned with the front window in the plane of focus, and calibrate the relation between I_0, ring current, I_{PC} and λ, for each undulator gap setting of interest. When we are operating the microscope for a normal image, the draining of the wet cell leaves water layers on both entrance and exit windows of the wet cell. These layers absorb anywhere from 20% to 80% of the incident flux, causing T_{loss} to be uncertain by a factor of at least 4. This is why we cannot estimate I_0 from I_{PC} in each image, but must work from tests with a dry wet cell for which we know T_{loss}.

The calibration is then based on the model T_{loss} that we've established above, with no helium flow(to avoid needing to estimate f_{He}). Equations 3.10 and 3.11 basically describe this simple calibration method. F_0 is the incident photon flux rate in Hz per

100mA ring current, i_{ring} is the synchrotron ring current in mA, τ is the pixel dwell time in sec used in the measurement of I_{PC}. The rate F_0 is a number convenient to use at the console to estimate what a pixel will receive for any given STXM settings, since the user must choose the dwell time τ for each image.

$$I_0 = \frac{I_{PC}}{T_{loss}} \qquad [3.10]$$

$$F_0 = \left(\frac{I_{PC}}{T_{loss}}\right)\left(\frac{100}{i_{ring}}\right)\frac{1}{\tau} \qquad [3.11]$$

In Figure 3.8 we go through this calibration procedure for an undulator gap of 43.4mm. Figure 3.8A gives the ratio $1/T_{loss}$ that relates I_{PC} to I_0 (or F_{PC} to F_0.) Using 3.8A we can convert the observed $I_{PC}/(\tau\ i_{ring})$ data in 3.8B to calculate the F_0 graph in 3.8B. And we can do this for several useful undulator gaps, as in figure 3.9. The data in figure 3.9 are made by taking a wavelength spectra of each undulator gap with the PC (i.e., watching I_{PC} vs. λ) with the dry wet cell in line.

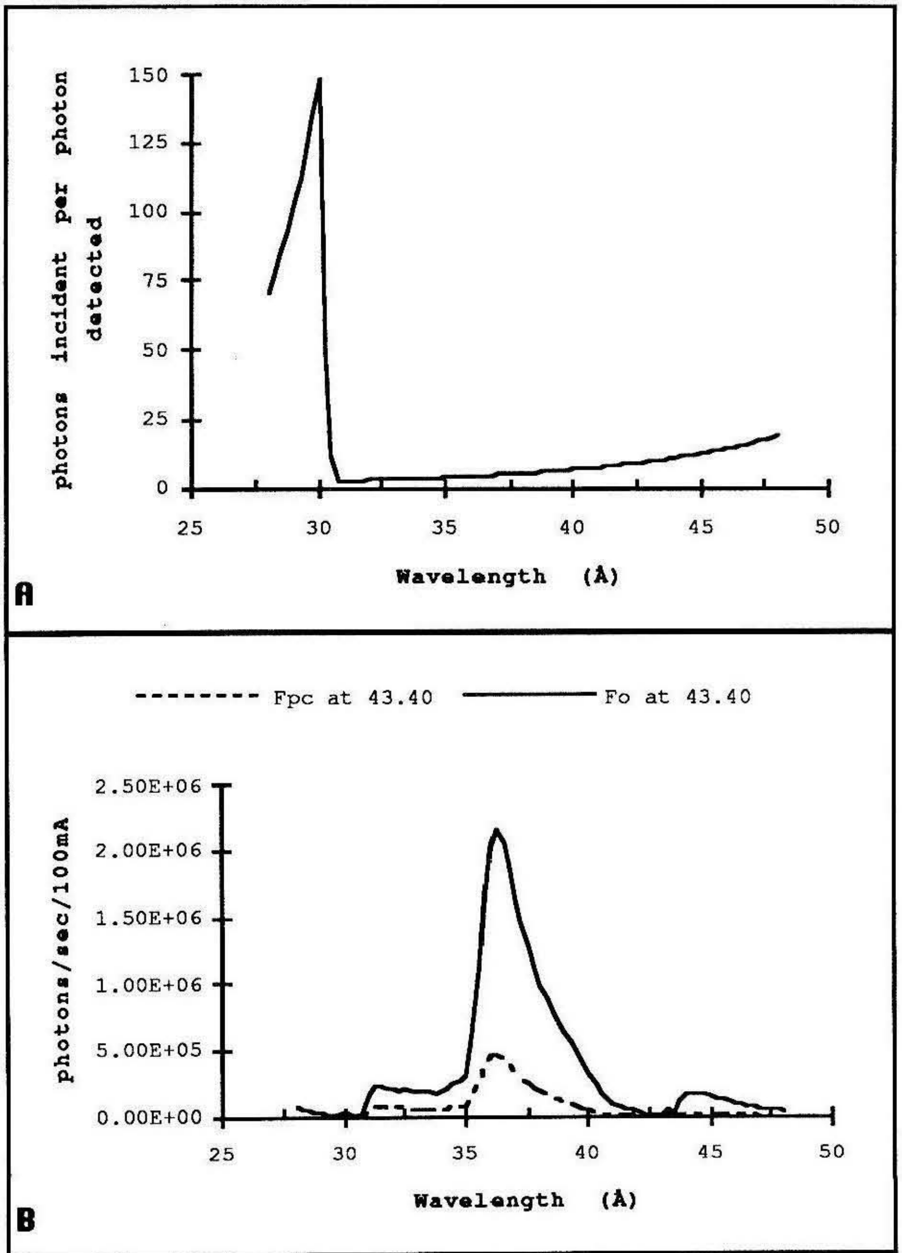

Figure 3.8 Predicting Losses A is a graph of photons incident vs photons detected using the same T_{loss} model as in figure 3.7A. **B** is a graph of the flux rate observed at the PC with the dry wet cell in line, and the estimated incident flux rate. Both are in Hz/100mA. The undulator gap was 43.4mm.

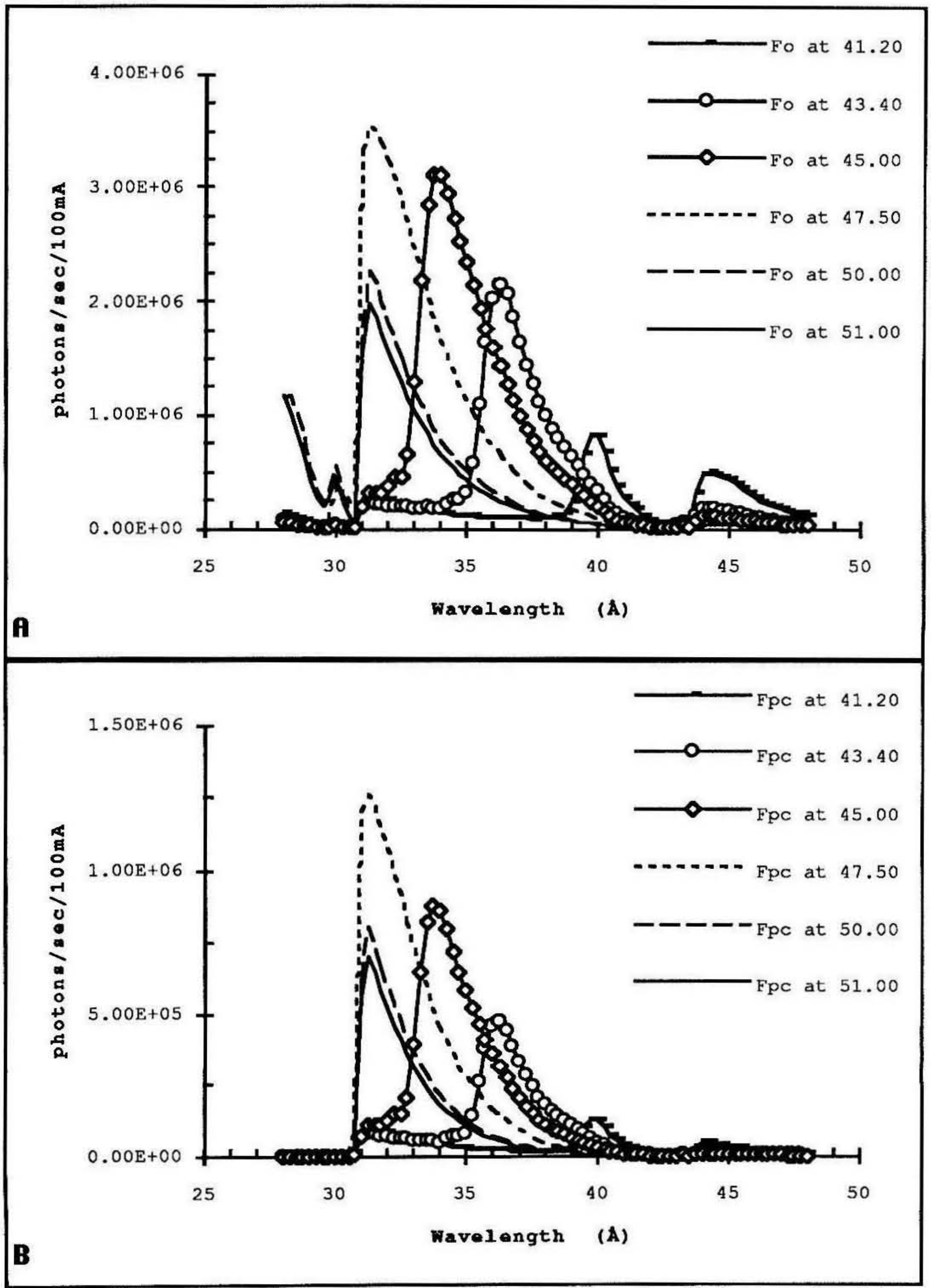

Figure 3.9 Several Undulator Gaps **A** is F_0 vs wavelength for several undulator gaps. **B** is the corresponding F_{PC}, from which F_0 is derived.

3.4.1 How good is our flux estimation?

When we calibrate the ring current vs. F_0 relationship, we can make a solid estimate of F_0. We use this to predict I_0 from the ring current and our chosen τ when imaging. Their are two types of error in using this calibration. Errors in making the calibration are in measurements of physical dimensions of Z_{PC} and Z_{wcell} and the nitride layers, which go into the model of T_{loss}. Errors in using the calibration when imaging are due to stability of the STXM upstream of the sample, over the period between making and using the calibration. We believe the calibration can be done to within 10%, at least above the Nitrogen edge, and off the Carbon edge itself. However, the stability of the upstream components over time is another matter. The components that contribute to the flux in the focal point of the zone plate are: the quality of the orbits in the ring (which has been as bad as ±50% in the nov '90 run), the dimension Z_{ex} (remember we move the zone plate to focus in z, Z_{ex} stays fixed), the helium flow fraction (f_{He}) between vacuum exit window and sample, and the thickness of the sample's SiN window.

measurement or parameter	**value**	**measurement error estimate**	**error effect*** λ=36Å
Z_{PC}	2mm	10%	1% @f_{He}=95%
Z_{wcell}	1.25mm	±50μm	5%
Z_{ex}	2mm	10%	1% @f_{He}=95%
SiN window thickness	1000Å	10%	4.3%
orbit stability (fill to fill)	------	-------	up to ±50%
f_{He}	95% in 2mm gaps	5%	±3%

Table 3.2 Flux Estimate Errors A table of values, error estimates, and estimates of the errors effect on the flux, for the parameters that go into the F_0 calibration vs ring current. *We estimate an effect of these errors at a fixed frequency λ=36Å since the effect of a given thickness error will depend on wavelength.

We summarize the various error estimates in Table 3.2. One must bear in mind that these are not statistical errors to be measured precisely, they are just upper bounds we put on the accuracy of our measurements. It would be best to be able to measure the incident flux directly for each image or each pixel, since that is not yet possible we've been forced to develope the system of calibration described above. The principle we're operating under is "do the best we can". No one could consider this situation optimum.

The error in making the calibration comes from errors in Z_{wcell}, Z_{PC}, and two SiN windows. Factoring these errors together for an upper bound we get ±16% (they are in fact independent errors so this should be an upper bound). On the other hand the error in applying the calibration to a given image is due to the upstream elements of the STXM, that is Z_{ex} and whatever problems exist in the ring and the beamline. Clearly the application of the calibration has error dominated by the stability of the orbits in the ring, and indeed that dominates the entire flux estimate error. From here on we'll use ±50% for the error in the flux estimate, it will be most relevant to the discussion of radiation damage in chapter 5.

3.5 Resolution

One of the most important qualities of any microscope is its resolution. Roughly speaking, resolution is a measure of how accurately the relative positions of features in a sample can be observed. In a microscope that basically produces 2-d images there is a transverse resolution, in the x-y plane, and a longitudinal or depth resolution, given by the depth of focus. In the case of the STXM, the transverse resolution is on the order of 100nm, while the depth resolution is closer to 2μm. Because of the disparity between the depth and transverse resolutions, the smallest features we can see in the image plane are much smaller than the depth resolution (as we'll see in chapter 6 we can find and measure features that are on the order of 200nm across.) That disparity is one of the differences between the STXM and modern high resolution visible light microscopes.

The STXM is a transmission/absorption microscope, and absorption in one depth of focus is a significant fraction of the incident radiation, so we need to keep our samples thin. This is another difference between the STXM and visible light microscopes, in which it is usually no problem to look through samples that are many times thicker than the depth of focus. In fact our best images are of samples that are at or below the thickness of the depth of focus. When the sample is thinner than the depth of focus the microscope behaves as a pure projection microscope, all features in the sample are projected unmodified onto a plane. We cannot separate them in z, to any significant degree.

3.5.1 What does resolution mean?

There are two different goals in imaging that underly notions of resolution. The first goal, which leads to the rayleigh resolution criteria, is the desire to discriminate between near but separate point objects. The second goal is the need for accuracy in the measurement of the optical density of all parts of a complex object. This second goal, as we shall see, is somewhat more demanding on the concentration of the x-ray probe provided by the zone plate. Both views of resolution are, of course, linked to each other. Indeed we can quite reasonably choose to use whichever view is more convenient for a given application.

The zone plate produces its 1st order diffraction pattern in the focal plane f, (sketched in figure 3.10). For a plate of many zones N>100 or so, the pattern is approximately an Airy function,[4] modified appropriately to account for a central stop blocking some percentage (by radius) of the zone plate.[5] The radial dependence of the probe intensity in the focal plane is shown in figure 3.11. Here we show the intensity for several different possible central stop sizes. The zone plates we have used have had 33%

stops. The radial coordinate is in normalized units of $1=\lambda f/\pi d_{Zp}=d_r/\pi$ which is 16.54nm for our favorite zone plate.

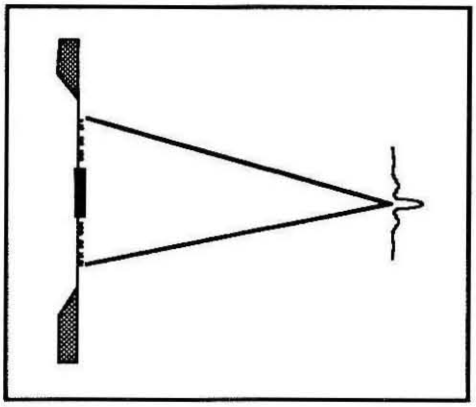

Figure 3.10 Probe Formed by Zone Plate The zone plate forms a probe of x-rays at its first order focus. This probe is shown with its profile expanded, to give its orientation.

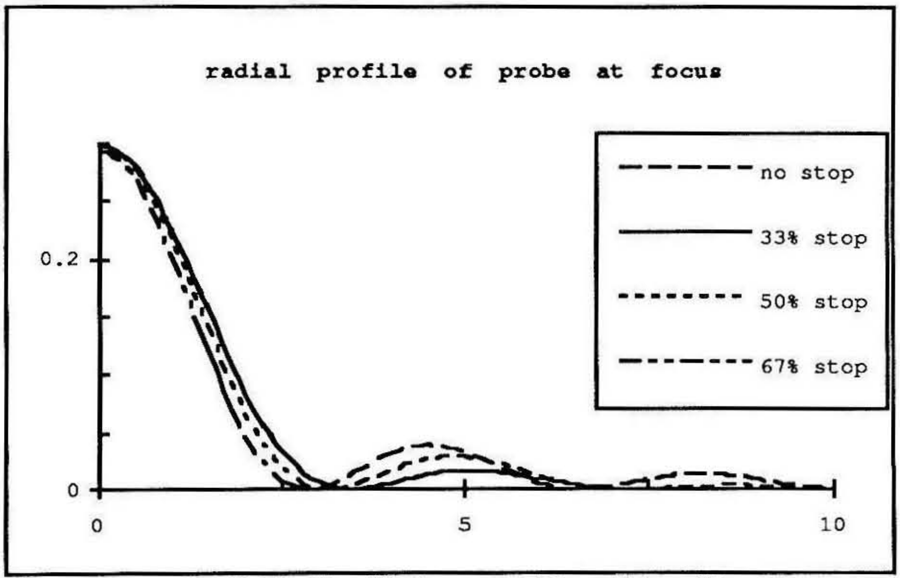

Figure 3.11 Radial Profile of Probe The radial profile of the x-ray probe intensity in the focus plane. Profiles are normalized to have same volumes over the plane. The normalized radial units are $1=\lambda f/\pi d_{Zp}=d_r/\pi$ which is 16.54nm for our usual zone plate.

One of the most important things to notice about the profiles in figure 3.11 is that the first minimum occurs at smaller radii as s, the stop fraction, increases. Increasing the stop size narrows the central maximum. However, it also increases the size of the outer maxima.

The Rayleigh resolution criterion considers that two point objects can just be separated in an optical system if the peak in the diffraction pattern of one occurs in the first minimum of the other. A similar criterion is to say that the full width at half max (FWHM) of the diffraction pattern gives a distance that will separate the patterns of two points. Figure 3.12 graphs these and other measures of resolution vs. stop size.

Both the Rayleigh criterion and the FWHM of the probe have similar absolute magnitudes and vary in a qualitatively similar way against stop size. However, if we ask how the density of an object is replicated in our image then we are lead to another set of criteria.

stop %	Rayleigh	FWHM	50% Flux	67% Flux	90% Flux	units
0	3.83	3.23	3.28	4.19	10.44	$\lambda f/\pi d_{Zp}$
0	63.39	53.48	54.25	69.38	172.68	nm (at 36.4Å)
0.33	3.45	3.05	3.67	5.46	12.04	$\lambda f/\pi d_{Zp}$
0.33	57.05	50.51	60.69	90.39	199.20	nm (at 36.4Å)

Table 3.3 Different Measures of Resolution Gives measures of resolution in normalized units of $1 = \lambda f/\pi d_{Zp} = d_r/\pi$ which is 16.54nm for our usual zone plate. Rayleigh is the standard Rayleigh resolution,modified in view of the stop size. FWHM is the full width at half max of the central peak. The 50% Flux, 67% Flux, and 90% Flux columns contain the diameters that catch that percentage of the x-ray flux.

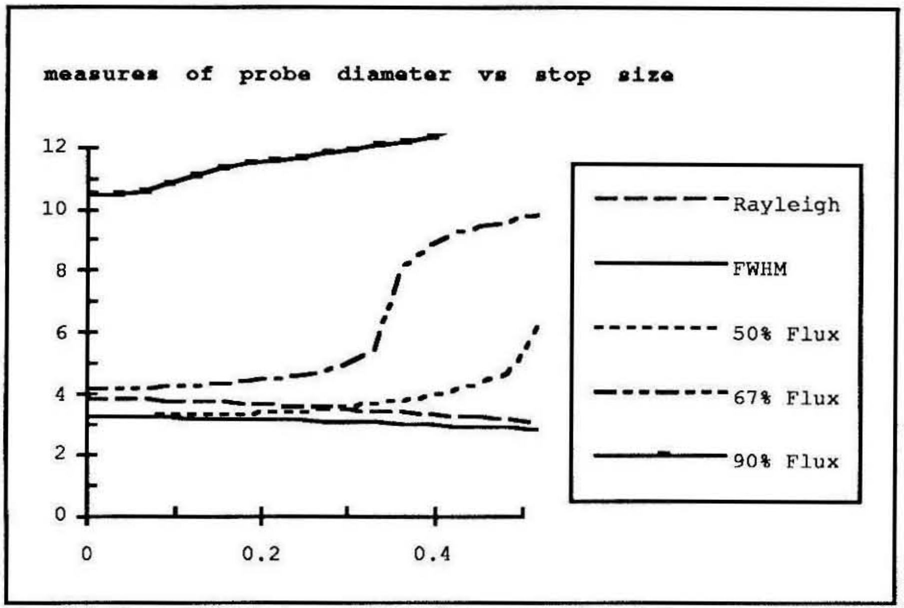

Figure 3.12 Resolution Several measures of resolution vs zone plate stop size. The dimensions of spatial resolution are $1 = \lambda f/\pi d_{ZP} = d_r/\pi$ which is 16.54nm for our usual zone plate. Selected values from this graph can be found in Table 3.3

Consider an opaque cube of side d_c. If we image that cube in the STXM we expect to get 100% transmission far from the cube, and in the center of the cube we expect no transmission if the cube is big enough to block the entire probe. The model is sketched in figure 3.13.

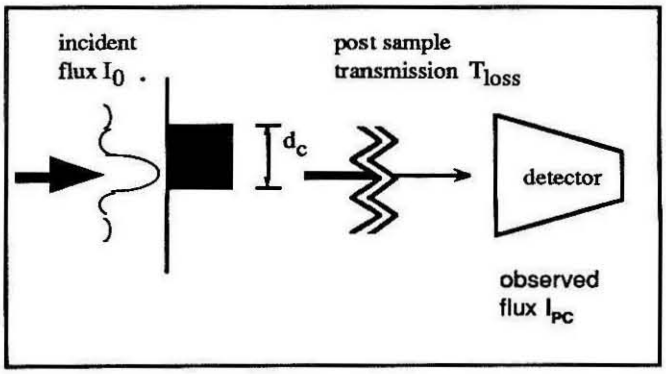

Figure 3.13 Model Cube An opaque cube of side d_c is the sample.

We can calculate the exact result of such an experiment and we show it in figure 3.14. For cubes of 2x the Rayleigh radius or 2x the FWHM we can see that we get a considerably reduced signal, even at the cube center, than the 100% blockage that would represent faithful replication of the object.

We are led to the criteria for faithful replication of small objects, that is the diameter within which x% of the flux from the probe falls. This type of criteria is shown in the other three graphs in figure 3.12, which show the diameters that capture 50%, 67% and 90% of the flux in the probe. Numerical results for no stop and 33% stop are shown in Table 3.3. The 50% flux criterion produces a similar resolution estimate to the Rayleigh and FWHM criterion, though that is really telling us that objects that size are reduced in signal by a factor of two.

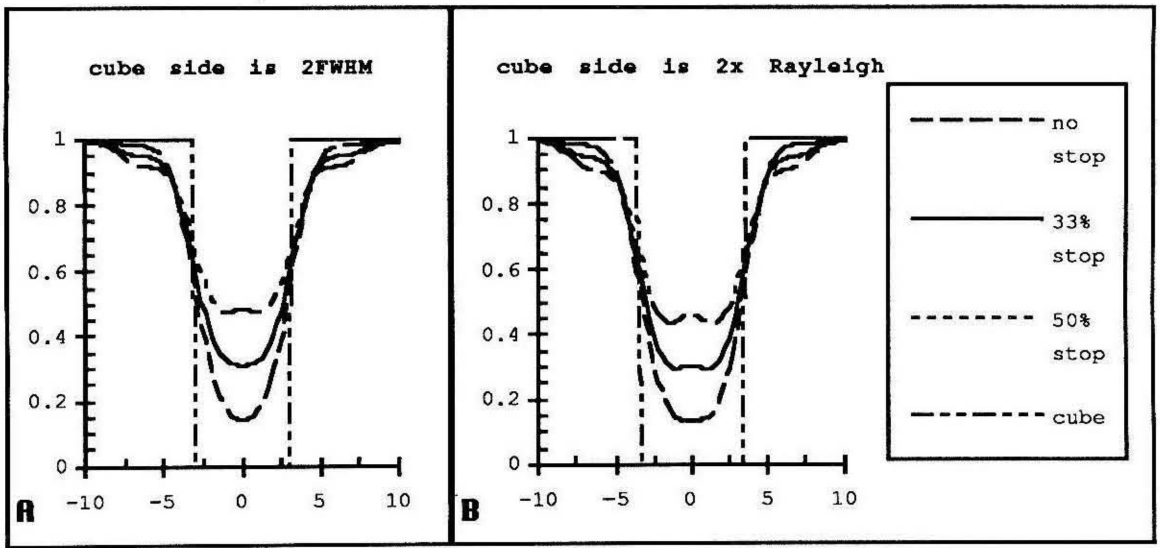

Figure 3.14 Cube Profile Shows the effect of zone plate stop size on cube profile. **A** uses a cube side of 2x the FWHM of the 33% stop probe (6.107), **B** uses a cube of side 2x the Rayleigh radius to the first minima in the 33% stop probe (6.896.) The x axis is in the same units as figure 3.12.

Looking again through the model, in figure 3.15 we graph the transmission in the center of an opaque cube vs the side of a cube (again in normalized units).

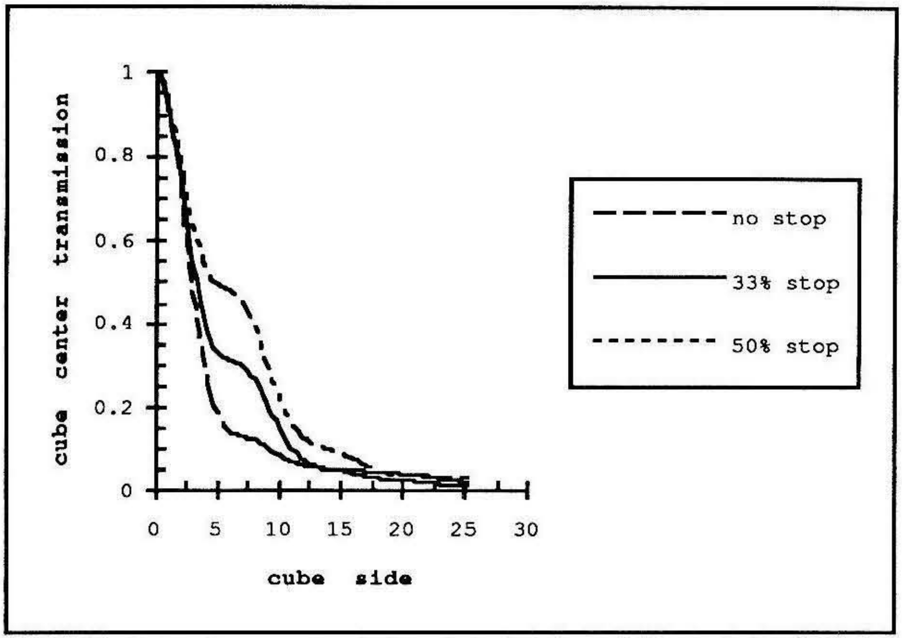

Figure 3.15 Center Transmission Calculated center transmission in a cube profile, vs. the cube side. We graph this for three different central stop sizes in the zone plate. Cube side is in normalized units again. $1=d_r/\pi=16.54$nm.

The intriguing step in the curves of figure 3.15 is the capture (or failure to capture) the secondary maxima as well as the central maxima. Here it is clear that at regions near what the Rayleigh criteria would consider the resolution (about 3 to 6 in normalized units) the smaller the stop the better. Figure 3.15 essentially shows us how the thickness of small objects will be reduced in STXM images. Much of that effect can be taken out by proper image processing in software, if an object is detectable at all. However, when the signal from an object falls below the noise in its image the object is undetectable.

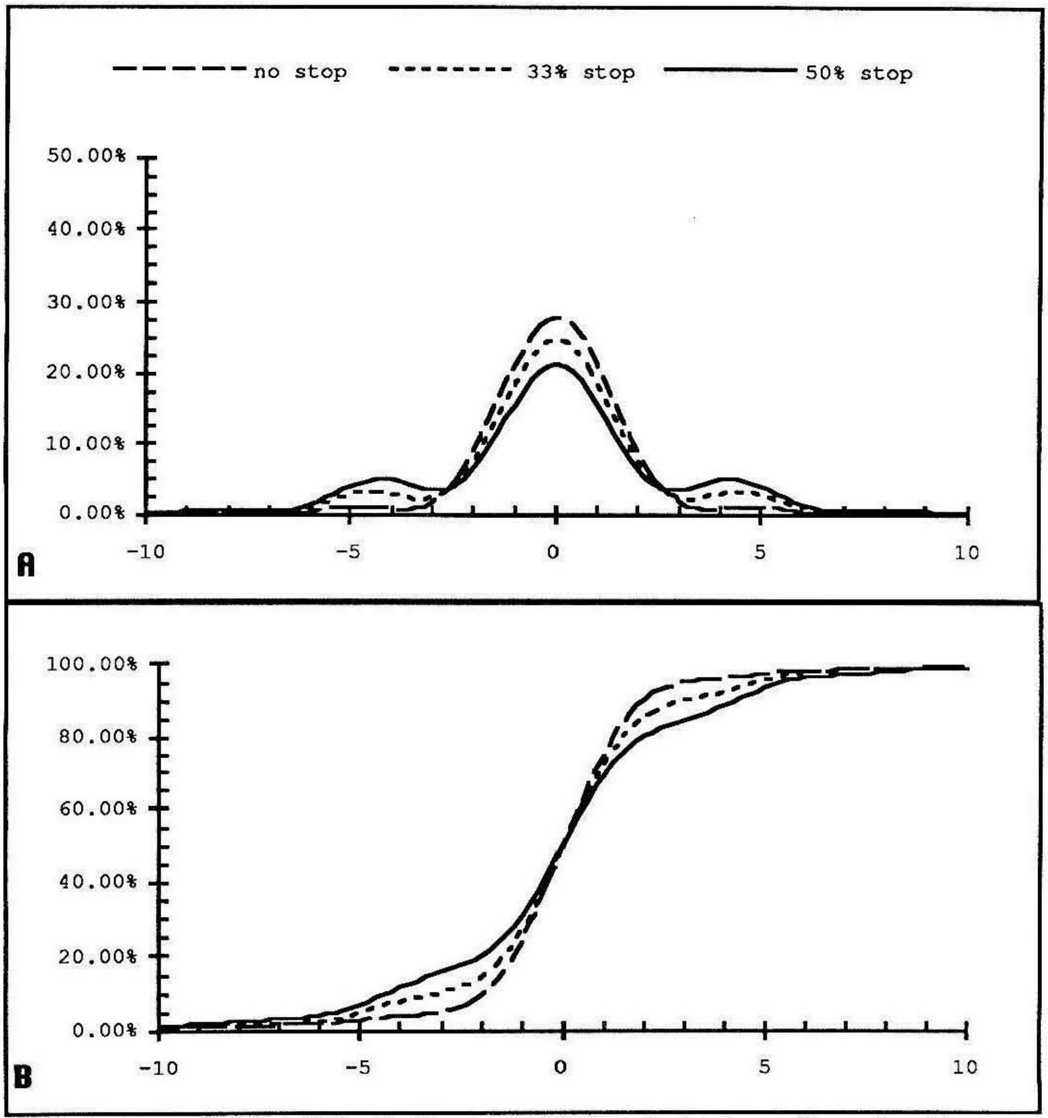

Figure 3.16 Calculated Edge Profiles **A** is the calculated x profile produced by a zone plate, unobstructed or with either a 33% or 50% central stop. **B** gives the result (in % of flux transmitted) of passing a knife edge (with edge parallel to y) along the x-axis in front of the probes in A.

Calculations aside, we constantly need to check the resolution that we are getting with the microscope, to make sure it is operating correctly and the sample is in focus. The easiest test of resolution is the knife edge test.[6] This involves using an edge parallel to the y axis and observing one x scan. We can measure the change in transmission at the center of the edge and deduce the resolution from that. This is what we do in the focus scan explained in the previous chapter. There we were interested in the z coordinate of the qualitatively sharpest focus, here we are concerned with just how quantitatively sharp that focus is. The STXM on line software does not as yet automatically extract a quantitative value for the resolution from a focus scan. Typically the operator must evaluate the edge profile by eye.

In figure 3.16A we show the expected probe profile as it will be scanned over the edge of a focus mark. This is no longer in radial coordinates, instead we have integrated from $-\infty$ to $+\infty$ in y at each x to get the given profile. The minima no longer reach zero, but most of the qualitative features of the probe are similar to its radial profile. In figure 3.16B we integrate the profiles of 3.16A from $-\infty$ to x in order to get the expected profile of a perfect edge. This edge profile gives us an expected curve to work with and with which to fit our observed profiles.

We can then take the observed I_{PC} photon counts for an edge profile and fit it to the 33% stop curve that we expect from our zone plate. This is shown in figure 3.17, where we have done a least squares fit to the observed photon count profile. The procedure the microscope operator usually uses is to measure the x distance in nm between the intercepts of the 25% and 75% line this gives 68nm in this case. That is quite reasonable for a focus mark in a real sample. In this manner resolutions as small as 50nm have been observed.[7] The intercepts from 25% to 75% have an obvious correspondence to the 50% Flux criterion for resolution, since they represent 50% of the total flux passing over the edge. However they are not identical, since the 50% Flux criteria of figure 3.12 and Table 3.3 is based on a radial diameter and a radial integration, while the knife edge criteria involves a strip of the x-y plane from $y=-\infty$ to $+\infty$. In fact the number we measure off the edge profile for x% of the step will be less than the the diameter that captures x% of the total flux.

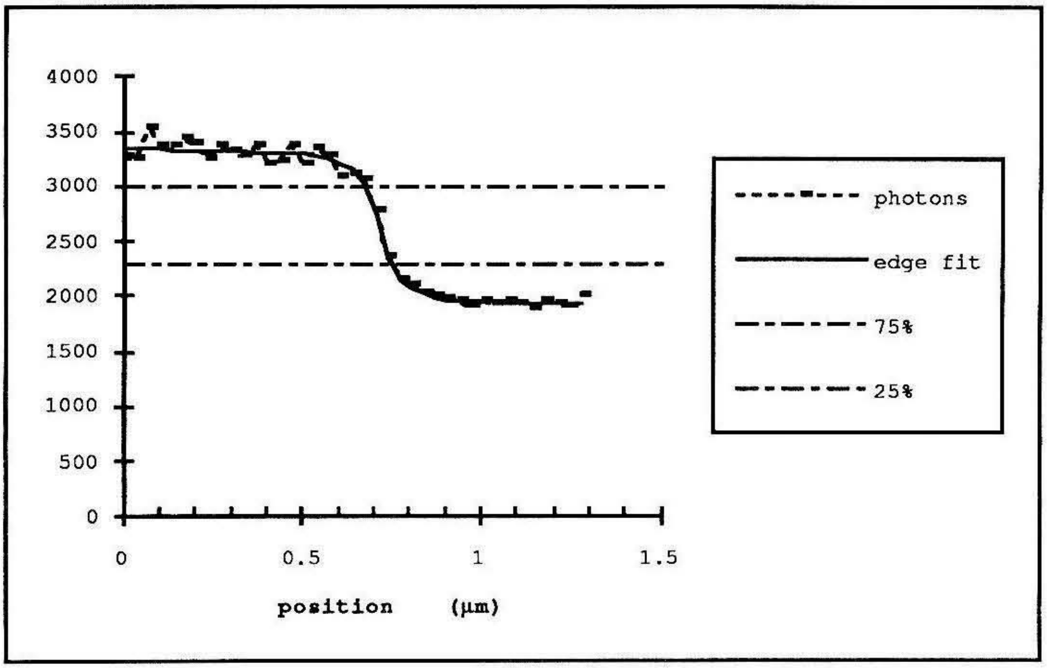

Figure 3.17 Observed Edge Profile We graph here the photon count in an x scan line across a focus mark edge. We also graph the fit to this data of the 33% stop edge profile in figure 3.14B. The horizontal lines give the 25% and 50% levels of the edge step. The intercepts of those levels with the fit curve give us 68nm for this edge.

3.6 Contrast

All microscopes, or imaging techniques operate due to some mechanism of generating contrast in the image from features in the sample. In the STXM x-ray absorption provides the contrast mechanism. Consider a sample composed of n elements. Over each pixel of the sample there is a mass ρ_i of each element i having mass absorption coefficient μ_i. The total transmission through the sample is given in equation 3.12. All variation over the image is due to variation of the column mass $\rho_i(x,y)$. All variation with respect to wavelength is due to variation of the absorption coefficients $\mu_i(\lambda)$. The ρ_i are in units of gm/cm^2 and the μ_i are in units of cm^2/gm For biological samples 3.12 is particularly good because the μ_i are just absorption coefficients, since there is little scattering in C, O, N and H at soft x-ray wavelengths. These coefficients are well known in our wavelength range[8].

$$T_{sample} = e^{-(\sum_i \mu_i \rho_i)} \qquad [3.12]$$

In this dissertation we will make use of two simplified models of a cell. First the "one component model", which assumes that all signal in an image is due to carbon column density. In the one component model T_{sample} is written as in equation 3.13, where ρ_c is the carbon column mass and μ_c is the carbon mass absorption coefficient. This model assumes that the mass of water in the cell is the same as the mass of water on the window outside the cell, and thus absorption due to water (i.e., the bulk of absorption in oxygen) is completely removed by the 2nd normalization. We will use column mass ρ most of the time in this dissertation, because in the STXM it is what we measure directly. Usually we can only infer thicknesses and true densities. The only exceptions will be as a paranmeter of the models we will build. In those cases (see below) a feature thickness and its true density will be some of the free parameters of the model.

$$T_{sample} = e^{-(\mu_C \rho_C)} \qquad [3.13]$$

$$T_{sample} = e^{-(\mu_{Nc} N_c)} \qquad [3.14]$$

An alternative formulation of the one component model is given in equation 3.14, in which N_c is the number of carbon atoms over a 1 μm^2 column, and μ_{Nc} is the atomic absorption coefficient of carbon. So $\mu_{Nc}=\mu_c x 1.992x10^{-15}$. This formulation is particularly useful for discussing radiation damage where we seek a relation between atoms lost and photons absorbed. That discussion will take place in chapter 5.

A slightly more complicated model of the material making up a sample cell will be needed in chapter 7, in which we discuss using imaging at different wavelengths to separate the different components of equation 3.12. What we will use in chapter 7 is a "two component model" in which the cell is made up of carbon and oxygen or alternatively protein and water. This model is summarizd in equation 3.15.

$$T_{sample} = e^{-(\mu_C \rho_C + \mu_O \rho_O)} \qquad or = e^{-(\mu_P \rho_P + \mu_W \rho_W)} \qquad [3.15]$$

Where ρ_C, ρ_O,ρ_P,ρ_W are the column masses of carbon, oxygen, protein, or water, respectively. μ_C, μ_O,μ_P,μ_W are the mass absorption coefficients of carbon, oxygen, protein, or water, respectively. We use an average value for protein.[9]

3.7 Detection

An important quality of any microscope is its ability to detect small features. What is the smallest feature that can be detected by the STXM? For hard features (100% absorption) this is on the order of the transverse resolution. The question gets much more complicated for real features, of which many provide only some small absorption above background. In that case it is instructive to model the features, the signal they generate in an image, and the statistical noise against which they are observed.

3.7.1 The Model Cell and Granule

In order to discuss the Signal to Noise ratio in images of cells, and understand the constraints and limits of operation of the STXM, we need a simple model of a cell, with a feature to generate a signal of interest. We'll call this the model cell and granule. The model is illustrated in figure 3.18. In a cell body of thickness Z_B, and carbon density ρ_B

we consider a granule of thickness Z_G, and carbon density ρ_G above the density of the cell body. The model granule allows us to calculate the relationship between the wavelength λ, the incident flux I_0, the post sample transmission T_{loss}, the absorption of photons or energy in a pixel column, and the S/N we get when observing the granule in an image. Simplifications are that we are using the one component model above, the cell is of uniform thickness, and the feature (granule) is uniform. Furthermore we will assume the probe formed by the zone plate is perfect and we image the granule at its peak.

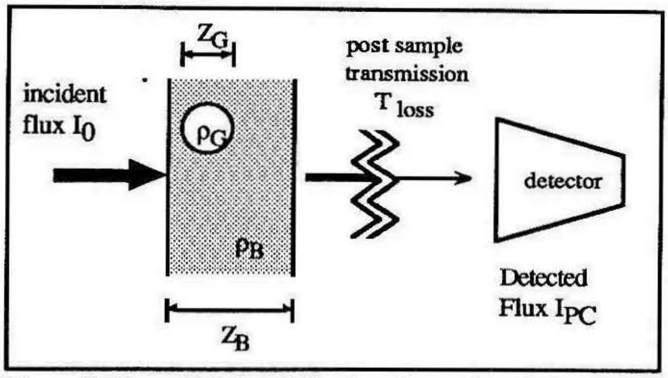

Figure 3.18 Model Cell A schematic of the model cell and granule, listing parameters of the model, Z_G, ρ_G, Z_B, ρ_B, T_{loss} and I_0. The other variables in the model are λ, dx, and the desired Signal to Noise ratio S/N. [T_{loss} is the post sample transmission]

The basic equations for the model are eq 3.16 and 3.17 which describe the transmission away from the granule and on the granule, respectively. Z_B is in cm, ρ_B is in gm/cm^3, so their product is column mass in gm/cm^2, as in the one component model above. The same is true of Z_G and ρ_G. By convention we define the density ρ_G as the incremental granule density above the cell background, so when $\rho_G=\rho_B=.1$gm/cm3 then the granule has twice the density of the cell. The fractional transmission signal due to the granule is given by equation 3.18. That fractional transmission gives us a signal, and we use expected shot noise to estimate the Signal/Noise ratio that the granule will give in an image illuminated by I_0 photons per pixel. As a useful measure of required illumination we can calculate the energy absorbed in a 1 μm^2 column, due to the same I_0, and that energy ΔE is shown in equation 3.20. It depends on the inverse square of the pixel size (in µm). This is one of the major constraints on imaging, to get the same S/N, while reducing dx requires the energy deposited to rise as dx^{-2}.

$$T_{Body} = e^{-(\mu_C Z_B \rho_B)} \qquad [3.16]$$

$$T_{Body\_and\_Granule} = e^{-(\mu_C Z_B \rho_B)} e^{-(\mu_C Z_G \rho_G)} \qquad [3.17]$$

$$\left(\frac{\Delta T}{T}\right)_{\text{granule}} = 1 - e^{(-\mu_C(\lambda) Z_G \rho_G)} \qquad [3.18]$$

$$\frac{S}{N} = \frac{I_0 T_{Body} T_{loss} \left(\frac{\Delta T}{T}\right)_{\text{granule}}}{\sqrt{\left(I_0 T_{Body} T_{loss}\right)}} = \sqrt{\left(I_0 T_{Body} T_{loss}\right)} \left(\frac{\Delta T}{T}\right)_{\text{granule}} \qquad [3.19]$$

$$\Delta E = \frac{hc}{\lambda} \frac{I_0\left(1 - T_{Body}\right)}{dx^2} \qquad [3.20]$$

Now to get a better feel for these equations we'll model them numerically. For T_{loss} we will use a model of the space between the sample cell and the PC with no water layers, 1.25mm of air in the wet cell, 2mm of 95% Helium, and two 1000Å SiN windows (one wet cell exit window and the window to the proportional counter.) This model has parameters Z_B, ρ_B, Z_G, and ρ_G, and we will define four regimes of the model: a hard granule and thick cell ("hard thick") with parameters 1µm, 0.1gm/cm^3, 0.1µm, and 1gm/cm^3 respectively. A hard granule in a thin cell ("hard thin") with parameters 0.1µm, 0.1gm/cm^3, 0.1µm, and 1gm/cm^3. A soft granule in a thick cell ("soft thick") with parameters 1µm, 0.1gm/cm^3, 0.1µm, and 0.1gm/cm^3. And a soft granule in a thin cell ("soft thin") with parameters 0.1µm, 0.1gm/cm^3, 0.1µm, and 0.1gm/cm^3. Examples of these regimes in real cells are, looking at small granules in the cell body near the nucleus for "thick" cell regime, or looking at them in a veil or a growth cone for the "thin" cell. Examples of the granule regimes are the features like a protein or lipid storage granule, which may look "hard" and features like mitochondria or overlying axons which do not offer much contrast i.e., which fall in the "soft" regime.

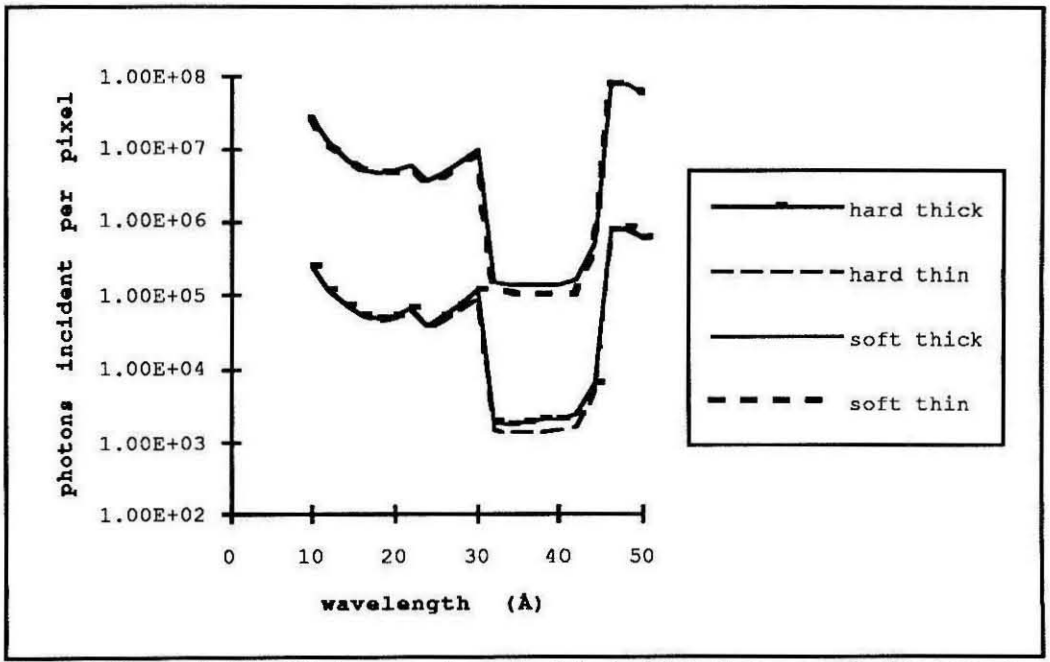

Figure 3.19 Incident Photons A graph of the incident photons required to generate a signal to noise ratio of 5:1. Using the cell and granule model described in the text. Parameters of the model are Z_B, ρ_B, Z_G, ρ_G and they are: for "hard thick" 1µm,.1gm/cm^3 ,.1µm and 1gm/cm^3 respectively. For "hard thin" .1µm,.1gm/cm^3 ,.1µm and 1gm/cm^3. For "soft thick" 1µm,.1gm/cm^3 ,.1µm and .1gm/cm^3. For "soft thin" .1µm,.1gm/cm^3 ,.1µm and .1gm/cm^3.

What is the relation between the wavelength we image with and the incident flux that we require to detect a fine feature like our granule? Figure 3.19 shows the minimum number of incident photons per pixel, I_0, that are required to detect the granule with S/N=5. S/N=5 is called the Rose criterion, and it is commonly used as a benchmark level of detectability for features in 2D images. From equation 3.19 we see that S/N varies as the square root of I_0, so we expect to need only 1/4 the photons to get a signal to noise ratio of 2.5. In figure 3.19 we graph I_0 vs wavelength, for each of the four versions of the model listed above. There is a clear window, between the nitrogen edge and the carbon edge, in which the microscope needs more than an order of magnitude fewer photons to achieve the same signal to noise ratio. That window is mostly due to the effects in T_{loss} of the air in the wet cell and the SiN windows.

Using equation 3.20 the model describes the corresponding absorbed energy in $eV/\mu m^2$ that is required to detect the granule, under the same circumstances as above. The results of this calculation are shown in figure 3.20. In figure 3.20A we graph energy absorbed vs wavelength. The same window that we saw when looking at I_0 is apparent. However, the graphs of the different regimes are more separated than in figure 3.19, since the absorption in the cell background separates the "thick" from "thin" cases

In figure 3.20B we show the energy absorbed vs pixel size (in μm) for all four regimes of the model. As expected from equation 3.20 the energy absorbed varies as dx^{-2}.

The purpose of these calculations is to show how the factors of desired S/N on a feature, desired pixel size dx, and wavelength all fold together to require a minimum incident flux, I_0, or absorbed energy, ΔE. The model so far has no damage effect in it, so we can get to any dx and any S/N by adding photons until we get tired of sitting by the STXM waiting for an image. In chapter 5 we will add in some estimates of visible radiation damage, to explore true limits on imaging with the STXM.

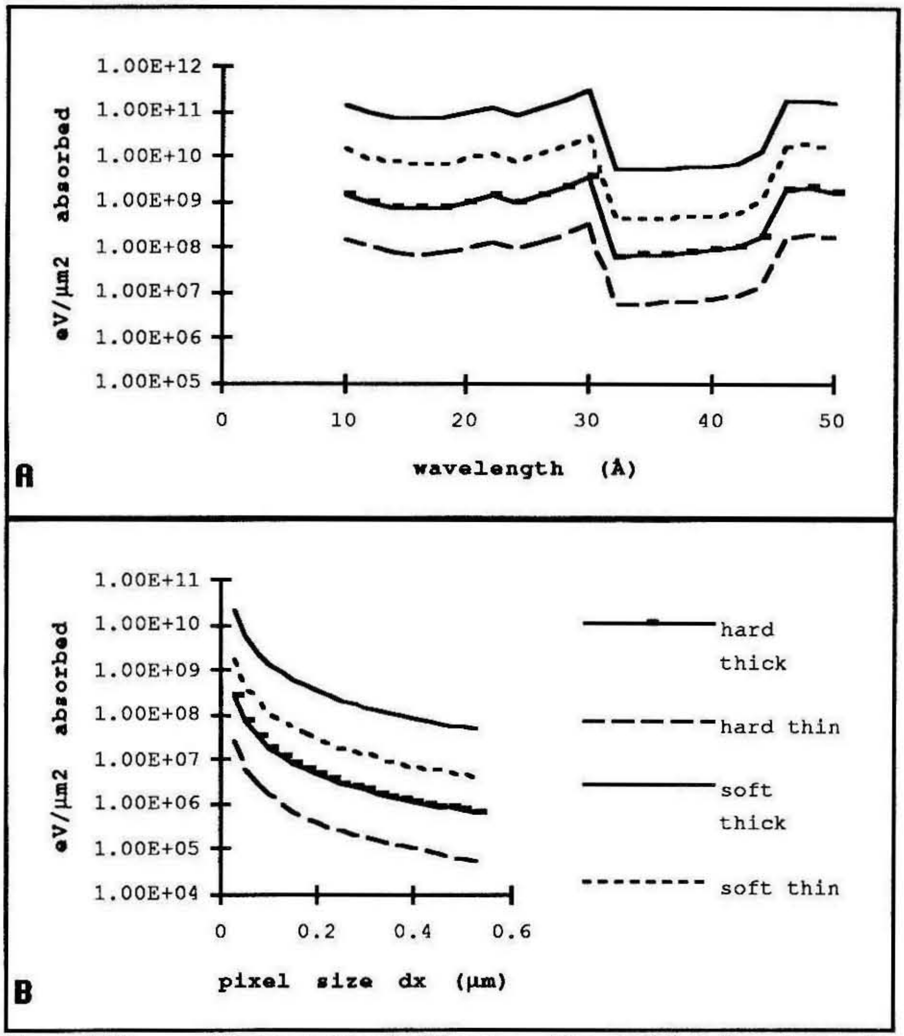

Figure 3.20 Minimum Absorbed Energy The model cell and granule allows us to calculate the minimum absorbed energy required to observe a granule with S/N=5, the absorbed energy is in eV/µm^2. **A** is the graph of minimum absorbed energy vs λ at dx=.05µm., **B** the same vs pixel size at λ=36Å. The calculation is done with model T_{loss} having 95% He, and no post sample water layers

3.8 Chapter 3 References

---

1 H. Rarback, C.J. Buckley, K. Goncz, H. Ade, E. Anderson, D. Attwood, P. Batson, S. Hellman, C. Jacobsen, D. Kern, J. Kirz, S. Lindaas, I. McNulty, M. Oversluizen, M. Rivers, S. Rothman, D. Shu, and E. Tang, "The Scanning Transmission Microscope at the NSLS," Nucl. Instrum. Meth. A **291** pp.54-59 (1990).

2 J.R. Gilbert, ObjectImage v1.0 Manual, 1992 in preparation.

3 D. Shu, D.P. Siddons, and H. Rarback, "Two-dimensional Laser Interoferometric Encoder for the Soft X-ray Scanning Microscope at the NSLS," Nucl. Instrum. Meth. A **266**, pp.313-317 (1988).

4 A.G. Michette, Optical Systems For Soft X-Rays, chapter 8 (Plenum Press, London, 1986).

5 M. Born and E. Wolf Principles of Optics chapter 8 2nd edition 1964

6 C.J. Buckley, "Measurement of Resolution in Zone Plate X-ray Microscopy," in X-ray Microscopy II, edited by D.Sayre, M. Howells, J. Kirz, and H. Rarback, (Springer, Berlin, 1988) pp.146-150.

7 Y. Vladimirsky et al., "Zone Plate Lenses for X-Ray Microscopy," Nucl. Instrum. Meth. A**266** pp.324-328 (1988).

8 B.L. Henke, P.Lee, T.J. Tanaka, R.L. Shimabukuro, and B.K. Fujikawa, "Low Energy X-ray Interactions: Photoionization, Scattering, Specular and Bragg Reflection," in Atomic Data and Nuclear Data Tables **27**, 1 (1982) and the SF software as described in: M.M. Thomas, J.C. Davis, C.J. Jacobsen, and R.C.C. Perera, "A Program for Calculating and Plotting Soft X-ray Optical Interaction Coefficients for Molecules," (Lawrence Berkeley Laboratory, Berkeley, 1989) document LBL-27668

More References:

9 see reference 8.

4 Sample Handling

In this chapter we will start by describing the Caltech Wet Cell, both its design and operation. We will also discuss the relative merits of the Caltech wet cell design vs the LBL wet cell design, for particular imaging applications, and for effects on the STXM images taken with them. We will then give a brief look at the two primary culture systems that we've used in our work with STXM. We will summarize some tests which establish that exposure in the wet cell, without x-ray irradiation, causes no significant damage to live neurons or fibroblasts. Finally we will discuss the design and fabrication of the culture substrates we make at Caltech to work with the wet cell.

Many different types of cells have been cultured successfully, by dissociating them from intact animals or by growing them as replicating cell lines *in vitro*. Many cells of particular interest, such as nerve cells and fibroblasts, grow as monolayer cultures, in which they must attach to a substrate for survival. In soft x-ray transmission microscopy the absorption coefficients favor studies of tissue thicknesses of ten microns or less, as does the depth of focus of our x-ray optics (as discussed in chapter 2). When we grow tissue culture cells on a thin flat membrane, they are naturally confined to a plane. We can mount that membrane in the plane of focus of the STXM, and all the cells or all the features of any given cell, are then in focus. In that sense surface adherent monolayer cultures are mechanically well-matched to the STXM.

4.1 Principles of the Caltech Wet Cell system

In order to image whole live cells, two types of wet cells can be envisioned. One, a "thin" wet cell, provides a space perhaps 2-10μm thick filled with culture medium, over a substrate on which cells have been grown, or through which medium containing cells or sub-cellular structures can be passed for imaging. Another, a "thick" wet cell is designed to be filled with culture medium for maintenance of cultures and drained for imaging. During imaging the air thickness in the wet cell is the only significant x-ray absorber other than the cultured cells, so the wet cell can be about 1mm. thick.

At Caltech we have chosen to develop this second type of wet cell, for two reasons. First, because such a design lets us use cell culture substrates that are completely compatible with conventional primary tissue culture, and then mount selected (by visible light microscopy) cultures in the wet cell for imaging with the STXM. And second, because it minimizes the absorption by the medium when imaging thin structures such as dendrites and axons in neuron cultures with thick cell bodies. The "thin" wet cell is similar to the design of the LBL wet cell.[1] The group at LBL has been primarily interested in looking at extracted sub-micron granules, which are floating in the medium. The "thin" (~2μm) wet cell is essential to constrain the granules to the focal plane.

Figure 4.1A schematically illustrates some of the main attributes of the stainless steel wet cell. The horizontal scale is about five times the vertical one, and the chamber diameter is 5 mm. The x-ray beam is seen coming from the right, and as we discussed in chapters 2 and 3 the distance to the OSA is the working distance of the microscope.

Presently, the zone plate/OSA system gives us a working distance from the specimen window to the OSA of about 250 microns, but we have designed the wet cell to allow this to be as small as 100 microns. The substrate places the cells at the front surface, and a clamp plate, not shown, which holds the substrate, adds a thickness of just 75 microns.

Our culture chips are shown in figure 4.1B. They are made from silicon, partly, etched away to produce the recess in which cultures are grown. The thin film which forms the culture substrate is 1000Å of silicon nitride. We have tried to maximize the area on which cells can be cultured, subject to the limits imposed by the strength of this film. This maximizes the population of cells available for observation, and minimizes the effect of a meniscus around the rim of the well when the wet cell is drained. On the silicon nitride film we produce a pattern of gold focussing marks and an array of locating numbers. These facilitate locating cells of interest previously identified in an optical microscope and also focussing the STXM on the plane of the substrate in the vicinity of a given cultured cell. There is a further discussion of the chips at the end of this chapter.

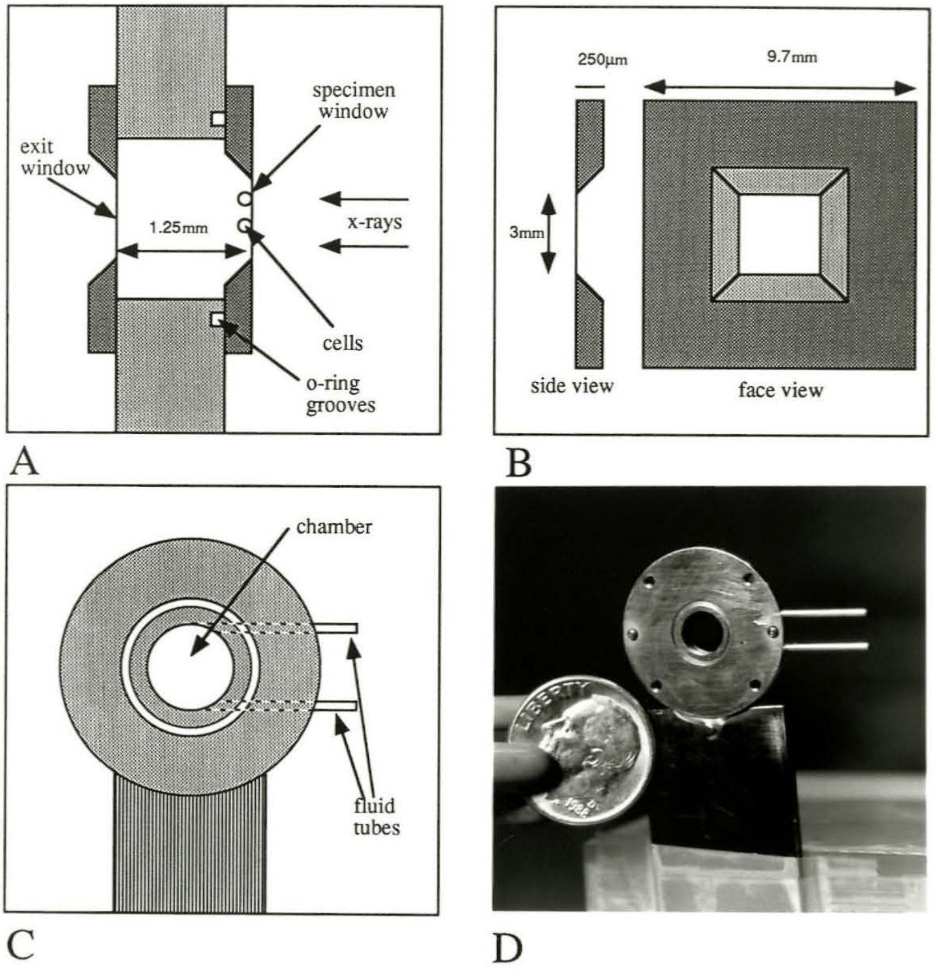

Figure 4.1 Views of the Wet Cell A is a schematic of the basic wet cell, side view. B is a drawing of the culture chips in front and side views. C is a front view of the wet cell body, without the specimen and exit windows, this drawing shows the fluid tubes, the o-ring groove, and the wet cell holder.

Figure 4.1C shows the front of the wet cell, with inlet and outlet tubes. Culture medium is pumped in and out of the cell as desired by a precision syringe pump attached to the lower tube. The upper tube leads to a reservoir of humidified air. For wavelengths shorter than the nitrogen edge the absorption by gas in the cell can be reduced by using a helium-oxygen mixture instead of air. However, we have not yet verified that this is tolerated by living cells. Figure 4.1D is a photograph of the front, without a substrate and clamp. Two aligning pins and four threaded holes are seen, for positioning and attaching the clamp, and the cell is attached to a holder appropriate for the stage of the BNL STXM.

A more precise drawing of the parts of the wet cell, and its assembly is shown in figure 4.2, which gives a two part view of the wet cell assemblage. On the left we have an exploded view of the pieces of the wet cell, and on the right we show the pieces assembled. The drawing is to scale, the scale bar is 1cm. A labels the clamping screws that hold the brass plate and thus the specimen chip to the body of the wet cell. There are 4 of these screws, though only 2 are shown here, (see figure 4.1 for their relative positions). B labels the brass plate -- which is one piece, though it appears here as two due to the crossection. C labels the specimen chip which is held to the wet cell body by the brass plate. D labels the body of the wet cell, which is machined from a 2 cm stainless steel disk 1 mm thick. E labels the exit window, which we glue onto the back of the wet cell body. The exit window typically lasts through several changes of the specimen chip. F labels the o-ring, in its groove. The o-ring provides a tight seal between the clamped on culture chip and the body of the wet cell.

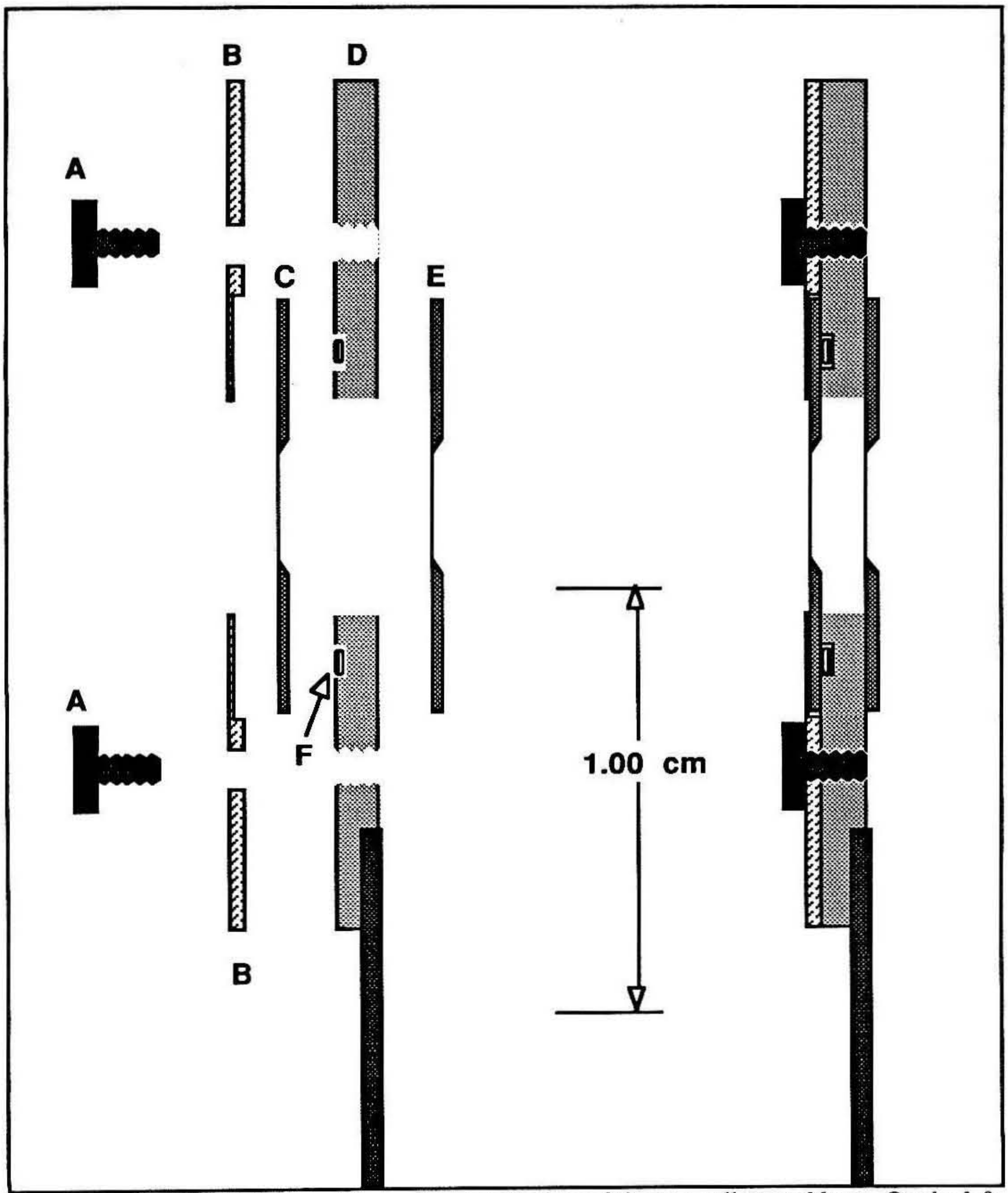

Figure 4.2 Wet Cell Assembly A two part view of the wet cell assemblage. On the left we have an exploded view of the pieces of the wet cell, and on the right we have the assembled pieces. The drawing is to scale, the scale bar is 1cm. **A** labels the clamping screws that hold the brass plate and thus the specimen chip to the body of the wet cell. There are 4 of these screws, though only 2 are shown here. **B** labels the brass plate -- which is one piece, though it appears here as two due to its crossection. **C** labels the specimen chip which is held to the wet cell body by the brass plate. **D** labels the body of the wet cell, which is machined from a 2 cm stainless steel disk 1mm thick. **E** labels the exit window, which we glue onto the back of the wet cell body. **F** labels the o-ring, in its groove. The o-ring provides a tight seal between the clamped on culture chip and the body of the wet cell.

4.2 Operation of the Caltech Wet Cell

The operation of the wet cell has two parts, loading a chip into the cell and operating the cell on the STXM. Ease of loading was a major design constraint on the wet cell.

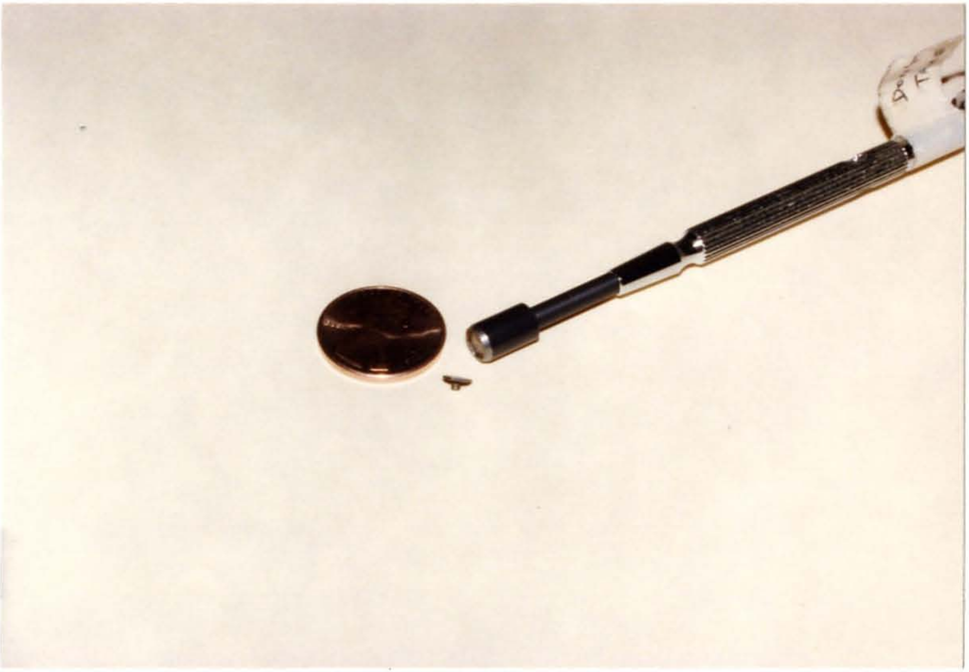

Figure 4.3 Wet Cell Screwdriver The special tool for tightening wet cell screws.

4.2.1 Loading the wet cell

The procedure for loading a chip into the wet cell is illustrated in figure 4.4A-C. To load a chip into the wet cell we attach a standard 1ml syringe to the lower inlet tube through a length of intramedic PE-90 tubing. Then the wet cell is placed face up on a surface and filled with media from the syringe until a convex meniscus is formed without bubbles, see figure 4.4A.

The specimen chip is then placed cell side down on the drop of medium in the wet cell. Using a piece of filter paper we wick up excess medium, until the chip lies flat against the body of the wet cell, figure 4.4B. The chip can be nudged sideways, with a forceps, to the center if necessary. Then the brass plate is placed over the chip and the 4 clamping screws are used to tighten it down to the body of the wet cell, figure 4.4C.

The screws would be impossible with an ordinary screwdriver, but we have built a special tool, shown in figure 4.3, with a hexagonal magnetic cavity that fits the steel screw heads. This makes the task of screwing down the brass plate easy, quick and reproducible. A trained person can load a chip in 5 minutes or less, with chip breakage that is no worse than 20%.

4.2.2 Operations on the STXM stage

After loading a chip into the wet cell, we bring the wet cell to the STXM stage and mount it using the magnetic pad on the sample mount. Then the humidity chamber is connected to the upper or exit tube on the wet cell, and the syringe pump is connected to the lower or inlet tube. The connections are made with intramedic PE-90 tubing, and can be made easily without bubbles at the unions. A schematic of the complete set up is shown in figure 4.5. In figure 4.5 the wet cell is shown from the rear. The design locates the tubes always to inboard, where the STXM stage is most physically accesible.

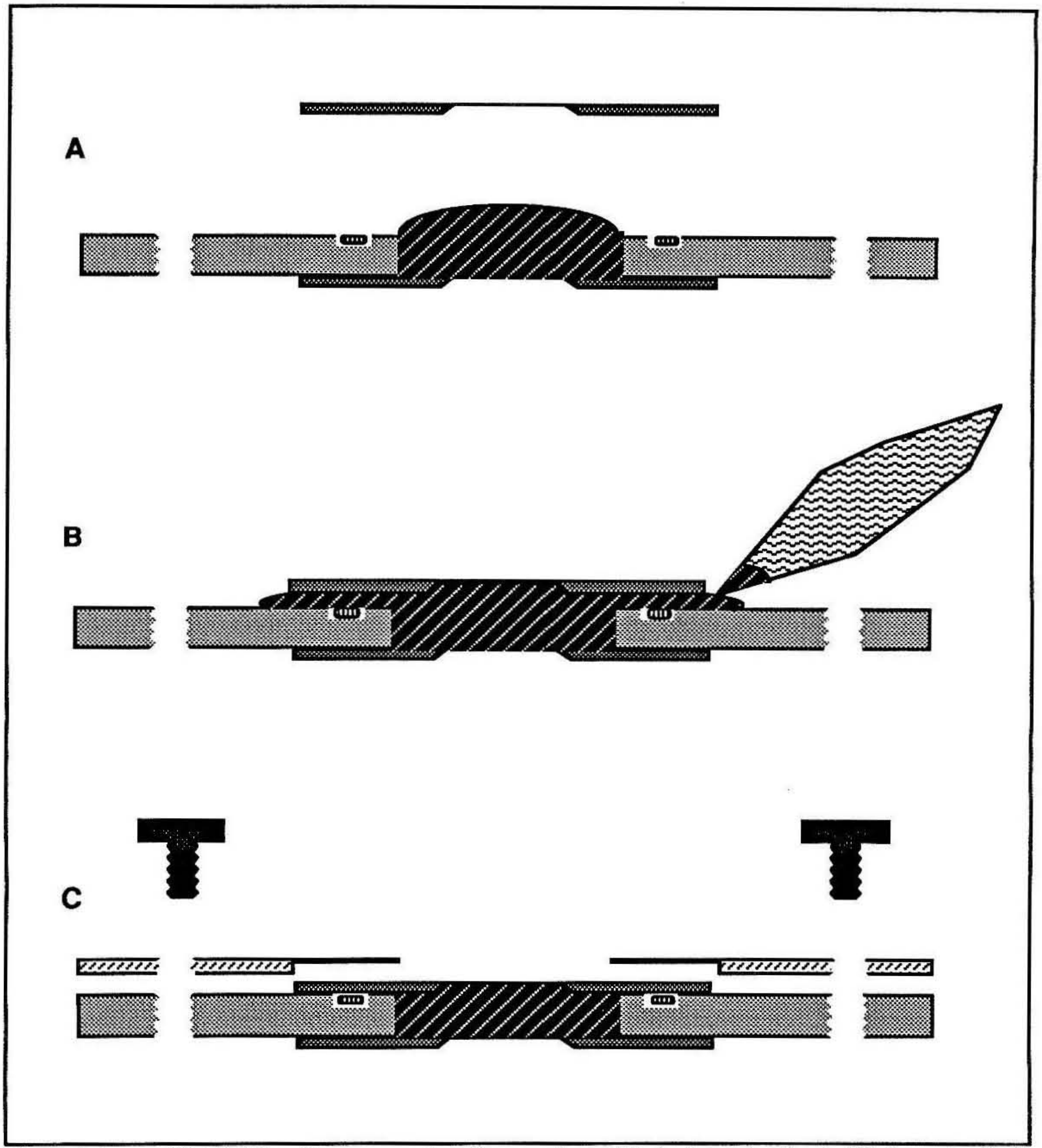

Figure 4.4 Wet Cell Loading Loading a culture chip in the wet cell. **A**, fill the wet cell. **B**, place sample on top of the drop of liquid, and wick away excess. **C**, screw down brass clamping plate.

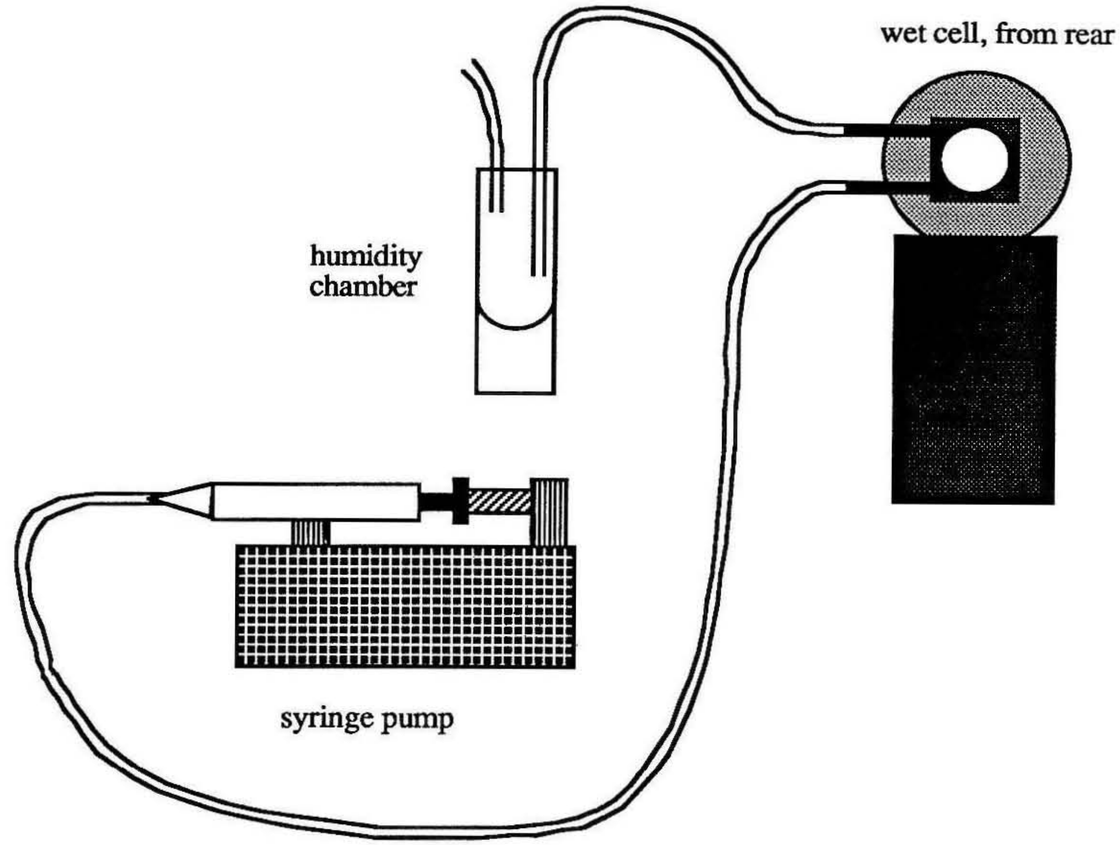

Figure 4.5 Wet Cell Operation Schematic of the wet cell as is is hooked up to the syringe pump on its inlet side and the humidity chamber on its exhaust side.

The first thing to be done once the wet cell is mounted and connected up is to cycle it at least once to find and remove any bubbles. A cycle has 2 phases, "fill" and "drain". In the fill phase we run the pump forward, filling the wet cell and pushing first bubbles and then media all the way through the wet cell and out to the humidity chamber. The fill phase is complete when the fluid/air interface moves into the humidity chamber. The drain phase is the reverse, with the fluid/air interface being drawn back through the chamber to a position about 1 inch outside the inlet tube where it is visible to the operator.

The humidity chamber is kept wet with medium, with a filter paper wick. The exhaust outlet, which is there to prevent back pressures from building up is a small piece of

PE-90 tubing, and we have found has low enoungh flow to allow high humidity to build up in the chamber. The medium used is usually the standard medium for the cells, with Methocel, a long carbohydrate polymer to increase viscosity, and to prevent droplet formation on the windows. Methocel appears to make the liquid film more uniform than it would be with plain medium.

A full cycle, with drain following fill immediately, takes about 6 minutes and the chamber is full for about 3 minutes of that. At times we have added a "hydrate" phase between fill and drain which is a pause to allow cells to rehydrate for a longer period, or just a safe interval while preparing for imaging at the microscope.

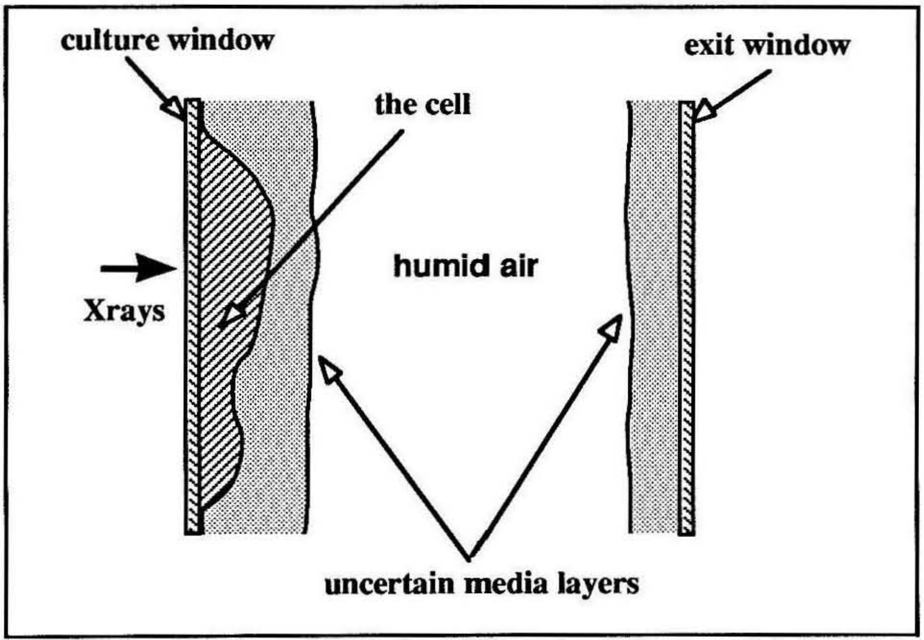

Figure 4.6 Water Layers A figure illustrating a simple model of what the cell environment is when the wet cell is drained, and we are able to image with the STXM.

4.3 The Drained State

In order to understand what we see in an image we need a simple model of the cell environment when the wet cell is drained and ready for imaging. Figure 4.6 illustrates the simplest model. The cells to be imaged are grown on the culture window. There should be some medium layer on both the culture window and the exit window. And there is a gap filled with 100% humidity air in between the windows. Figure 4.6 is not to scale. The air gap is fixed by the design of the wet cell at 1.25mm.

The water layers we cannot measure directly, but when we observe the flux in background areas of a cell image and compare that flux to what we expect from the ring current or the dry wet cell we find from 20% to 80% extra absorption at 36Å. This corresponds to a total water thickness (culture and exit window) of 0.7 to 5.1µm. Note that all this extra absorption is after the sample cells, and serves to reduce the detected flux not the incident flux on the cells, so it can be expected to increase the radiation flux required to reach any given level of S/N in an image.

4.4 Cell Culture

In most of the work reported in this dissertation we have used cells from primary tissue culture of chick dorsal root ganglion (DRG) or rat hippocampus. The DRG cells include both fibroblasts and neurons, while in the hippocampal preparations we imaged only neurons. As a system for exploring the imaging of live cells with the STXM we used the DRG cultures. These are dissected from 8-12 day embryonic chickens (i.e., fertile eggs) and the cells are attractive for imaging from 12 hours after plating, both of which made the system very convenient for working with at the NSLS.

4.5 Testing the Wet Cell with Live Cultures

In order to study the imaging of live cells in the STXM we needed to show that the fill and drain cycle of the wet cell does not unduly damage the cultured cells. We have therefore performed a series of tests using the wet cell to support live cultures. These tests have also been reported elsewhere.[2] The culture system we have been using for initial tests are neurons and fibroblasts from the chick dorsal root ganglion. To observe the cultured cells as they are drained and rehydrated in the wet cell, we have arranged a phase contrast inverted microscope so it is on its back, and can view vertical cultures. A typical test sequence is shown in figure 4.7. The cells are on substrates (not our usual ones) which are cover slips imprinted with a grid of 50 micron squares.

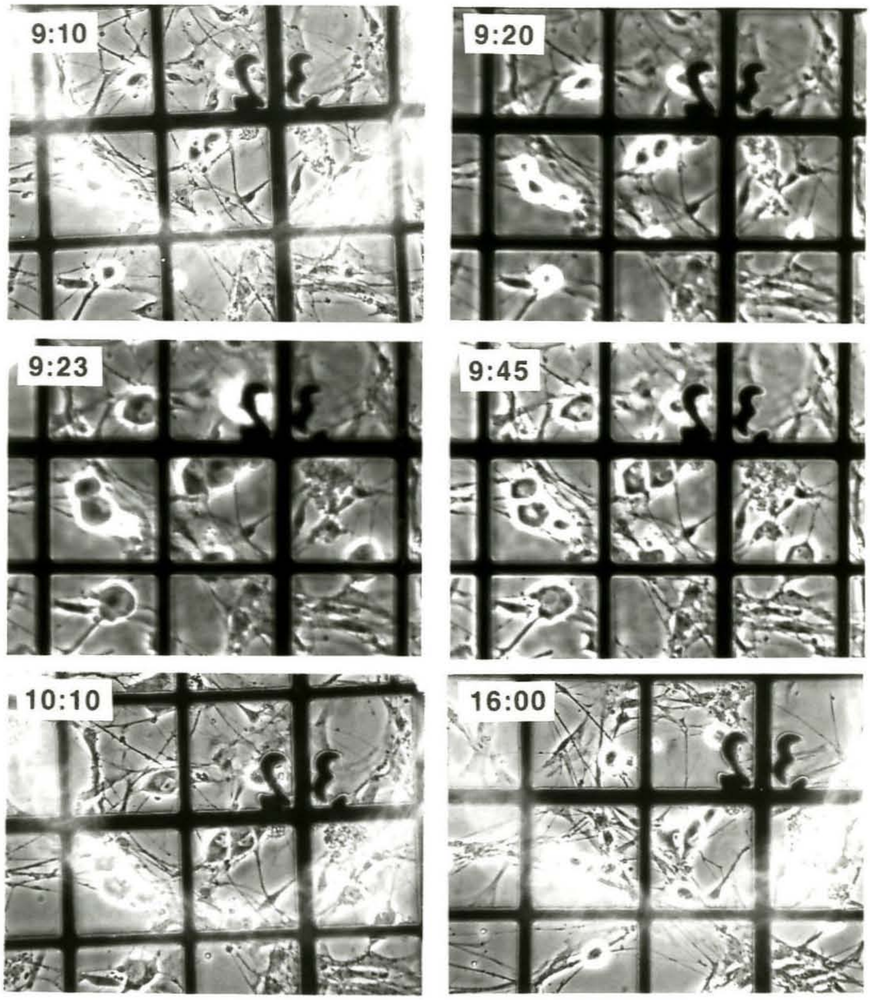

Figure 4.7 Wet Cell Test An example of a test of the wet cell with a live DRG culture. The identifying numbers are times. 9:10, an image of the culture before it is mounted in the wet cell. 9:20, the culture is in the filled wet cell. 9:23, the culture has now been drained. 9:45, the wet cell has just been filled. 10:10, the wet cell has just been filled after a 20 minute drain. 16:00, the culture several hours after it has been returned to a culture dish, and its incubator.

The earliest image in figure 4.7, at 9:10, was photographed in a conventional tissue culture phase contrast microscope before the substrate was clamped to the wet cell. The cells with bright halos around them are neurons which are roughly spherical. There is a network of fine axons growing from them, and there are also some thin fibroblasts which are poorly shown in these pictures. Images of such cells are shown in chapter 6.

The image at 9:20 is of the same region after the culture was in the filled wet cell. The picture quality suffers, but the cells look similar. The transfer to the wet cell typically does no damage. At 9:23 the wet cell has been drained, and the neurons are now gray and larger in area. They have been flattened by surface tension as the cell drained. All have survived, although sometimes a few will "explode" because their outer membranes are ruptured by the stresses. The axons and fibroblasts tolerate the draining unchanged. The cells are shown just after rehydration at 9:45. The neurons have changed their structure so that they remain flat even though they are now fully immersed in culture medium.

The two final pictures in figure 4.6 are just after a second 20 minute drain and rehydration, and several hours later in a culture dish. The flattened neurons at 10:10 recover so that the last picture bears a close resemblance to the first.

At Caltech we have performed about 20 successful tests of the type discussed above, including single drainings for times up to 90 minutes and multiple drainings for up to three hours, with twenty minute drain periods and two minute rehydrations.

4.6 The Culture Chips

We grow tissue culture cells on "culture chips" that are designed to satisfy the demands of microscopy as well as tissue culture. There are several requirements that the chips needed to meet. They must be mechanically standardized, so they all will mate well with the wet cell. They must provide a surface that is uniform and flat for cell growth, that is compatible with tissue culture, and that can be coated with appropriate protein layers (as is necessary for some tissue culture systems). Their growth surface should be at least 3mm x 3mm across, in order to take advantage of the range of the STXM steppers. Their membranes must be as thin as possible in order to minimimize x-ray flux losses. Their membranes must also be impermeable to water, because we do not want the wet cell to dry out through its windows. We need marks (location marks) on each chip so that individual cells or regions of interest can be found repeatedly. We need marks (focus marks) on the chip membranes that have sharp edges (<50nm if possible) and are present in or near all possible fields of view, so that we can focus the STXM near any targets. The chips must be clean after fabrication and sterilizable. Finally, we must be able to make the chips in reasonably large batches, because they will be used as standard cover slips are for tissue culture.

To meet all these requirements we turned to the techniques of silicon microfabrication. The basic mechanical design of our chips was shown in figure 4.1B. They are made of a silicon frame 9.7mm square, and 250μm thick. They have a 3mm square membrane of silicon nitride in their centers. The membrane is 1000Å thick. Cells are grown on the inside (towards the frame) of the chip. Both location marks and focus marks are on the outside of the chip.

The detailed fabrication procedure is included in appendix B. We will just give a general outline here. This outline is illustrated in figure 4.10, at the end of this section. We start with 3" diameter single crystal silicon wafers, lapped to 225±25μm thick, and polished flat on both sides. The wafers we use are <100>, meaning that the surface of the wafer is the 100 plane of the silicon lattice.

We deposit 1000Å of low stress LPCVD silicon nitride[3] on both sides of each wafer. This is done in batches of 10 wafers, and takes about 2 hours a batch. The SiN layer is under tension, enough to hold it flat, but not enough to break a free standing membrane. It is quite strong, and a 300μm square membrane of this material can withstand a pressure of one atmosphere.

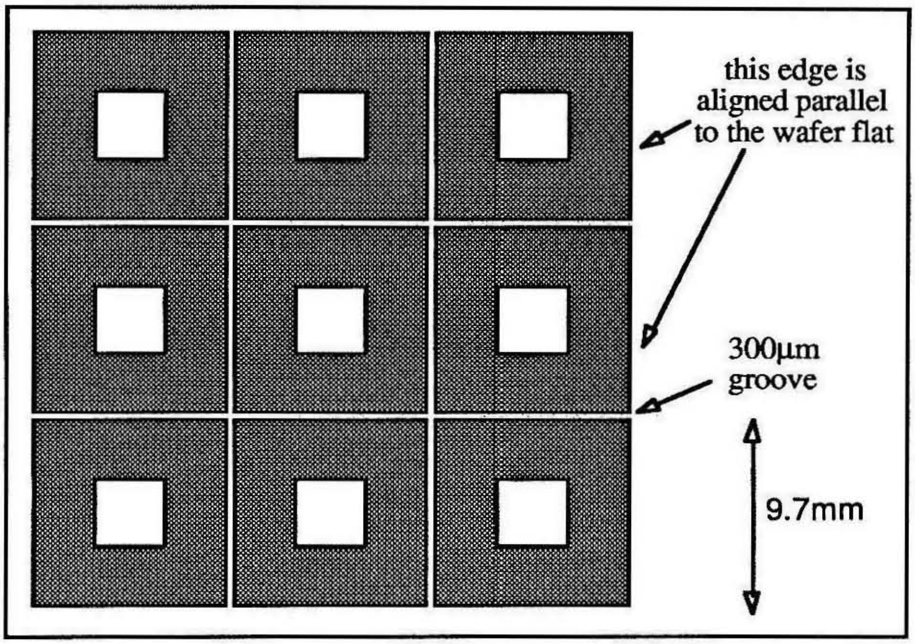

Figure 4.8 Backside Mask Pattern This is the pattern we use to expose the back of the silicon wafers. Grey is opaque in the mask, white is transparent. Transparent areas expose the resist, and cause it to develop away, leaving the SiN layer in those regions exposed. The exposed SiN is then removed by a CF_4 plasma.

One side of each wafer is designated the back side and on that side we deposit, expose and develop photoresist using the EDP mask pattern (which is shown in figure 4.8). We then etch away the exposed regions of the SiN layer in a plasma etcher. There is a flat on one side of each wafer along the <110> crystal plane. The pattern of figure 4.8 is aligned with this crystal plane.

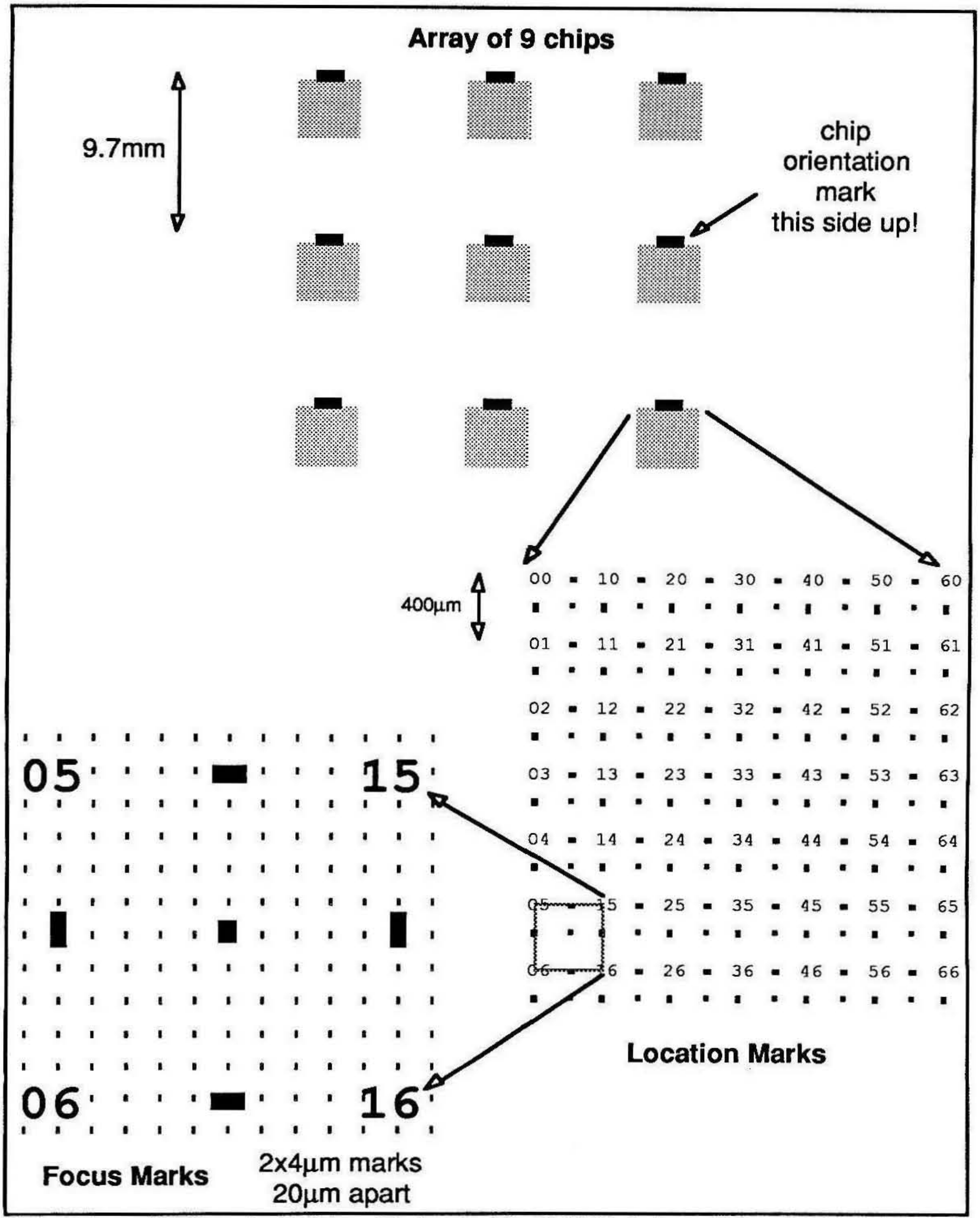

Figure 4.9 Gold Location and Focus Marks The Gold Mark Array Pattern is at top. The true mask is the negative of this figure. The figure has an inset expansion showing the Location Marks, a 7x7 array of row and column numbers 400µm on centers, with extra rectangles every 200µm. The Focus Mark array is a background over the location mark area, 2x4µm marks in a 20µm array, as shown by final inset.

On the front side of each wafer we deposit, expose and develop resist in the pattern of the location and focus marks (which is shown in figure 4.9). Then we deposit 50Å chrome and 150Å of gold over the wafer, on both resist and exposed SiN surface. Removing the resist removes all the unwanted metal ot top of the resist, leaving the metal that was deposited directly on the exposed SiN regions. This process is known as liftoff; it gives edges that are almost as sharp as the edge of the developed resist, they should be on the order of the thickness of the metal, ~ 200Å.

In order to form the suspended membrane we use the SiN pattern on the back side of the wafer as a mask, and disolve away only the exposed silicon. We etch the wafers in EDP (ethylene-diamine, pyrocatechol and water.) EDP is an anisotropic silicon etch, which etches fast at <100> surfaces and very slowly at <111> surfaces. The LPCVD SiN is quite immune to EDP, so the 1000Å membrane is free standing and intact in the center of each chip. EDP also leaves the Cr-Au marks untouched. The net effect of the EDP process is to etch all the way through the center of the chips, making a truncated pyramid, with sides that are <111> planes, and a top which is a suspended SiN membrane. The etch also makes v-grooves separating the chips from each other. These groves being only 300µm wide at the surface, they do not go through the 250µm wafer. The grooves are used to break individual chips apart.

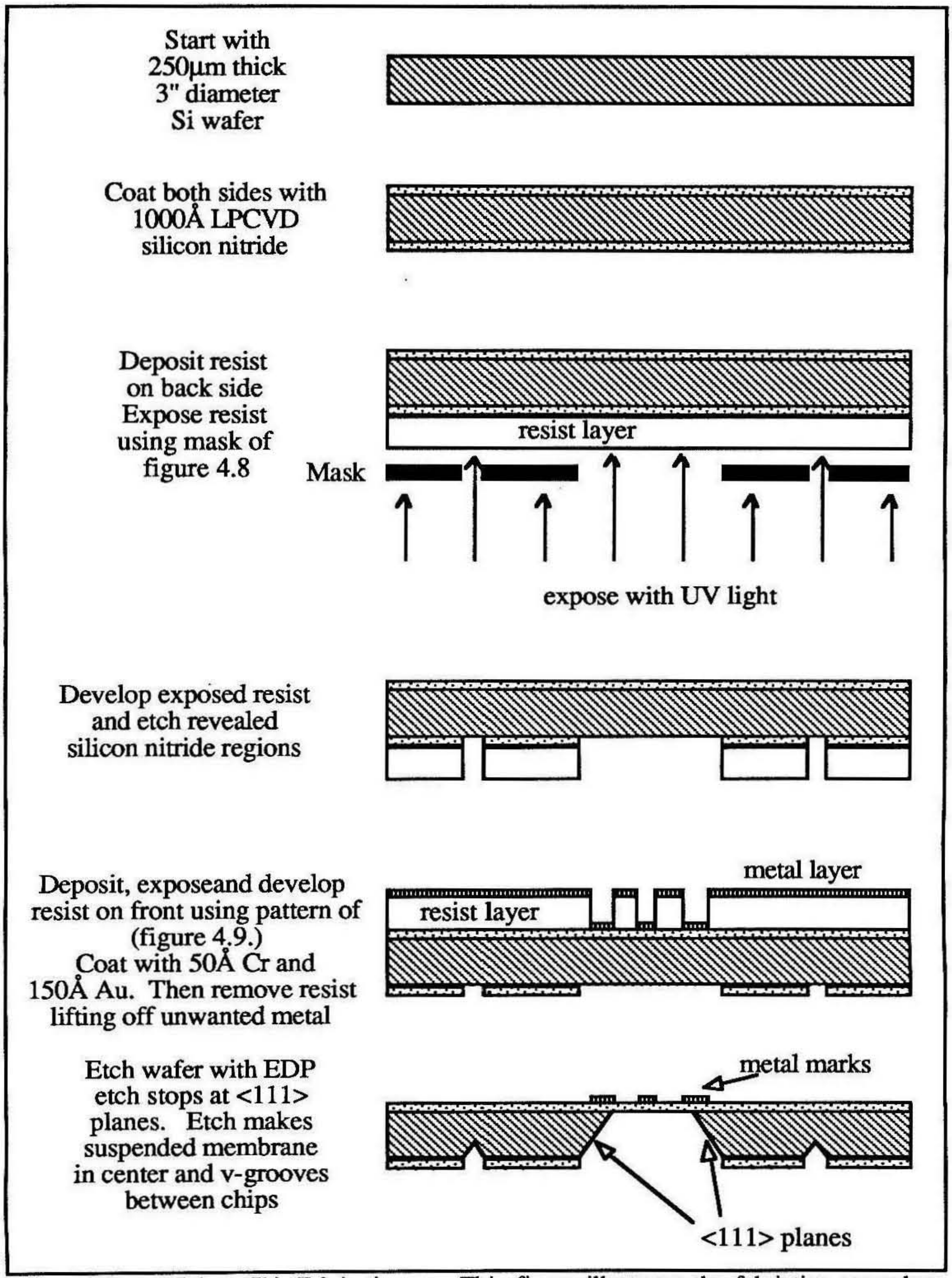

Figure 4.10 Culture Chip Fabrication This figure illustrates the fabriction procedure outlined in the text. At the end one wafer contains an array of chips, and the chips can be cleaved apart along the etched grooves.

What is illustrated in the figures 4.8-4.10 is one of our versions of the culture chips, with its design patterns for location and focus marks. That version did not come out quite as well as its design, though it was functionally close. The chips do meet all the basic requirements listed above. We find a 1000Å membrane of our silicon nitride blocks 27% of the x-ray flux at 36Å. We have also made 2000Å chips in an effort to trade off flux for increased durability of the chips. We do make the chips in batches that are 50-100 chips at a time, and like all silicon microfabrication the process will scale up excellently. Meaning that if the process is scaled up (say by contracting it out or dedicating a technician) it will make more chips, better chips and cheaper chips, all together.

4.7 Chapter 4 References

---

[1] K. Goncz, personal communications.

[2] J. Pine and J.R. Gilbert, "Live Cell Specimens for X-ray Microscopy," in X-ray Microscopy III, edited by A.G. Michette, G.R. Morrison, and C.J. Buckley, (Springer, Berlin, to be published 1991).

[3] C.H. Mastragelo, Y-C Tai, and R.S. Muller "Thermophysical Properties of Low-Residual Stress, Silicon-Rich, LPCVD Silicon Nitride Films," Sens. Actu. A, 23, (1-3) pp.856-860 (1990).

5 Radiation Damage in the STXM

In this chapter we discuss radiation damage in STXM imaging and the limits it imposes on resolution. We discuss the observation of such damage on fixed cells and then the data that we have taken, along with its shortcomings. We will use the results of our observations to generate some limits on what we think can be done with fixed tissue, and to find the optimum wavelength region in which to operate the STXM. We finish this chapter with a discussion of the physical nature of radiation damage in the STXM including some comments on damage to live cells.

There has been some discussion of soft x-ray radiation damage in imaging in the literature,[1,2] but little data. At least with regard to real images. We begin to rectify that in this chapter.

5.1 Introduction to Radiation Damage in X-ray Microscopy

One of the fundamental limits of microscopy (and the hardest one to come to grips with) is the damage induced in the sample by the absorbed radiation dose due to recording of an image. If the particle that passes through the sample to make an image deposits energy in the sample, then it is capable of damaging the sample. In imaging, the commonly used particles are; electrons (in electron microscopy) and photons (in optical microscopy) at either visible, UV or x-ray energies. In our case, we are interested in the damage to cells caused by soft x-rays, from λ=23Å to 50Å, or 250 to 550eV. In fact we are interested in two very limited questions about radiation damage: How does the absorption of x-rays affect the structures we see in a STXM image? What limits does the radiation damage impose on the operation of the STXM?

In general the damage done by radiation can either be to the function of cells, if they are alive, or directly to the structure of the cells. The damage that can be done to live cells is (in order of energy deposition required) changing the information content of DNA, inactivation of enzymes, crosslinking structures that normally need to be able to move, or gross destruction of structural proteins or membranes. Beyond the kinds of damage that affect cell function is the type of damage that affects the structures in cells that we can observe with the STXM. In the STXM we observe the x-ray absorption of the cell, pixel by pixel, where all pixels together form our image. So for any damage to be visible to us it must change the absorption in one or more pixels.

Generally incident photons are absorbed or scattered from the sample, at our energies scattering is negligible, and photons are absorbed or transmitted straight through with no loss of energy. In the STXM we count those transmitted photons for our signal. The absorbed photons deposit energy in the column of material over a pixel. Traditionally, in discussions of radiation damage, the energy absorbed in a given volume, divided by the mass of that volume is the quantity of absorbed dose. The units of absorbed dose are 1Gray=100Rads=1Joule/Kg $=6.24\times10^{12}$ MeV/Kg.

Experimentally, it is easy for the deposition of energy to grossly effect our samples. This is shown in figure 5.1, which is an image of some holes in a fixed chick fibroblast. Each of the holes in figure 5.1 was formed by allowing the sample to sit at rest (i.e., not scanning) with the shutter open for less than one minute. Between each exposure we moved the stage a few microns. After making the series of holes we took a standard transmission image of that entire region of the cell, at λ=36Å, with pixel size dx=0.1µm, and dwell time τ=4msec.

The holes are interesting (actually rather alarming when we first saw them), but they are not well controlled. Their diameters are much greater than the size of the x-ray probe, so we are in fact watching the x-ray probe etch at the cell, while the sample jitters relative to the probe. (A slow jitter that moves pixels in seconds would not be easily visible in regular images.) The actual dwell time in any given pixel (and thus the absorbed radiation dose) cannot be established. Later in this chapter we will present a better method of observing radiation damage.

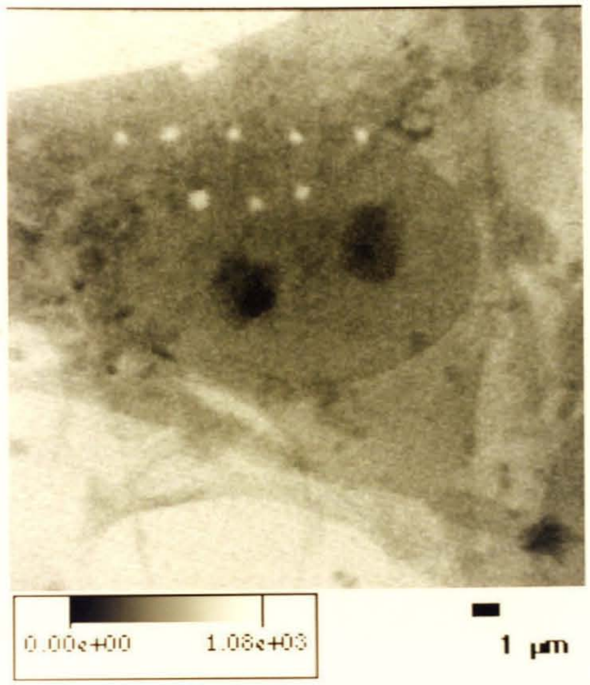

Figure 5.1 Damage Holes This is a STXM image of a fixed fibroblast taken at dx=0.1μm,. The focussed x-ray beam has been allowed to dwell at several positions in the image. This intense exposure to x-rays makes holes in the fixed fibroblast. Such holes can be made by dwelling less than 30sec.

5.2 Damage to Biological Tissue from Soft X-rays

For our cultured cells the incident x-ray photons may be absorbed in either the organic components of tissue, (protein, lipid, and, DNA mostly) or in water. Only a fraction of the photons are actually likely to stop in the organic components. Figure 5.2 shows the fraction of the x-rays that stop in the protein plotted vs the wavelength, for a simple model cell that is 1μm thick and contains 10% protein in water by mass. Over the wavelength region in which we do most of our imaging we can expect about 50% of the absorbed photons to stop in the protein.

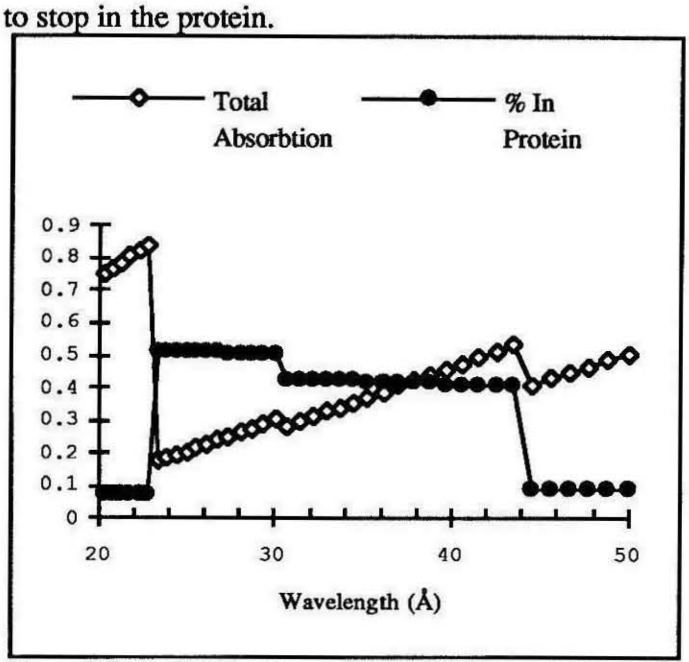

Figure 5.2 X-Ray Absorption This graph shows the fraction of x-rays that are absorbed in a model cell, and the fraction of them that are absorbed in protein. The model cell composed of 10% protein by mass, and is 1μm thick. The absorption is graphed vs. λ over the region we can operate in at the BNL STXM.

How do we get from photon absorption to visible damage? At the energies of our soft x-rays (250-550eV), the dominant process is the atomic photo-effect, in which an electron is ejected from the atom that absorbs the incident photon.[3] If the photon was absorbed in a core level, as it may be near the K edges of carbon, nitrogen or oxygen, then an auger electron can be also be emitted.[4] Electrons with energies of 100 to 500 eV, produced in the initial absorption event, have short tracks of 3-20nm in water or tissue.[5,6] Such electrons lose energy in the formation of primary ions and excited states in the molecules along their tracks. All the formation of primary excitations happens in the first 10^{-11}sec after the initial event. After that primary ions diffuse and interact, sometimes forming secondary ions and other reaction products.[7] It is believed that some reactions, especially those involving oxygen radiacals, may propagate themselves over several generations.[8]

For the most part it is the primary and secondary ions and excitations that may break bonds, and cell structures, and release large or small molecules to diffuse away. And so we can expect, during the formation of an image, that bonds will be broken and reactions will take place consequent to the absorption of x-rays which represents our signal.

We need to ask how can that damage can be visible in a STXM image. After all, we observe the sample at scales of 50nm, far in excess of the size of the bonds that might be broken. And the absorption of x-rays will never, by itself, change the atomic composition of the material in a pixel, i.e., carbon stays carbon, and oxygen stays oxygen. In order to get a detectable change in absorption we must have mass transport out of the entire pixel that is imaged, and indeed out of that region of the image. A visible decrease of absorption due to radiation damage implies that the energy deposited by the x-rays can cause net absorbing mass ($-\ln(T_{sample})$) transport out of the pixel-column. Just the simple breaking of bonds is not sufficient to be observed directly by the STXM. Actual mass transport must be done by diffusion. A reasonable process of damage is that photons deposit energy in the sample, directly and indirectly breaking bonds in the tissue which frees small molecules to diffuse away. It is reasonable to ask how fast this might take place, and how fast it might be visible. The first deposition of energy by the primary electrons is thought to take place in 10^{-11} seconds.[9] Secondary effects can take longer, but the underlying reaction rates of the radicals and ions produced in water are high, on the order of $10^8 M^{-1} sec^{-1}$. When we image with the STXM the dwell time in a pixel is on the order of 1-10msec. Therefore the key question is how long does mass, liberated in about

10^{-6}sec, take to diffuse out of the pixel or the region? Diffusion coefficients of protein vary from 10^{-5} at glycine, to 10^{-6} for cytochrome c (13kD), to $6x10^{-7}$ for hemoglobin (64kD).[10] This gives a range of diffusion times of 0.5 to 8 msec for a distance of 1μm, and 5 to 80μsec for a distance of 100nm. So within a small fraction of a pixel dwell time diffusion takes material outside the size of the x-ray probe, and in times of the order of the dwell time diffusion spreads mass over a 1μm radius. Diffusion is fast enough to cause observable damage during the imaging of a pixel.

In order to begin to understand the effect of radiation in STXM imaging of fixed tissue culture cells we made some observations that ask a simple phenomenological question: how many carbon atoms are released from the sample by the deposition of 1eV during an image? We will call this quantity "α" the "hardness" of the sample, it is proportional to the slope of a [-ln(T_{sample})] vs [cumulative energy absorbed] curve. Underlying this phrasing of the radiation damage problem is the one-component model of a cell that we discussed in chapter 3, and in particular the fomulation of equation 3.14, repeated here as equation 5.1. We will also make use of the model cell and granule of chapter 3 in understanding the response to radiation damage in the STXM.

$$T_{sample} = e^{-(\mu_{Nc} N_c)} \qquad [5.1]$$

5.3 Experimental Measurement of Damage in STXM Imaging

The absorption of x-ray photons was crudely observed to cause loss of absorbing material in images such as figure 5.1. However, due to the jitter described above, this method of observation was not adequate to quantitate the damage. To get better control over the energy deposition per pixel we took three sets of data as "radiation series". A radiation series is a series of image pairs observing the same cell. Each pair is made up of a low exposure "observational" image followed by a high exposure "damaging" image of a sub-region of the observational image. Figure 5.3 shows a single such observational image (the first in the Nov15 series), and figure 5.4 is the array of observational images in that series. The images in the figures are the standard transmission images, with the open background having been normalized to 100% transmission in the green background regions.

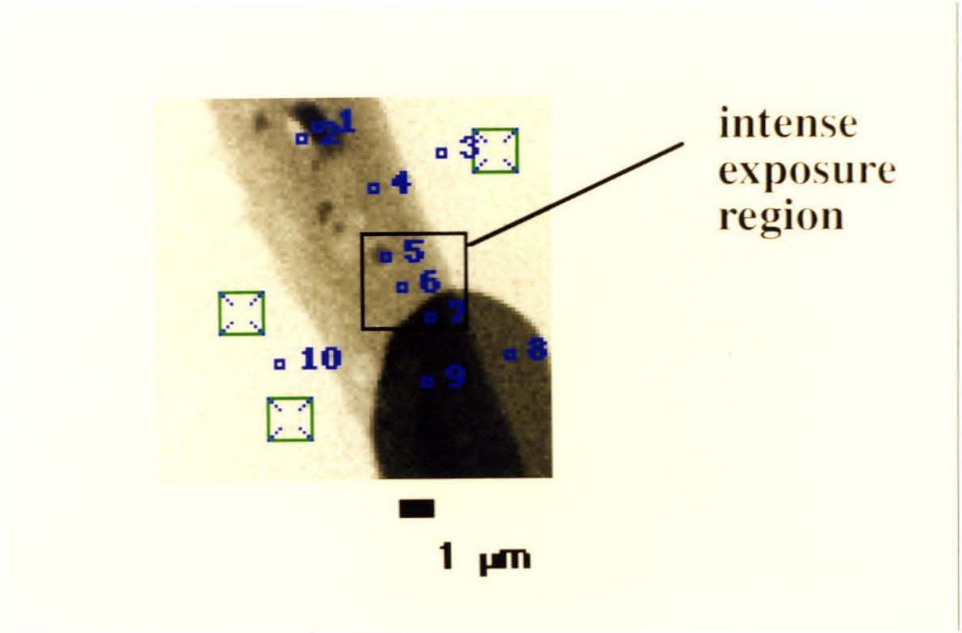

Figure 5.3 Rad Series Master Image This is the first observational image of the Nov15 radiation series. Image marks are described in the text. The image was taken at λ=36.4Å and dx=0.1µm.

In figure 5.3 there are several different marks that have been linked to the image by the ObjectImage software. The square labeled "intense exposure region" illustrates the high exposure region, which can be seen to have been totally destroyed in the last image in the series(see lower right image in figure 5.4). The destroyed area has soft edges, as we expect from the size of the holes in figure 5.1. The three rectangles with ticks at their corners are normalization regions. These are the normalization regions for the background normalization of chapter 3, however all "observational images" in the series share the same background regions. And thus the normalized 100% transmission matches for all the images.

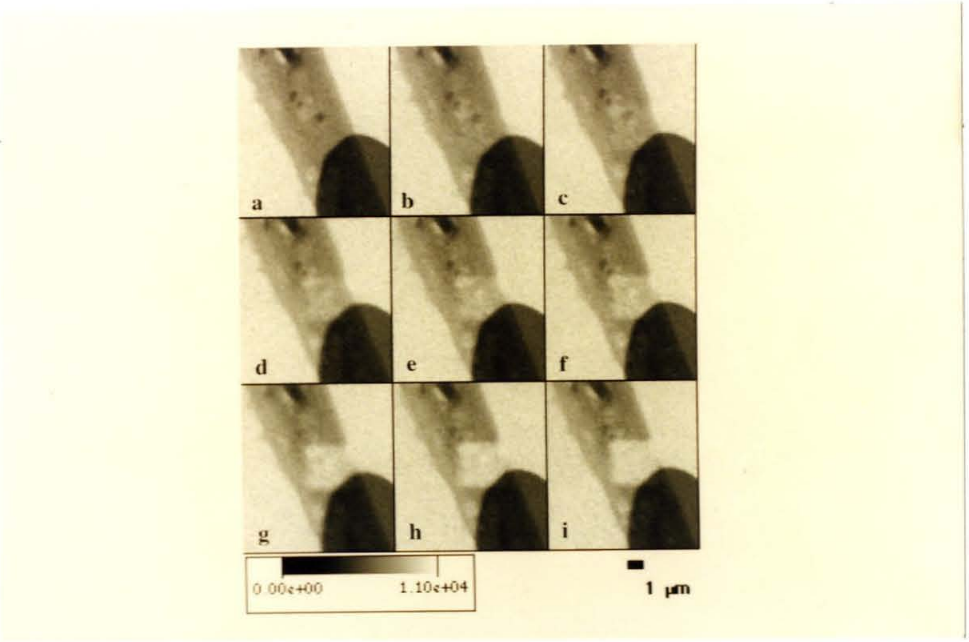

Figure 5.4 Rad Series Array An array of the observation images in the Nov15 series. Each image has been slightly cropped relative to the image in Fig 5.3 , which is the first image in the array(upper left). All the images have been normalized together to give background transmission 100%, and full black is 0% transmission.

The small numbered squares in figure 5.3 locate the data regions of this series. They are 3x3 pixel regions whose means give us one data point per observational image, and the set of data points corresponding from one region give the data series that are graphed in figures 5.5, 5.6 and 5.7 (discussed below). This type of data provides the basis for the rest of the analysis in this chapter. In figure 5.3, regions 3, 8, and 10 are in background areas, regions 1, 2 and 4 are control regions of the cell which receive only observational doses, regions 5, 6 are in the high exposure area of the cell, region 7 is in the high exposure area--but over the gold focus mark, and region 9 is a control region over the gold mark. Gold focus marks are always upstream of the sample and in this batch of sample windows the gold mark transmitted 57% of the normal flux, which give a lower incident flux to regions 7 and 9.

The background data regions from the Nov15 series are graphed in figure 5.5, vs image number. This transmission graph shows the stability of the measurement and the quality of the normalization. That is, no damage (i.e., change in transmission) is visible in correctly normalized regions outside the cell.

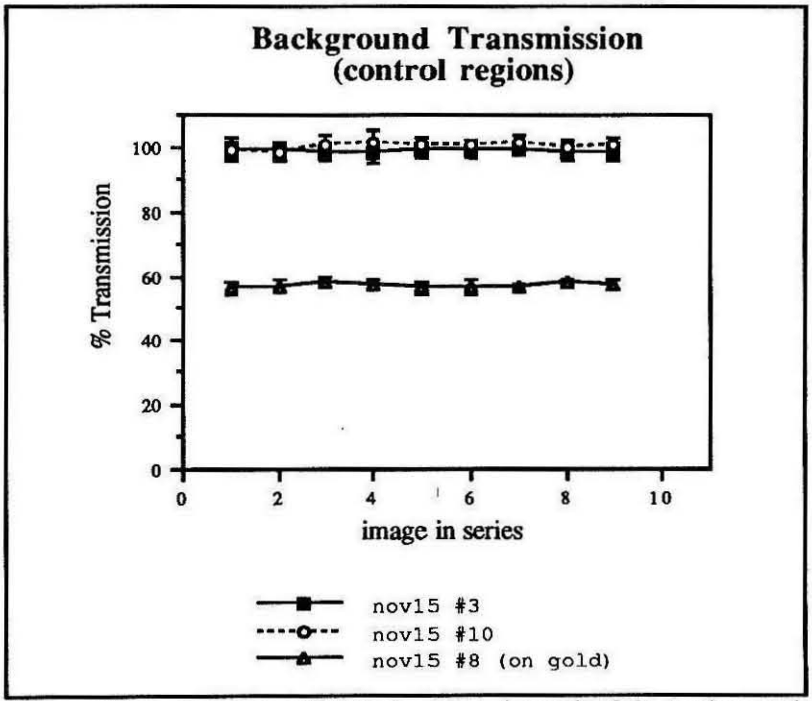

Figure 5.5 Background Controls A graph of the background data regions, showing % Transmission found in each of the images of the series. Error bars are sd of the average over the 9 pixels in each region.

However, graphing the data vs. image number is not appropriate for the data regions in which damage occurs, because different regions receive different incident flux, and absorb different amounts of energy. A better way of looking at the data is shown in figure 5.6, where we graph [-ln(T_{sample})] vs cumulative photons absorbed/µm^2.

A brief digression is in order here. We are looking at data reflecting how a column of crosslinked cell tissue in liquid water responds to absorption of x-rays. The only way in which we "look" is by watching the absorption of those x-rays change. So it seems reasonable that looking at the "instantaneous" absorption vs the cumulative absorption of photons or energy might be a good thing to observe. Indeed this appears to be the case, especially when we look at "instantaneous" absorption by using the quantity [-ln(T_{sample})], as we do in figure 5.6.

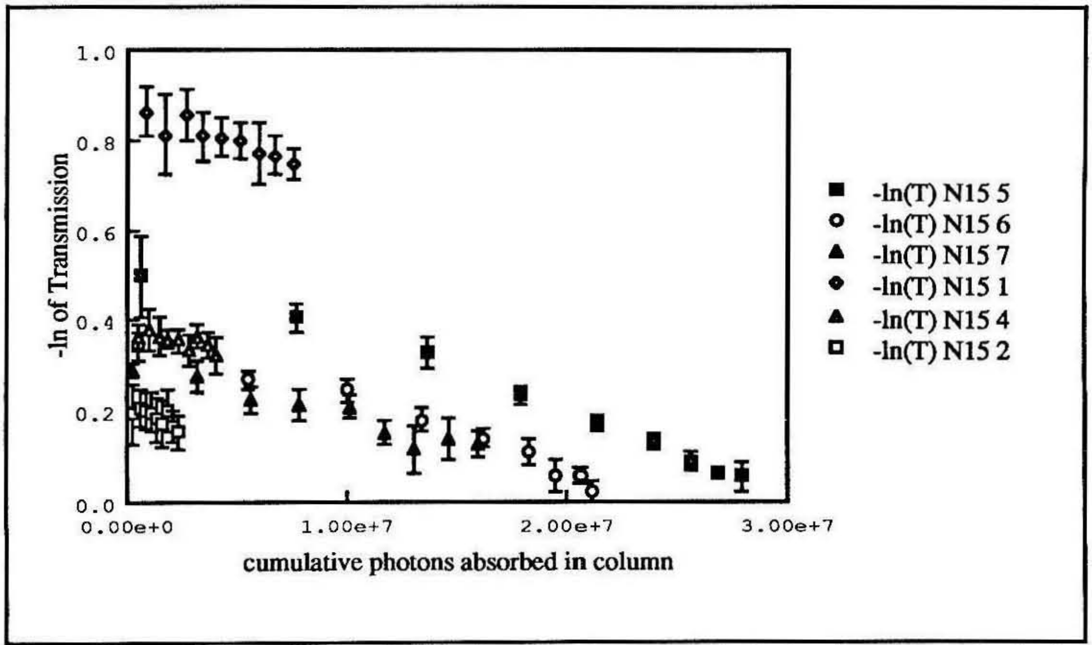

Figure 5.6 Radiation Damage I A graph of some of the 3x3 region data series in the Nov15 radiation damage series Regions 1, 4, and 2 are low exposure series. Regions 5,6,and 7 are high exposure series. Note that series 7 is over gold, and thus receives 57% of the incident flux of the high exposure regions. The x-axis is the cumulative number of photons that are absorbed in the column during the radiation series.

In figure 5.6 we graph the low exposure data series 1, 2, and 4 as well as the high exposure series 5, 6, and 7, all from the Nov15 radiation series. All look quite linear, though estimating the slopes of the lines will clearly be more difficult with the low exposure series.

Figures 5.5, 5.6 and 5.7 have error bars on each point. These show the standard deviation of the 9 pixels that are averaged to get the value of the point. This estimate of variability reflects the statistical noise in the original image (basically shot noise) any oscillations in the x-ray beam (beam oscillations) and also bad choices of the 3x3 regions. The choice of 3x3 region affects the variation in the sense that if the region is over a part of the cell that has some structure (in the transmission image) then the spread of the pixels from the average will be increased over what we would expect in a uniform region. That said, the reason we use the 3x3 regions is to smooth out the inherent noise (shot noise is reduced by a factor of 3), and also to reduce the effects of the images not being aligned to better than 1 pixel.

The contributions to the expected variation at each point are essentially independent of the flux I_0 that is incident on the sample between each observational image. The signal, however, (change in T_{sample}, or $-\ln(T_{sample})$) becomes larger for greater I_0. Therefore we expect the slope of any of the lines in figure 5.6 to be signifigantly easier to measure with high exposure series than with low exposure series.

Now the quantity $[-\ln(T_{sample})]$ is $\mu_{Nc}N_c$ following equation 5.1. Where μ_{Nc} is the atomic absorption coefficient of carbon in μm^2/atom and N_c is the number of carbon atoms per μm^2. This makes use of the one-component model in which we consider all atoms to be carbon. For each observed transmission point we find an equivalent N_c, i.e., the number of carbon atoms in a $1\mu m^2$ column that gives that transmission at that wavelength.

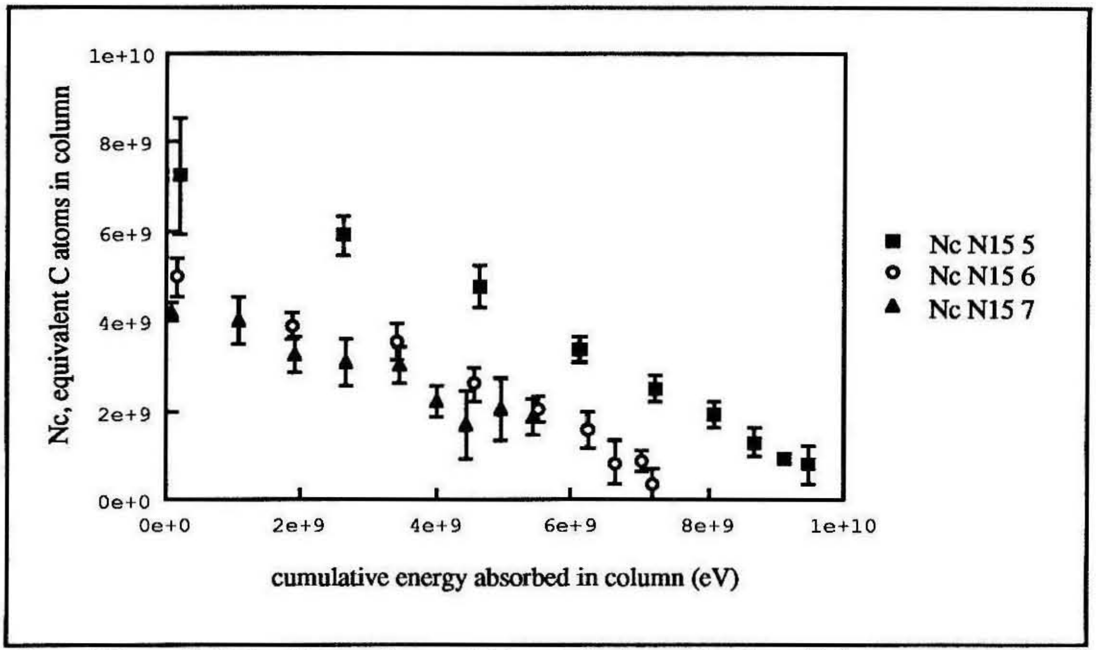

Figure 5.7 Radiation Damage II This graph shows the three high exposure series of figure 5.6, with the y-axis scaled to N_C, the equivalent number of carbon atoms in a column above a $1 \mu m^2$ area. The x-axis is the cumulative energy that is absorbed in the column during the radiation series.

In figure 5.7 we graph the same high exposure data series as in figure 5.6, scaled to use N_C vs deposited energy in eV. When we use the cumulative energy or photons absorbed as the x-axis in these plots, we see that the points get closer together as the radiation series procedes. This occurs because between each observation point we subject the sample to the same I_0, but the transmission increases due to damage, so less of that flux is absorbed. At the end of series 6 the transmission has risen to 100%, and the points are clustering at the same x-coordinate. As in figure 5.6, we show error bars in figure 5.7 from the standard deviation of the transmission in our 3x3 regions.

To say that the series in figure 5.7 look linear is to say that radiation damage fits the model of equation 5.2. That is, the quantity $\alpha \Delta E$ gives the change in number of carbon atoms due to the absorption of energy ΔE. The series graphed in figure 5.7 look pretty linear, and a straight line fits quite well. And the slopes of the fit lines look similar. We ask how linear does the damage process look, and what kind of estimates can we get for the ratio of atoms lost to energy absorbed (the "hardness" α)? These questions will require going over to a larger data set and pooling more 3x3 regions.

$$T = e^{\left(-\mu_{Nc}(\lambda)N_i - \alpha\mu_{Nc}(\lambda)\Delta E\right)} \qquad [5.2]$$

Consider the the entire data set that was acquired. We took three radiation series that were complete. Series Nov14, Nov15 and Nov21. Nov14 and Nov15 were taken at λ=36.4Å while Nov21 was acquired at λ=31.25Å. The Nov14 and Nov15 series were of fixed chick DRG fibroblasts, while the Nov21 series used a fixed rat hippocampal neuron We collected at least 10 high exposure 3x3 regions worth of data from each radiation series.

Most traces at high exposure are quite linear, and there are many such traces in the three radiation series. Following the framework of equation 5.2, each 3x3 region series was fit to a line, generating a slope α, a y intercept and a coefficient of determination, r^2. N_c is the starting number of atoms in the column, ΔE is the absorbed energy in the column (as in Eq. 5.4) and α is the slope of the fitted line. In figure 5.8 we show histograms of slopes of all the high exposure data series (42 measurements) and also histograms of each radiation series by itself.

Overall the linearity of the data series is good. We can use the coefficient of determination r^2 as a measure of quality of fit. All the 13 series of Nov15 have $r^2>0.9$. In the Nov14 set, 9 of 14, or 64% have $r^2>0.9$, and in the Nov21 series 14 of 15, or 93% have $r^2>0.9$. The criteria that $r^2>0.9$ is often interpreted to mean that 90% of the variation in N_c is determined by the absorbed energy ΔE.

The histograms are also fairly tightly clustered. The outliers in the Nov14 series (in figure 5.8C), labeled 6 and 7, are located between a peak and a valley that are only 4 pixels apart, probably causing trouble with our 3x3 regions. The outlier in the Nov21 series (in figure 5.8D), labeled o6, is at the very edge of the cell, and probably slips off it due to misalignment.

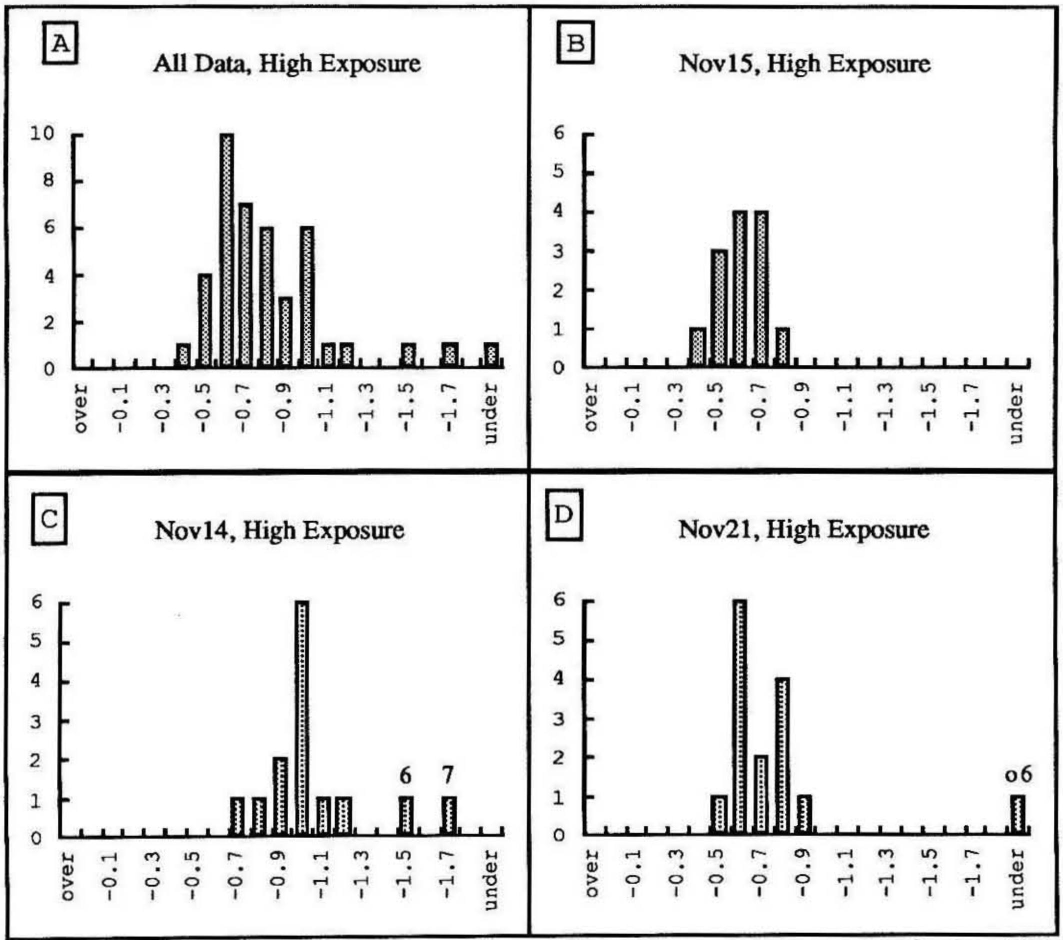

Figure 5.8 Histograms of Radiation Damage Slopes I Histograms of the high exposure data series slopes α. The statistical analysis is in Table 5.1

To make an estimate of the hardness α from this data, we will prune the data set down to just the series with $r^2 > 0.9$. This produces a large subset of series with good quality least squares fits. This subset is histogrammed in figure 5.9. The worst outliers in Nov14 and Nov21 are eliminated by this cut.

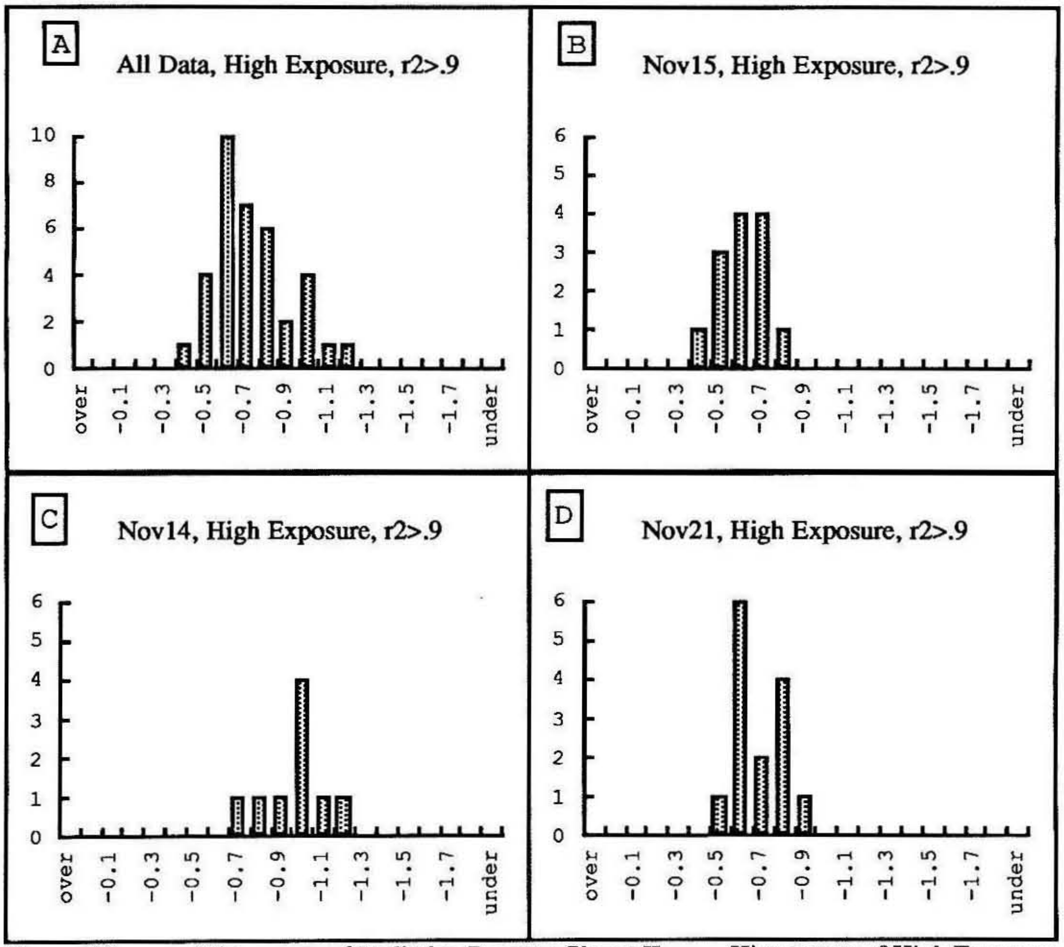

Figure 5.9 Histograms of Radiation Damage Slopes II Histograms of High Exposure data, with samples limited to those series that fit a line better than $r^2 = 0.9$. Statistical analysis is in table 5.1

The statistical analysis of the data presented in figures 5.8 and 5.9 is tabulated in Table 5.1. The set of all high exposure series has a mean of α= -0.88±0.06(sem) with

N=42. The subset with $r^2>0.9$ has N=36 and mean of $\alpha= -0.78\pm0.03$(sem). For the individual series, the means are -0.65 ± 0.03(sem), $-1.02\pm.06$(sem), and -0.74 ± 0.03(sem), for Nov15, Nov14, and Nov21 respectively. Each radiation series gives a fairly compact distribution.

		All	**Nov15**	**Nov14**	**Nov21**
High Exposure	N	42	13	14	15
	mean	-0.88	-0.65	-1.11	-0.87
	sd	0.40	0.10	0.26	0.54
	sem	0.06	0.03	0.07	0.14
	95% by t test	0.12	0.06	0.15	0.30
with r^2>.9	N	36	13	9	14
	mean	-0.78	-0.65	-1.02	-0.74
	sd	0.19	0.10	0.17	0.11
	sem	0.03	0.03	0.06	0.03
	95% by t test	0.06	0.06	0.13	0.06

Table 5.1 Estimates of α An analysis of the histograms in Fig 5.10 and Fig 5.11. The analysis includes outliers (over and underflow in the histograms if present).

In fact the distributions of α in each radiation series are tighter than the spread of means between the different series. Using the calculated standard errors, the means of each population are different beyond the 95% confidence level (by a t-test). One might be tempted to conclude from this observation that the cells involved are signifcantly different in their radiation hardness. However there is an important underlying uncertainty in these observations. Remember we lack good incident intensity monitoring in the STXM. As discussed in chapter 3, we actually expect the underlying estimates of incident flux to have at least 50% uncertainty from fill to fill. That error is very systematic in regard to the measurements in this chapter. Flux in each radiation series should be quite stable, (each series was taken in a short time in a single fill) and thus the the distribution of slopes of data series for Nov15, for example, should be good. Its mean, when compared to the mean of another series (taken on another day with another synchrotron fill) should reflect all of that incident flux estimation error. The observed differences in the means of our three radiation series, -0.65, -1.02, and -0.74 are all within the 50% uncertainty that we have on their underlying incident flux estimation.

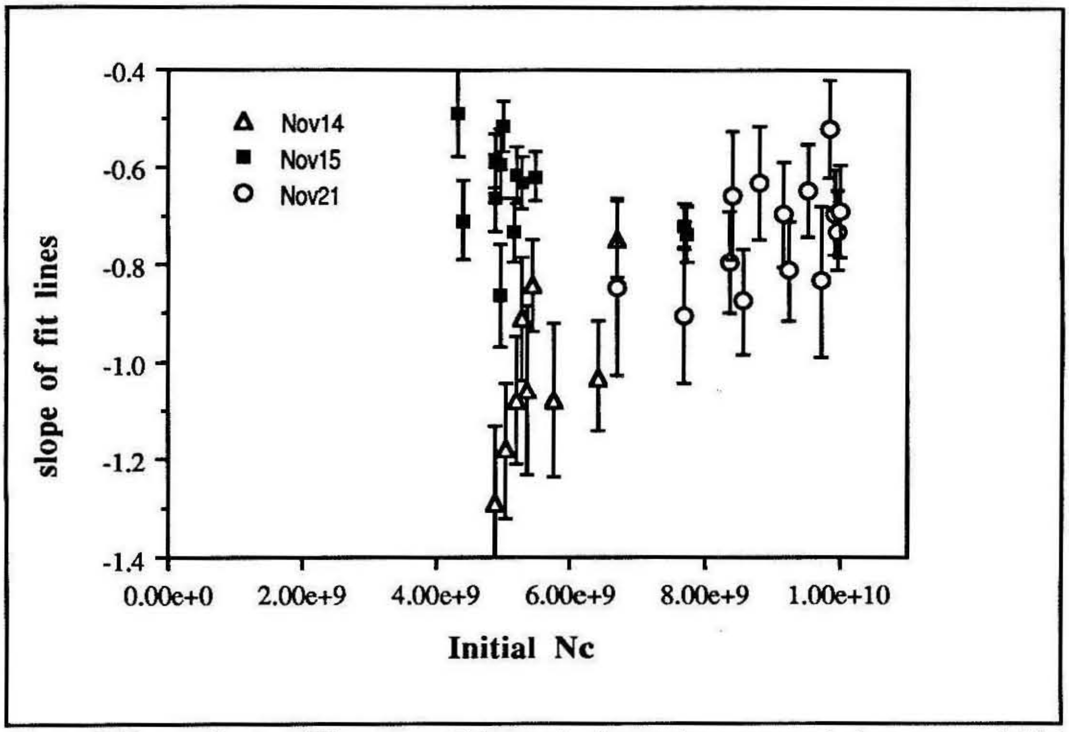

Figure 5.10 Scatter of Slopes This graph shows the scatter of slopes α vs initial column N_c. Error bars show the standard error on each fit slope.

What causes the actual width of the population histograms of figure 5.9? We cannot answer this in any definitive way, the data is just able to give us two facts. Figure 5.10 is a scatter plot containing all the high exposure data points with $r^2>0.9$. The figure is a plot of slope α vs. initial N_c. The figure shows no correlation between hardness and initial density in our 3x3 regions. That is we have no simple evidence that different structures have significantly different hardnesses. The other thing the figure shows is that the standard error on calculating α for each data series (which is the error bar on each point[11]) is comparable in size to the spread of each radiation series histogram. The average error on α is ±0.07 for Nov15, ±0.13 for Nov14, and ±0.11 for Nov21, which is comparable to the standard deviations of the $r^2>0.9$ populations of each radiation series, ±0.10 for Nov15, ±0.17 for Nov14, and ±0.11 for Nov21. We can only conclude that we have no particular evidence of real cell structure causing broadening of the hardness estimates for each cell.

There are two more questions we should ask about our radiation series data. First, how well do these results reflect all cell types? Second, do we understand the wavelength dependence of the damage phenomenon? We have, among our radiation series only two cell types, and two different wavelength points-- fundamentally not enough to establish the variation in response among cells or enough to do a reasonable regression of damage against wavelength. That said, we do discover from this data that the effect of x-ray absorption on fixed tissue fits a linear relation between column-mass and energy absorption. Furthermore, we find an estimate of $\alpha = -0.78 \pm 0.35$ (in our units of [C atom in column]/[eV absorbed in column]) for the slope of that line.

We will take these results and explore their implications for STXM imaging in the following sections of this chapter.

5.4 Evaluating Images for Damage

The model of radiation damage and the numerical estimate of α that we arrived at in the previous section give us the tools to estimate the radiation damage that is done to each sample in producing a STXM image. But first, we should go over the interplay of the various ways we can look at an image and its damage. Essentially we have two ways of viewing an image, as a transmission image, or as a column mass image (as ρ_C in gm/μm^2

or N_c in C atoms/μm^2). We also have two possible ways of quantifying the radiation the sample is subjected to, either absorbed column energy (ΔE), or incident photons per column (I_0). Each view will actually have some use, and all are neatly tied together by the phenomenological model of equation 5.2.

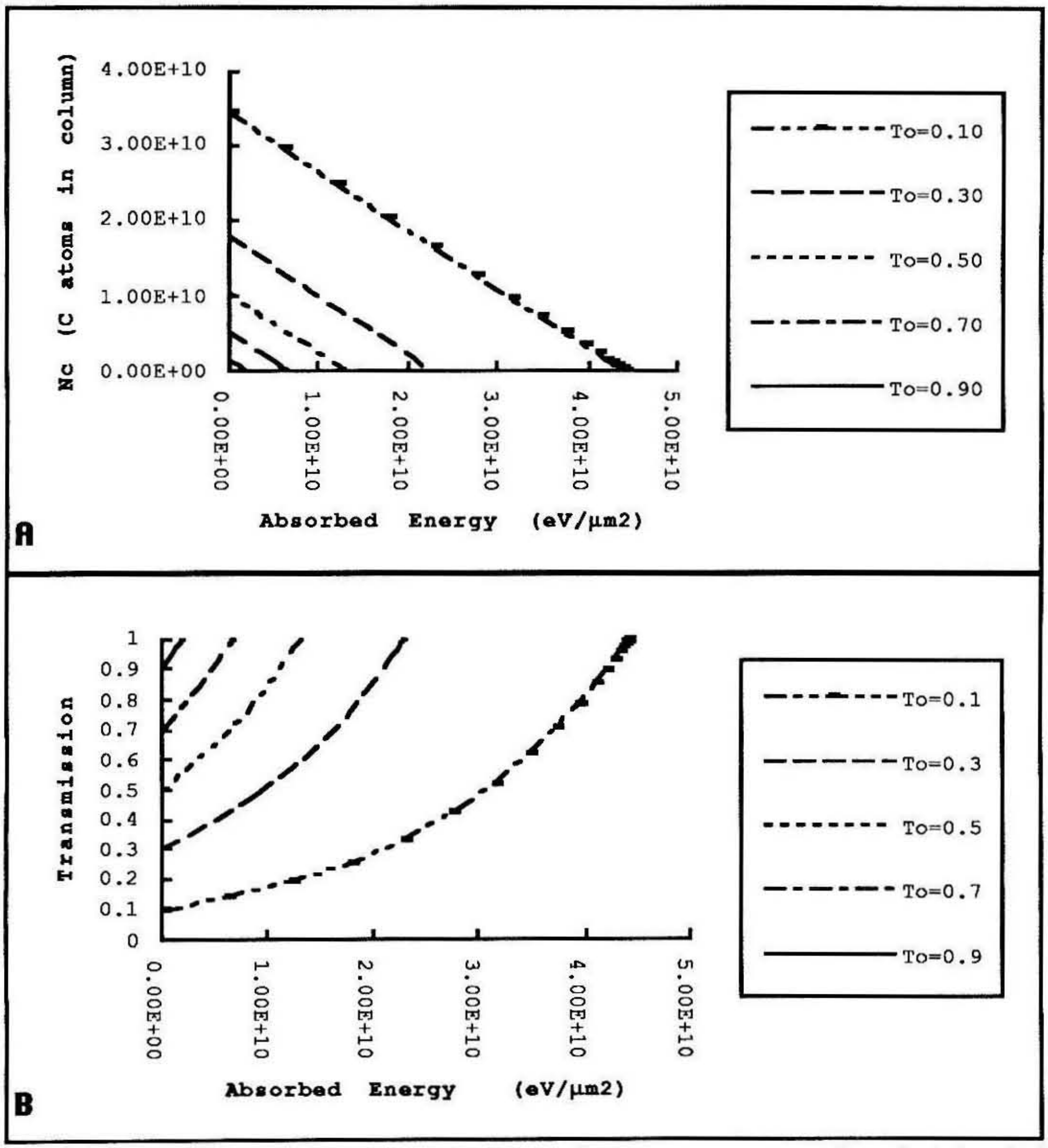

Figure 5.11 Damage vs. ΔE To observe damage we can present it against absorbed energy in a column. Using N_c vs. ΔE (as in **A**) or Transmssion vs. ΔE (as in **B**). In either case, according to our model, the initial transmission T_0 and the hardness α are sufficient to generate the full curve for any pixel.

In recognizing the linearity of radiation damage we had to look at the damage in terms of N_c vs. ΔE, as in the previous section. A graph of the damage behavior in those terms is shown in figure 5.11A, which shows the relation between N_c and ΔE for several different initial transmissions T_0. Note that by our radiation damage model the entire course of a progressively destroyed pixel is determined by the initial transmission T_0 and α.

We may also present the effect of radiation damage as transmission vs. ΔE, which is shown in figure 5.11B. The transmission view of the image, which is the most natural view at the microscope, begins to show us effects of damage on the structures in an image. Consider the $T_0=0.1$ and $T_0=0.5$ curves of figure 5.11B. After a column has absorbed about 10^{10} eV, the $T_0=0.1$ curve has barely changed (about 0.05) , while the $T_0=0.5$ curve has changed by 0.2. When we give a transmission image a linear gray scale (250 greys for full scale in ObjectImage) we will see larger changes in high transmission regions than in low transmission regions for the same absorbed energy.

Of course absorbed energy is not independent, in imaging, from the actual transmission of the sample. In chapter 3 we calculated ΔE from the incident flux I_0 and the transmission using equation 3.20. Equation 3.20 is only good when the transmission does not change much during the irradiation. More generally we use equation 3.20 and 5.2 to generate equation 5.3, which is a differential equation for ΔE as a function of I_0.

$$\frac{\partial \Delta E}{\partial I_0} = \left(1 - T(I_0)\right)\frac{hc}{\lambda} = \left(1 - T_0 e^{-\left(\alpha \mu_{Nc}(\lambda)\Delta E(I_0)\right)}\right)\frac{hc}{\lambda} \qquad [5.3]$$

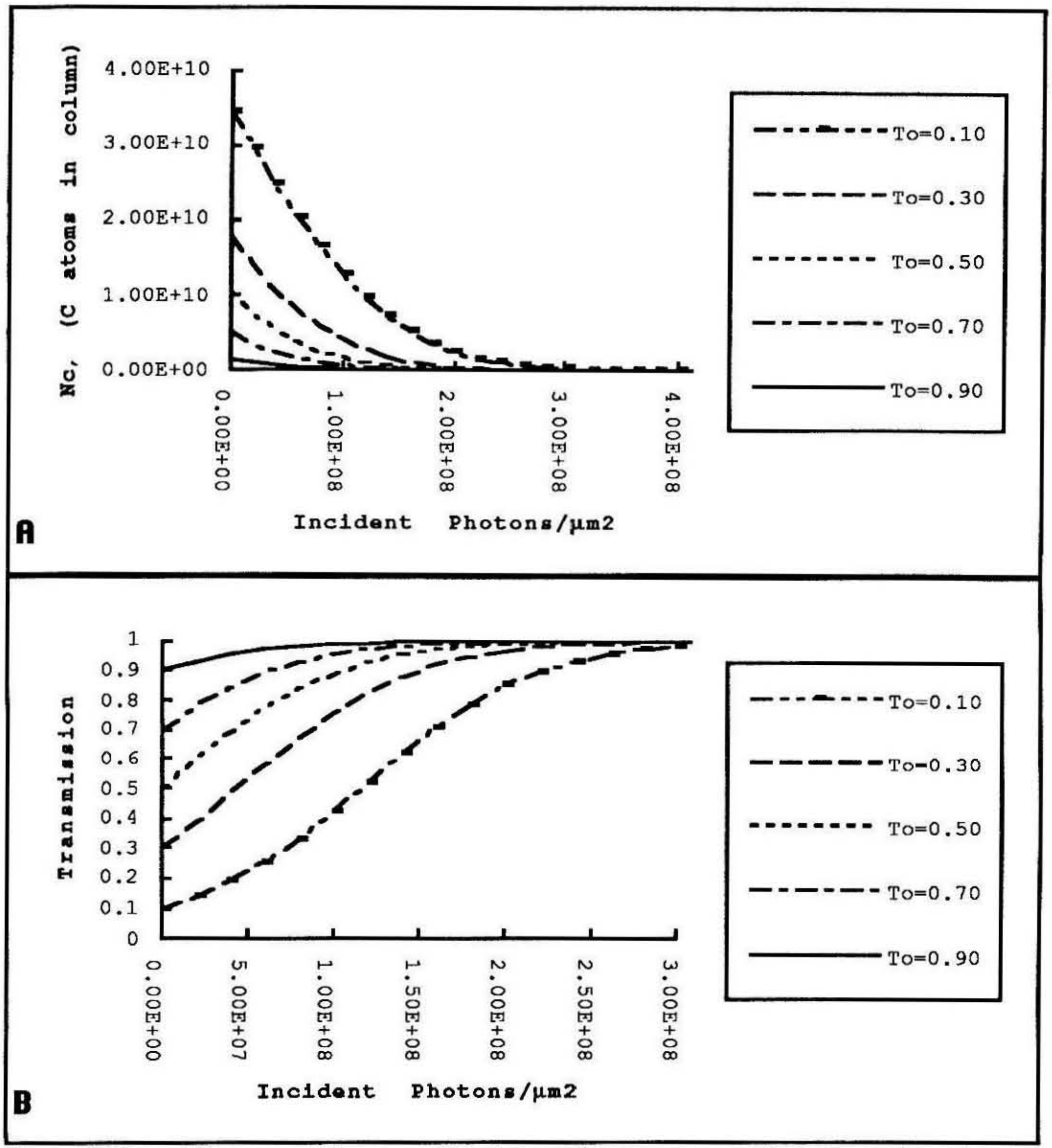

Figure 5.12 Damage vs. I_0 To observe damage we can also present it against I_0. Using N_c vs. I_0 (as in **A**) or Transmssion vs. I_0 (as in **B**). In either case, according to our model, the initial transmission T_0 and the hardness α are sufficient to generate the full curve for any pixel. The I_0 in this figure is the photons incident on a μm^2 column.

In equation 5.3 T_0 is the initial transmission in the pixel, and $\Delta E(0)=0$. This is the equation that we solved numerically to generate the curves of figures 5.11. When finding $\Delta E(I_0)$, or when operating the STXM, I_0 is the natural independent variable. In figure

5.12 we show the effects of radiation for essentially the same curves as figure 5.11, but we use I_0 as the x-variable. We graph the curves as N_c vs. I_0 in 5.12A and Transmission vs. I_0 in 5.12B. As before all we need to determine the curves is the initial transmission, T_0, and the hardness α.

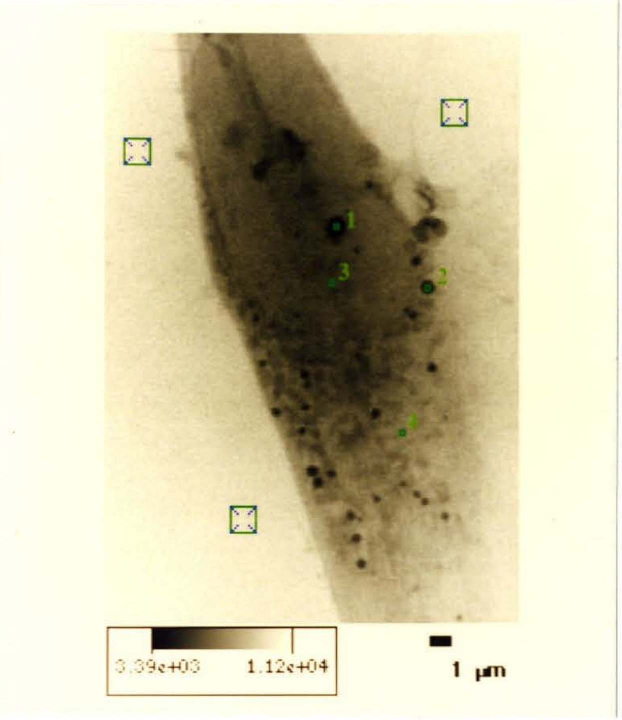

Figure 5.13 Damage in an Image We mark this image at 4 points and estimate damage to the cell, due to taking this image, at each one.

In figure 5.13 we show a STXM image of a fixed fibroblast. The image is taken at λ=33.77Å, and dx=0.1µm. We estimate that the incident flux I_0 on a per μm^2 basis is 10^7 photons. There are four labeled points in the image, two on dark granules, one in the nucleus and one in the cytoplasm. Their initial transmissions are listed in table 5.2 as T_0. Using the model of equation 5.3 we find the estimated new transmission T', after taking the image.

Mark	T_0	T'	ΔT	Δm/m
1	0.35	0.39	0.04	-0.10
2	0.45	0.49	0.04	-0.11
3	0.57	0.61	0.04	-0.12
4	0.71	0.74	0.03	-0.13

Table 5.2 Damage Evaluation Estimated damage at the marked points of figure 5.13. The background noise in the image of figure 5.13 is 0.019, and that quantity should be compared to ΔT. The measures ΔT and Δm/m are discussed in the text.

Table 5.2 introduces two measures of damage. ΔT is the simple change in T ($\Delta T = T' - T_0$). Δm/m is the fractional change in column mass (which is the same as the fractional change in number of atoms, N_c, in the column). Both of these measures are useful to us, and generally we will quote them both when discussing damage. Their relationship is not simple, and one cannot deduce Δm/m from ΔT without knowing T_0.

Δm/m is the more physical quantity, it is produced naturally when the absorption of a photon causes the loss of some C atoms. The fact that 10% of the carbon atoms in the sample have been lost at point 1 in figure 5.13, certainly has physical implications for the structures that we are looking at. Δm/m is the quantity that we will use when we return to discussing the physical nature of radiation damage.

ΔT, on the other hand, is the measure of damage that is relevant to looking at our images. In every image we can estimate the statistical noise level by the measurement of background noise as described in chapter 3. By that criteria the image of figure 5.13 has background noise of 1.96% (=0.02 in fractional units) which is the relative standard deviation of the pixels in one of the three large background normalization boxes. At point 1 in the image we have ΔT=0.04, which we can compare with a background noise of 0.02, to learn that the effects of damage in the image are down near the limits of what we can see. A comfortable situation would be one in which the noise in an image was comparable to or greater than the damage level. Then we could say with some certainty that the damage was not affecting the image. ΔT will be the quantity we will use in the next section in estimating the limits that radiation damage imposes on STXM imaging.

We also can estimate the absorbed dose in Rads for an imaged cell. Start with a measure of the transmission in the cytoplasm of the cell, T_c. Using the simple model that the cytoplasm of the cell has carbon density 0.1gm/cm^3 and water density 1gm/cm^3, we can use T_c to deduce D_z the cell thickness (in µm). Then the mass of cell can be estimated, this time counting both carbon and water, in a volume that is D_zx10^{-12}cm^3. Also using I_0, we can calculate the absorbed energy in both the carbon and the thickness D_z of water. The ratio of that absorbed energy in a 1µm^2 column of cell to that mass in 1µm^2 column of cell is the dose in Rads (translsted to 0.01J/Kg of course). For the cell of figure 5.13 we have cell thickness of D_z=1µm, and an absorbed dose of 3x10^7 Rads.

In figure 5.14 we show the behavior of these damage measures vs. incident flux, for the various T_0 of figures 5.11 and 5.12. There is an important feature to notice about figure 5.14. In the graph of $\Delta m/m$ (5.14A) we can see that for a given I_0 a greater fractional loss of mass takes place in the curves for higher T_0 (lower initial N_c and lower absorption) than for low T_0. This is in spite of the fact that a pixel of lower transmission will absorb more of the incident flux. What is going on here? It can be stated in terms of the relative efficiency with which mass or atoms catch photons. The ratio of absorption to column mass is higher in high transmission regions than in low transmission regions. We see this mathematically because $(1-T)/(-\ln(T))$ is an increasing function of T. Physically this is because the upstream parts of a column shield its downstream end, thus making a slice of mass on the downstream end absorb less than it would if on top of a shorter column.

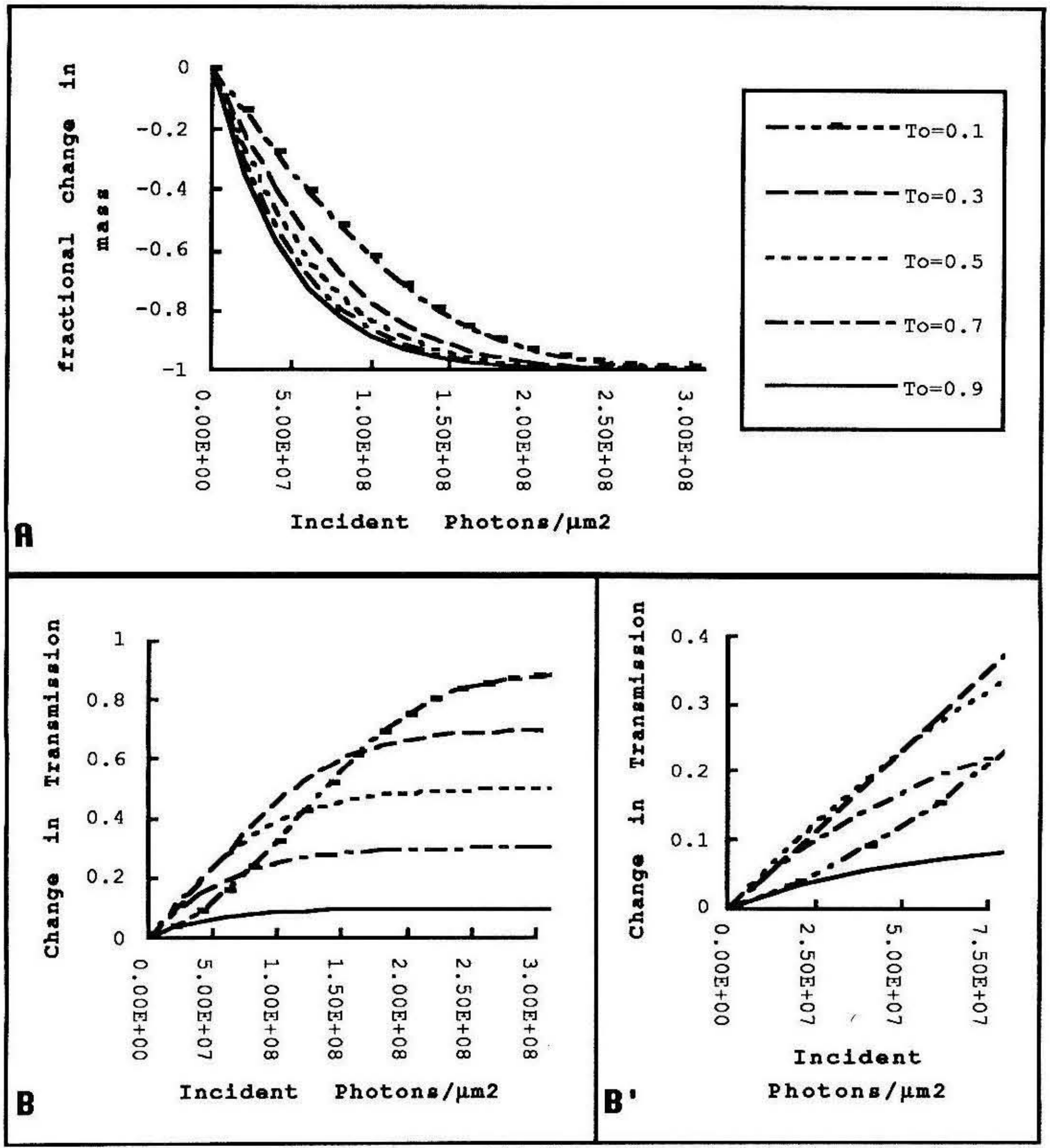

Figure 5.14 Damage Measures This figure shows curves of the fractional changes in mass (or N_c) in **A**, and the change in transmission in **B**. **B'** is an expansion of the graphs in **B**, near the origin. The curves are for the various T_0's of the figures 5.11 and 5.12. The legend in **A**, also applies to **B** and **B'**.

The same phenomenon can be seen in figure 5.14B and 5.14B'. The curves for $T_0=0.1$and $T_0=0.3$ exhibit an inflection. Photons incident early have less effect on transmission than those incident later. Figures 5.14B and 5.14B' tell us what we see in an image when pixels are damaged. A pixel having initial transmission of 0.1 (for example a hard granule) follows the trajectory labeled T_0=0.1 as we subect it to incident flux. Another pixel may follow the trajectory labeled T_0=0.7 (cytoplasm of our cells is usually near this). After 10^8 incident photons the first pixel is still more than half there (in the transmission image) while the second pixel is almost gone. Different features will respond differently to illumination. Generally more massive features will last longer in the microscope. This does not contradict the linearity of N_c vs. ΔE, it is a reflection of the difference between I_0 and ΔE.

5.5 Limits Due to Radiation Damage

In chapter 3 we established a model cell and granule to allow us to relate the incident flux I_0, the pixel size dx, the wavelength λ, the desired signal to noise S/N, and the parameters of the cell and granule (as in figure 3.18). That "undamageable" model allows any resolution to be reached, with enough photons. The only prohibitive costs are operational ones; STXM has a finite flux rate to work with and so imaging time gets out of control for very high statistics images. But now we can relate the absorbed energy to some damage to the cell and granule. We can, therefore, constrain the model of chapter 3 by placing limits on the acceptable radiation damage. We will numerically compute the minimum size a given granule can have and still be detectable without too much damage to the cell.

To put that all more firmly we will recap some of the equations of chapter 3. The model starts with equations 5.4 and 5.5:

$$T_{Body} = e^{-(\mu_C Z_B \rho_B)} \qquad [5.4]$$

$$T_{Body\_and\_Granule} = e^{-(\mu_C Z_B \rho_B)} e^{-(\mu_C Z_G \rho_G)} \qquad [5.5]$$

We can calculate the observed change in T due to the granule (the signal) and the S/N ratio for the granule over the cell as background. This is given in equations 5.6 and 5.7:

$$\left(\frac{\Delta T}{T}\right)_{\text{granule}} = 1 - e^{\left(-\mu_C(\lambda) Z_G \rho_G\right)} \qquad [5.6]$$

$$\frac{S}{N} = \frac{I_0 T_{Body} T_{loss} \left(\frac{\Delta T}{T}\right)_{\text{granule}}}{\sqrt{\left(I_0 T_{Body} T_{loss}\right)}} = \sqrt{\left(I_0 T_{Body} T_{loss}\right)} \left(\frac{\Delta T}{T}\right)_{\text{granule}} \qquad [5.7]$$

Now we define the change in transmission, due to radiation damage, in equation 5.8, with ΔE as in 5.9. And we constrain the damage to be less than 50% of the granule S/N in equation 5.10 .

$$\left(\frac{\Delta T}{T}\right)_{\text{damage}} = \left(1 - e^{\left(-\alpha \mu_{Nc}(\lambda) \Delta E\right)}\right) \qquad [5.8]$$

$$\Delta E = \frac{hc}{\lambda} \frac{I_0 (1 - T)}{dx^2} \qquad [5.9]$$

$$\left(\frac{\Delta T}{T}\right)_{\text{damage}} \leq (.5) \frac{\left(\frac{\Delta T}{T}\right)_{\text{granule}}}{\left(\frac{S}{N}\right)} = \frac{.5}{\sqrt{\left(I_0 T_{Body} T_{loss}\right)}} \qquad [5.10]$$

In the previous section of this chapter we used a full differential formulation of the radiation damage (in equation 5.3). In this section's model we fall back to a small damage approximation, (equation 5.8 and 5.9) which will let us do a simpler numerical minimization.

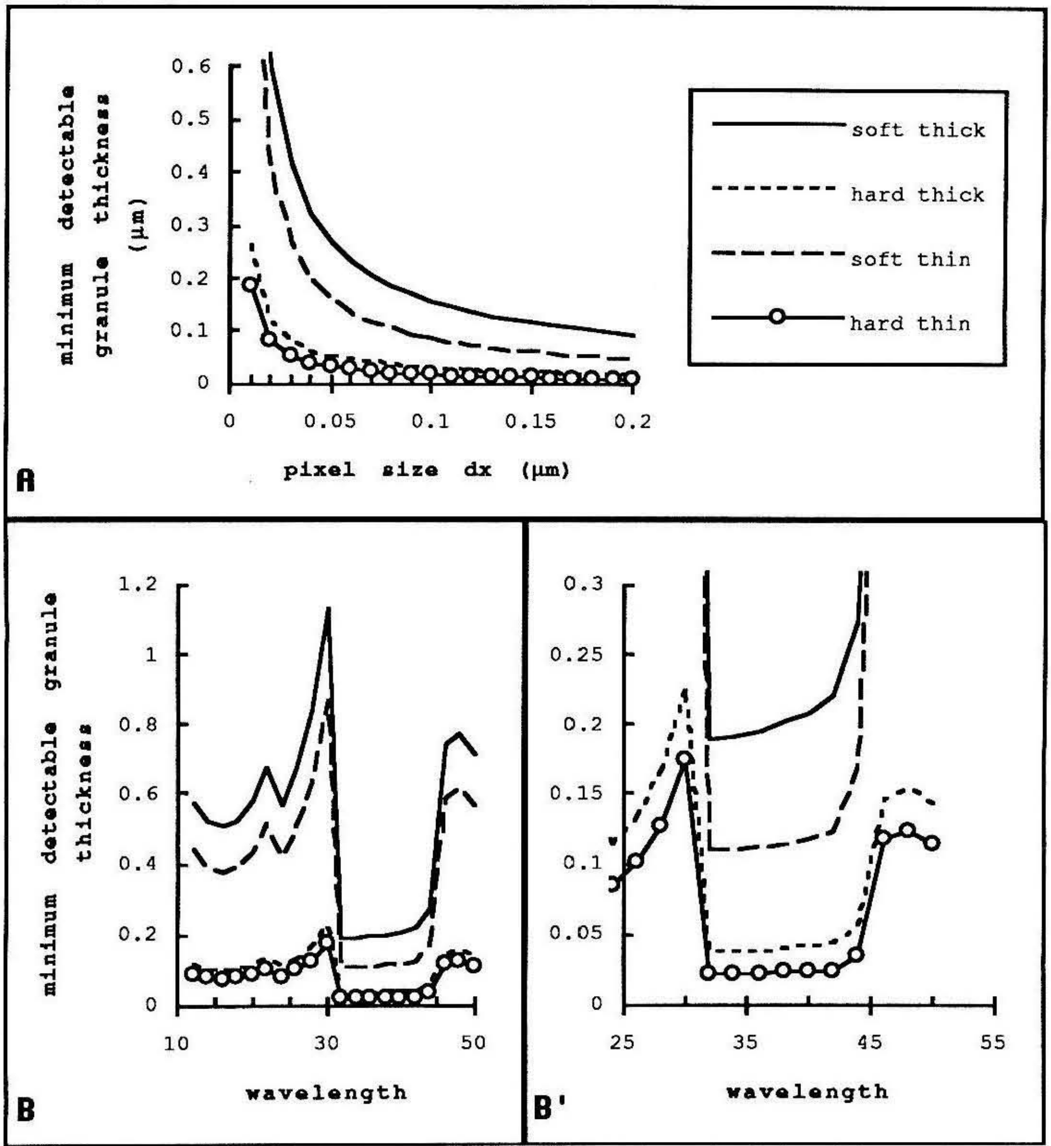

Figure 5.15 Minimum Detectable Granule A graph of the minimum detectable granule thickness demanding S/N = 5 and radiation damage at 50% of the shot noise level, T_{loss} is modeled at 2mm 95% Helium, 1.25mm air in wet cell, and 2 SiN windows (1000Å each) In **A** we graph the minimum detectable granule size Z_G vs. dx at λ=36Å. In **B** we graph Z_G vs. λ for dx=0.075µm. **B'** is an expansion of **B**, showing the region of best imaging. The curve legend of **A** also labels **B** and **B'**. The curve labels refer to the other parameters of the cell and granule model ρ_G, Z_B, and ρ_B. "Soft Thick" has parameters 0.2gm/cm^3, 1µm, and 0.1gm/cm^3. "Hard Thick" has parameters 1gm/cm^3, 1µm, and 0.1gm/cm^3. "Soft Thin" has parameters 0.2gm/cm^3, 0.1µm, and 0.1gm/cm^3. "Hard Thin" has parameters 1gm/cm^3, 0.1µm, and 0.1gm/cm^3.

In figure 5.15 we show calculated curves illustrating the relation between the minimum detectable granule thickness and the wavelength or pixel size used in the STXM image. Basically, as shown in figure 5.15A, the larger the pixel size the less radiation is deposited per $1\mu m^2$ column, and so the more photons we may use in a pixel, while getting the same level of column damage. That is good for detecting a thin or soft feature, but of course it restricts our ability to resolve the structure of any such feature. The various curves are similar to the thick and thin cell and soft and hard granule that we used in chapter 3. Other parameters used in this model are: S/N=5, and λ=36Å in figure 5.15A. In figure 5.15B we do the calculation vs. λ while dx=.075μm. In both cases the calculation is done by a numerical minimization. In both cases the standard estimate for T_{loss} is a critical part of the model.

From figure 5.15 we learn that at a pixel size of .075μm, we should be able to detect 0.025μm thick features if they are "hard", but we probably can't get below a thickness of 0.1μm for soft features. We can also see in figure 5.15B and B' that the best place for imaging is just above the nitrogen edge, near λ=31Å. This is particularly true if the losses are not as good as we have modeled them, or there are water layers present in the wet cell. In the observed window between the nitrogen edge and the carbon edge, the absorption of all in line materials N, O, or C is increasing, so any extra absorption will be worse at the long side of that window. In fact the signal due to any given granule is increasing as carbon becomes more absorbing. The advantage of that increased signal is almost exactly offset by increased losses in our standard model T_{loss}, and the result is the flat window of figure 5.15B. When, in practice, T_{loss} is worse than the model the window is no longer flat, and we get a much stronger advantage for imaging nearer to the nitrogen edge. Operationally this is good, since the STXM has more flux available at the lower wavelengths.

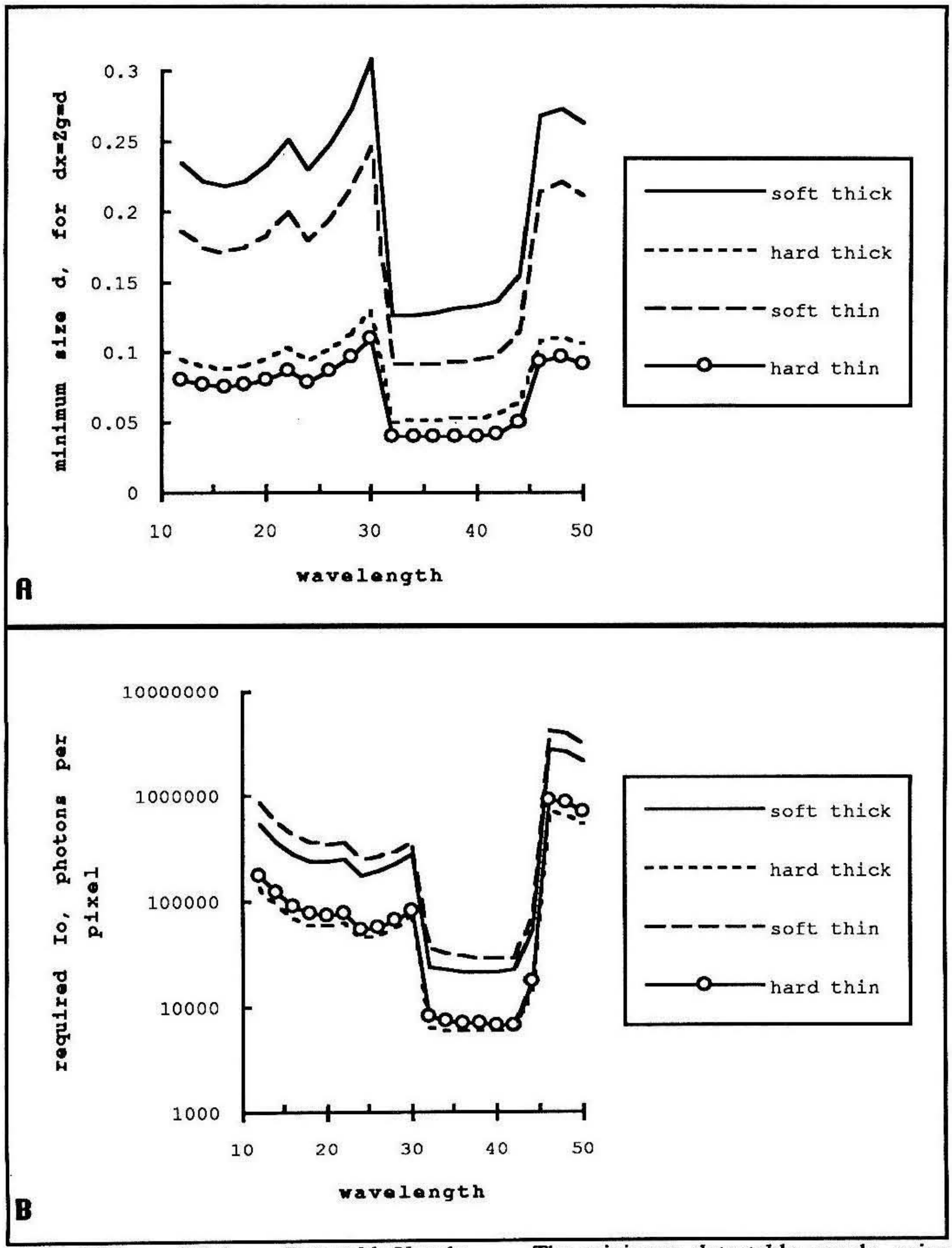

Figure 5.16 Minimum Detectable Voxels The minimum detectable voxels, using T_{loss} calculated as in figure 5.15. We define the model in terms of a smallest detectable volume, by setting $d=Z_G=dx$, and finding the minimum detectable d, with fixed signal to noise of $S/N=5$. The curve labels refer to the free parameters of the cell and granule model: ρ_G, Z_B, and ρ_B. Those parameters are set as in figure 5.15. A graphs d vs. λ. B graphs I_0 vs λ.

To make figure 5.15 we treat Zg, the granule diameter, and dx, the pixel size, as separate parameters. This is indeed appropriate for some classes of features, however it is also instructive to consider the ability of the STXM to detect a "voxel" or volume element having a different x-ray absorption from its background. If we use the model cell and granule with dx=Zg, and ask what the smallest detectable granule is, then we get figure 5.16, which contains the same four curves as figure 5.15. As before S/N=5, and we use the same T_{loss} with no water layer, 95% Helium in the 2mm external gap, and 1.25mm air in the wet cell. By this model the best we can do at any wavelength is near 0.05µm, and that requires hard objects. However again we have a window between the nitrogen edge and the carbon edge. At the same time that we calculate the minimum detectable voxel we find I, the incident photons per pixel that are required to detect that voxel That photon count is graphed in figure 5.16B, and it does have a bias towards the long side of the window. However the remarks about the effects of extra losses are still true, and the available flux in the STXM that was examined in chapter 3, still makes it easier to work near the nitrogen edge.

The requirement that S/N=5 is sometimes known as the rose criterion. For some features this will be overly restrictive. However, all our modelling of signal to noise has been done with the assumption that the x-ray probe is a point probe. As we saw in chapter 3, the real probe formed by the zone plate has a width near 50nm by most measures, and when such a probe images a feature of comparable size the signal due to the feature will be reduced by near 50%. So a S/N of 5 can easily become 2.5 or less when we consider features near the real probe size.

In both figures 5.15B and 5.16A we see an advantage in looking at a feature in the thin cell case. Radiation damage after all, does damage the cell background as well as any interesting features. Also a general cell background can be looked on as an extra absorbing layer, just costing the microscope valuable photons. Because of these effects it may be advantageous to look at isolated features in an extract using a wet cell like the LBL wet cell, in which granules flow through a 2µm layer of medium, between two silicon nitride windows such as the ones in our culture chips. The 2µm layer would still absorb photons, but being simple medium it would not be subject to damage itself. This sort of wet cell would be very awkward for whole cells, but has certainly been used for an isolated zymogen granule preparation.[12]

5.6 Effects on the Operation of STXM

We have suggested that from our data and analysis about radiation damage that the best region for imaging with the STXM is at wavelengths just above the nitrogen edge. But when we take images with the STXM we also must estimate how much flux a given sample can tolerate. And we need to know this in terms of readily observable quantities. The easiest quantity to observe at any feature or cell is I_{PC} (the photons detected in the proportional counter per pixel). We can use the full equation 5.3 to estimate the two damage measures of ΔT and $\Delta m/m$ vs. I_{PC}. In figure 5.17, we show the results of such a calculation for λ=31.25Å and dx=0.1µm. In figure 5.18, we do the same for λ=36Å. To scale the I_{PC} axis for any other dx, just multiply I_{PC} by $(dx)^2/(0.1)^2$. In both figures we provide curves matching five initial T_0's.

The figures 5.17 and 5.18 lead to the following procedure for imaging. For each wavelength we want to operate at and dx we want to image with we make up a graph as in figure 5.17. (This involves measuring T_{loss} at that wavelength). Then take a low flux image of the sample, and observe the photon count I_{PC} in a background region, as well as I_{PC}' in the region of peak absorption (lowest transmission). Then calculate T_0 as I_{PC}'/I_{PC}. Then follow the correct curve down to a tolerable damage level, and read off the matching

I_{PC}, from the graph. Knowing the permitted I_{PC} per pixel allows the user to set the dwell time τ. Note that the I_{PC} in the figures is for pixels having initial transmission T_0.

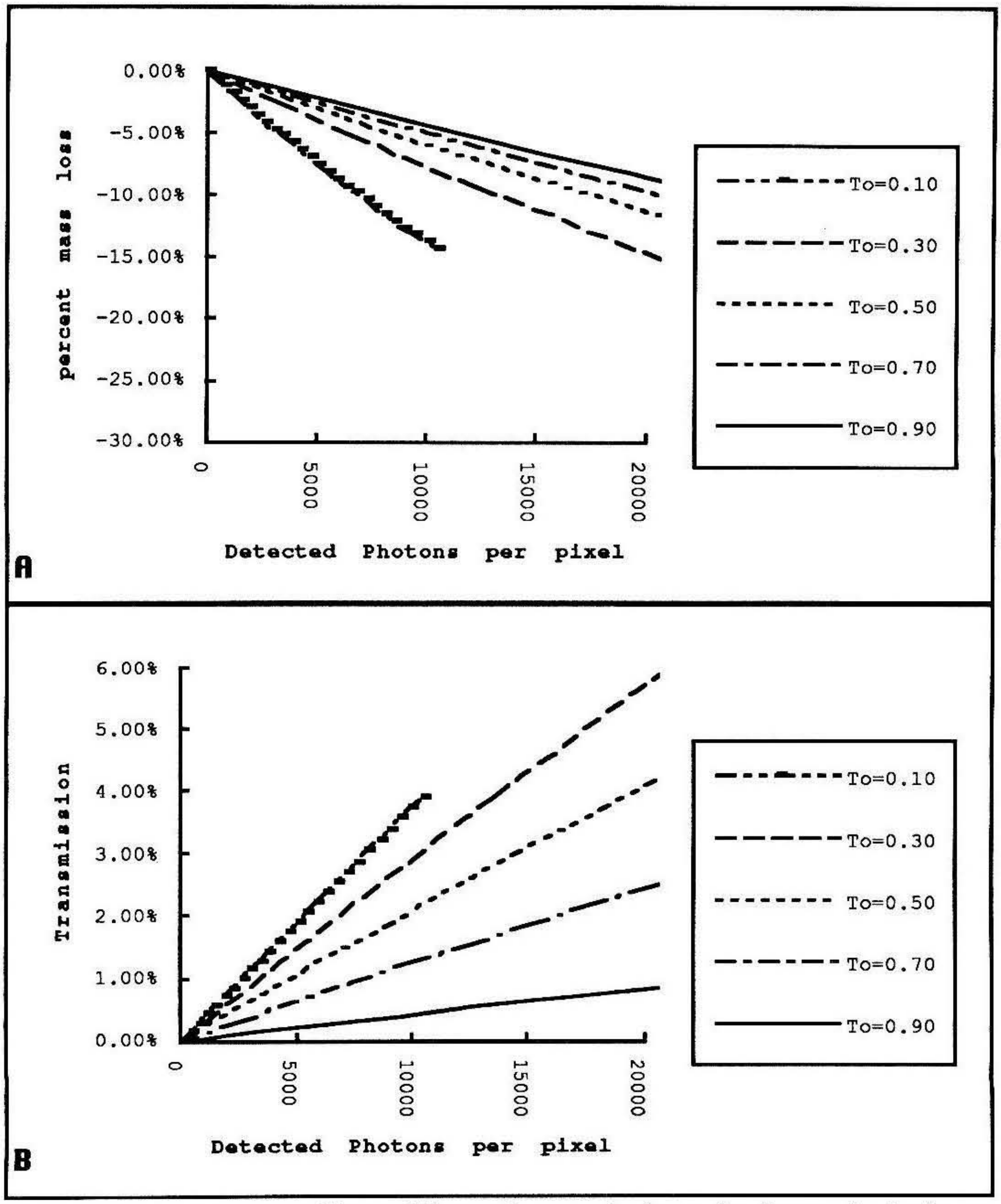

Figure 5.17 Damage vs. Observed Photons I **A** shows the damage in $\Delta m/m$ vs. detected photons per pixel (I_{PC}). **B** shows the change in transmission ΔT vs I_{PC}. Each graph has curves for five different initial transmissions, T_0. These curves are calculated for λ=31.25Å, dx=0.1μm, and T_{loss} is the same as in the previous figures in this section (no water layers, 95% He in 2mm external gap, 1.25mm air in wet cell).

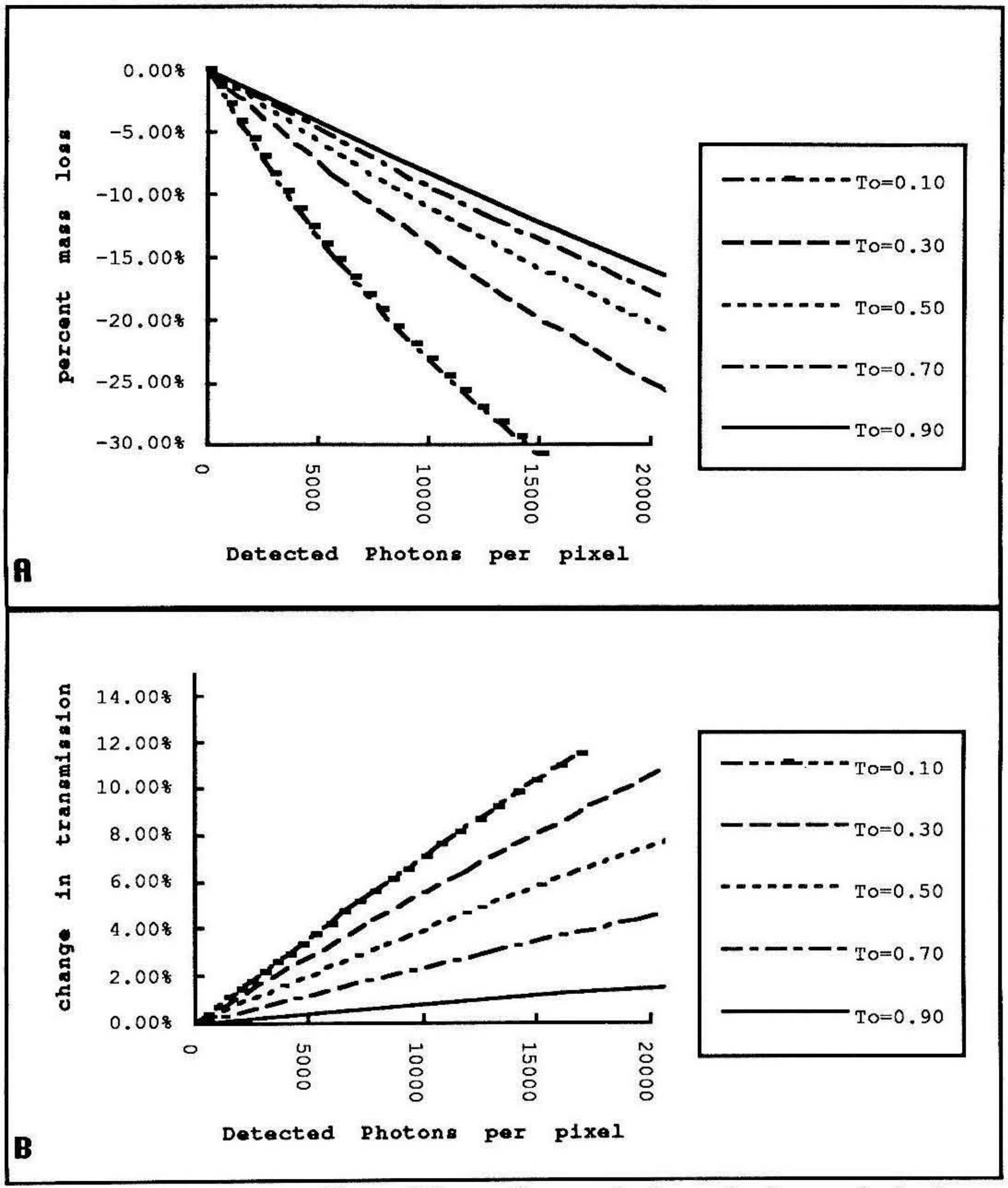

Figure 5.18 Damage vs. Observed Photons II **A** shows the damage in $\Delta m/m$ vs. detected photons per pixel (I_{PC}). **B** shows the change in transmission ΔT vs I_{PC}. Each graph has curves for five different initial transmissions, T_0. These curves are for λ=36Å, dx=0.1µm, and T_{loss} is the standard model of the previous figures in this section (no water layers, 95% He in 2mm external gap, 1.25mm air in wet cell).

There are several things to notice about the curves in figures 5.17 and 5.18. First, as expected 31.25Å is a better place to image than 36Å. Second, its quite easy to get to the 5% mass loss level in an image, catching 5000 photons will do it on dark features, and going to a pixel size of 0.05µm, will do it four times faster. And third, the orders of the damage curves have reversed from figure 5.14. That is in figures 5.17 and 5.18 the T_0=0.1 curves show more damage than the higher transmission curves, just the opposite of what we found in figure 5.14, where the damage was graphed vs. I_0. This difference is totally due to the absorption in the sample itself. It takes more I_0 photons to make one I_{PC} photon when the sample has T_0=0.1 than when it has T_0=0.9.

5.7 Conclusion

Two principal facts have been gleaned from the data in this chapter. One, the damage caused by absorption of radiation in fixed cells is a linear loss of x-ray absorbing mass with cumulative energy absorbed. Two, a fair value for the slope of that linear relationship is α=-0.78±0.35 in units of [C atom equivalent absorption] per [eV absorbed]. These observations have allowed us to model several different aspects of the imaging of fixed tissue.

The modelling leads to several conclusions. The best operating point of the STXM in regards to detecting the smallest features with the best signal to noise is just above the nitrogen edge at wavelength (31-32Å.) The exact limits of resolution depend on just how much contrast the feature to be detected has, however the best features are high contrast ones in a thin cell or no cell at all. A high contrast feature, having carbon density near 1gm/cm^3, might be detectable at S/N=5 at thicknesses down to 0.025µm if it can be found with pixel sizes of dx=0.075µm or more. On a voxel basis, i.e., if we want to observe an object of diameter d with a pixel size dx=d at S/N=5, we might be able to reach d=0.050µm. Doing better than that is unlikely, and will involve trading pixel size for S/N.

An S/N of 5:1 will actually be reduced by about 50%, when an object to be imaged approaches the size of the x-ray probe, following the analysis of chapter 3. All this does suggest that the soft x-ray STXM is approaching the best it can do on wet biological specimens, even though the actual x-ray optics may still improve by quite a lot.

We expect almost all of the energy of a soft x-ray photon to be deposited in biological samples by producing one or more energetic electrons. The understanding of the primary and secondary excitiations due to energetic electrons, is reasonably developed in the case of pure water,[13] or uniform aqueous solutions with simple constituents,[14] but not well developed for for more complex organic matrices in the wet state. In fact just in generating a number of atoms liberated per eV deposited, we have provided an unusually simple quantitative number to the field of radiation damage. α=-0.78 implies about 450 carbon atoms worth of absorption are lost due to each 36Å photon (~350eV). What this implies about the average number of bonds broken through secondary excitiations, and the average size of molcules that diffuse away from the pixel, is not modellable from our data.

We are operating at levels of radiation damage where all the molecules in the cell are being affected. A damage level of only $\Delta m/m$=10% implies that essentially all proteins of MW greater than 450x12x10=54kD have been damaged. This conclusion depends on the observed linearity of mass loss vs. absorbed energy, which is really telling us that the damage that each photon does is independent of all other photons, even down to the complete destruction of the sample. This independence of damage due to photon absorption is consistent with what others find when studying radiation inactivation of enzyme function,[15]

All our data is from work on fixed wet tissue. It can only be used to speculate about imaging live cells. However, the speculation might go as follows: The live cell will have some extra resistance, at least initially, to the damage induced by secondary chemistry (particularly oxygen radicals) this may help to reduce the damage due to each photon. On the other hand the live cell will be much more vulnerable to structural damage. Examples of possible structural damage affecting an image are: damage to cytoskeletal elements that cause motion, or damage to membranes that cause mass leakage from the cell or osmotic effects. And after the cell has taken enough dose to inactivate its enzymes, it will lose any extra resistance it might have had initially.

Clearly this is the begining of a line of experiments directed at radiation damage in the STXM. Our biggest source of error is the estimation of I_0. A direct monitor for I_0 should allow the measurement of α at an accuracy of 10% or better. Better alignment of images with each other, might also allow the measurement of α on a pixel by pixel basis. If these improvements can be implemented one could begin to search for variations in radiation sensitivity among cell types or cell substructures. We might be able to watch the detailed time course of the damage. We could also pin down the relation between wavelength and radiation sensitivity. In the present work using deposited energy looks good, but using number of photons deposited would also fall within the overall error in estimating α, that is because the greatest error is in our estimates of incident flux, and we have only two different wavelengths in our radiation series data set.

5.8 Chapter 5 References

---

1 D. Sayre, J. Kirz, R. Feder, D.M. Kim, and E. Spiller, "Transmission Microscopy of Unmodified Biological Materials: Comparative Radiation Dosages with Electrons and Ultrasoft X-Ray Photons," Ultramicroscopy, **2**, (1977) pp.337-341.

2 J. Kirz, "Specimen Damage Considerations in Biological Microprobe Analysis," Scanning Electron Microscopy, 2, (1980) pp.239-249.

3 J. Kirz, "Scattering of X-rays from Electrons and Atoms," X-ray Data Booklet, edited by D. Vaughan (CFXO, Berkeley, 1986) p.3-3.

4 C.D. Wagner, "The Role of Auger Lines in Photoelectron Spectroscopy," in Handbook of X-ray and Ultraviolet Photoelectron Spectroscopy, edited by D. Briggs, Heyden, London, 1977), chapter 7.

5 D.E. Lea, Actions of Radiations on Living Cells, (Cambridge University, London, 1955) pp.23-27.

6 see reference 4 pp.3-6.

7 I.G. Draganic and Z.D. Draganic, The Radiation Chemistry of Water, (Academic Press, New York, 1971) pp.30-40.

8 H. Wolters, C.A.M. vanTilburg, and A.W.T Konings, "Radiation Induced Lipid Peroxidation: Influence of Oxygen Concentration and Membrane Lipid Concentration," Int. J. Radiat. Biol., **51**, 4 pp.619-628 (1987).

9 see reference 7.

10 S.B. Tuwiner, L.P. Miller, and W.E. Brown, Diffusion and Membrane Technology, (Reinhold, NewYork, 1962) pp.90-100. and A.L. Lehninger, Biochemistry, 2nd Edition, (Worth, New York, 1976) p.176.

More References:

11 Each slope α is generated by the least squares fit of a line to N observed points. Each point is the mean of 9 pixels, and as such has an observed standard deviation σ_i. The standard error on α, SE_α, is:

$$SE_\alpha = \frac{\sigma}{\sum (x_i - \bar{x})^2}$$

Where we have used $\sigma=\Sigma\sigma_i/N$ (the average of the observed standard deviations) and the x_i are the x-coordinates of the N points. This is not exact, for a discussion see: N.R. Draper and H. Smith, Applied Regression Analysis, (Wiley, New York, 1966) pp.18-21.

12 K. Goncz, personal communications.

13 see reference 7.

14 G.V. Buxton, "Radiation Chemistry of the Liquid State: (1) Water and Homogeneous Aqueous Solutions," in Radiation Chemistry, edited by Farhataziz and M.A.J. Rodgers, (VCH, New York, 1987) chapter 10.

15 G.R. Kepner and R.I. Macey, "Membrane Enzyme Systems Molecular Size Determinations by Radiation Inactivation," Biochim. Biophys. Acta, **163** (1968) pp.188-203.

6 Cell Images

We have taken images with the microscope arranged to have underlying resolution of better than 75nm on fixed cells, and 100-200nm on unfixed cells. This is approaching the current diffraction limited resolution of the STXM, which at the latest report[1] is about 43nm for Rayleigh resolution, reaching 36nm if the image is oversampled and deconvolution techniques are applied. In this chapter we will show selected images of fixed chick fibroblasts and fixed rat hippocampal neurons and the best set of initially live fibroblast images that we recorded. These series of images will also show how the flexibility of the microscope, with regard to magnification (i.e., pixel size), lets us zero in on regions of interest. We will also look at some quantitative feature profiles, as a concrete measure of what high resolution means to observing cell structures.

6.1 Working with a Culture Chip

Normally we are interested in only a few cells on a given culture chip. We examine each chip in a standard visible light microscope, with phase contrast optics, and select the cells of interest. Locations of these target cells are recorded, using the location marks on the chip. At the same time reference photographs are usually taken. We then load the chip into the wet cell and mount the wet cell on the STXM stage. The first image we take of the chip is usually a low resolution orientation scan of whatever region is centered on the beam at loading. That orientation scan shows the location marks of the starting region. We can then move the STXM stage in x and y to center the region containing the target cells. Then another orientation scan is taken to find the target cells. This orientation scan is usually taken at 1 to 4 μm per pixel. Examples of a reference view of the culture in phase and a corresponding STXM orientation scan are shown in figure 6.1.

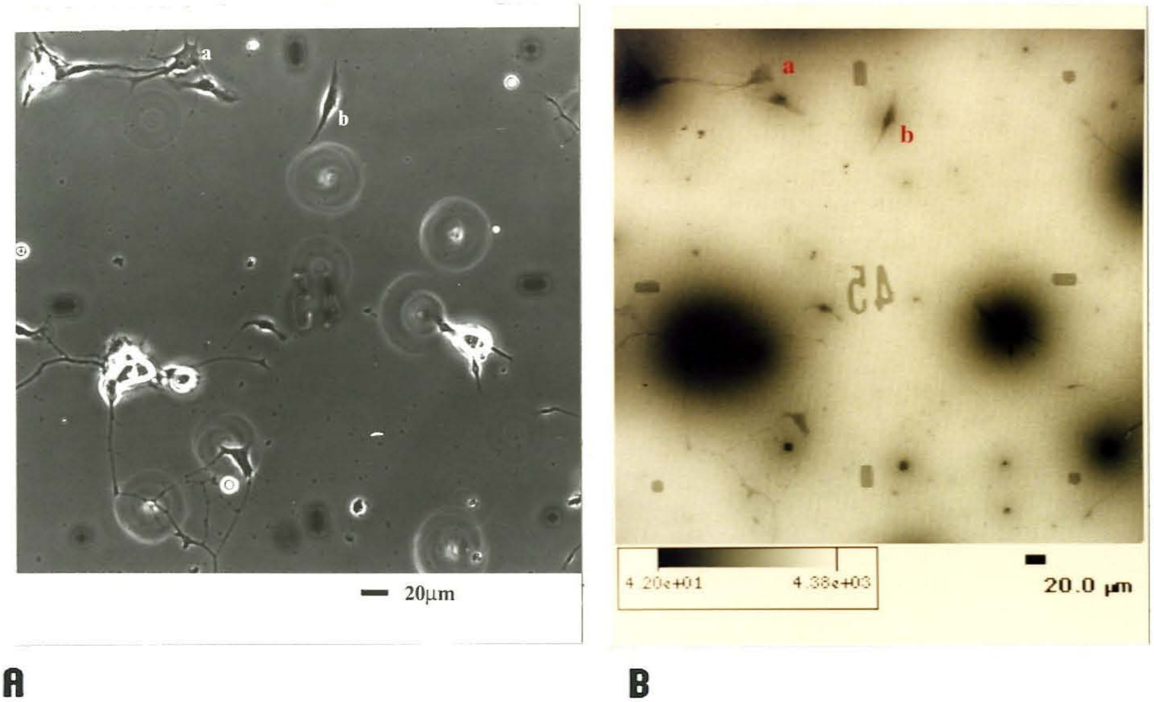

Figure 6.1 Orientation Images A is a phase contrast image of the target region of the culture taken at 20x, B is a STXM image of the same region taken at 2μm per pixel for an orientation scan. The same cells **a** and **b** are labeled in both images.

One of the tools provided by the on-line STXM software is the ability to have the computer record the locations of points we designate on an image. We can point to a target cell in an orientation scan (using a mouse driven cursor) and record its STXM_X and STXM_Y coordinates, allowing the computer to center an image at that location on command. After we find the target cells in the orientation scan, we can image them individually. Usually it is necessary to re-focus as we move laterally from target cell to cell. This is a natural result of the wet cell and culture chip not being perpendicular to the beam to better than 10-20 milliradians. When we move laterally 200μm, we expect a shift in z coordinate of order of 2-4μm at least, i.e., more than the depth of focus at finest resolution. For best image quality we re-focus on an edge (preferably a focus mark) every time we move more than 100μm, or more often if possible. In the orientation scan taken with the STXM, we see some large-scale dark regions, with soft edges. These regions are water droplets usually associated with some clumps of debris or cells. We believe that such clumps can anchor water droplets several microns thick, making dark or opaque regions in the image.

6.2 Images of Fixed Fibroblasts

About 75% of our images of fixed cells are of chick fibroblasts, either dorsal root ganglion cultures (DRG) or a chick skin prep. The fibroblasts proved to be very attractive cells in the STXM. Below we will show some of our images, and try to give some feel for what can be seen with the microscope.

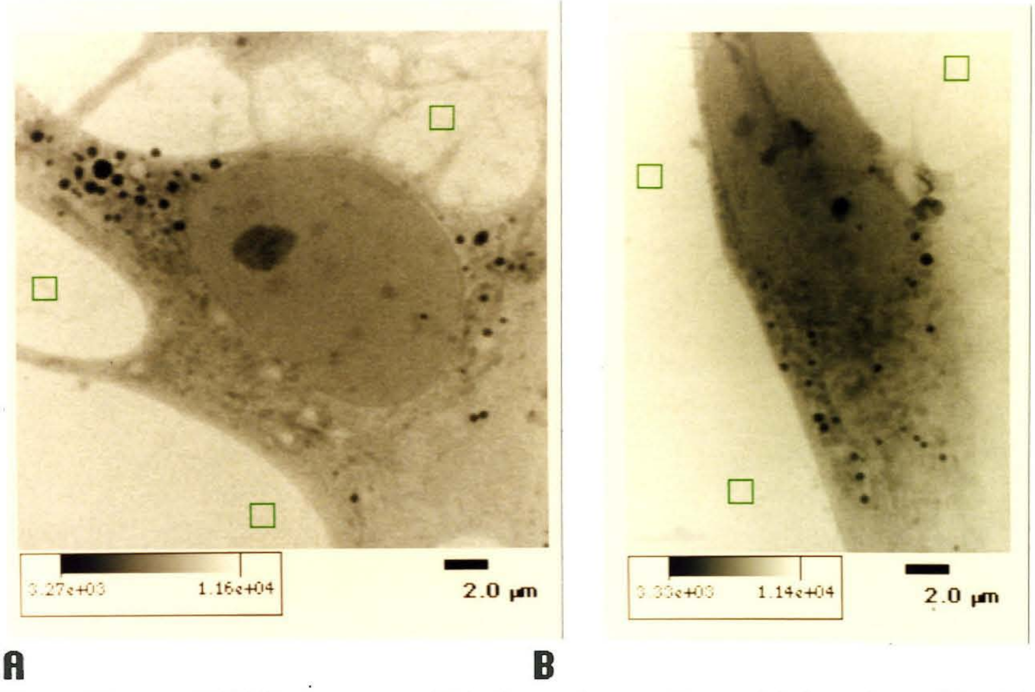

Figure 6.2 STXM Images This figure shows cells **a** and **b** from figure 6.1. **A** is cell **a**, taken at 95nm/pixel and 10msec/pixel, achieving a background noise of 1.67%. **B** is cell **b**, taken at 95nm/pixel and 10 msec/pixel, achieving a background noise of 1.96%.

In figure 6.2 we show the STXM images of cells **a** and **b** as identified in figure 6.1. These are chick fibroblasts, imaged at 95nm per pixel. The cytoplasm of these cells had an estimated thickness of 1.2μm and 1.0μm respectively. And they received corresponding radiation dose of about 3×10^7 Rads. These images caused estimated damage ΔT to the cells equal to a 4% increase in transmission in the cell cytoplasm, or a mass loss $\Delta m/m$ of -15% in **a**, and -14% in **b**. The methods for estimating damage and dose in Rads were discussed in chapter 5. Further data about these images can be found in table 6.3, towards the end of this chapter.

Both images show both dense granules and vacuoles (structures less dense than the cell body), as well as some elongated structures in the cell cytoplasm. We can also see rather well defined nuclei, as well as nucleolei. Cell **b** in figure 6.2B also shows an uncommon amount of structure in its nucleus.

More images of fixed chick fibroblasts are shown in figures 6.3 through 6.6. General facts about all the STXM images in this chapter can be found in table 6.3, located near the end of the chapter. Figure 6.3 shows images, at medium resolution, of two chick fibroblasts. 6.3A is the right side of a large thin extended fibroblast, and 6.3B is a large isolated fibroblast. Figure 6.4 shows a montage of 4 images covering a large fibroblast (6.4A) with a close up of a region in which a thin process intersects the fibroblast (6.4B). In 6.4B we have taken several profiles, labeled 1, 2, and 3, and they are graphed in figure 6.10. Sructures sectioned by the profiles are also labeled in 6.4B. They are a b, and d, which are granules having FWHM's of 0.27μm, 0.27μm, and 0.25μm respectively, c which is the edge of the nucleus (a step of about 0.16μm) and a process e, having FWHM of 0.28μm. Figure 6.5 shows another fibroblast, with several labeled features, and a high resolution sub-image 6.5B of one nucleoleus. We can see some definite, but as yet unidentified other structures in the nucleus.

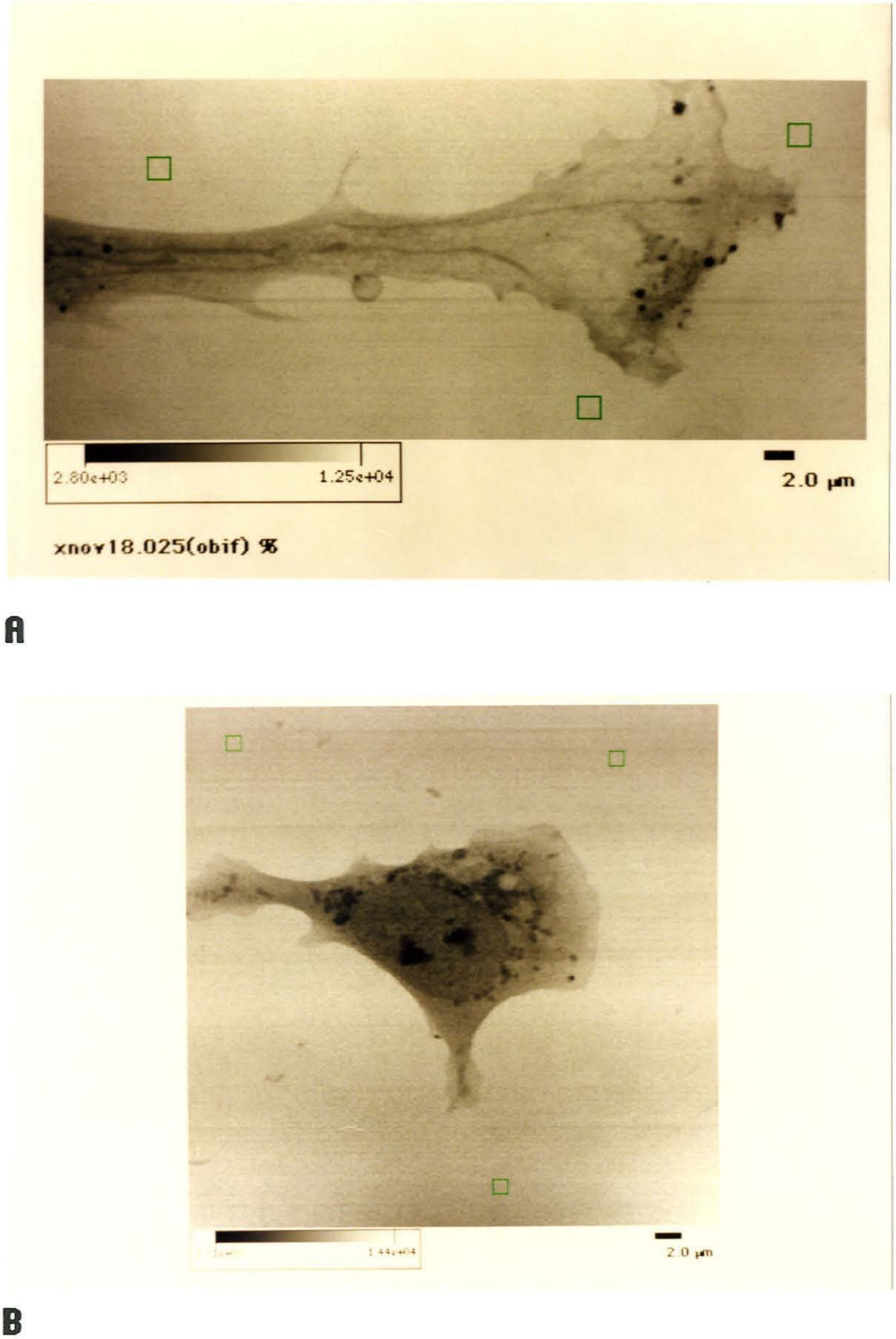

Figure 6.3 Fixed Fibroblasts I A is an image of a fixed chick fibroblast taken at 126nm/pixel and 14msec/pixel, achieving 1.43% noise. B shows a fibroblast imaged at 95nm/pixel and 10msec/pixel, achieving 2.49% noise.

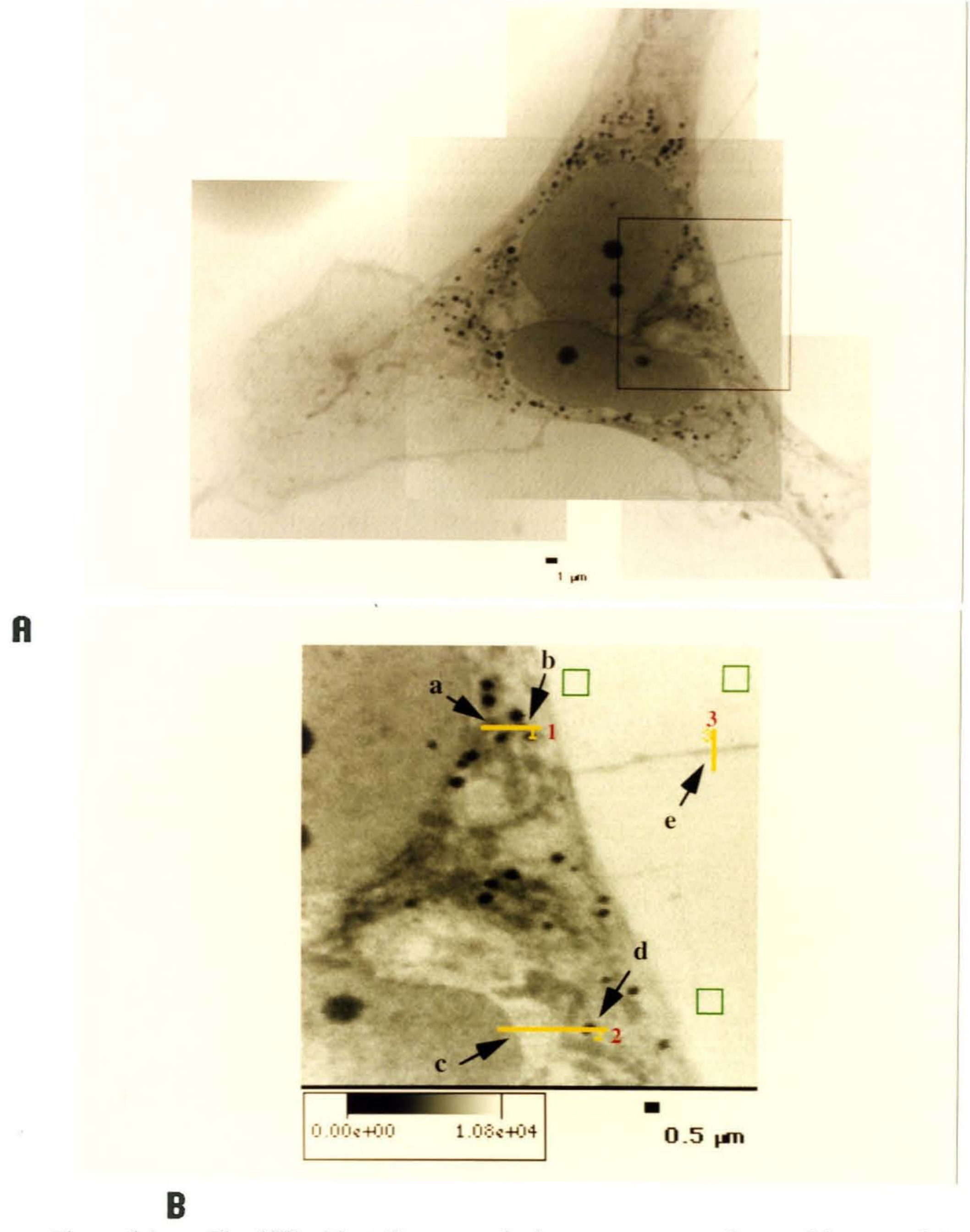

Figure 6.4 Fixed Fibroblasts II **A** shows a montage of several images of the same cell. The fibroblast was fixed while dividing, as a result it has 2 nuclei, and each has 2 nucleolei. Each sub image of A was taken at 95nm/pixel. Its scale bar shows 1µm. The rectangle in **A** outlines a region which was imaged at 32nm/pixel and is shown in **B**. Background noise in the larger montage is 3.29%, and 2.57% in the high resolution region. **B** has profiles labeled 1, 2, and 3 that are graphed in figure 6.10. several structures are also labeled in **B**. They are a b, and d, which are granules having FWHM's of 0.27µm, 0.27µm, and 0.25µm respectively, c which is the edge of the nucleus (and has a step of about 0.16µm) and a process e, having FWHM of 0.28µm.

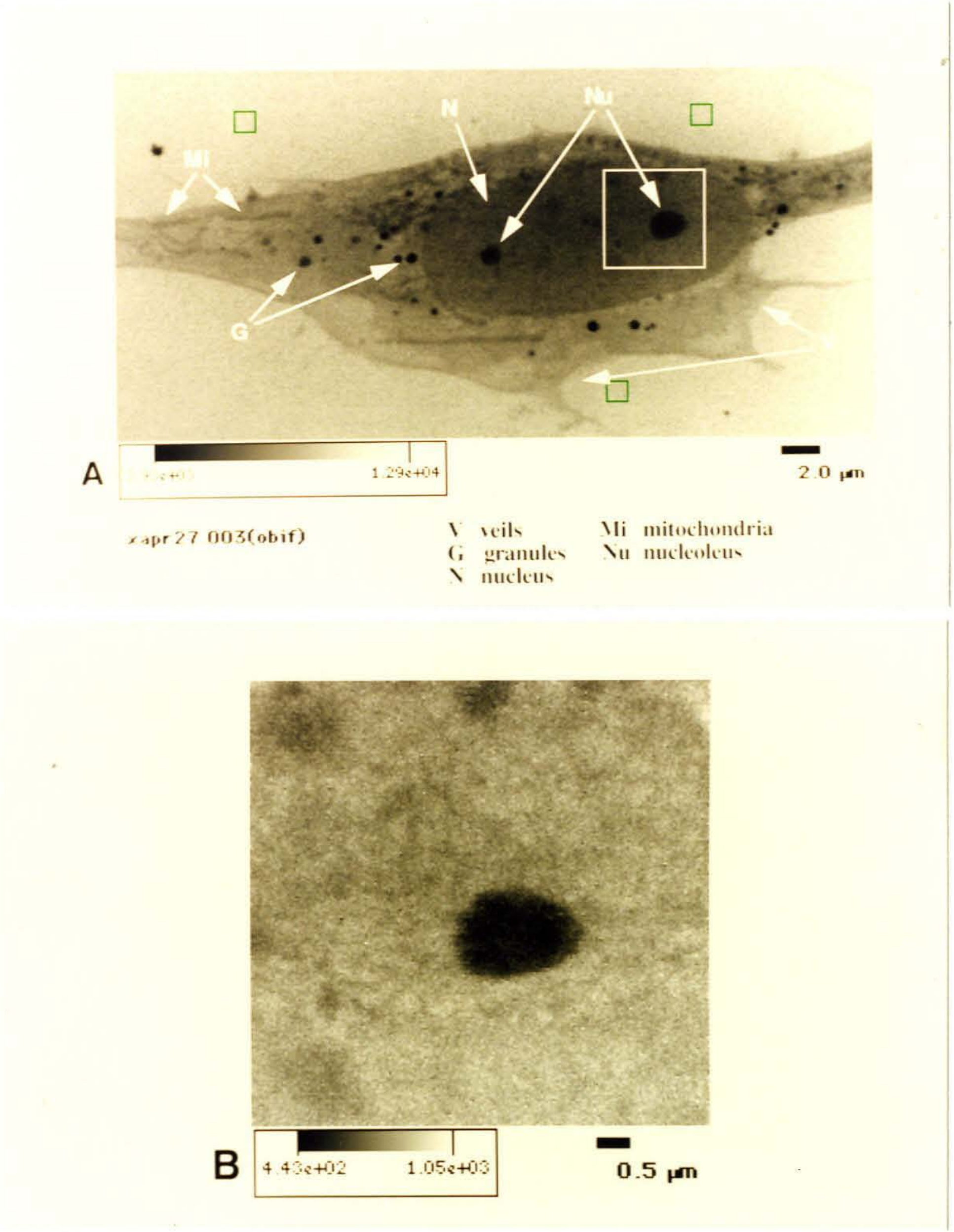

A

B

Figure 6.5 Fixed Fibroblasts III A is an image of a fibroblast taken at 95nm/pixel and 15msec/pixel, achieving 2.37% noise. **B** is a close up of the nucleoleus taken at 32nm/pixel and 20msec/pixel (no background was visible in the close up, so equivalent background noise could not be measured directly, but was estimated at 3%.) A wide variety of features are visible. Labeled features are granules, veils, and mitochondria. The close up of the nucleoleus shows some visible, but unidentified, structure in the nucleus of the cell.

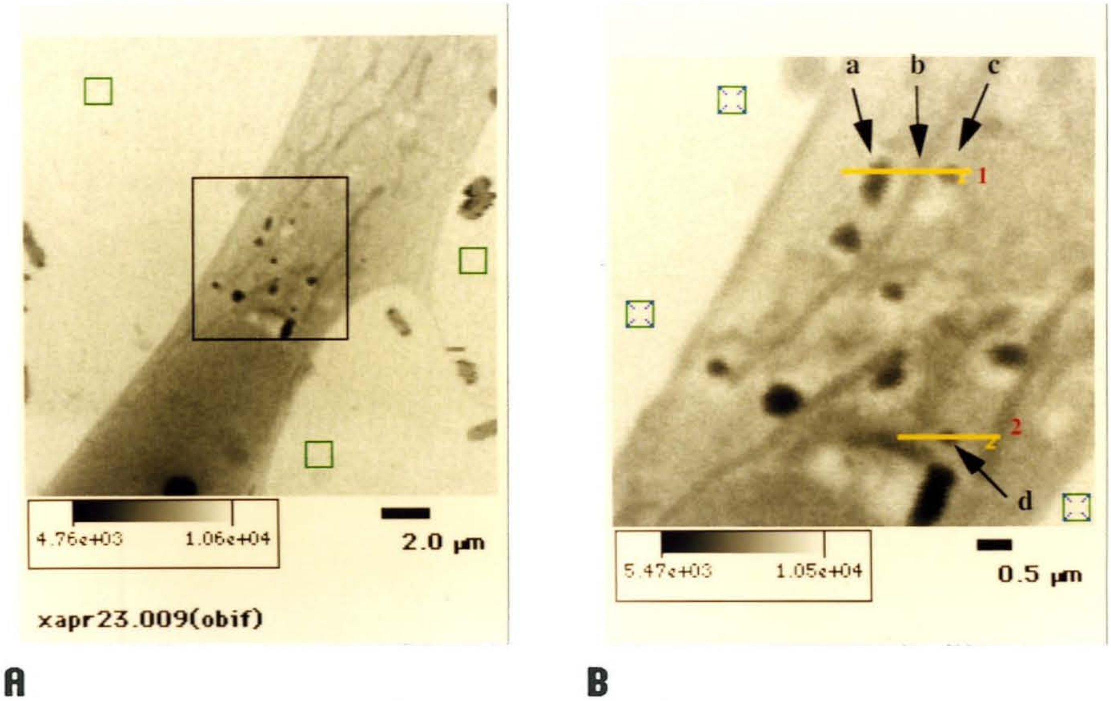

Figure 6.6 Fixed Fibroblasts IV An image of a fixed fibroblast. **A** is taken at 95nm/pixel and 10msec/pixel, achieving 1.62% noise. **B** is a close up of a region of the cell in **A**, taken at 32nm/pixel and 10msec/pixel, achieving 1.35% noise. The labeled profiles 1 and 2 are graphed in figure 6.10. The labeled structures a, b, c and d that are profiled have estimated FWHM's of 0.30µm, 0.15µm, 0.30µm, and 0.28µm respectively.

Figure 6.6 shows another fixed fibroblast, along with a close up of its most feature rich region . The close up image, 6.6B has two profiles, labeled 1 and 2, that are graphed in figure 6.10. The labeled structures are a, c and d, which are granules, and b which may be a mitochondrion. The labeled structures are profiled, and have estimated FWHM's of 0.30µm, 0.15µm, 0.30µm, and 0.28µm respectively.

6.3 Images of Fixed Hippocampal Neurons

The second cell type that we have used in imaging is from a primary culture of rat hippocampal neurons. This culture system is particularly interesting because it is known to exhibit synaptic structures in culture, and to produce processes similar to dendrites in culture. We have attempted to find synaptic structures with the STXM, so far without success. In figures 6.7, 6.8 and 6.9 we we show images of several fixed neurons from such cultures. Figure 6.7 contains images of regions of one neuron. 6.7A shows two dendrites of the neuron, taken at dx=0.10µm. 6.7B and 6.7C are higher resolution images of particular regions of 6.7A. In figure 6.7C we have labeled the profiles 1, 2, and 3 which are graphed in figure 6.11A. Three sharp features, a, b, and c, are labeled on the profiles. These have FWHM's 0.16µm, 0.19µm, and 0.18µm respectively.

Figure 6.8 shows another fixed neuron. The cell body is almost totally opaque, and shadowed by a water droplet. However the cell has a collection of fine processes. In 6.8B we show a high resolution image of a region containg some of those fine processes. Two profiles are labeled, sectioning three fine processes at a, b and c as well as one granule like object at d. The sizes, by FWHM, of the labeled structures are 0.25µm, 0.32µm, 0.13µm and 0.37µm respectively.

Figure 6.9 shows a montage of images of a long dendrite, and in 6.9B a high resolution image of a swelling in the dendrite similar to the object in 6.7C. We took two profiles, 1 and 2, in 6.9B and they are graphed in 6.11C. The labeled structures a and b have measured FWHM's of 0.11µm and 0.26µm respectively.

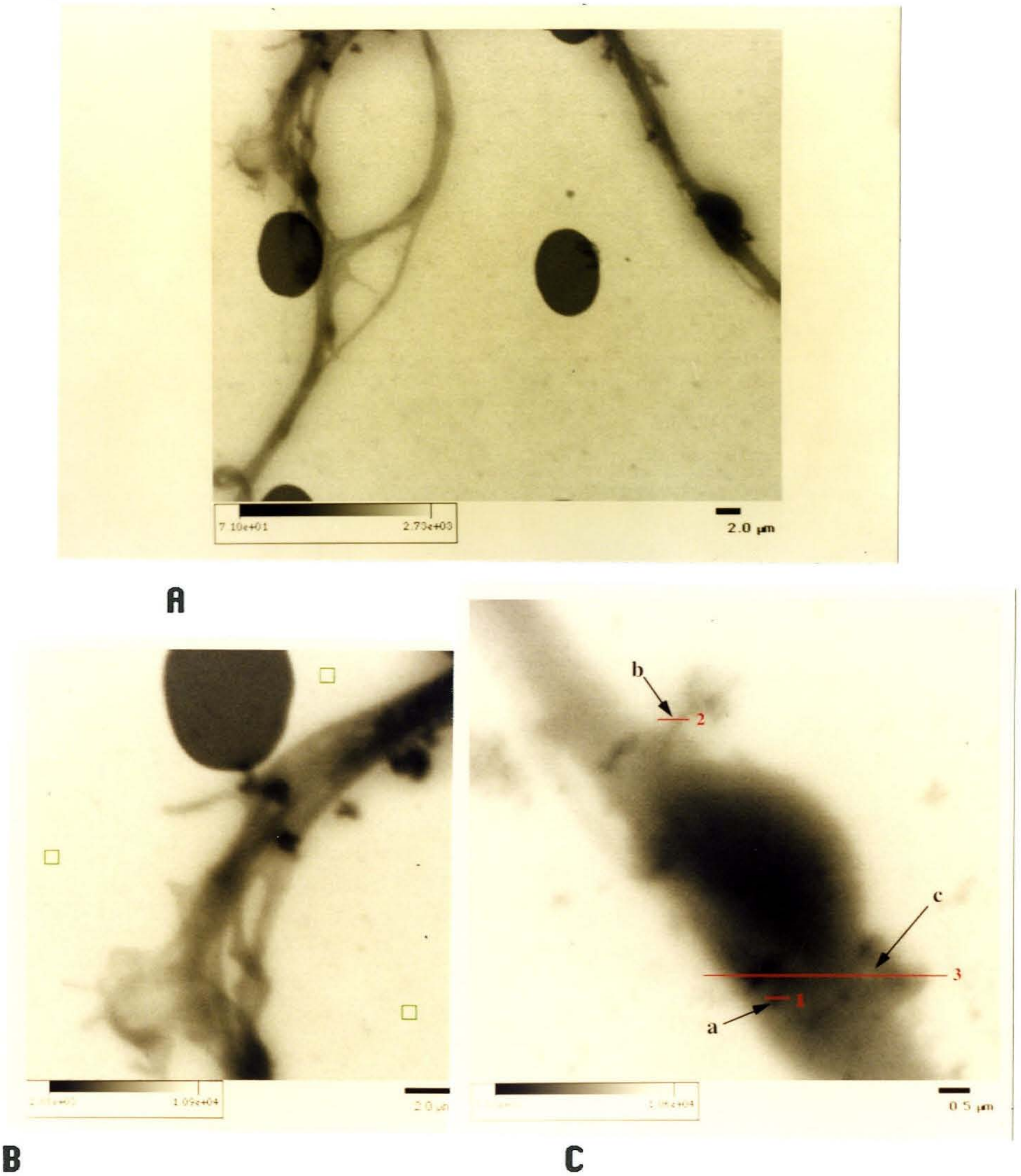

Figure 6.7 Fixed Neuron I A shows an image of two dendrites of a neuron B and C are higher resolution images of two sub regions of A. A is taken at 101nm/pixel and 10msec/pixel, achieving 2.31% noise. B is taken at 48nm/pixel and 10msec/pixel achieving 2.10% noise. C is a higher resolution image of the bulbous feature in A, taken at 19nm/pixel and 8msec/pixel, achieving 1.06% noise. C has labeled profiles, 1, 2, and 3 which are graphed in figure 6.11A. For the labeled structures in the profiles we have estimated a FWHM, **a** is 0.16µm, **b** is 0.19µm and **c** is 0.18µm.

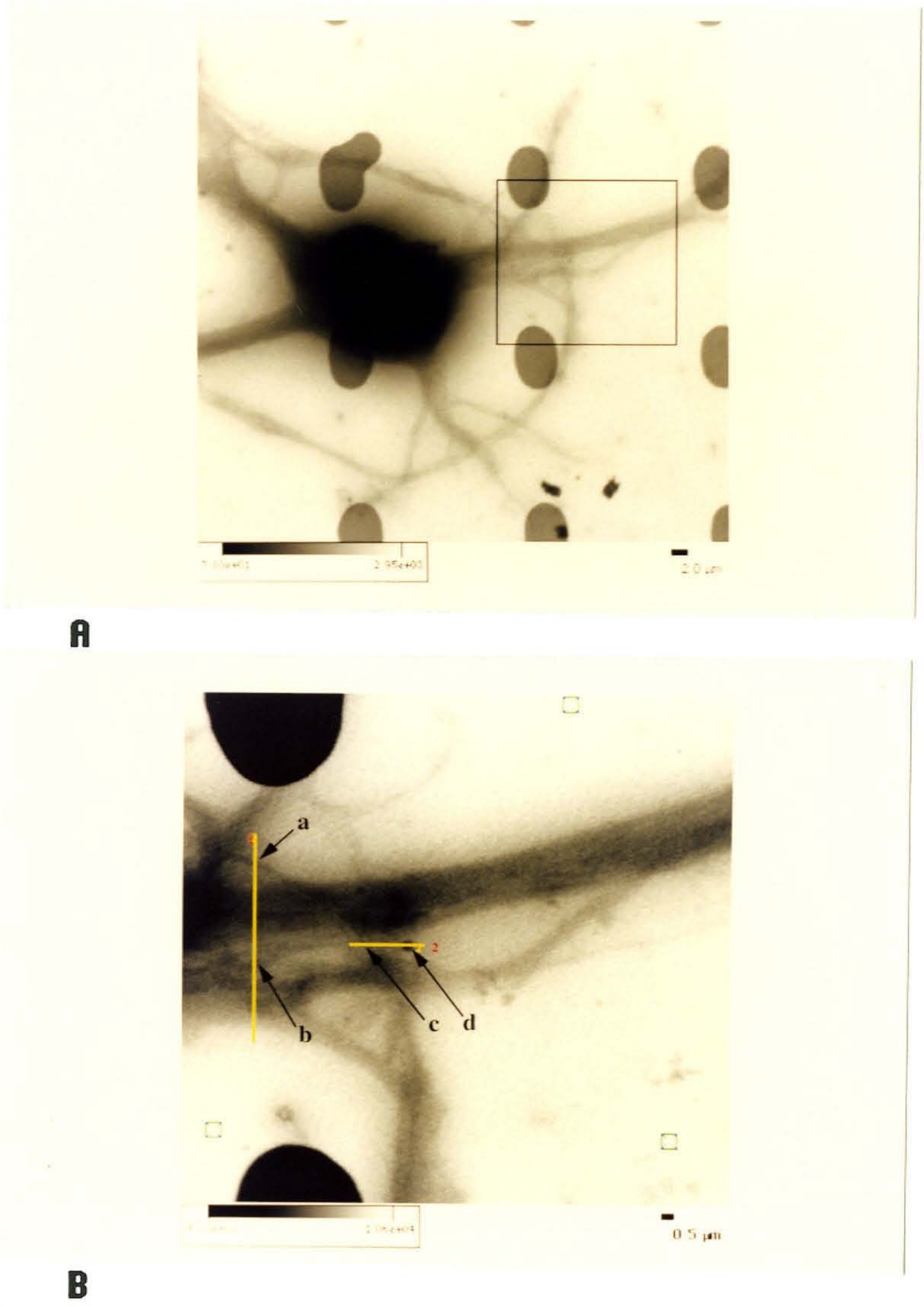

Figure 6.8 Fixed Neuron II A is an image of a neuron taken at 149nm/pixel and 3msec/pixel, achieving 1.73% noise. The neuron is near spherical, and shows no sharp features, as well as being bluured by a water droplet. However the processes of the cell are much thinner and do show some fine features. B is a high resolution image of the area outlined in A, it was taken at 48nm/pixel and 4msec/pixel, achieving 1.4% noise. Profiles 1 and 2 are graphed in figure 6.11B. The profiles show some sharp features, measuring FWHM, a is 0.25µm, b is 0.32µm, c is 0.13µm and d is 0.37µm.

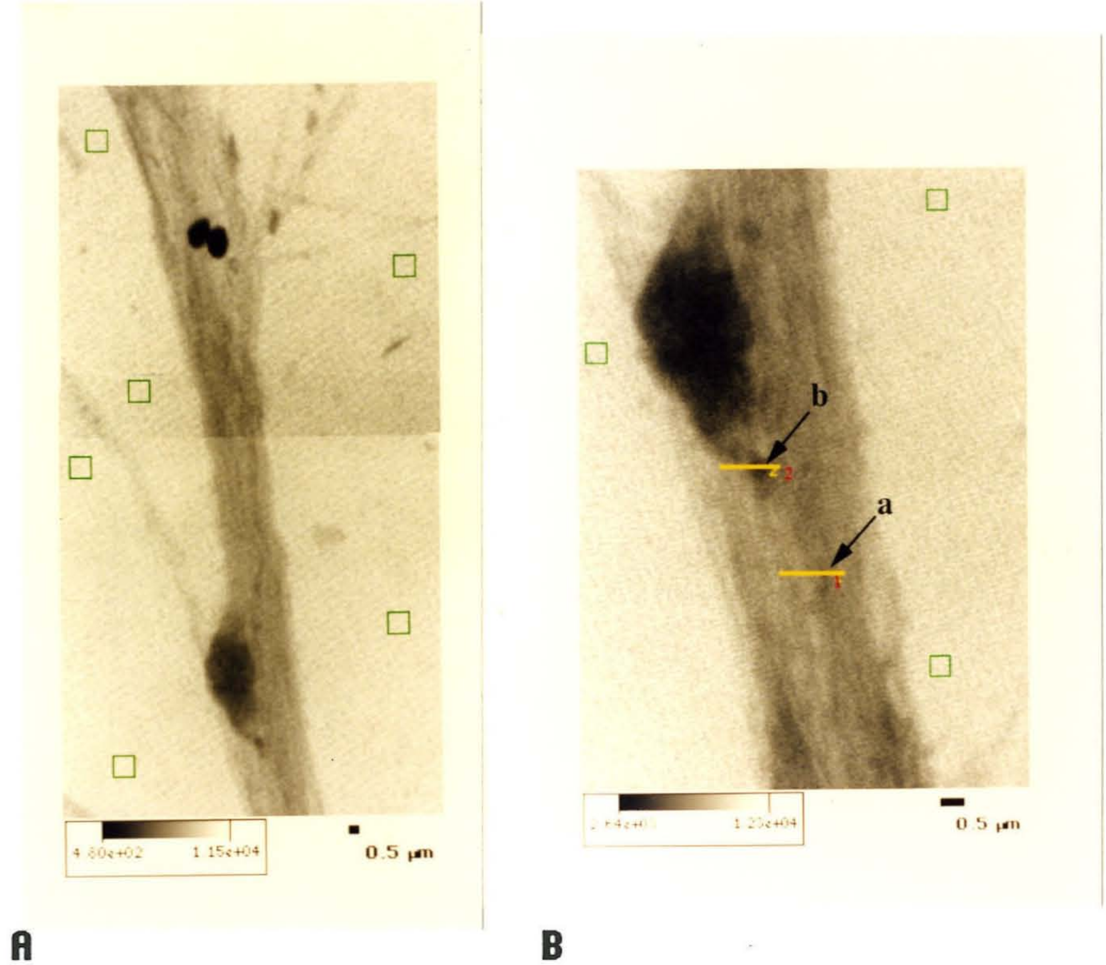

Figure 6.9 Fixed Neuron III A is a composite image of a neuronal dendrite, taken at 82nm/pixel, and 10msec/pixel. The image gave the dendrite an absorbed dose of 7×10^6 Rads. We estimate the dendrite thickness as .77µm. This image has a background noise of 4.25%. **B** is an close up of the swelling in the dendrite. It was taken at 34nm/pixel and 8msec/pixel. The **B** image has a background noise of 3.97%. There are two labeled profiles in B, they are graphed in figure 6.11C, in profile 1 we have a sharp feature a, with FWHM of .11µm, though it is very close to the noise level. Profile 2 crosses a larger granule at b with FWHM of .26µm.

6.3.1 Resolution and Noise for Fixed Cells

We've discussed in previous chapters the underlying resolution of the microscope. Considering the settings of the microscope that we used for these images we expect the underlying resolution of the microscope to be between 50nm and 100nm. However for several of the images above we used a pixel size of 95-100nm, and for any pixel size real discrimination among separate features will only appear somewhere above that size. With that said the real question is what size features are we able to see and observe quantitatively? In figures 6.10 and 6.11 we graph the profiles that were labeled in figures 6.4B, 6.6B, 6.7E, 6.8B and 6.9B. The estimated FWHM diameters of the features that the profiles cross are tabulated in table 6.1. We are clearly able to measure real features down to almost 100nm, with the acceptable background noise levels of the images above.

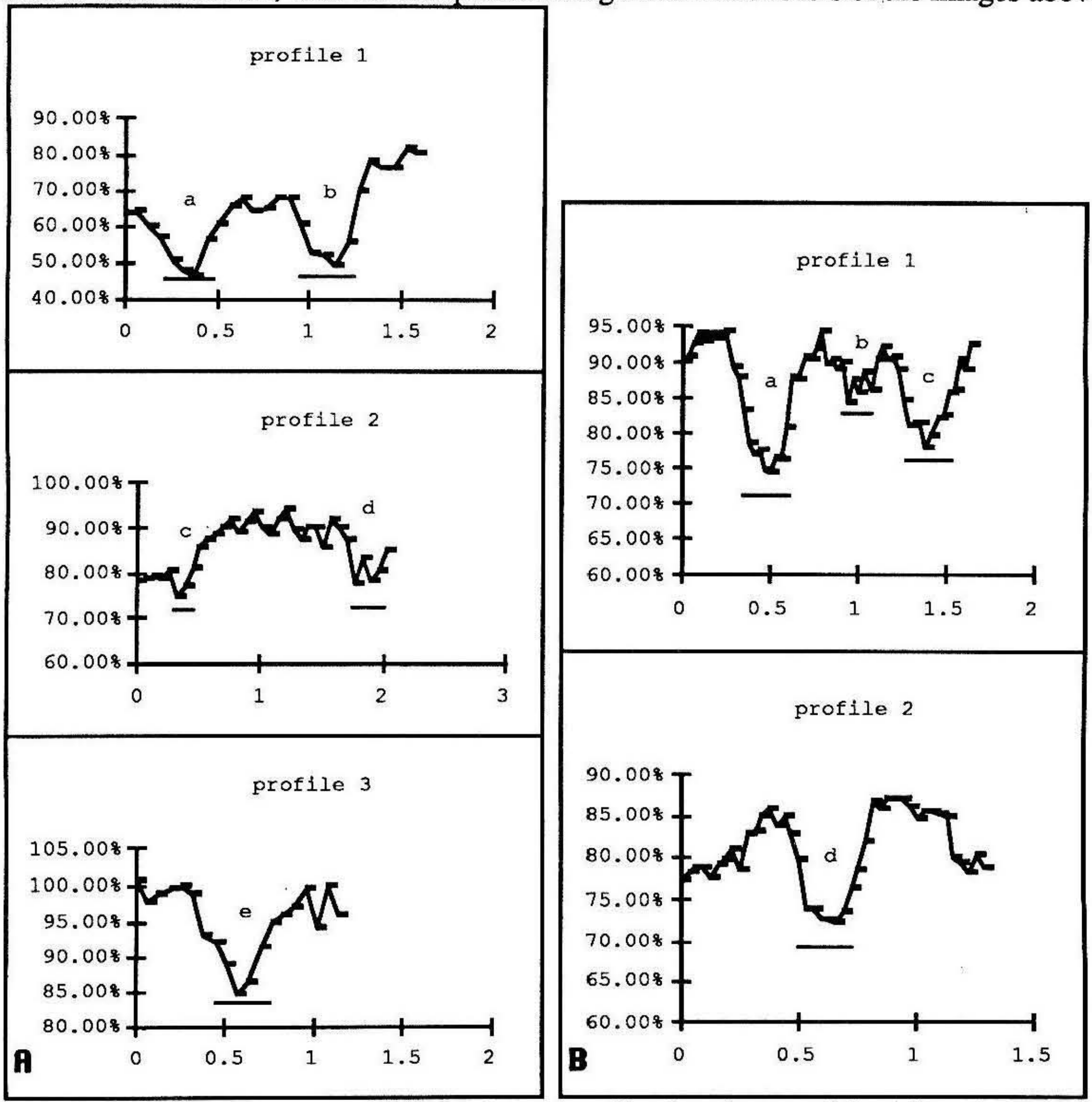

Figure 6.10 Feature Profiles I Several profiles from images of fixed fibroblasts. **A** is from figure 6.4B, **B** is from 6.6B. Numerical estimates for the FWHM diameters of the labeled features are listed in table 6.1. All labeled features are granules except for c in **A** which is the edge of a nucleus and e in **A** which is a process. The edge appears to be about 0.16μm. The process has FWHM of 0.28μm. The profile position axis is in μm.

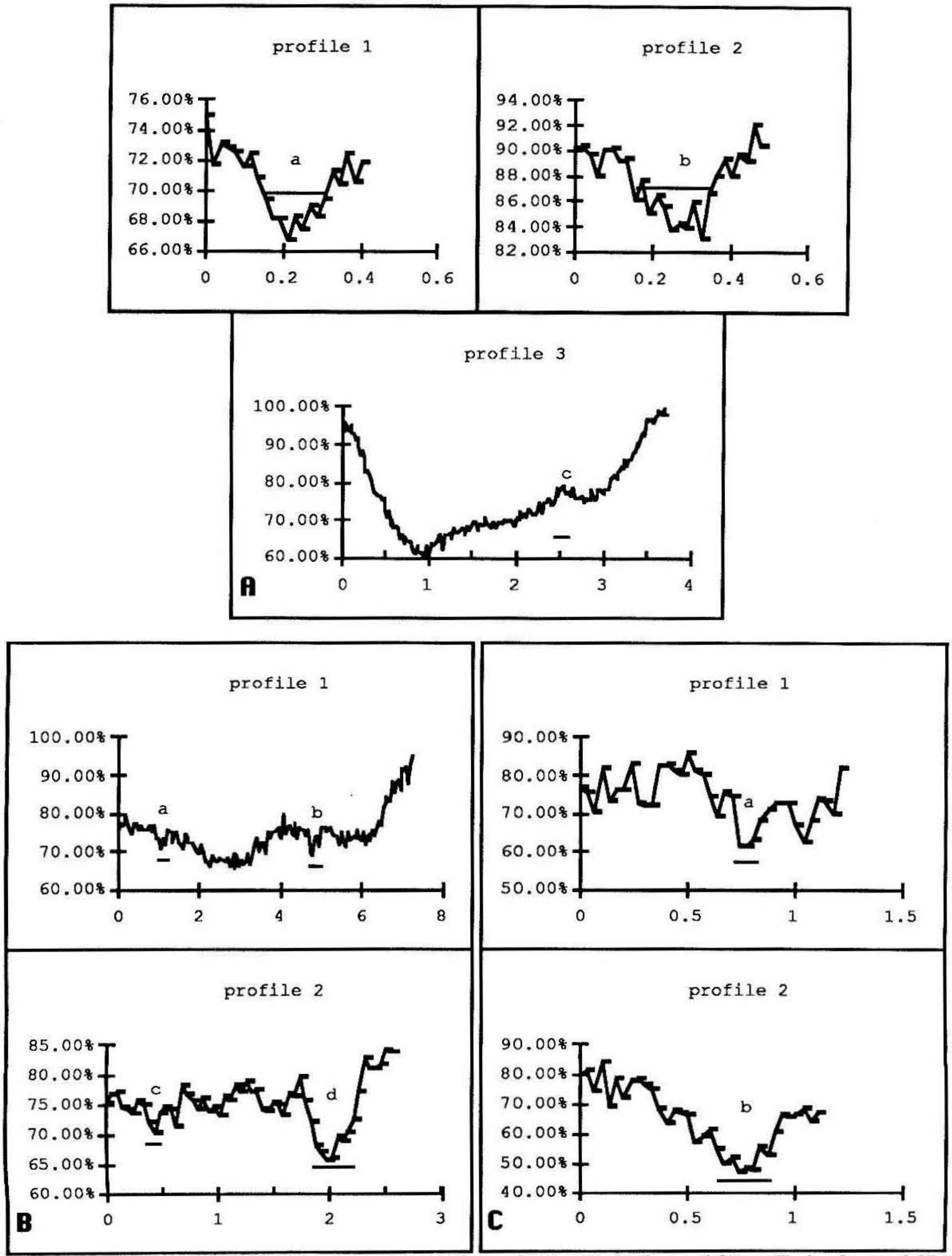

Figure 6.11 Feature Profiles II A is from 6.7C. B is from 6.8B. C is from 6.9B. Estimated FWHM sizes of labeled features can be found in table 6.1. The profile position axis is in μm.

Even more than the progress that has been made in resolution of STXM images, we have in this work reached practical levels of background noise. All the images shown in figures 6.2 - 6.9 have measured background noise levels of 4% or better, and some are down below 2%. (These noises are tabulated in table 6.3, near the end of this chapter.) This lets us observe features that give only 10% signals in transmission, and it essentially makes the images look as good to the eye as those we are used to from visible light microscopy.

Figure	From Image	Feature	FWHM (μm)	Feature type
6.10A	6.4B	a	.27	granule
		b	.27	granule
		c	.16	nucleus edge
		d	.25	granule
		e	.28	process
6.10B	6.6B	a	.30	granule
		b	.15	mitochondria?
		c	.30	granule
		d	.28	granule
6.11A	6.7C	a	.16	granule?
		b	.19	process
		c	.18	hole
6.11B	6.8B	a	.25	process
		b	.32	process
		c	.13	process
		d	.37	granule
6.11C	6.9B	a	.11	-?
		b	.26	granule

Table 6.1 Measured Feature Sizes A table of feature sizes and types for the profiles in figures 6.10 and 6.11.

6.4 Images of Un-Fixed Fibroblasts

One of the goals of x-ray microscopy has always been to image live cells, or as we sometimes call them, un-fixed cells. What we have succeded in doing is to put cells into the wet cell alive, image them with the STXM so that control (un-irradiated) areas appear intact, and the target cells appear undamaged (when observed in a phase microscope) 30 minutes after imaging. However the irradiated cells certainly received a lethal dose during imaging (about 10^7 Rads), and moreover showed gross damage (again in phase) 3 hours after irradiation.

In our efforts to follow the procedures just described we had more failures than successes, but we did acquire images of the three cells shown below. In figure 6.12A we show a region of the culture chip as viewed in a visible light phase microscope. In figure 6.12B we have the corresponding orientation image taken with the STXM. The target cells are labeled a, b and c in figure 6.12. In figures 6.13, 6.14 and 6.15 we show images of the target cells a, b, and c respectively. In each figure **A** is the STXM image, taken at 200x200 pixels, 95nm/pixel, and 5msec /pixel. **B** is an image of the same cell about 30 minutes after imaging with the STXM, and **C** is the same cell 3 hours after STXM imaging. In all three cases the 30 minute images show cells reasonably intact, that is having clean cell edges, and appear still attached to the surface. The 3 hour images all show a high level of gross damage, i.e., they look dead.

In each case the process of taking the STXM image for figures 6.13-6.15 gives the cells a dose of about 10^7 Rads. We can estimate the resulting damage caused by taking these images. In the cytoplasm of these three cells the damage is estimated to be 2%, 2% and 1% increase in transmission, respectively. This corresponds to about -6%, -5%, and -6% change in carbon column mass ($\Delta m/m$).

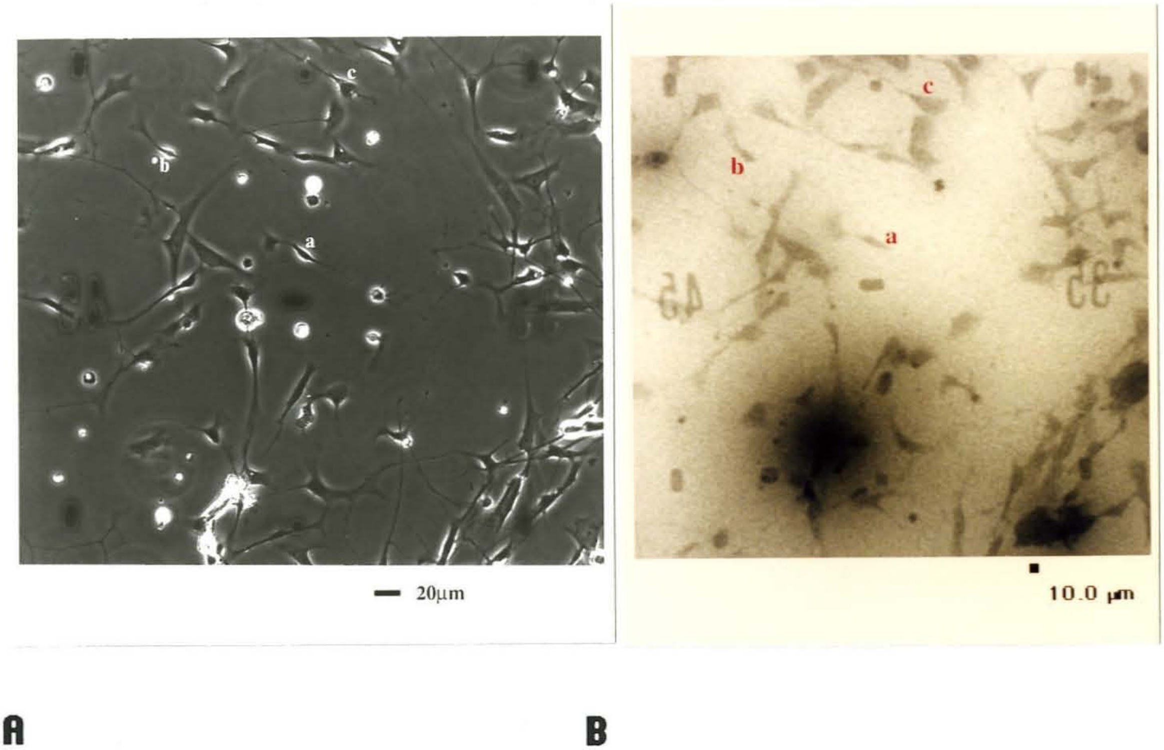

Figure 6.12 Un-Fixed Cell Orientation **A** is a visible light phase contrast image of the target region containing cells a, b, and c. **B** is the STXM orientation scan in the same region. **B** is taken at 1.993µm/pixel with a dwell time of 2 msec/pixel, it has a high noise level of 5%, and inflicts a low absorbed dose on the cells of about 10^4 Rad.

When we examine the cells 30 minutes after irradiation, using a conventional phase contrast microscope, we see that the cells look relatively good. These pictures are shown in figures 6.13B, 6.14B, and 6.15B. We expect the cells to look somewhat flattened and dark after cycling through the wet cell. About 3 hours later all the cells look seriously damaged or dead, as shown in figures 6.13C, 6.14C, and 6.15C. Now the dose we are talking about is far in excess of a lethal dose. In fact when we see decay by 3 hours we are seeing damage acting faster than through DNA damage, though it is not clear at all what the physiological underpinnings of the observed damage are. We cannot tell whether the first damage that we see is due to stopped metabolism from enzyme inactivation, or membrane destruction or actual cytoskeletal damage, or all of the above.

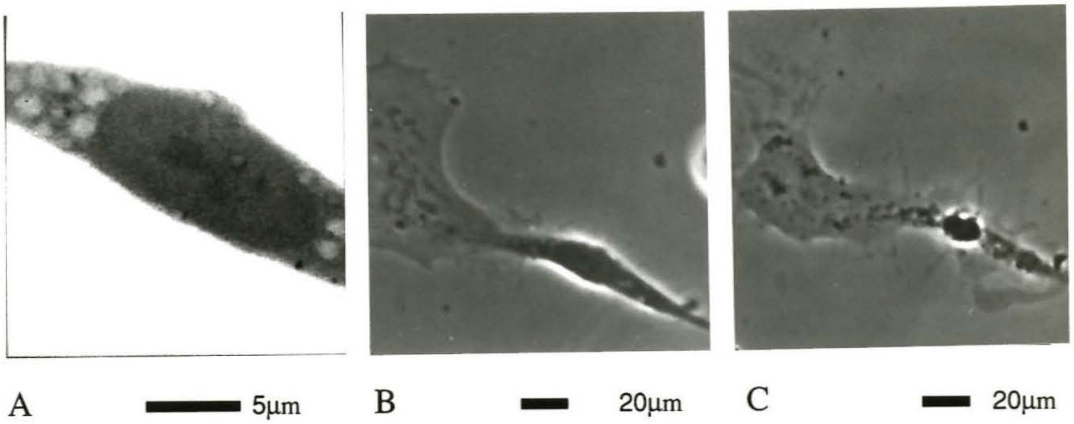

Figure 6.13 Un-fixed Cell I **A**, is the STXM image of cell a, taken at 95nm/pixel, with a dwell time of 5msec/pixel. The cell received an absorbed dose of 10^7 Rads. **B** is a visible light phase contrast image of the cell about 30 minutes after STXM imaging, showing the cell still relatively intact. **C** is another phase contrast image taken 3 hours after irradiation, showing extensive damage.

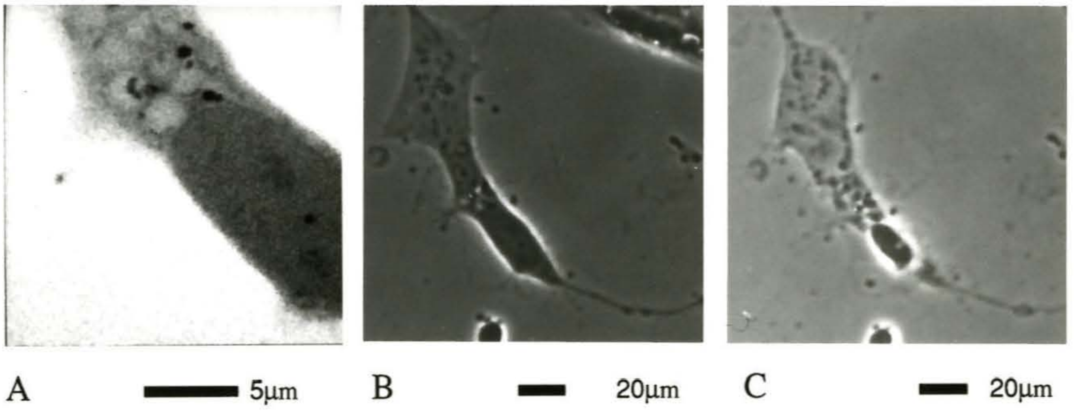

Figure 6.14 Un-fixed Cell II **A**, is the STXM image of cell b, taken at 95nm/pixel, with a dwell time of 5msec/pixel. The cell received an absorbed dose of 10^7 Rads. **B** is a visible light phase contrast image of the cell about 30 minutes after STXM imaging, showing the cell still relatively intact. **C** is another phase contrast image taken 3 hours after irradiation, showing extensive damage.

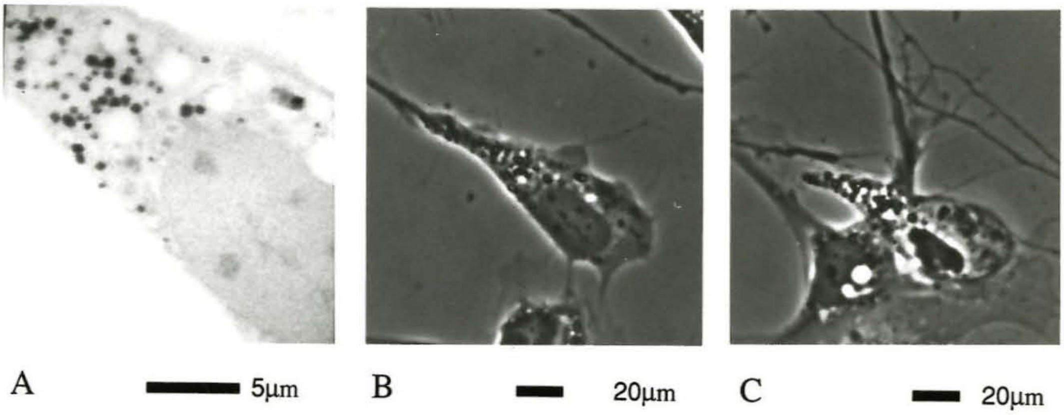

Figure 6.15 Un-fixed Cell III A, is the STXM image of cell c, taken at 95nm/pixel, with a dwell time of 5msec/pixel. The cell received an absorbed dose of 10^7 Rads. **B** is a visible light phase contrast image of the cell about 30 minutes after STXM imaging, showing the cell still relatively intact. C is another phase contrast image taken 3 hours after irradiation, showing extensive damage.

6.4.1 Resolution and Noise for un-fixed cells

In spite of the fact that we imaged these un-fixed cells in a manner that did eventually kill them, we have reached a resolution that should allow clear examination of sub-micron features, and separation of features, also at a submicron level. Figure 6.16 shows some profiles through the image of figure 6.15. The profiles clearly show features down to 0.3 μm, and separate them at similar distances. Estimated FWHM sizes of the features can be found in table 6.2. We believe that we can measure features down to 0.25μm The microscope, as shown above with fixed cells, is capable of somewhat better resolution, however we have not yet been able to reach those levels with un-fixed cells.

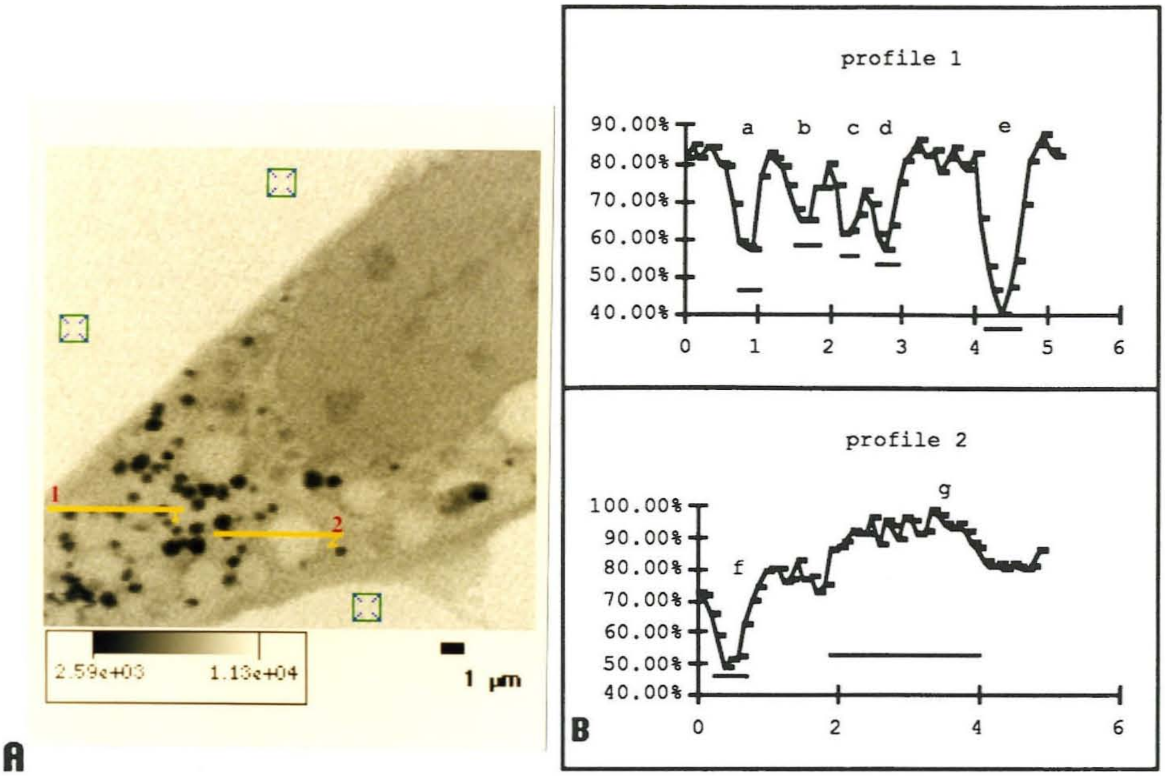

Figure 6.16 Un-fixed Cell Profiles A shows the cell from figure 6.15, with lines denoting two profiles through several granules. B shows those profiles. Profile 1 cuts through 5 granules a-e , and profile 2 cuts through a granule and a vacuole. Dimensions of labeled features are listed in table 6.2.

Figure	Feature	FWHM (µm)	feature type
6.16B	a	.42	granule
	b	.46	granule
	c	.23	granule
	d	.30	granule
	e	.56	granule
	f	.37	granule
	g	2.12	vacuole

Table 6.2 Un-fixed Feature Sizes FWHM sizes for the features profiled in figure 6.16.

The background noise that we have achieved for the un-fixed cells is also not as good as that for our fixed cell work. This is natural in view of the desire to minimize the dose given to these cells. The images 6.13A, 6.14A, and 6.15A, had noise of 2.97%, 3.43%, and 3.13% respectively.

6.5 Estimated Radiation Effects

Using the data and methods from chapter 5 we can estimate the effects on the cells of absorption of photons. The resulting numbers are given in two columns, labeled **ΔT** and **Δm/m**, of table 6.3. We estimate the effects of radiation on the observed transmission (ΔT), and on the equivalent column mass of carbon that could generate that transmssion (Δm/m). We use the quantity T_c as the sample transmission of each cell (in the column $\mathbf{T_c}$ in table 6.3). We find T_c by sampling a point in the cytoplasm of the cell, or a point in the thickest part of a dendrite that is not an identifiable feature, the object being to find a reasonable background number for the cell. T_c is usually found to be around 70% transmission. Using that transmission and the estimated incident count per μm^2 (the column $\mathbf{I_0}$ in table 6.3) we can calculate the absorbed energy in a 1 μm^2 column. Applying the ratio (of absorbed energy to equivalent carbon column mass lost) that we found in chapter 5 we get damage as mass fraction lost, Δm/m, and as change in transmission, ΔT. These quantities are listed in their respective columns of table 6.3. Δm/m is a negative percentage (since we lose mass), and ΔT is a positive percentage since we absorb less and thus transmit more as we lose column mass. As table 6.3 shows, when we image near dx=0.1μm the damage we get is ~1-4% ΔT, and usually 4-15% Δm/m. On going to higher resolutions the estimated damage jumps sharply to 50%-100% in terms of mass lost, i.e., in taking our highest resolution images we probably destroyed the cells. In particular the images 6.5B, 6.6B, 6.7C and 6.9B were very destructive.

	sd %	µm	msec	min	Å	%	%	Rads	%	µm	count	count/um^2
Fig.	**Noise**	**dx**	**τ**	**time**	**λ**	**ΔT**	**Δm/m**	**Dose**	**T_C**	**D_z**	**back**	**I_0**
6.1B	1.77%	1.993	4	4	33.77	0%	0%	23299	70%	1.2	3500	9.78E+03
6.2A	1.67%	0.095	10	8	33.77	4%	-15%	3E+07	70%	1.2	4200	1.07E+07
6.2B	1.96%	0.095	10	10	33.77	3%	-14%	3E+07	75%	1.0	3500	1.04E+07
6.3A	1.43%	0.126	14	17	36.4	1%	-7%	1E+07	76%	0.8	5900	4.35E+06
6.3B	2.49%	0.095	10	27	36.4	1%	-7%	1E+07	78%	0.7	2000	4.42E+06
6.4A	3.29%	0.095	5	NA	36.4	1%	-3%	6E+06	65%	1.2	2300	2.27E+06
6.4B	2.57%	0.063	12	8	36.4	2%	-8%	1E+07	65%	1.2	3600	5.63E+06
6.5A	2.37%	0.095	15	20	34	2%	-8%	1E+07	68%	1.3	2300	5.47E+06
6.5B	NA	0.032	20	13	34	18%	-60%	9E+07	68%	1.3	1300	3.68E+07
6.6A	1.62%	0.095	10	7	34.1	1%	-8%	1E+07	87%	0.5	5500	5.08E+06
6.6B	1.35%	0.032	10	7	34.1	9%	-69%	1E+08	87%	0.5	6100	4.48E+07
6.7A	2.31%	0.101	10	30	38.8	0%	-1%	2E+06	60%	1.3	2500	8.44E+05
6.7B	2.10%	0.048	10	20	38.8	2%	-5%	9E+06	60%	1.3	2500	3.50E+06
6.7C	1.06%	0.019	8	24	31.25	31%	-86%	2E+08	62%	2.0	6900	1.12E+08
6.8A	1.73%	0.149	3	8	31.25	0%	-1%	2E+06	66%	1.7	2700	8.02E+05
6.8B	1.40%	0.048	4	11	31.25	3%	-12%	2E+07	66%	1.7	3700	9.98E+06
6.9A	4.24%	0.082	10	13	36	1%	-5%	9E+06	77%	0.8	1000	3.11E+06
"	4.29%	0.082	10	17	36	1%	-4%	7E+06	62%	1.4	1000	3.09E+06
6.9B	3.97%	0.034	8	17	36	21%	-96%	4E+07	78%	0.7	800	1.36E+08
6.12B	5.00%	1.993	2	2	34.1	0%	0%	9418.4	70%	1.2	560	3.90E+03
6.13A	2.97%	0.095	5	3	34.1	1%	-6%	1E+07	75%	0.9	1300	4.19E+06
6.14A	3.43%	0.095	5	3	34.1	1%	-6%	1E+07	74%	1.0	940	4.19E+06
6.15A	3.13%	0.095	5	3	34.1	1%	-6%	1E+07	79%	0.8	1100	4.16E+06

Table 6.3 Image Facts Assorted facts about the images in this chapter. **Fig.** is the label for the image. **Noise,** is the relaative standard deviation of the counts recorded in a 12x12 square located in a background region of the image. **dx** is the size of a pixel in µm. **τ** is the dwell time in each pixel in msec. **time** is an estimate of how long it took to record the image. **λ** is the wavelength in Å. **ΔT** is the estimate of damage as change in transmission caused by irradiation, when imaging ΔT should be compared with Noise. **Δm/m** is damage as fractional change in column mass of carbon due to irradiation. Both **ΔT** and **Δm/m** are calculated following the results of chapter 5, from observed absorption in the pixel column and I_0. **Dose** is the dose in Rads of the cell using the thickness estimate D_Z, it includes the absorption in the water in that thickness and that model. **T_C** is the transmission observed at one point in the cytoplasm of the cell, usually about 70%. **D_z** is an estimate of the thickness of the cell, from T_c and the assumption that T_c is due to carbon at 0.1gm/cm^3 (i.e., a model of the cell as about 1gm/cm^3 water + 0.1gm/cm^3 carbon.) **back** is the observed counts per pixel in the 12x12 background region of the image that was used to measure Noise. **I_0** is the estimated incident photons/µm^2 on the cell.

In the case of the un-fixed cells (live on entering the STXM) we quote damage arrived at by the methods of chapter 5, though we do not in fact have equivalent data for un-fixed cells. Still the notion that fixed cells are tougher than live ones is not unreasonable, especially at high doses, and so we might take these numbers as lower limits of expected damage. When we calculate that the column mass change is about -5% for the un-fixed cells we are estimating that 5% of the Carbon atoms have been lost. Asking what the detailed effects of 5% loss of mass are on the membranes or the cytoskeletal structures of a cell, is beyond the scope of this dissertation. Further work with simpler structures, perhaps isolated granules, may illuminate this question.

6.6 Conclusion

This chapter shows a sample set of images which demonstrate the state of the art in whole cell imaging with soft x-rays. We have also tried to show the flexibility of the microscope, in terms of operating from the scales at which one looks at whole cultures (100-200μm, or more, in the field of view) to the scale at which one looks at whole cells (20-30 μm in the field) down to our highest resolution scale (perhaps 5μm full field), all with appropriate pixel size. For fixed whole cells we have taken images at theoretical resolutions of ~50-75nm, and in practice have measured FWHM of features down to near 100nm, without any exotic processing. For un-fixed (i.e., initially live) cells we have imaged with 100nm pixels and measured features down to 250nm. However, the initially live cell work has not been reproduced beyond the three cells shown here. Our set of procedures for handling live cells is not yet developed to the point where it is reliable. What we have done with live cells may best be considered in the nature of an existence proof, and we hope that improvements in technique will let this be done reliably.

6.7 Chapter 6 References

---

[1] C. Jacobsen, S. Williams, E. Anderson, M.T. Browne, C.J. Buckley,D. Kern, J. Kirz, M. Rivers, and X. Zhang, "Diffraction-Limited Imaging in a Scanning Transmission X-ray Microscope," submitted to Optics Communications (1991).

7 Elemental Analysis

One of the potential features of x-ray microscopy is the ability to do elemental analysis on wet biological samples. Such analysis might provide elemental desity maps at the same resolution as the basic imaging discussed in the previous chapters. This possibility of elemental analysis arises from the nature of contrast in transmission x-ray microscopy. We measure directly the absorption of all the elements in each pixel of the sample, and we can tune the microscope to take images at any wavelength from 20Å to 50Å. It is convenient that several of the elements making up biological specimens have differently varying x-ray absorptions in this region. In particular, this region contains the K edges of oxygen, nitrogen and carbon, as well as the L edges of Calcium. Theoretically if a sample contained N elements, and we could take N images of the sample at N different wavelengths then, assuming the NxN matrix of mass absorption coefficients at those wavelengths is non-singular, we could decompose the set of N images into N elemental column mass images. One column mass image for each component of the sample. This chapter is really about our first attempt at a two component decomposition. We'll discuss our current results and make some remarks about the fundamental and operational limitations of elemental analysis with the BNL STXM.

7.1 Introduction to Elemental Analysis

In figure 7.1 we show the mass absorption coefficients of several elements of biological interest, oxygen, carbon, nitrogen and calcium (in 7.1A), as well as averages for Lipid, Protein, Water and DNA[1] (in fig 7.1B). Important features of these curves are the absorption edges: O at 23Å, N at 31Å, Ca at 36Å, and C at 43.5Å.

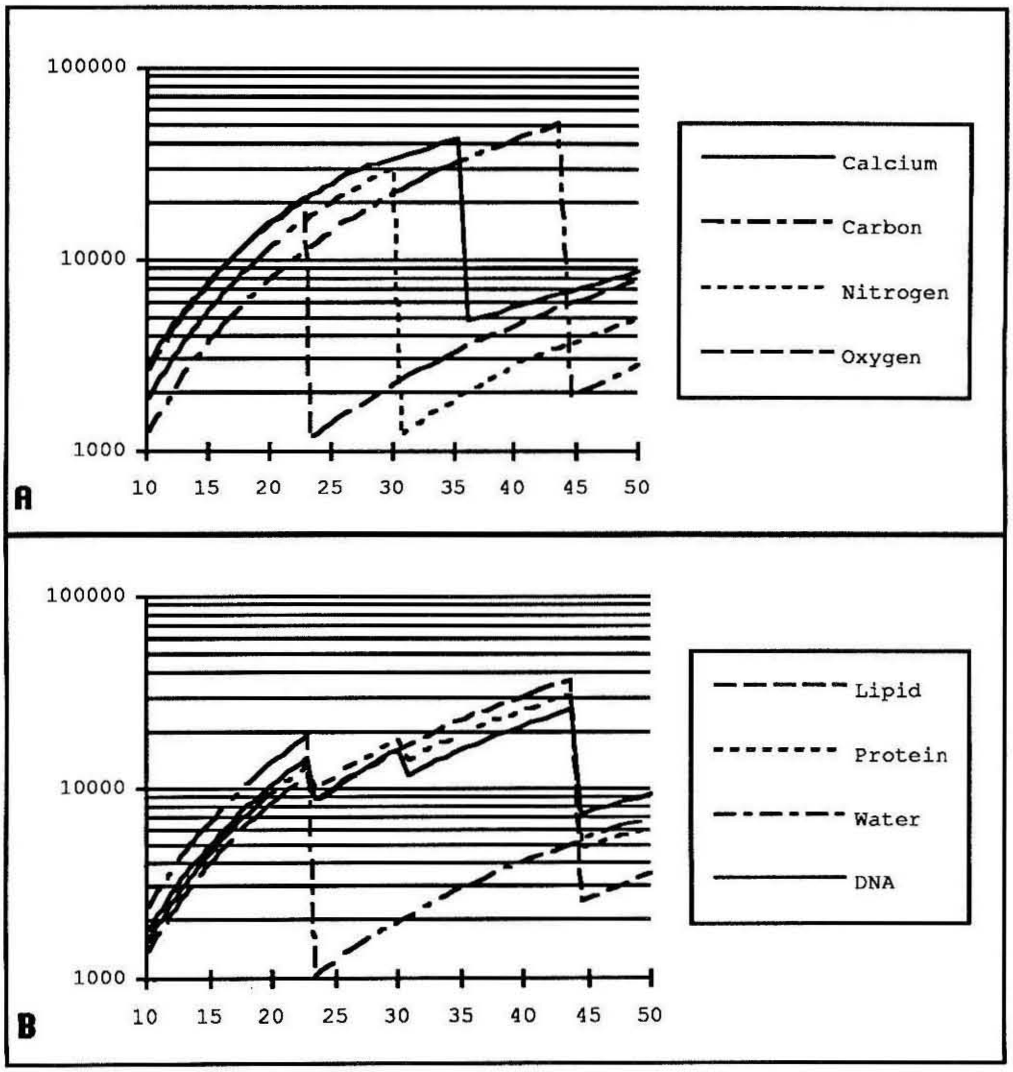

Figure 7.1 Mass Absorption Coefficients **A**, is a graph of the mass absorption coefficients of the elements of interest that make up tissue culture cell samples: carbon, oxygen, nitrogen, and calcium. **B**, a graph of mass absorption coefficients of several molecular components of cell samples: Lipid, Protein,Water and DNA .

The simplest form of elemental analysis is subtraction across an edge, in which an image is taken just above, and just below the edge, and the two images are normalized together and subtracted. This procedure relies on the fact that near any elemental edge, all other elements are only slowly varying, so the absorption due to contributions from all other elements drop out on subtraction. This has been done for calcium biomineralization samples by others.[2,3] This method of elemetal analysis uses a one component view of the sample (the significant is the one with the edge, the rest are background).

We are interested in analyzing the distribution of the elements that make up the bulk of biological materials, carbon and oxygen. Unfortunately the C and N edges are accompanied by gross reduction of the available flux in the STXM. In the case of the carbon edge this is due to carbon present on all optical surfaces of the beamline (the mirrors and the SGM). Near the nitrogen edge the flux is reduced by the nitrogen in the silicon nitride windows (there are after all five of these between vacuum and the inside of the PC), as well as in the atmosphere.

7.2 Flux Available at Various Wavelengths

We discussed the way the microscope is tuned to use different wavelengths in Chapters 2 and 3. The flux through the dry wet cell, as observed in the PC, is shown in figure 7.2. This figure graphs the observed flux rate in the PC for undulator settings which center the fundamental peak of its output near the C-edge (gap = 41.2mm) and near the N-edge (gap = 50mm.) The important facts are first, that no one gap setting covers all desirable regions, second that the flux is very depressed around the C-edge so that the nearest peaks of flux are at 40Å and 44Å a full 4Å (or 10% of λ) apart, and third that there is almost no flux just below the N-edge for several angstroms. So while the optics of the microscope can be tuned over 20Å to perhaps 50Å, we can really image from about 31Å to 40Å and with less flux, above 44Å.

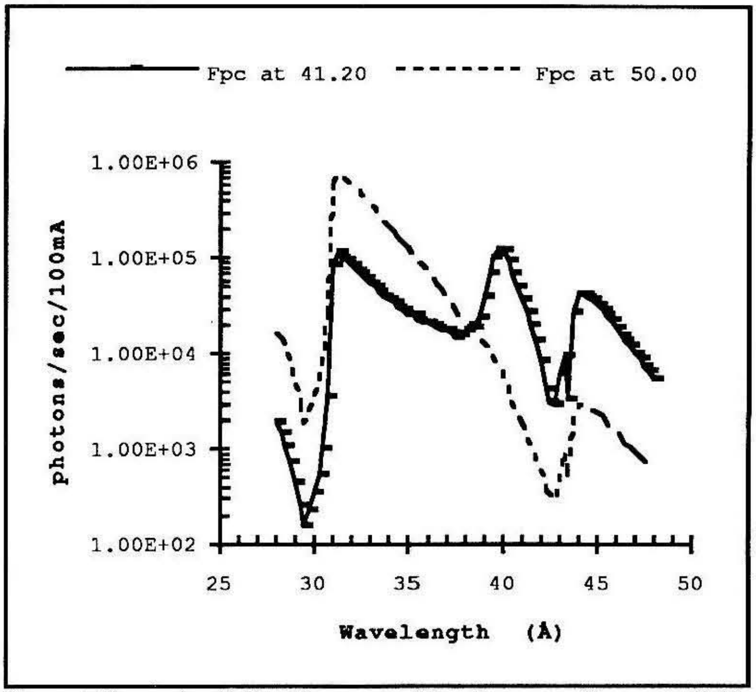

Figure 7.2 Available Flux The flux rate, F_{PC}, available from undulator settings placing its fundamental over the C-edge (41.2mm gap) and the N-edge (50mm gap.)

Since we cannot work directly on the carbon edge, we must use a larger step in wavelength. Both the carbon and oxygen absorption will change over any step of several Å. Therefore we use a full two component decomposition. Such a decomposition could be in terms of carbon and oxygen, or protein and water. The relation between transmission and column mass may be posed as a system of equations. For a given pixel, and a step in wavelength from λ_1 to λ_2 we have the system of equation 7.1 (in this case we use C and O). These equations are solvable pixel by pixel if the matrix of equation 7.2 is non-singular. The solution has the form of equation 7.3. Since the ρ's vary from pixel to pixel, equation 7.3 gives us two column mass images. One for carbon and one for oxygen in this case.

$$
\begin{aligned}
-\ln(T(\lambda_1)) &= \mu_C(\lambda_1)\rho_C + \mu_O(\lambda_1)\rho_O \\
-\ln(T(\lambda_2)) &= \mu_C(\lambda_2)\rho_C + \mu_O(\lambda_2)\rho_O
\end{aligned}
\qquad [7.1]
$$

$$
\mathbf{M} = \begin{bmatrix} \mu_C(\lambda_1) & \mu_O(\lambda_1) \\ \mu_C(\lambda_2) & \mu_O(\lambda_2) \end{bmatrix} \qquad [7.2]
$$

$$
\begin{pmatrix} \rho_C \\ \rho_O \end{pmatrix} = \mathbf{M}^{-1} \begin{pmatrix} -\ln[T(\lambda_1)] \\ -\ln[T(\lambda_2)] \end{pmatrix} \qquad [7.3]
$$

Our ability to solve the two component system of equations, depends on the matrix M, of equation 7.2. In order for the system to be solvable we must have the mass absorptions of our components vary differently over the step from λ_1 to λ_2.

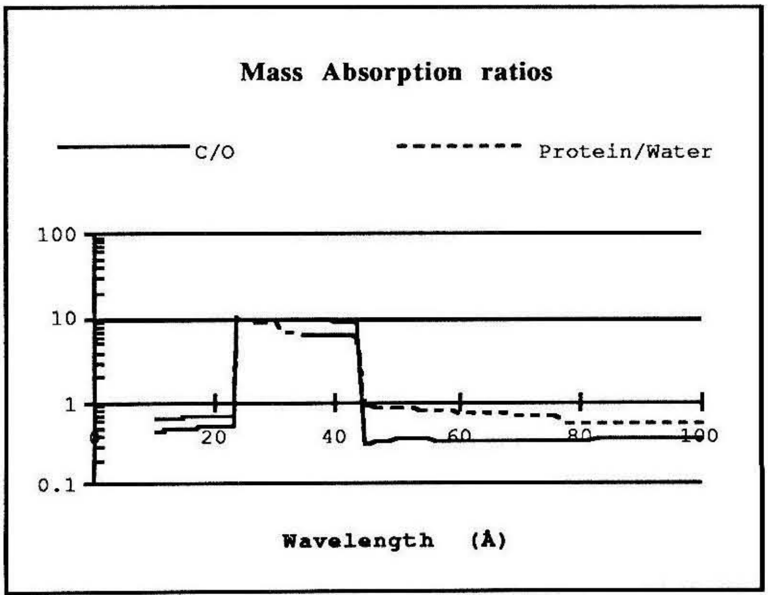

Figure 7.3 Mass Absorption Ratios Ratios of two pairs of mass absorption coefficients.

Figure 7.3 illustrates the wavelength dependence of the change in mass absorption. In it we graph the ratios μ_C/μ_O and μ_P/μ_W. A choice of λ_1 and λ_2 should be made to maximize the change in these ratios from the wavelength step. Important features of the figure are that there is some change in ratio if λ_1 and λ_2 are both in the water window, or both outside it, but the greatest change to be obtained involves stepping across the carbon edge or oxygen edge.

7.3 Operational Issues

In order to produce the transmission images for a decomposition we have established a basic procedure. We select two λ_i for the wavelength series (there could be more than two, though we have not successfully analyzed such a complex series). We set the undulator gap to give the maximum flux over our series range. We place the OSA appropriately bearing in mind that the OSA will limit the maximum step (λ_2 - λ_1), as we discuss below. We find focus on a region of the sample chip, near the cell, for each λ_i , and record the $STXM_Z$ coordinate, z_i, of each plane of focus (this allows us to get close to the desired image planes by dead reckoning). Then we are ready to image. Ideally we cycle the wet cell at the beginning, and get the whole series in one cycle (though typically we have taken more than one cycle to acquire a series). The series is taken by starting at the shortest wavelength image (largest working distance) and working up in wavelength. For each λ_i we go to the recorded z_i and find focus with a focus scan and take the image.

In trying to take wavelength series, and perform elemental decompositions, we must line up the images taken at each λ_i. It is important to have alignment marks in the sample itself, they should be sharp, and ideally there should be three of them. Such marks could be features in the sample if they show up in all images, or marks on the sample substrate. If we have three of them we can align the images in software (ObjectImage will do this) with a general linear transformation (rotations, stretches and offsets). Two marks will give just stretches and offsets, while a single mark will only give us an offset. In the series of figure 7.5 and 7.6 we had only one alignment mark (a sharp piece of debris) which, fortunately, was sufficient.

7.3.1 Placement of the OSA

The need to be able to shift in λ and z requires that the OSA be correctly placed to give us access to the full range in λ that we desire. That means the OSA must have been placed so that at small f (larger λ) we do not lose our working distance, and at large f (smaller λ) the OSA does not clip the x-ray focus cone. Operationally we must place the OSA in its optimum place at each change of the gap, and we cannot necessarily use the full range of the undulators' peak without changing the OSA position--an irritating and time consuming task, at present (at the very least it involves removing the sample).

7.3.2 Errors of Image Alignment

A consequence of working at different wavelengths is that it always involves a shift in $STXM_Z$, typically many microns. This always causes some lateral shifting of the images, and in fact causes the two images to be misaligned. We will always need to align the images in software, a task that cannot be done perfectly, even with an arbitrary linear transformation. Some of this misalignment is well understood, being due to a 10-30mradian (1-3%) skew of the stepper z-axis from the x-ray z-axis, causing x and y offsets in images of different λ. Other types of misalignment, that appear as scaling changes or rotations are not so well understood, though we believe they are associated with the pzt stage motion. However, we must remark here that the z shifts associated with misalignments are typically 100 to 1000 times the pixel size in the images so even 0.1% to 1% errors can be observed (all too well). This is to say that though the stage alignment is quite good, as we evalulate it with a single image, the test of aligning images after a z step is severe.

7.4 Image Normalization and Units

In order to form the transmission T, of equation 7.1, we must perform a background normalization on the transmission images taken at λ_1 aand λ_2. In order to form a meaningful system of equations the two images must be normalized together, that is using the same three background regions (as in chapter 3). When this is done, the transmissions that make up the image are, as usual, scaled to have 100% transmission in the background regions. And therefore by normalization the ρ's are zero in the background regions. This is very important , it means that the ρ of the column mass images that we produce is column mass relative to whatever is in the background normalization regions.

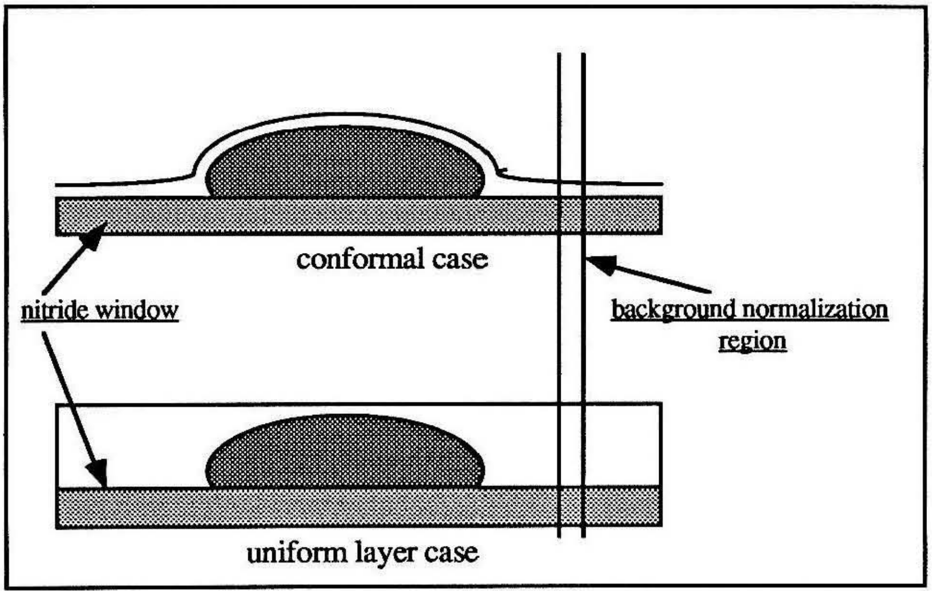

Figure 7.4 Water Layer Models A drawing illustrating the possible sample environments to be found in the caltech wet cell. In the conformal case the cell is coated with a thin conformal layer. Alternatively the liquid layer may be uniform and thicker than the cell. These are meant to be cases for analysis, the actual layers we get in the wet cell are probably less uniform and are certainly somewhat variable from fill to fill. The column on the right represents a background normalization region.

The question will arise, what do we have in the background regions? We do not have very good control of the sample environment in those regions, so we go back to the diagram of the sample in a Caltech wet cell. In our wet cell the sample is coated with an uncontrolled medium layer. This may be seen in figure 7.4, in which we sketch two possible models for the drained cell environment, the "conformal coating" and "uniform layer". These two models are extreme cases of course, and we really expect to find some intermediate situations (and some variation from fill to fill).

The two cases in figure 7.4 can help us understand the normalization of the column mass ρ that is calculated in elemental decompositions. If we are in the conformal case, then the ρ's in the background region are $\rho_C=\rho_O=0$. In that case the ρ's deduced through equation 7.3 will be the true column mass on the sample, both ρ_C and ρ_O are positive. But, if we are in the uniform layer case then we have background ρ's of $\rho_C=0$ but $\rho_O \sim D\text{x}10^{-4}\text{gm/cm}^2$, where D is the thickness of the water layer in μm. (This is approximatly the mass of oxygen in a column of water D μm high.) Now one implication of this is that the calculated ρ_C is still the true carbon column mass in the sample, but now ρ_O is the difference between the oxygen in the sample and in the background column. As a result, if the cell materials have protein or lipid displacing water we can expect to find pixels in the sample with less oxygen (or water) than is present in the background column. In that case we can expect the calculated ρ_O to be negative.

In essence the decomposition requires that the transmission images must be normalized together, and the resulting calculated component column mass images (ρ_C and ρ_O in eq. 7.3) have in each pixel the column mass of their component relative to the column mass of that component in the normalization regions.

7.5 Image and Decomposition

Figure 7.5 shows a transmission image of a fixed chick DRG fibroblast, taken at λ=40.3Å, the rectangle outlines the region we analyze and decompose in the images of figure 7.6 and 7.7. Several facts about the cell of figure 7.5 can be calculated following the methods of chapter 5. We estimate the thickness D_z=0.7µm, damage ΔT=0.03, damage Δm/m=-0.133, and the absorbed dose=2x10^7 Rads. Figure 7.6 is a pair of transmission images, normalized together, of the region outlined in figure 7.5. The pair is labeled by the wavelength at which the images are made, λ=40.3Å (where carbon absorbs a lot) on the left and λ=44.1Å (where carbon does not absorb much) on the right.

As we see in figures 7.5, and 7.6 a cell with plenty of structure on the absorbing side of the carbon edge can have almost no sharp structures on the non-absorbing side. This is consistent with the uniform layer model of the liquid coating in the wet cell. With a conformally coated cell, even without any carbon absorption at all we would expect to see a signal at the cell edge due to its water content.

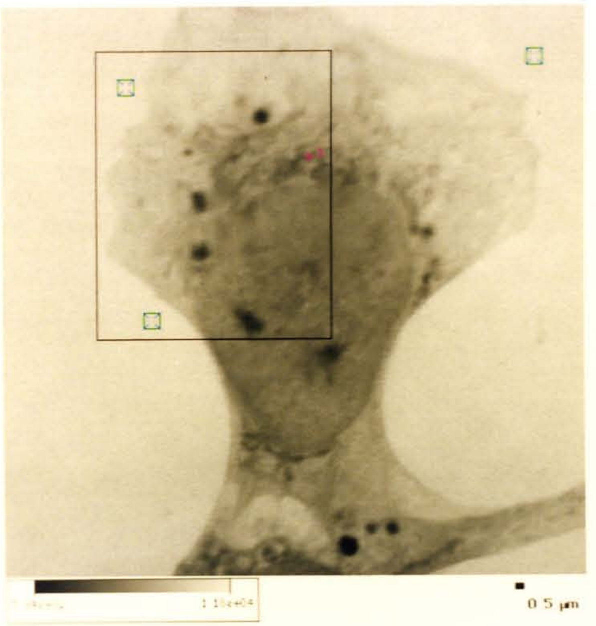

Figure 7.5 Fibroblast at λ=40.3Å A transmission image of a chick fibroblast taken at λ=40.3Å. The rectangle illustrates the more closely analyzed region of figure 7.6 and 7.7. The red cross is a mark on a piece of opaque debris that is used to align this image with another image of this cell taken at λ=44.1Å.

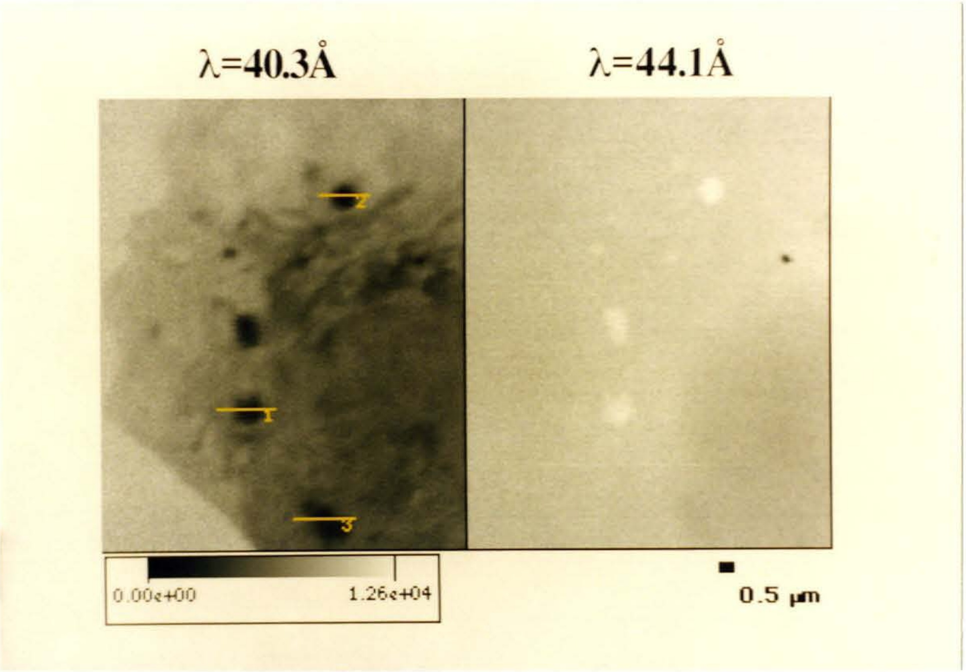

Figure 7.6 Transmission Image Pair The figure shows transmission images at λ=40.3Å and 44.1Å of the region outlined in figure 7.5. These images are cut from the image in 7.5 and its matching image taken at λ=44.1Å. The density (grey) scale in **B** is scaled to T=100%=10000. The three labeled profiles are in figures 7.8 and 7.9.

The image on the right of figure 7.6 which is taken at λ=44.1Å, on the non-absorbing side of the carbon edge, has several granules that have transmission of more than 100%, after normalization. These are the white structures with sharp edges in the image. Since these features correspond to very dense granules when imaged on the absorbing side of the edge (in the image on the left of figure 7.6) they may be examples of the displacement of water by carbon, leading to less water over pixels in those features than in the background columns. The existence of some features with normalized transmission greater than 100% is more evidence for a uniform layer of liquid in the wet cell.

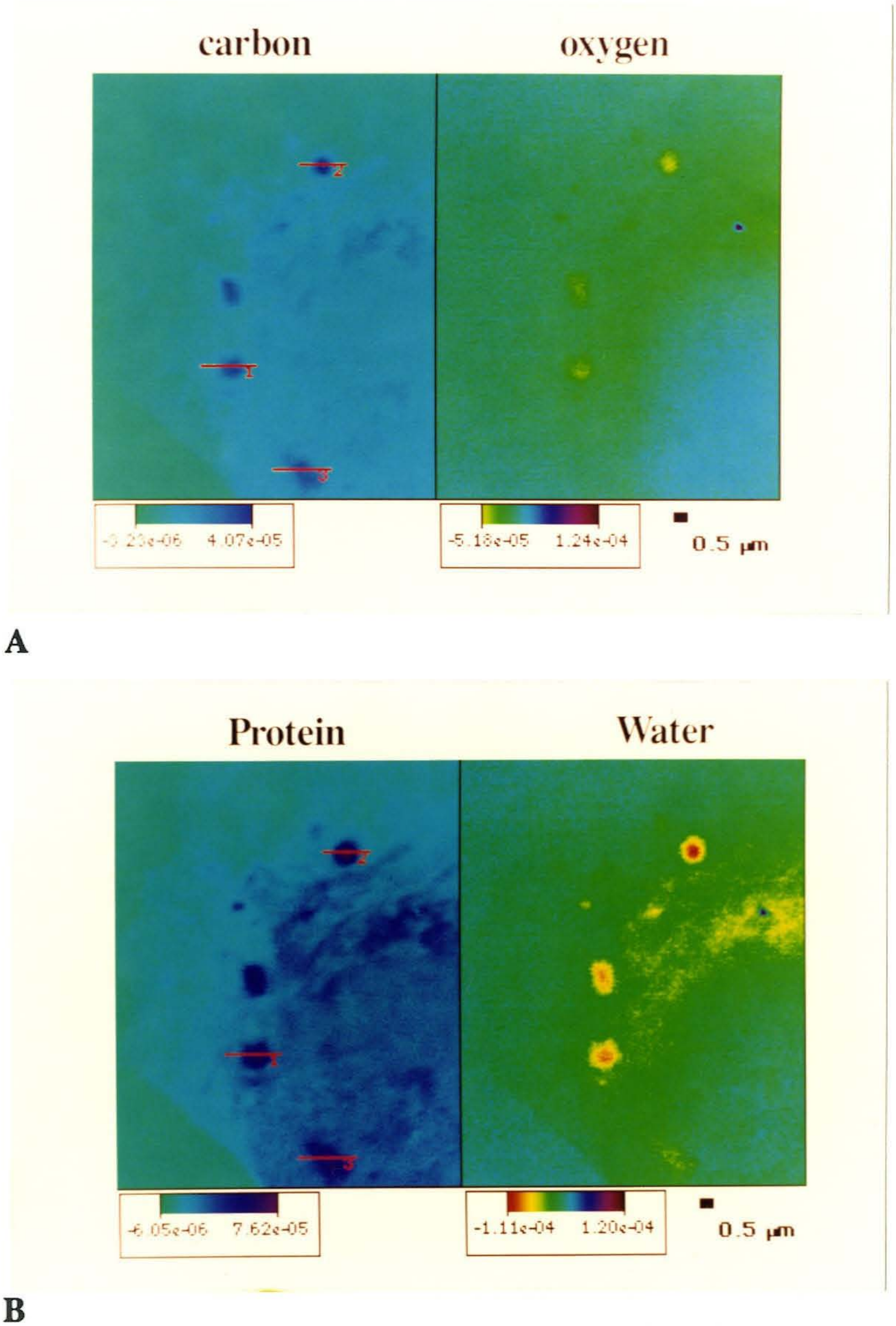

Figure 7.7 Decomposed Images A is the decomposition of figure 7.6 into carbon and oxygen column mass images. B is the decomposition into protein and water column mass images.

Figure 7.7 shows decompositions of the image pair of figure 7.6 into carbon and oxygen maps (figure 7.7A) and protein and water maps (figure 7.7B). These decompositions are also consistent with a view that we have a uniform liquid layer, and that organics can displace water. In figure 7.7 the lower left corner in each image is a region of unobstructed nitride window, and it has transmission near background in both images of figure 7.6. In the decompositions that background region has column mass near zero for both carbon (or protein) and oxygen (or water). Each image of figure 7.7 has a color scal from its minimum to its maximum. Greenish-light blue is zero, the full color scale runs from red (which is $-1.1\text{x}10^{-4}\text{gm/cm}^2$) to black (which is $+1.25\text{x}10^{-4}\text{gm/cm}^2$). The oxygen (or water) density is negative throughout the cell, and the carbon (or protein) density is positive. Just what we expect from a uniform water layer as thick as, or thicker than, the cell in a situation in which water could be displaced by carbon or protein.

7.5.1 Observed Values of Column Mass

In figures 7.6 and 7.7 we mark three profiles through dark features in the transmission image at λ=40.3Å. Profiles 1 and 2 section granules that exhibit T>100% in their λ=44.1Å image. Profile 3 sections an feature that appears equally dark in its λ=40.3Å image but does not have T>100% in its λ=44.1Å image. Referring back to the whole cell image in figure 7.5 we can see that the feature of profile 3 is in the nucleus and may be a nucleoleus. The profiles are in figures 7.8 (profiles 1 and 2) and 7.9 (profile 3).

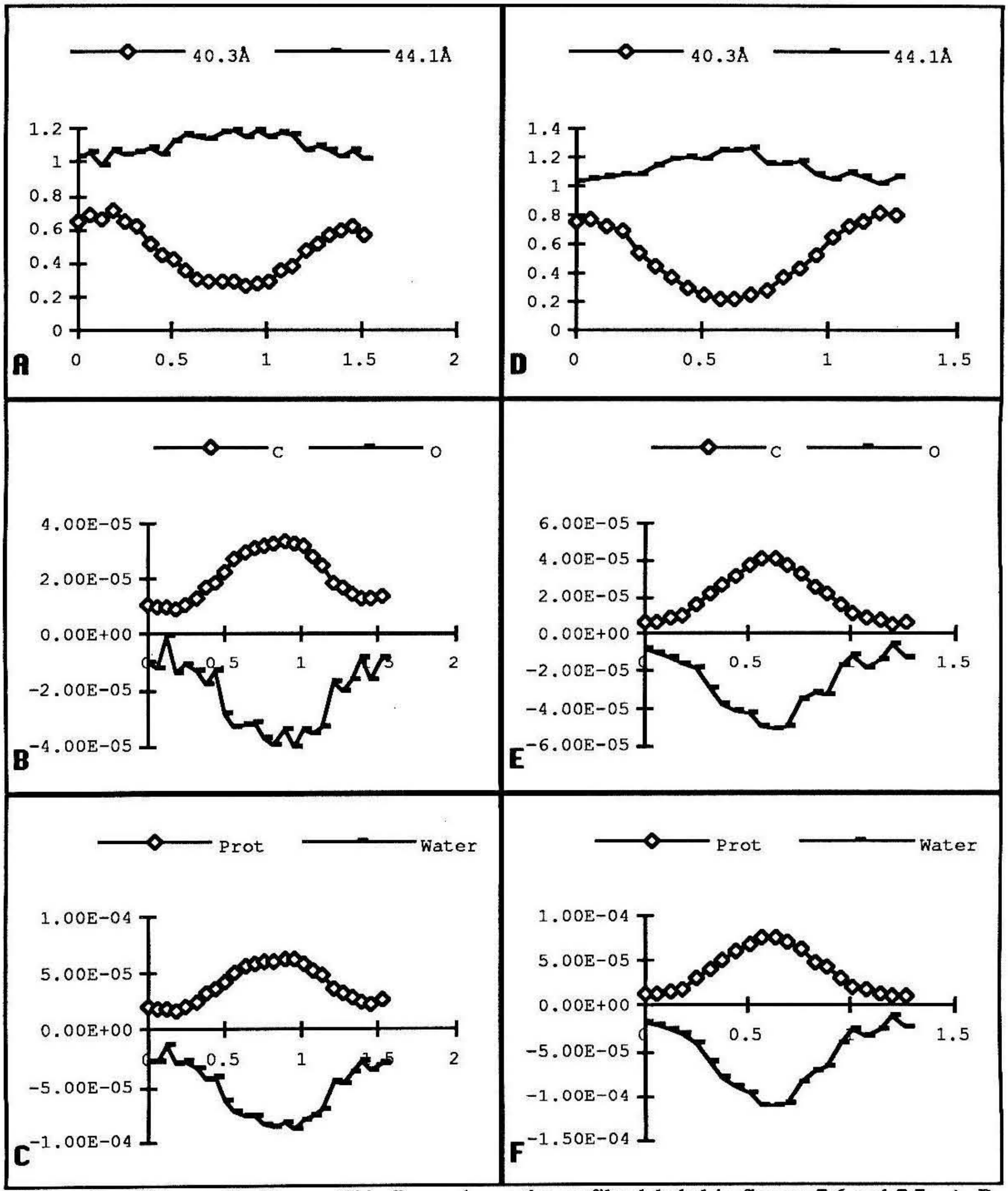

Figure 7.8 Feature Profiles This figure shows the profiles labeled in figures 7.6 and 7.7. **A**, **B**, and **C** are from profile 1. **D**,**E** and **F** are from profile 2. The x-axis units are in µm. **A** and **D** are transmission graphs from the images in figure 7.6. **B** and **E** are column mass graphs from figure 7.7A. **C** and **F** are column mass graphs from figure 7.7B.

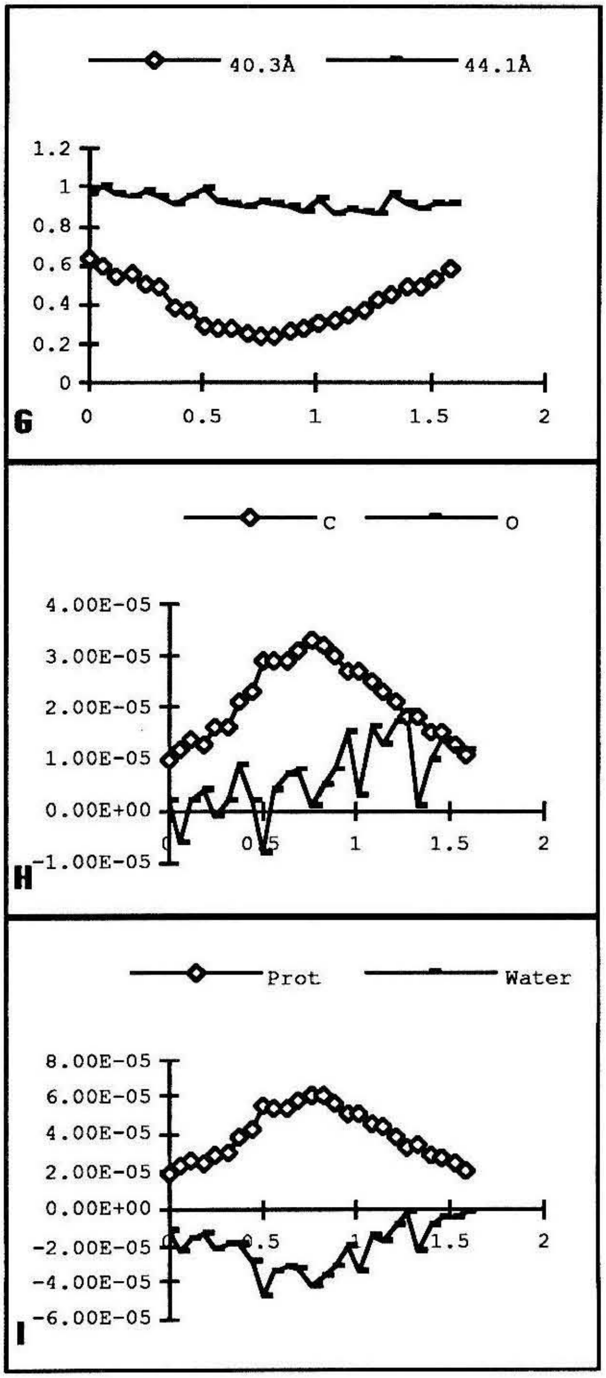

Figure 7.9 More Feature Profiles

This figure shows profile 3 from figures 7.6 and 7.7. **G** is a transmission graph from figure 7.6. **H** is a column mass graph from figure 7.7A. **I** is a column mass graph from figure 7.7B. The x-axis units are in µm.

In profiles 1 and 2 we see a clear displacement of water by protein. Profile 3, shown in figure 7.9 does not show the same tradeoff, and does not exhibit the T>100% feature in the λ=44.1Å image of figure 7.6. We can in fact model these granules and essentially replicate the results of the profiles. We use a two component cell and granule model, following chapter 3. Figure 7.10 shows the results of such a model, and duplicates the figures 7.8A and 7.8C. The model uses a spherical granule of radius 0.4μm in a cell of thickness 0.7μm and a uniform 1μm water layer. The granule has protein density 0.8gm/cm^3 and water density 0.1gm/cm^3. The cell body has protein density 0.1gm/cm^3 and water density 1gm/cm^3. These parameters are given in table 7.1. The granule material replaces the cell, it does not add to it in this model, that is a slight difference from the models of chapter 3. We do let the model granule be slightly thicker than the cell body, however this is not un-physical, it means that the granule causes the cell body to bulge a little over the granule center.

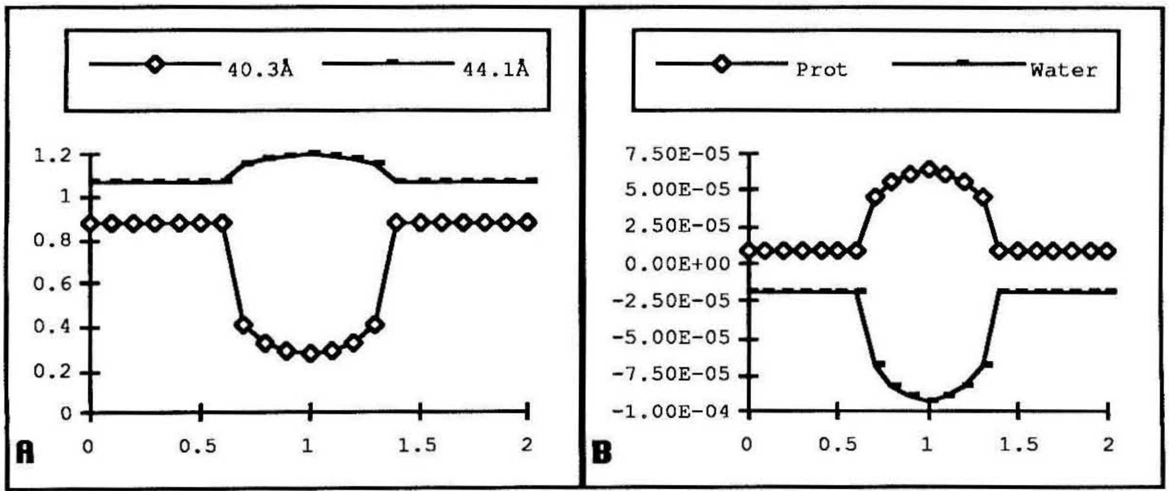

Figure 7.10 Model of Profile 1 A two component cell and granule model that qualitatively replicates the observed profile 1 of figures 7.6 through 7.8. The parameters of the cell and granule model are: listed in table 7.1. The ρ's in that table are densities, not column masses, the model includes a granule radius and a cell thickness. The model uses a 1μm uniform water layer. **A** is the transmission of the model for both λ=40.3 and λ=44.1Å, it should be compared to figure 7.8A. **B** is the protein and water column masses of the model relative to the 1μm water layer (i.e., relative to 10^{-4}gm/cm^2 water) in the background normalization regions. B should be compared to figure 7.8C.

ρ_{GW}	0.1gm/cm^3	ρ_{GP}	0.8gm/cm^3	granule radius	0.4µm
ρ_{BW}	1gm/cm^3	ρ_{BP}	0.1gm/cm^3	cell thickness	0.7µm

Table 7.1 The Two Component Model The ρ's here are densities, not column masses, the model includes a granule radius and a cell thickness. The model uses a 1µm uniform water layer.

7.6 The Limits of Elemental Analysis

The outlines of the analysis we have done should be clear. But, how accurate are our elemental mass estimations?. We must discuss the effect of noise in the original images, and the effect of radiation damage.

When we produce good images the noise in the transmission image, or the damage to the transmission image, is a small fluctuation on the transmission. That is, we can use $T'=T(1+\delta)$, for small δ and so obtain equation 7.4. With equation 7.3 and 7.4 we may write equation 7.5 as an estimate for the effect of Gaussian noise in the transmission images on the column mass decompositions. In the case of equation 7.5 δ is the relative standard deviation in each pixel of the transmission images. This result relies on the fact that statistical noise in the λ_1 image must be independent from the noise in the λ_2 image. The $\Delta\rho$'s are then estimates for the standard deviation of the calculated column masses.

We also derive a similar equation for the effect of radiation damage, equation 7.6. Here the first image, taken at λ_1, is unaffected by damge, but in the second, taken at λ_2, the sample has already been damaged in making the first image. That damage to the sample before the second image we estimate as ΔT and so $\delta=\Delta T/T$. This is of course mixing one and two component models, and should not be taken as more than a rough estimate.

$$-\ln[T(1+\delta)] = -\ln(T) - \delta + o(\delta^2) \qquad [7.4]$$

$$\begin{pmatrix}\Delta\rho_c\\ \Delta\rho_o\end{pmatrix}=\begin{pmatrix}\sqrt{(\mathbf{M}_{1,1}^{-1}\delta_1)^2+(\mathbf{M}_{1,2}^{-1}\delta_2)^2}\\ \sqrt{(\mathbf{M}_{2,1}^{-1}\delta_1)^2+(\mathbf{M}_{2,2}^{-1}\delta_2)^2}\end{pmatrix} \qquad [7.5]$$

$$\begin{pmatrix}\Delta\rho_c\\ \Delta\rho_o\end{pmatrix}=\mathbf{M}^{-1}\begin{pmatrix}0\\ -\delta\end{pmatrix} \qquad [7.6]$$

If we apply equation 7.5 to the protein and water decomposition of the images in figure 7.6 then we get $\Delta\rho_P=1.4\mathrm{x}10^{-6}\mathrm{gm/cm}^2$ and $\Delta\rho_W=5\mathrm{x}10^{-6}\mathrm{gm/cm}^2$, for noise in the decomposition due to noise in the original images. For radiation damage the original estimate of ΔT was 0.03 in the cytoplasm (which has $T_c=0.74$) , so $\Delta T/T=0.04$, and from equation 7.6 we get $\Delta\rho_P=1.4\mathrm{x}10^{-6}\mathrm{gm/cm}^2$ and $\Delta\rho_W=-9\mathrm{x}10^{-6}\mathrm{gm/cm}^2$. These are the systematic change in the calculated column mass due to radiation damage. All of these errors are significantly below the observations of the features profiled in figure 7.10. Remember the effect of radiation damage is not a fluctuation but a systematic error, quite capable of making a false signal in elemental analysis. If some structures are particulary vulnerable to radiation damage they could make still larger false signals in an elemental decomposition.

Working from a given noise or damage d, we can calculate the resulting noise or change in the calculated column mass $\Delta\rho/\rho$. Using the model of figure 7.10 we run this calculation with the first wavelength $\lambda_i=40.3$Å and the second wavelength λ_2 a variable. The results are graphed in figure 7.11 for noise, and figure 7.12 for damage. The 7.11A and 7.12A graphs are of $\Delta\rho/\rho$ for protein vs. λ_2. The 7.11B and 7.12B graphs are of $\Delta\rho/\rho$ for water vs. λ_2.

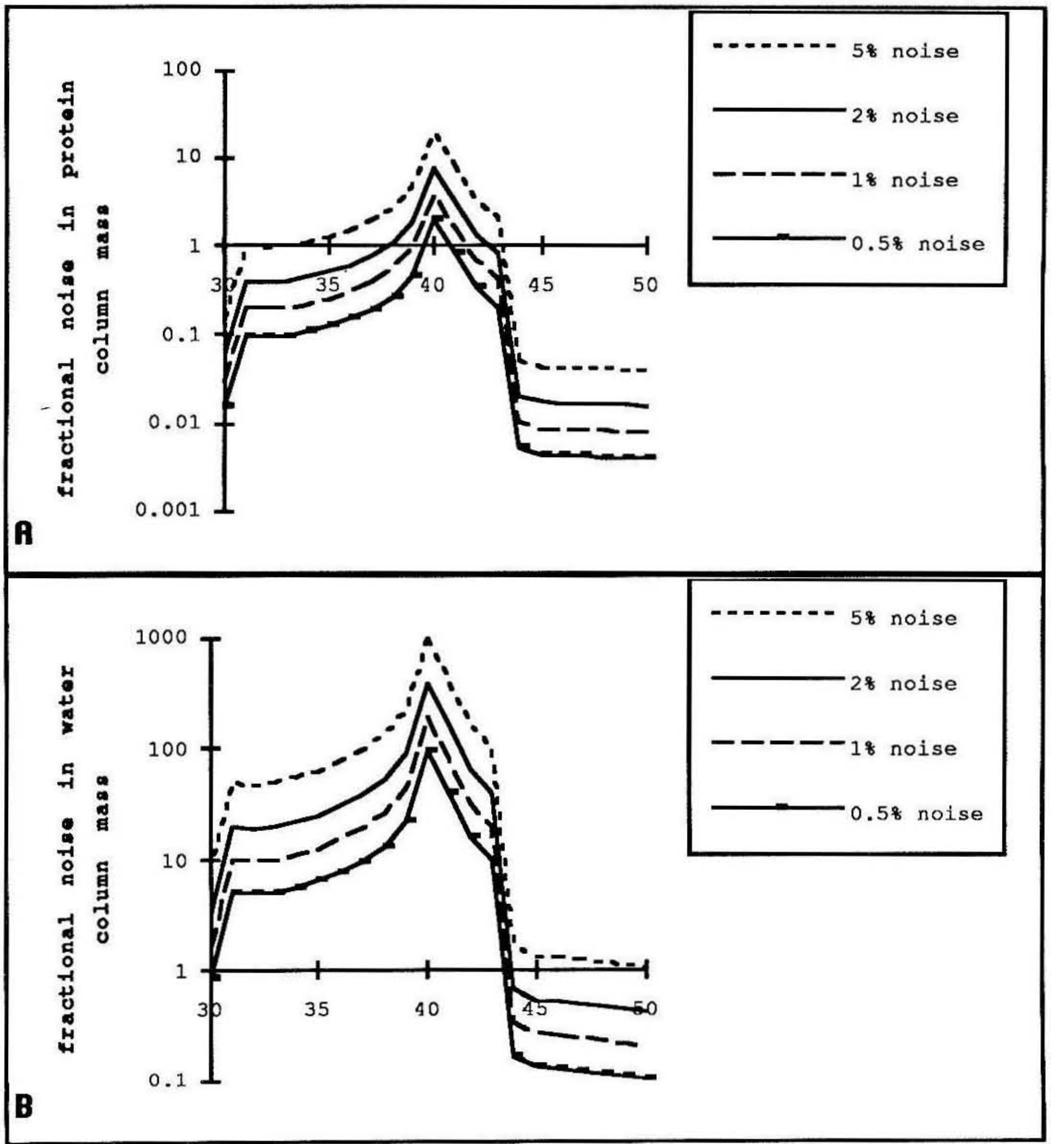

Figure 7.11 Effect of Noise on Decomposition From the cell and granule model, with the parameters that we used to model profile 1, we calculate the fractional noise in the calculated protein and water column masses due to fractional noise in the original transmission images. **A** is fractional noise in carbon column mass vs. λ_2 where λ_1=40.3Å. **B** is the fractional noise in water column mass vs. λ_2 where λ_1=40.3Å.

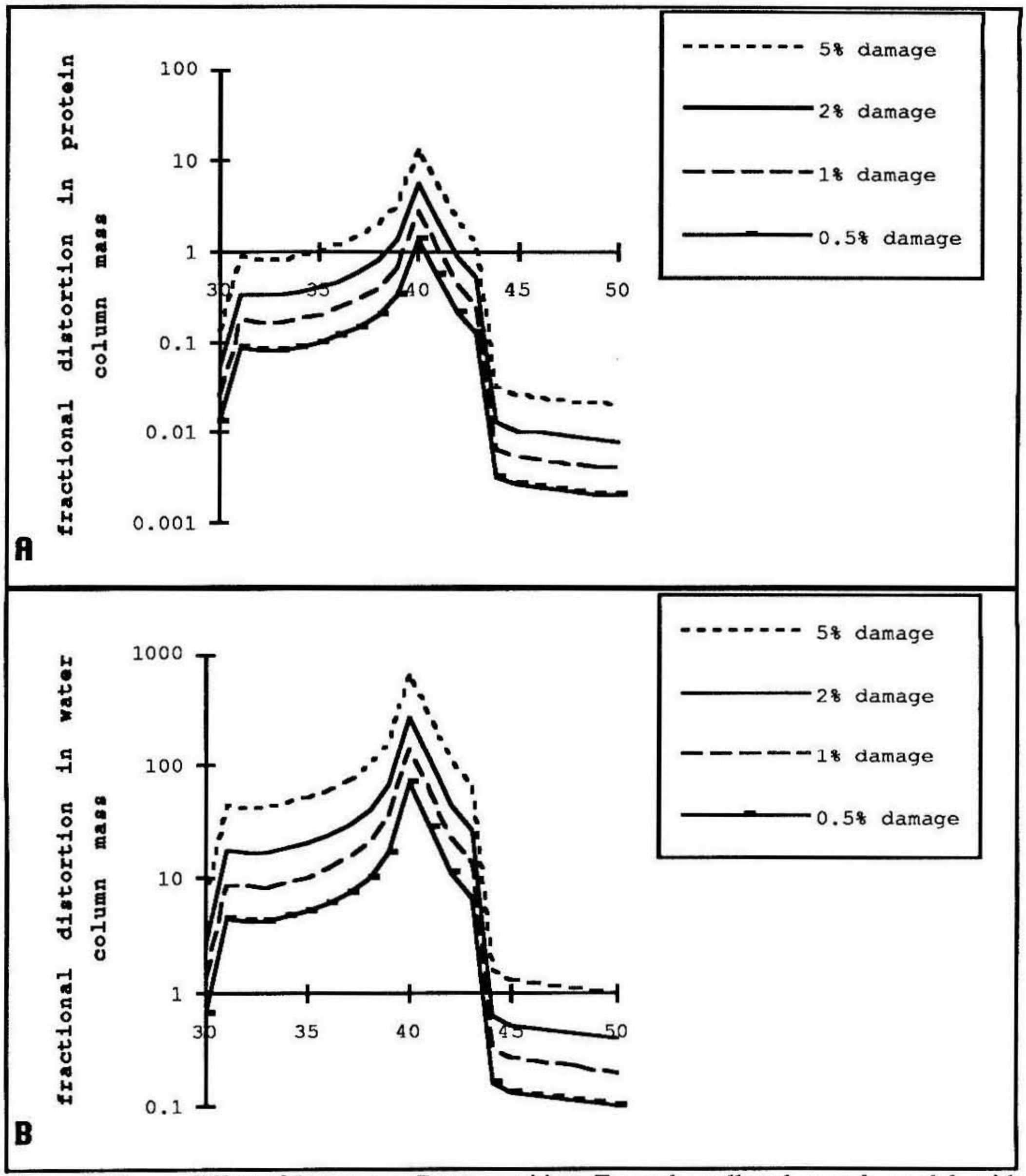

Figure 7.12 Effect of Damage on Decomposition From the cell and granule model, with the parameters that we used to model profile 1, we calculate the fractional change in the calculated protein and water column masses due to fractional damage ΔT/T in the first transmission image. **A** is fractional change in carbon column mass vs. λ_2 where λ_1=40.3Å. **B** is the fractional change in water column mass vs. λ_2 where λ_1=40.3Å.

Most qualitative features of the figures 7.11 and 7.12 would be the same for any λ_1 and any set of parameters of the cell and granule model. Results should improve as λ_2

moves away from λ_1 . And $\Delta\rho/\rho$ should be best when the step in λ crosses an edge. However, the fact that protein behaves better than water is due to this particular model cell. Other parameters could switch that behavior. It is possible for both protein and water column masses to have good behavior (say $\Delta\rho/\rho < 0.2$) for some features.

We expect to get the same type of tradeoff between noise and damage that we examined in chapter 5. Decreasing noise requires increasing flux which increases damage. This means that in principle, for any feature parameters, there is a "best we can do" $\Delta\rho/\rho$ for each given dx. Further improvement in $\Delta\rho/\rho$ requires going to larger pixel size dx, and giving up resolution. We have not yet done the detailed minimizations, similar to those in chapter 5, for general column mass decompositions.

7.7 Conclusion

This chapter has shown that bulk elemental analysis is possible with the STXM. We have produced elemental maps showing differences in composition amoung sub-micron features. The two component analysis that we have shown here can be developed in two related ways. The underlying equations clearly scale to the N image, N component case. N of three or four might be used to discriminate between protein, water, DNA and lipid. The same problems of noise and damage will of course appear in an N image analysis. Noise equations are essentially the same for N greater than two. The effects of damage will be complicated by multiple images, but the damage could be measured at each stage by inserting quick observational images between the images of the wavelength series. All this may be gone into as elemental analysis is developed further.

The other way in which it has been suggested that the STXM be used for elemental analysis is to do full spectra at particular points. This would mean finding a feature and taking a wavelenght spectrum of it with the microscope stage at rest. The issue of damage will be quite complicated. However producing spectra will offer the possibility of doing intense analysis of specific features that are found with regular images. It may also allow near edge structure to be explored for features in an image.

Our early steps in elemental analysis complement previous work in biomineralization[4] and suggest that one of the major virtues of the STXM may be in quantitative analysis of whole wet samples at high resolution.

7.8 Chapter 7 References

---

1 B.L. Henke, P.Lee, T.J. Tanaka, R.L. Shimabukuro, and B.K. Fujikawa, "Low Energy X-ray Interactions: Photoionization, Scattering, Specular and Bragg Reflection," in Atomic Data and Nuclear Data Tables **27**, 1 (1982) and the SF software as described in: M.M. Thomas, J.C. Davis, C.J. Jacobsen, and R.C.C. Perera, "A Program for Calculating and Plotting Soft X-ray Optical Interaction Coefficients for Molecules," (Lawrence Berkeley Laboratory, Berkeley, 1989) document LBL-27668.

2 J.M. Kenney, Ph.D. dissertation, State University of New York at Stony Brook, 1985.

3 Kenney J M, Jacobsen C, Kirz J, Rarback H, Cinotti F, Tomlinson W, Rosser R, Schidlovsky G , "Absorbtion microanalysis with a scanning soft X-ray microscope - mapping the distribution of calcium in bone," J. Microsc. Oxford (1985), 138, pp.321-328.

4 see references 2 and 3.

8 Conclusion

We have produced images which represent the state of the art in whole cell imaging with soft x-rays. For fixed whole cells we have taken images at theoretical resolutions of ~50-75nm, and in practice have measured FWHM of features down to near 100nm, without any exotic processing. For un-fixed (i.e., initially live) cells we have imaged with 100nm pixels and measured features down to 250nm. However, the initially live cell work has not been reproduced beyond the three cells shown in chapter 6.

We have developed, tested and used a wet cell for maintaining fixed or live cells on the STXM stage during imaging. Our design and the culture chips that go with it make the STXM compatible with almost all standard systems for surface adherent tissue culture. This compatibility is an essential requirement if biologists are to be able to use the microscope.

We have made some of the first measurements of radiation damage to images due to imaging. Those observations have led to a phenomenological model that can be used to build and test physical models of radiation damage. This model uses two observations derived in chapter 5. One, the damage caused by absorption of radiation in fixed cells is a linear loss of x-ray absorbing mass with cumulative energy absorbed. Two, a fair value for the slope of that linear relationship is $\alpha=-0.78\pm0.35$ in units of [C atom equivalent absorption] per [eV absorbed]. These observations have allowed us to model several different aspects of the imaging of fixed tissue.

The modelling led to several conclusions. The best operating point of the STXM in regards to detecting the smallest features with the best signal to noise is just above the nitrogen edge at wavelength (31-32Å). The exact limits of resolution depend on just how much contrast a feature to be detected has, however the best features are high contrast ones in a thin cell or no cell at all. A high contrast feature, having carbon density near 1gm/cm^3, might be detectable at S/N=5 at thicknesses down to 0.025μm if it can be found with pixel sizes of dx=0.075μm or more. On a voxel basis, i.e., if we want to observe an object of diameter d with a pixel size dx=d at S/N=5, we might be able to reach d=0.050μm. Doing better than that is unlikely, and will involve trading pixel size for S/N. All this does suggest that the soft x-ray STXM is approaching the best it can do on wet biological specimens, even though the actual x-ray optics may still improve by quite a lot.

We have produced elemental maps showing differences in composition among submicron features. The two component analysis that we have used in chapter 7 can be developed in two ways. One could make N image and N component analyses of whole cells. An N of three or four might be used to discriminate between protein, water, DNA and lipids as bulk components of whole cells. Alternatively the microscope could be used to make detailed wavelength spectra on features identified with standard STXM images.

The underlying result of this work is that the STXM has the ability to produce images of whole wet cells at resolutions of 50-100nm. However, our results on radiation damage suggest that the STXM may not be able to do much better than that on unprotected cell tissue. Both the ability of the STXM to measure the radiation hardness α and its ability to produce elemental decompositions suggest that the best feature of the STXM may be its ability to provide novel types of quantitative analysis of whole wet samples at high resolution.

9 Appendices

9.1 Appendix A Fabrication--Culture Substrates

Fabrication Process for STXM windows

9.1.1 The Starting Wafers

We get 3" Si wafers <100> un-doped and polished both sides to 8-10 mils (200-250um) Our source of lapped and polished wafers is PCA.

9.1.2 The Overall Procedure

9.1.3 Nitride layer

We get ~1000Å Low Stress LPCVD Nitride[1] (~Si_1N_1) deposited on both sides at Berkeley's Micro Lab (4th floor Cory Hall, mail to debra@argon.berkeley.edu). The optimum batch size is 10 wafers or less in their furnace. We get thickness of 1000Å±10%. Berkeley takes wafers as they come from PCA, and cleans with a piranah etch (4:1 H_2SO_4:H_2O_2.) Then deposit SiN for 20min at 835°C, 300mT total pressure, 3:1 DCS:NH_3.

We use wafer quarters for our processing (before '91) So we cut the wafers in quarters with edges along their crystal planes, and do a standard organic clean[2] in batches of 12 quarters (q's.)

9.1.4 The EDP mask

The procedure

soft bake 10 min

puddle then spin HMDS adhesion promoter 4k 30sec

spin AZ 1350J-SF 4k 30sec

soft bake 30 min

expose 11 sec @11 with 3mm EDP mask

develop in 1:1 Az developer:diH20 60 sec

cleaning & drying chuck first spin Adhesion promoter and 1350J as above on backside of q's

plasma etch EDP side

use teflon plate, 6q's at a time in small plasmod EDP side up.

flush 3 min with CF4

etch at full power for 20 min

strip resist 15min Acetone Ultrasonic

clean

15 min Ethanol Ultrasonic

15 min diH20 Ultrasonic

blow dry

9.1.5 Fiducial Marks

soft bake 10 min

puddle then spin HMDS adhesion promoter 4k 30sec

spin AZ 1350J-SF 4k 30sec

soft bake 30 min

expose 13 sec @11 with true Fiducial mask

6 q's at a time

5min Chlorobenzene immersion

blow dry

5min hard bake

develop in 1:1 Az developer:diH20 about 3-5 min its best to watch the first one to check the time.

this should give visible overhang in microscope

put q's 4 at a time in glass dish in plasmod for an O2 plasma (3 min full power)

Evaporate 50Å Cr and 150Å Au on q's (4 at a time try for better than 5x10-6T)

do liftoff with 15min Acetone Ultrasonic

clean

15 min Ethanol Ultrasonic

15 min diH20 Ultrasonic

blow dry

9.1.6 Bulk Silicon Etch

We do EDP 12 q's at a time, use the large reflux chamber and enough EDP to cover + 1" the q's

set the hot plate to 105C

put the q's in when T reaches 90C+

wafers should bubble almost immediately
etch will take 5-7 hours, check every hour after 3
q's should not fall apart, with current mask.
when done remove to diH20 for 3 rinses then to Ethanol
blow dry whole q's from Ethanol
yield should be 80% or better, of intact separate chips.

9.2 Appendix B Caltech Wet Cell Drawings

What follows are five drawings describing mechanical design and assembly of the Caltech wet cell.

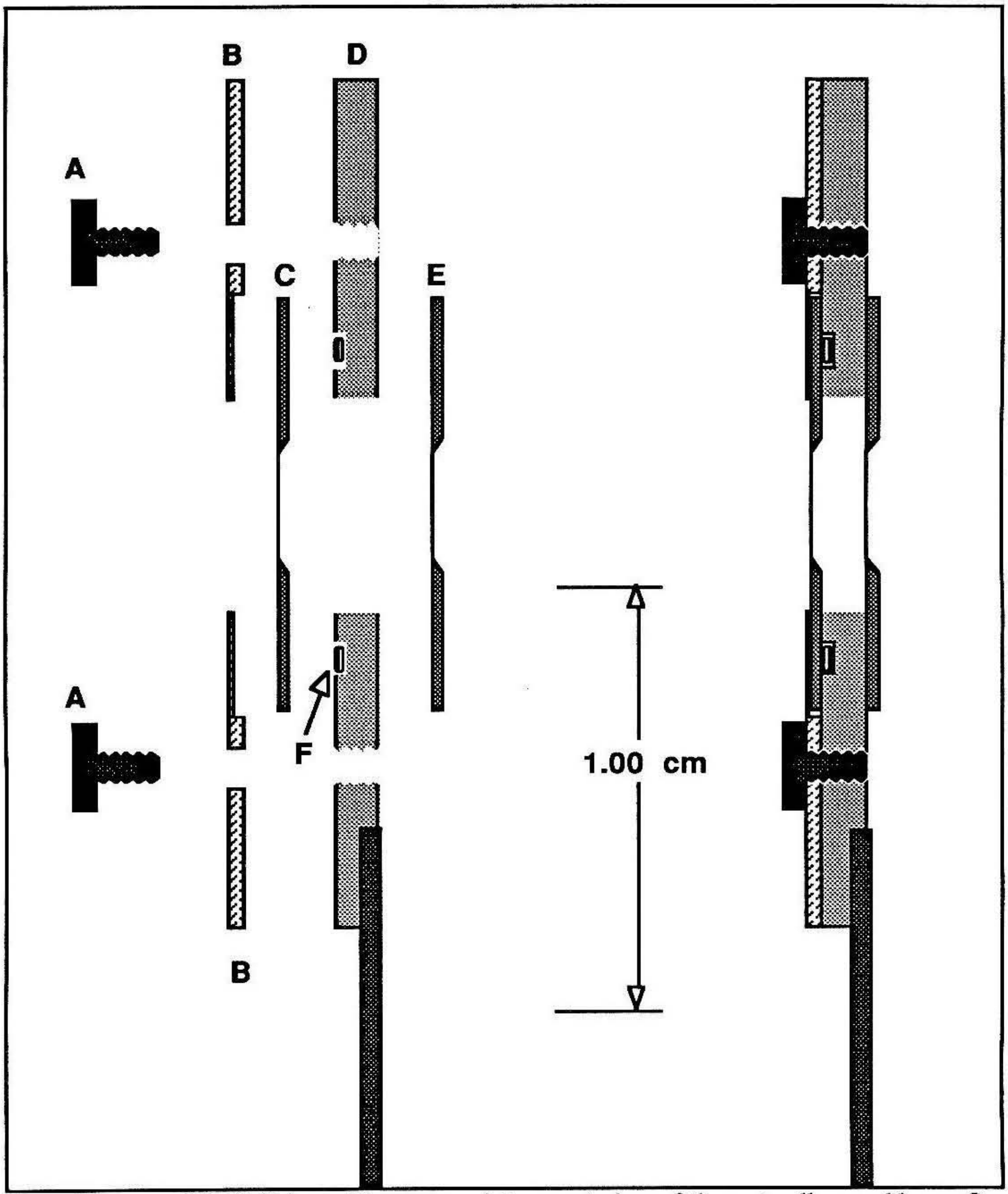

Figure B1 Wet Cell Assembly A two part view of the wet cell assemblage. On the left we have an exploded view of the pieces of the wet cell, and on the right we have the assembled pieces. The drawing is to scale, the scale bar is 1cm. **A** labels the clamping screws that hold the brass plate and thus the specimen chip to the body of the wet cell. There are 4 of these screws, though only 2 are shown here. **B** labels the brass plate -- which is one piece, though it appears here as two due to its crossection. **C** labels the specimen chip which is held to the wet cell body by the brass plate. **D** labels the body of the wet cell, which is machined from a 2 cm stainless steel disk 1mm thick. **E** labels the exit window, which we glue onto the back of the wet cell body. **F** labels the o-ring, in its groove. The o-ring provides a tight seal between the clamped on culture chip and the body of the wet cell.

Upstream (Front) face view of wet cell body

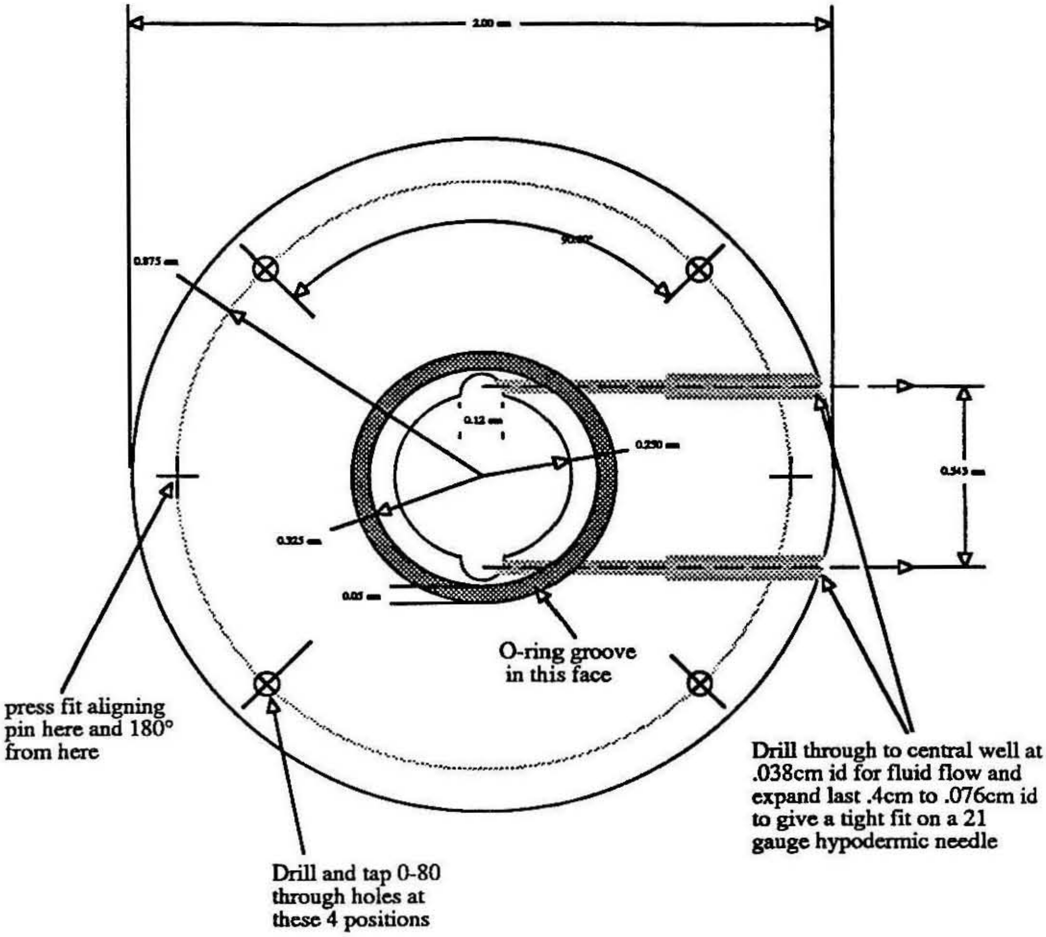

MATERIAL: Stainless 303

Figure B2 Front View of Wet Cell Body

Edge view of wet cell body from left when facing rear of wet cell

Rear view of wet cell body

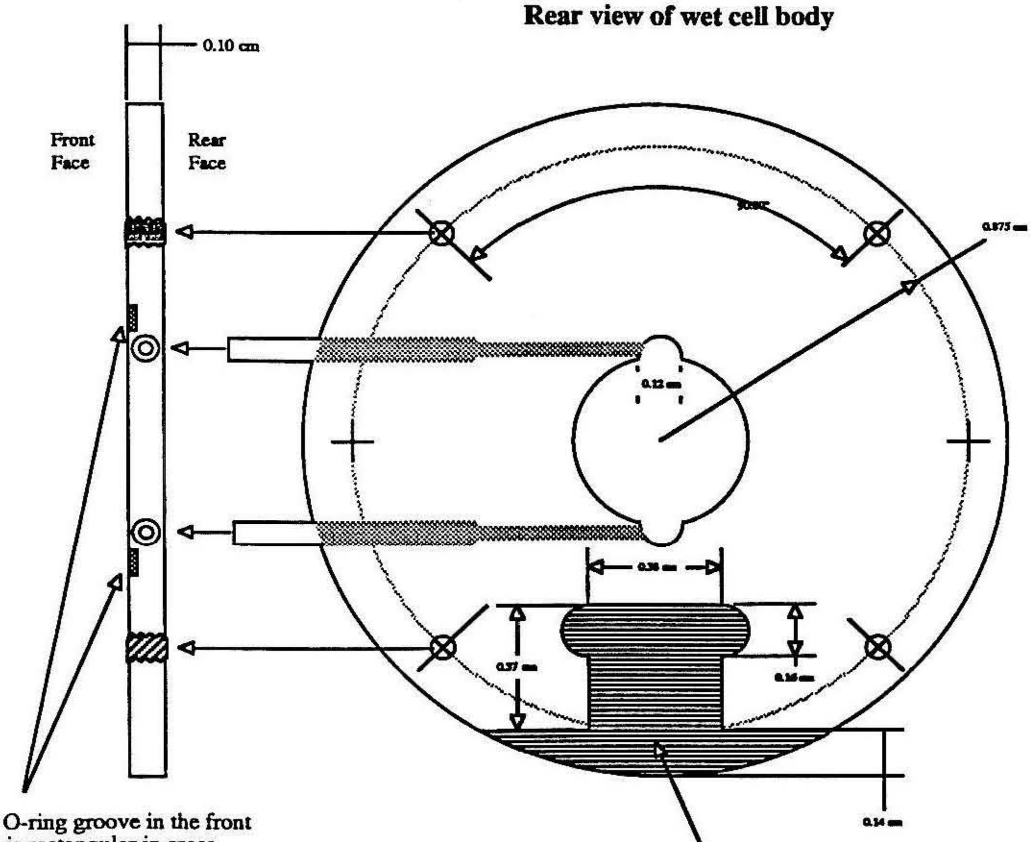

The O-ring groove in the front face is rectangular in cross section, .025cm deep and .076cm wide. The ring has .650cm id.

For mating to the wet cell holder this region is milled away .05cm deep, from rear of wet cell body (use .062' or .157cm end mill.)

Figure B3 Rear View of Wet Cell Body

Wet Cell cover plate

MATERIAL Brass

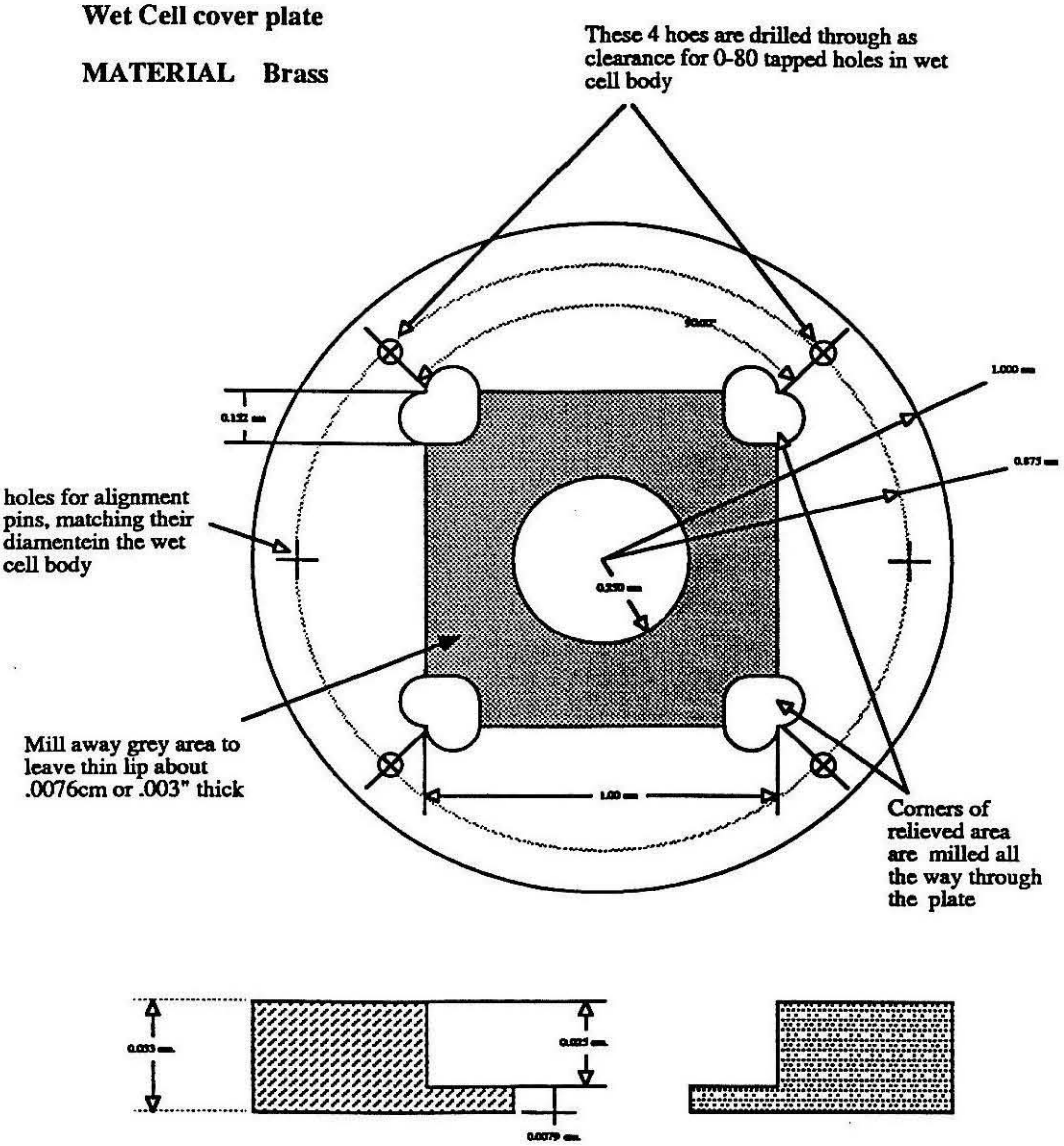

EDGE View of brass plate, at 10x vertical scale

Figure B4 Wet Cell Brass Cover Plate

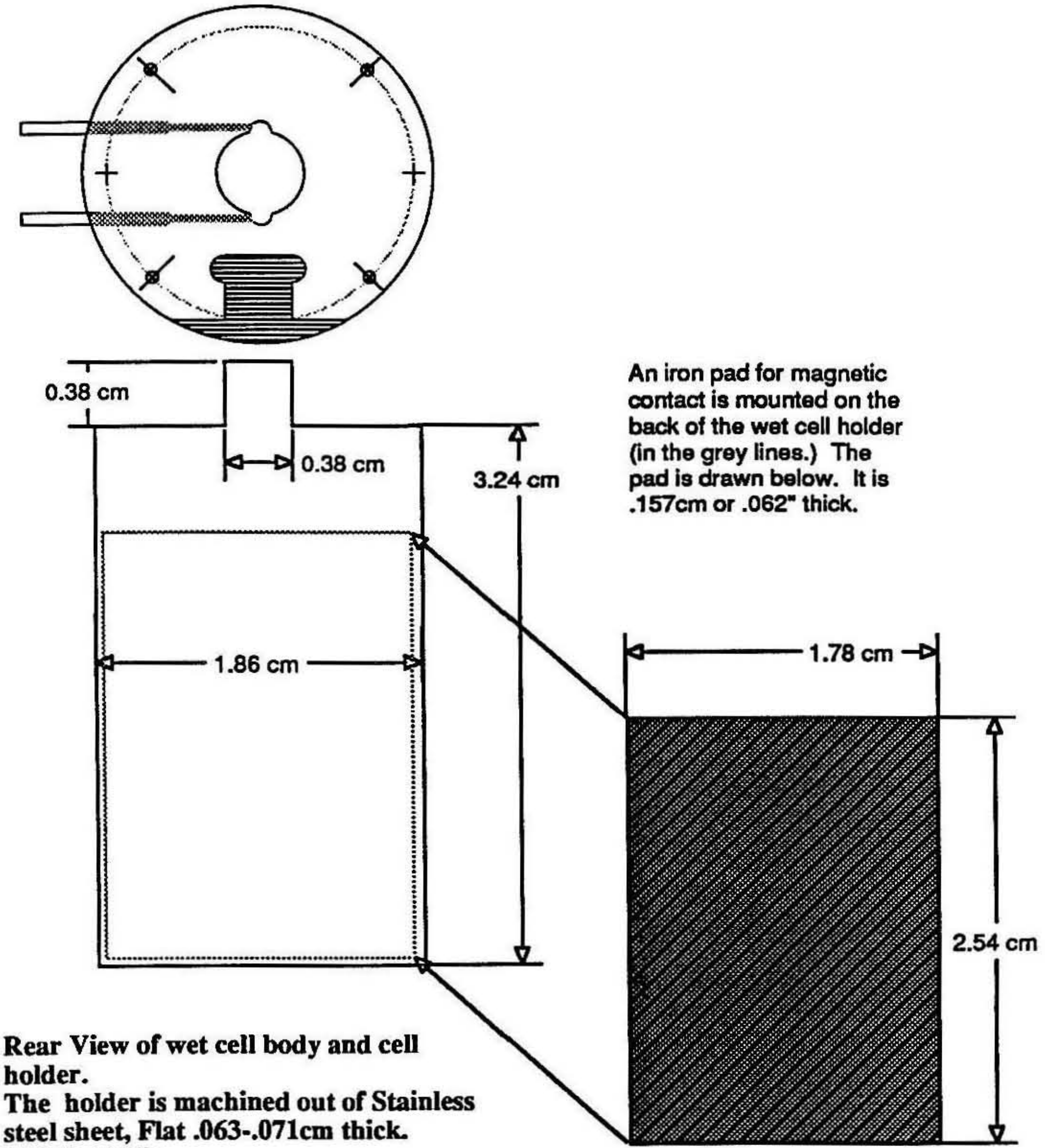

An iron pad for magnetic contact is mounted on the back of the wet cell holder (in the grey lines.) The pad is drawn below. It is .157cm or .062" thick.

Rear View of wet cell body and cell holder.
The holder is machined out of Stainless steel sheet, Flat .063-.071cm thick. (.025"-.028")

Figure B5 Wet Cell Body and Holder

9.3 Appendix References:

---

[1] C.H. Mastragelo, Y-C Tai, and R.S. Muller "Thermophysical Properties of Low-Residual Stress, Silicon-Rich, LPCVD Silicon Nitride Films" Sens. Actu. A, **23**, (1-3) p856-860 (1990).

[2] Standard Cleaning Procedure (Organic)

15min Ultrasonic in TCE
15min Ultrasonic in Acetone
15min Ultrasonic In Ethanol
15min Ultrasonic in diH$_2$0
blow dry